Rapid processing of dye-sensitised solar cells using near infrared radiative heating.

Hooper, Katherine Elizabeth Anne

Rapid Processing of Dye-sensitised Solar Cells using Near Infrared Radiative Heating

Katherine Elizabeth Anne Hooper

Dr. Trystan Watson

Prof. David Worsley

Thesis submitted to Swansea University in fulfilment of the requirements for the Degree of Doctor of Philosophy

Materials Research Centre, College of Engineering

Swansea University

2014

DECLARATION

This work has not previously been accepted in substance for any degree and is not being concurrently submitted in candidature for any degree.

Signed ..... (candidate)

Date 7/11/14

STATEMENT 1

This thesis is the result of my own investigations, except where otherwise stated. Where correction services have been used, the extent and nature of the correction is clearly marked in a footnote(s).

Other sources are acknowledged by footnotes giving explicit references. A bibliography is appended.

Signed ..... (candidate)

Date 7/11/14

STATEMENT 2

I hereby give consent for my thesis, if accepted, to be available for photocopying and for inter-library loan, and for the title and summary to be made available to outside organisations.

Signed ..... (candidate)

Date 7/11/14

Summary

Dye-sensitised solar cells (DSCs) have the potential to be a low cost solar cell candidate due to the relatively low cost of materials and ease of processing. Also, unlike traditional silicon solar cells, DSCs can be lightweight and flexible, and perform well in diffuse sunlight and indoors which make them an extremely attractive prospect. This thesis investigates the time intensive heating stages associated with the fabrication of a DSC which are currently a bottleneck for translating this technology from the laboratory to an industrial scale. In addition some steps associated with the fabrication of a DSC share similarity to other technologies so these methods could be extremely applicable and versatile.

Near infrared (NIR) radiative heating was used here to drastically reduce the heating times associated with DSC fabrication steps. NIR heating involves the absorption of NIR photons by the free electrons of an infrared absorbing substrate which releases thermal energy rapidly. NIR radiation has previously been used for the heating of metallic substrates but this is the first time it has been used to heat glass based substrates, which significantly broadens the potential applications of NIR heating. Upon 12.5 s of NIR exposure FTO and ITO coated glass reached significantly high temperatures, temperatures corresponding well to those required for the DSC heating steps.

NIR radiation was used to sinter TiO_2 working electrodes and thermally platinise counter electrodes on FTO glass in 12.5 s, 144 times faster than the conventional oven heating of 30 minutes. When assembled into DSC devices these electrodes performed identically to their oven equivalents. When combined with a faster dyeing process this enabled the overall laboratory manufacturing time of a DSC to be reduced from 123 min to 5 min with no compromise in efficiency which is an extremely promising step for the viability of DSC commercialisation.

Acknowledgements

Firstly I would like to thank my supervisors Dr. Trystan Watson and Prof. Dave Worsley. I am very grateful to Dave for the opportunities he has given me and for being instrumental in bringing fantastic resources for the important topic of solar cell research to South Wales. I am extremely thankful to Trystan for giving me such a positive introduction to the world of research when I was a lowly undergrad and for giving me great support and advice throughout this project. I would also like to thank my sponsors EPSRC and Tata Steel Colours for funding.

In particular I'd like to thank Dr. Matt Carnie for his help with transients and impedance spectroscopy, Dr. Cecile Charbonneau for her SEM and TiO_2 paste expertise, Dr. Matthew Davies for XRD measurements and help with pump dyeing, Jenny Baker and Dr. Alice Williams for their help with cyclic voltammetry, Dr. Bruce Philip for his help with IR camera filming and Dr. Ian Mabbett for general NIR advice. I'd also like to thank the rest of the PV team; Joel, Dan, Neil, Wraggy, James and Pete for making the lab such a fun and interesting place to work in!

Thanks to my family for their support. I would like to thank my partner Gareth Davies for his fantastic support and immense patience during the writing of this thesis. "I think I should be finished by next week..."

I would like to dedicate this thesis to the memory of my Grandfathers Ronald Michael Hooper (30/9/26-4/5/09) and Derek Rogers (15/6/33-10/9/14).

List of abbreviations

TCO – Transparent conducting oxide

DSC – Dye-sensitised solar cell

FTO – Fluorine-doped tin oxide

ITO – Tin doped indium oxide

FTIR – Fourier transform infrared

ATR – Attenuated total reflectance

CVD – Chemical vapour deposition

CB – Conduction band

VB – Valence band

EIS – Electrochemical impedance spectroscopy

CV – Cyclic voltammetry

IPCE – Incident photon-to-current conversion efficiency

EQE – External quantum efficiency

UV – Ultraviolet

IR – Infrared

NIR – Near infrared

List of contributions

Journal publications

C. Charbonneau, K. Hooper, M. Carnie, J. Searle, B. Philip, D. Wragg, T. Watson, and D. Worsley, "Rapid radiative platinisation for dye-sensitised solar cell counter electrodes," *Progress in Photovoltaics: Research and Applications* (2013) doi: 10.1002/pip.2368
Based on the work in Chapter 4

K. Hooper, M. Carnie, C. Charbonneau, and T. Watson, "Near infrared radiation as a rapid heating technique for TiO_2 films on glass mounted dye-sensitized solar cells" *International Journal of Photoenergy* (2014) in press
Based on the work in Chapter 5

Papers are also in preparation based on the work in Chapters 3/6 and Chapter 8

Conferences

- PVSAT-9, *Swansea* (April 2013): **Poster and conference proceedings paper**
- Great Western Photoelectrochemistry Meeting, *Bath* (June 2013): **Presentation**
- 11th International Conference on Materials Chemistry (MC11), *Warwick* (July 2013): **Poster**
- Challenges in Chemical Renewable Energy (ISACS12), *Cambridge* (Sep 2013): **Poster**
- Next Generation Materials for Solar Photovoltaics, *London* (Jan 2014): **Poster**
- Hybrid and Organic Photovoltaics (HOPV14), *Lausanne, Switzerland* (May 2014): **Poster**

Contents

1. Introduction

1.1 Background

1.1.1 Electricity sources

Electricity has become essential to modern life. Fossil fuels have always been the main source of electricity generation but are becomingly increasingly less desirable due to depleting natural reserves, environmental impacts and rising costs. Another major drawback is location of reserves with many countries forced to import electricity or fuels to generate it. Still oil, coal and natural gas remain the main energy generation sources [1] despite being unsustainable, with the adoption of more renewable sources of energy extremely slow (including hydroelectricity, wave, tidal, geothermal, biomass, wind and solar energy). In 2012 4.7% of the world's electricity generated by renewables but only 15 countries had over 10% of their electricity generated from renewables [2].

In the United Kingdom 10.8% of the electricity generated was from renewable sources in 2012 and wind farms are currently the dominant contributor with only 3% of the renewable electricity coming from photovoltaics [3]. Photovoltaics are an extremely promising source of renewable energy that could easily be integrated into existing or new buildings so that electricity could be generated without using extra space or adding a significant cost. Although there is less sunlight on average in the UK than countries to the south the potential electricity available to be generated from sunlight could meet the entire UK's demands. Certain solar cell technologies perform well or even better in diffuse sunlight than direct sunlight and even under indoor lighting conditions such as dye-sensitised solar cells.

1.1.2 Solar cell requirements

The photovoltaic effect is the direct conversion of light into electricity. In a solar cell a photon is absorbed to generate charge; this charge then requires separation and collection. Desirable criteria for an ideal solar cell material, both in terms of the material properties and commercialising into modules, are:

1. *Band gap between 1.1 and 1.7 eV*

A band gap is the forbidden space between the energy levels of the conduction band and the valence band in a semiconductor. Materials with a band gap between 1.1 and 1.7 eV relate to the energy of visible light photons which is where the majority of electromagnetic

radiation is emitted by sunlight (figure 1.1). For tandem solar cells (where more than one absorbing layer is used) often different band gaps of materials are used so that a wide range of photons can be collected (some that absorb nearer the ultraviolet, some in the infrared etc). The sensitizers used in dye-sensitised solar cells are discrete molecules so the energy levels between the highest unoccupied molecular orbital (HOMO) and lowest unoccupied molecular orbital (LUMO) is what determines their absorption range.

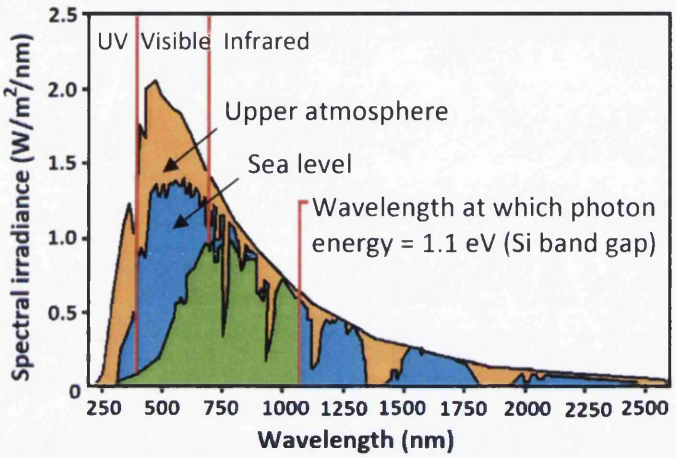

Figure 1.1: Distribution of the solar spectrum on Earth at the upper atmosphere and sea level with the absorption range of crystalline silicon shown in green (reproduced from [4])

2. *Direct band structure*

For inorganic semiconductors it is more desirable for the material to have a direct band gap (the top of the valence band aligns to the bottom of the conduction band gap), e.g. CdTe, than an indirect band gap, e.g. crystalline silicon. A direct band gap material has a higher light absorption coefficient which allows a thinner layer of material, saving, cost, and making processing easier.

3. *Readily available, abundant, non-toxic materials*

Ideally the solar cell should be made of abundant and easily available materials, so that the material source is secure for the future. Not only would non-toxicity be beneficial for the processing but it would enable the technology to be commercialised faster (easing the requirements of long term environmental impact testing and recycling after use).

4. *Easy, reproducible deposition technique suitable for large area production*

Ideally the material should be compatible with simpler deposition techniques with no requirements for vacuum and low temperatures to reduce the energy needed to make the device and thus improve the energy payback and lower the cost. It also needs to be suitable for large area production and fast processing is desirable.

5. *Long term stability*

Long term stability is critical especially for building integrated solar cells where they are not easily replaceable; silicon solar cells normally have a minimum lifetime guarantee of 25 years. Solar modules need to withstand extreme temperature cycling, exposure to moisture (usually encapsulated), and long term light exposure where the absorber or certain materials in the structure may be susceptible to certain types of light (e.g. ultraviolet).

6. *Good photovoltaic conversion efficiency*

A good energy conversion efficiency is necessary to validate the total cost of the module (materials, manufacturing and installation) and generate a certain amount of electricity.

1.1.3 Semiconductors and solar cell operation

In an inorganic solid material where the atoms are in close proximity to each other the electrons from surrounding atoms may influence each other and split into series of electronic states known as electronic energy bands. The space between these energy levels is called a band gap or forbidden band, where normally energies within this gap are not available for electron occupancy. The bands of greatest importance in terms of electronic and optoelectronic properties are those nearest the Fermi level (this is the top of electron energy levels at absolute zero, 0K). The closest band above the Fermi level is called the conduction band and the closest band below it is called the valence band. In a metal there is no band gap; the conduction band and valence band overlap so its electrons are dissociated from their parent atoms resulting in high electrical and thermal conductivity. In an insulator and a semiconductor the valence band is filled with electrons but the conduction band is unoccupied. The band gap, E_g, between the valence and conduction band is wide for an insulator and narrow for a semiconductor, typically below 2 eV in the latter. For an electron to become free in an insulator or semiconductor it needs to be promoted across the band gap into an empty state at the bottom of the conduction band, the energy required to excite an electron is equal to E_g. This energy could be supplied by electricity, heat or light.

For use in electronic devices the semiconductor is doped to improve conductivity of charge carriers which shifts the bands as shown in figure 1.2. An intrinsic semiconductor is one with no doping where the Fermi level, E_f, lies in the middle of the band gap. For an n-type semiconductor an impurity atom is introduced which donates an electron to the conduction band shifting the E_f upwards in the band gap to within vicinity of the donor state. The majority charge carriers in these semiconductors are electrons and the minority carriers are

holes. For a p-type semiconductor the impurity atom introduced devoids one of the covalent bonds of an electron, this deficiency is seen as a hole weakly bonded to the impurity atom. The carriers created in this case are holes; the E_f is shifted downwards towards the acceptor state near the valence band which accepts electrons. Traditional inorganic solar cells, such as crystalline silicon, are typically based on a p-n junction (figure 1.3).

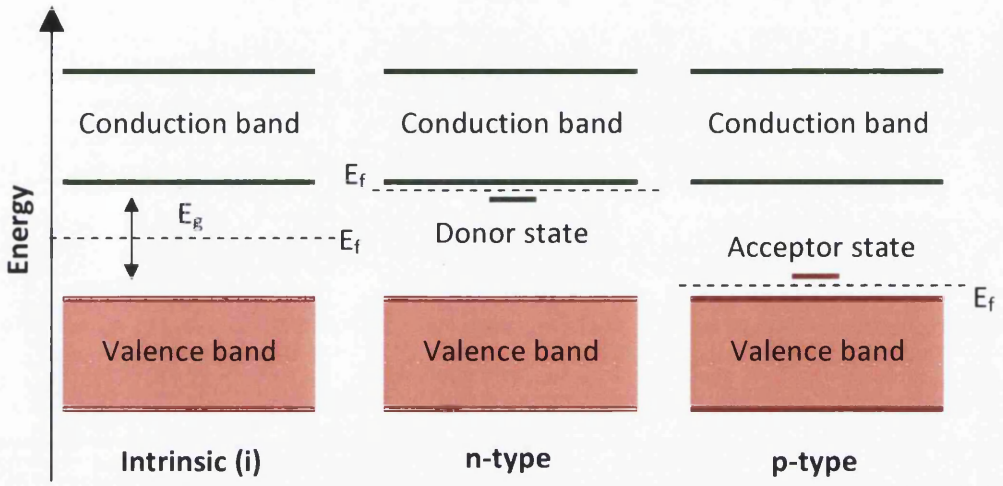

Figure 1.2: Band energy diagram of an intrinsic (i), n-type and p-type semiconductor

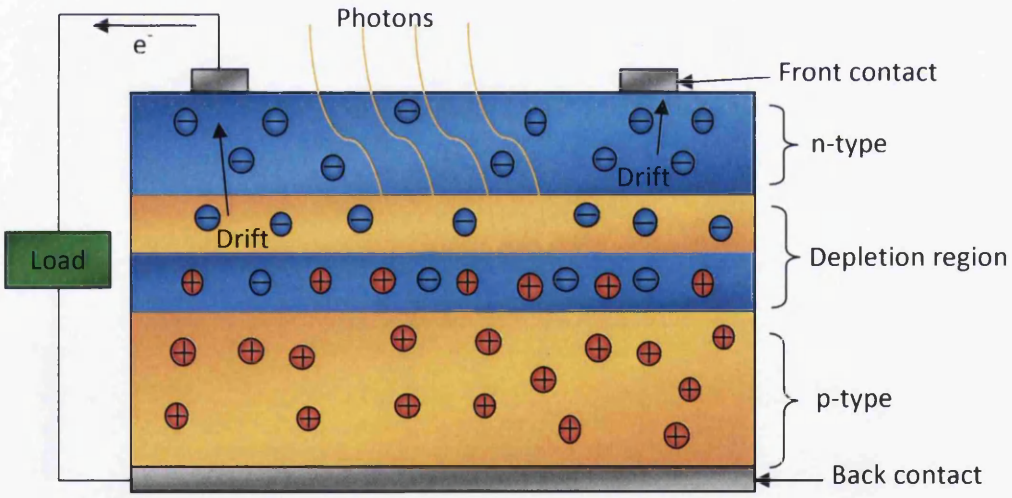

Figure 1.3: Diagram of the operation of a generic p-n junction solar cell such as crystalline silicon

In a p-n junction solar cell there is an n-doped layer and a p-doped layer and in between these is a junction where some of the electrons from the n-type have diffused into the p-type (depletion region). When a photon is absorbed a free electron and hole are created; the electrons drift to the front contact and the external circuit, the holes flow to the back contact to recombine with electrons that have been through the circuit. Only photons with sufficient energy to create an electron-hole pair (energy greater than the band gap) will

contribute to the energy conversion process, photons of energy less than the band gap pass through the material and release energy as heat. Solar cells with an organic component such as dye-sensitised solar cells (DSCs) and organic solar cells operate in a different way (see section 1.2.1) producing excitons (tightly bound electron-hole pairs) rather than free electron-hole pairs.

1.1.4 Solar cell technologies

Solar cell technologies (see figure 1.4) can be categorised as first generation (e.g. crystalline silicon), second generation thin films (e.g. cadmium telluride, copper indium gallium selenide (CIGS), and amorphous silicon), and emerging photovoltaics (organic, dye-sensitised and perovskite solar cells).

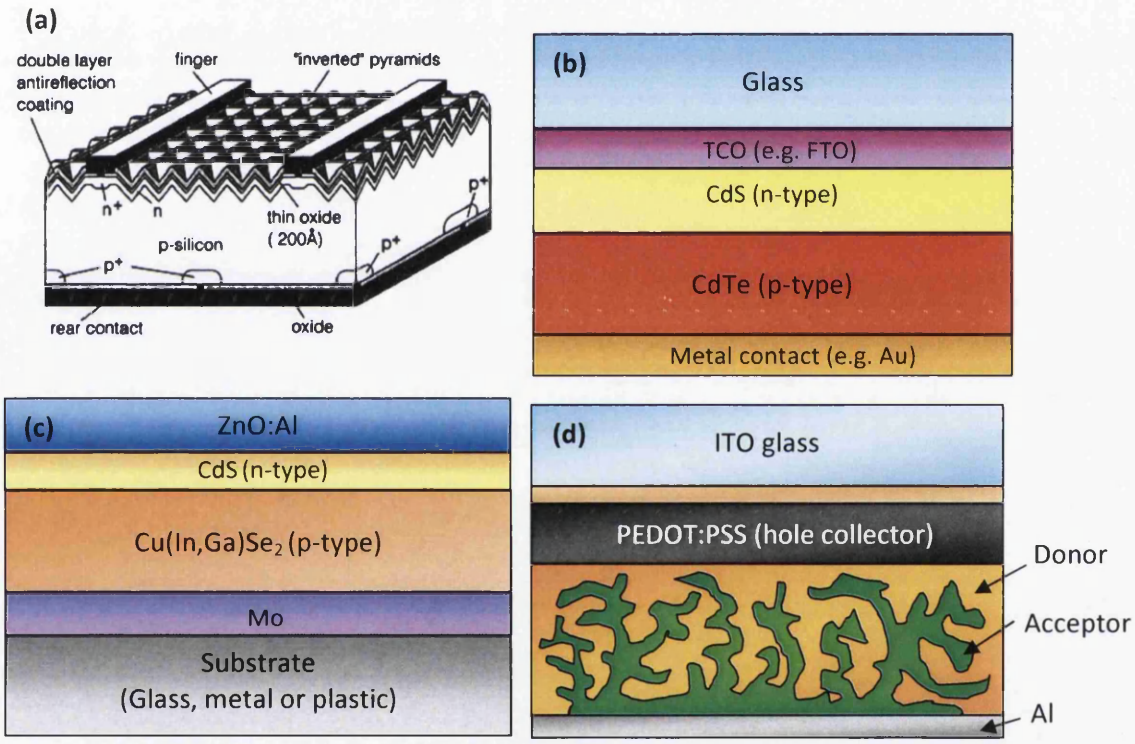

Figure 1.4: Different solar cells; (a) crystalline silicon [5], (b) CdTe, (c) CIGS, and (d) a polymer bulk heterojunction organic solar cell

Crystalline silicon solar cells (figure 1.4.a) have been extensively researched since 1954 [6] and currently account for over 80% of all solar module shipments [7]. Crystalline silicon has a band gap of 1.1 eV which is well suited for solar energy conversion but it is an indirect semiconductor (emission of a phonon is required to absorb a photon which costs additional energy) so it requires a thick layer of high purity material for sufficient light absorption. The main breakthroughs for silicon solar cells have been in device structure (to improve light

harvesting), wafer slicing techniques to minimise waste, and the employment of screen printing silver contacts.

Cadmium telluride (figure 1.4.b) has a band gap of 1.44 eV and is based on a heterojunction of p-type CdTe and n-type CdS. Research into CdTe solar cells began in the 1950s and recent progress resulting in over 20% efficiency in 2014. CdTe modules are very well developed with the main manufacturer being First Solar; they have a record module efficiency of 17% [8], a commercial module manufacturing time of 2.5 hours [9] and were the second biggest solar module manufacture in 2010 (the only manufacturer in the top ten not producing crystalline silicon) [10]. Issues for CdTe include the supply of Te which is mainly obtained from anode sludge waste during electrorefining of copper [11], the toxicity of cadmium, which has led to extensive studies of CdTe modules for the toxicity of Cd [12], and lower efficiencies on metallic substrates (13.6% on flexible metal foil [13]).

Copper indium gallium selenide (CIGS) solar cells (figure 1.4.c) have an absorber layer of the semiconductor compound $CuIn_xGa_{(1-x)}Se$ and CdS as the n-type layer. They have a similar cell efficiency to CdTe but high efficiencies are achievable on flexible substrates such as plastic [14]. Module efficiencies are currently lower than CdTe modules. The main issues for CIGS are the complexity and cost of manufacture and the low throughput with most research now focused on reducing the cost of manufacture and investigating alternative element systems.

Organic solar cells (figure 1.4.d) are based on small molecules or semiconducting polymer acceptor materials with small molecule donors. They are molecular absorbers so charge transport has to proceed by hopping between localised states which results in a lower charge carrier mobility than inorganic semiconductors and they produce excitons so efficient charge separation is necessary. The main developments of organic solar cells have been through the device architectures such as bulk heterojunctions [15] and the materials. Polymer based cells are now over 8% [16] and the record efficiency organic device is an oligomer based tandem [17].

Figure 1.5 shows the NREL research efficiency chart [18] which gives an indication of the performance progress of different types of solar cells over the last 40 years. The solar cell of interest in this work is the dye-sensitised solar cell which is extremely attractive for low cost and easily processed modules.

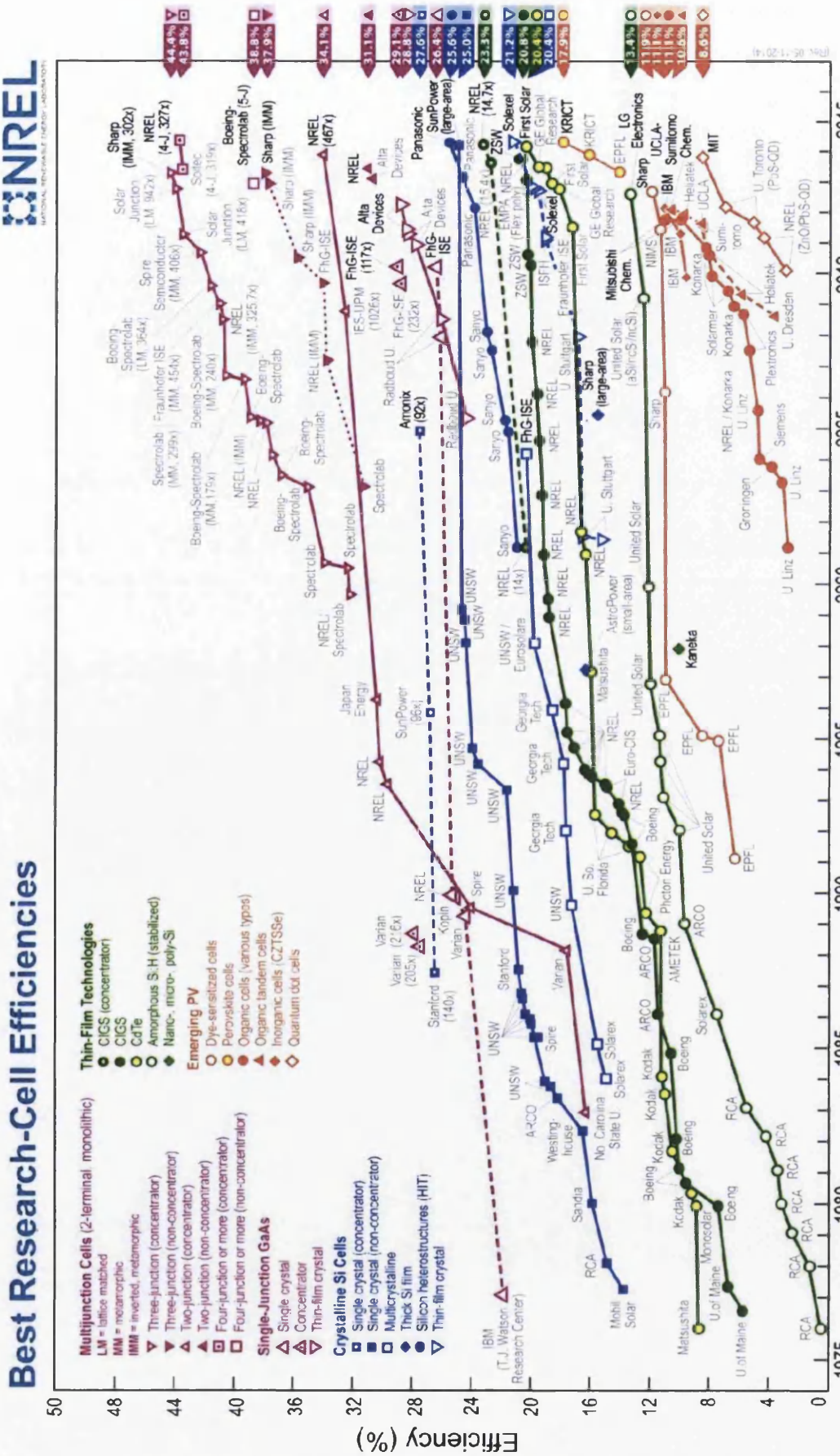

Figure 1.5: NREL certified best research solar cell efficiencies as of May 2014 [18]

1.2 Dye-sensitised solar cells

A dye-sensitised solar cell (DSC) operates differently to the previously discussed inorganic solar cells. A DSC is an excitonic solar cell so upon light absorption rather than a free electron-hole pair being produced an exciton is generated which is a tightly bound electron-hole pair so the charge requires separation. A DSC also differs from traditional solar cells in that the electron charge carrier does not absorb visible light photons, the semiconductor is instead sensitised to extend this. The operation of a DSC will be discussed in detail shortly.

One of the earliest examples of photosensitisation was in 1887 when Moser used sensitised silver halides with an erythrosine dye to absorb in the visible range [19]. This later led to colour photography. The studies that laid the foundations for understanding the mechanisms of dye-sensitisation of semiconductors were from the late 1960s on electrodes such as ZnO and SnO_2 [20][21]. This gave way to the understandings such as only the dye molecules in direct vicinity to the electrode contributed to the photocurrent. In 1977 a flat single crystal of rutile TiO_2 was sensitised using $Ru(bpy)_3^{2+}$ in aqueous electrolyte solution [22] which shifted the focus to research on titanium dioxide as the semiconductor.

As well as single crystal electrodes there have been studies on the light induced electron transfer of colloids and particulates in aqueous media. Using particles of nanometres in size seemed counterintuitive because traps and defects in single crystal systems are detrimental to charge carrier transport. However because the particles are of similar dimension to the diffusion length of the charge carriers recombination of the charge carriers back into the semiconductor is extremely unlikely. The mechanisms of interfacial electron transfer of colloidal semiconductors in aqueous suspension with redox reagents present was published in many papers including work by Grätzel and co-workers [23].

Grätzel et al. used fractal polycrystalline TiO_2 in 1985 sensitised with RuL_3^{2+} with a roughness factor of 100 [24] which provoked many follow up studies. Dye-sensitisation of colloidal particles in aqueous suspension was demonstrated here two years later [25]. In 1990 O'Regan et al. applied 8 nm colloidal particles of anatase TiO_2 onto FTO glass resulting in a film of 2.7 μm with a roughness factor of 50 [26]. A year later the first high efficiency dye-sensitised solar cell, 7.1%, was reported by Grätzel and O'Regan with a high surface area 10 μm thick TiO_2 film comprised of 15 nm particles and cementing the standard design of a DSC device [27]. Later developments will be discussed in the relevant sections.

1.2.1 Cell operation

Figure 1.6 shows the structure of a standard dye-sensitised solar cell with typical materials which will be assumed for the explanation of cell operation, such as TiO_2 the most common and efficient semiconductor for a DSC.

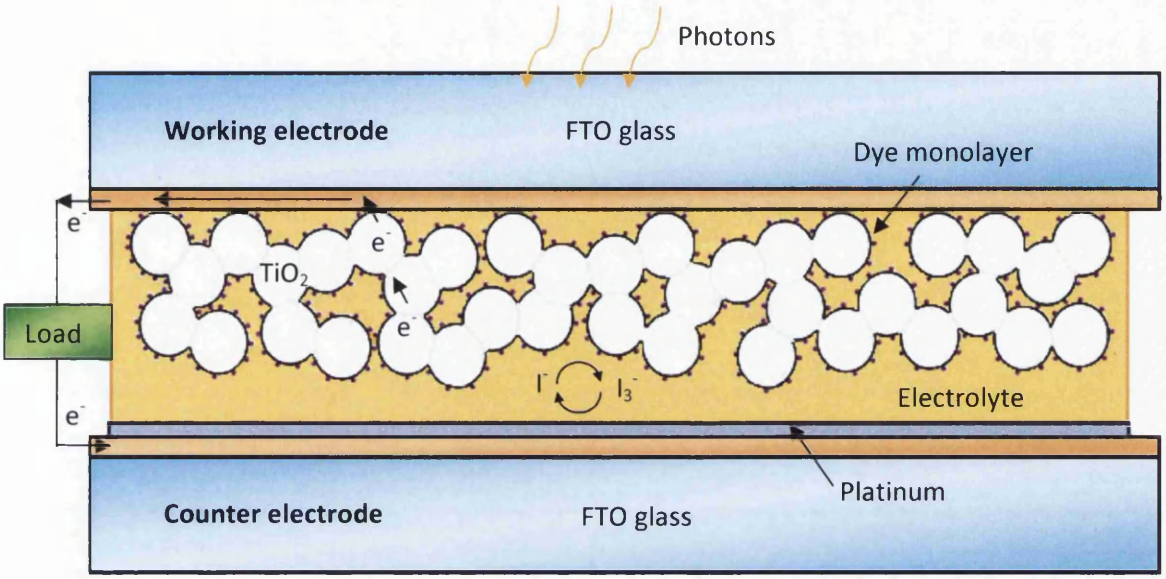

Figure 1.6: Diagram of a standard DSC device showing some of the simplified operation steps

When light enters a dye-sensitised solar cell a series of reactions take place. Firstly to be considered will be the processes at the working electrode. A photon is absorbed by the dye a.k.a the sensitizer (S) which promotes it from the ground state to an excited state (S*). This may also be considered as electrons moving from the highest occupied molecular orbital (HOMO) of the dye to the lowest unoccupied molecular orbital (LUMO) by a process known as metal to ligand charge transfer (MLCT).

$$S + hv \rightarrow S^* \text{ (photoexcitation)} \qquad (1.1)$$

The molecule in the excited state can either decay back to ground state or undergo oxidative quenching. The latter is energetically favourable so an electron from the LUMO is injected into the conduction band of adjacent TiO_2 which oxidises the dye (S^+).

$$S^* \rightarrow S^+ + \text{e-cb } (TiO_2 \text{ charge injection}) \qquad (1.2)$$

The injected electrons diffuse through the mesoporous TiO_2 film to reach the back-collector contact (FTO) where they are passed through the external circuit. Meanwhile the oxidised dye is reduced rapidly to ground state by the iodide of the electrolyte.

$$2S^+ + 3I^- \rightarrow 2S + I_3^- \text{ (regeneration of S)} \qquad (1.3)$$

The electrons that reached the counter electrode through the external circuit reduce oxidised triiodide so that the sequence of electron transfer between the dye and redox mediator is cyclic.

$$I_3^- + 2e^- \rightarrow 3I^- \text{ (regeneration of } I^-) \quad (1.4)$$

Overall these reactions directly convert sunlight to DC electricity; the efficiency at which this occurs is called the sunlight-to-electric power conversion efficiency which will be known as efficiency, η, for short. For a DSC this depends on the efficiency of light absorption by the dye, η_{abs}, efficiency of charge injection into the TiO_2, η_{inj}, and the efficiency of charge collection in the mesoporous TiO_2 layer, η_{coll}.

$$\eta = \eta_{abs} \times \eta_{inj} \times \eta_{coll} \quad (1.5)$$

As well as the constructive processes driving photogeneration, collection and regeneration there are counteracting processes to compete with which include:
Recombination of an electron from the TiO_2 layer with the oxidised dye (S^+) to reduce it in absence of the redox mediator returning the dye to ground state:

$$S^+ + e^- (TiO_2) \rightarrow S \quad (1.6)$$

Reduction of oxidised species in the electrolyte, I_3^- and I_2, by an electron from the conduction band of the TiO_2 (intercepting it on the way to the back-collector) to the reduced species I^-. This is known as dark current and significantly reduces the maximum cell voltage obtainable. Dye is adsorbed onto most of the porous TiO_2 surface but any uncoated area is a site for dark currents to be produced and in reality this always occurs. These also occur where the FTO layer is exposed, due to the porous nature of the TiO_2 and the roughness of FTO grains (for the most common FTO deposition method) there is not a continuous layer coating the FTO.

$$2e^- + I_3^- \rightarrow 3I^- \quad (1.7)$$

A schematic diagram of the energy levels, electron transfer processes and the rates at which these reactions occur (for a typical Ru based dye and I-/I3- electrolyte[28]) is shown in figure 1.7. Electron injection into the conduction band of TiO_2 (1.2) competes with recombination (1.6) and dark current (1.7) competes with electron transfer through the TiO_2. Electron injection is ultrafast, much faster than the recombination between electrons in the conduction band of the TiO_2 and the dye cations [29] so charge separation is effective. In the case of N3 dye (a similar dye system to N719 used in this work) the distance required for charge injection (between the bipyridyl ligand and the TiO_2) is shorter than that required for recombination of the electron (between the TiO_2 and the Ru(III) metal). Therefore recombination has a slower electron transfer rate and is less efficient than injection. Additionally reduction of the dye by the iodide (1.3) is a slightly faster reaction than

recombination [29]. The transport of photoinjected electrons through the nanocrystalline TiO_2 is relatively slow; TiO_2 is not very conductive although its conductivity is greatly enhanced by the electron injection and increasing light intensity [30]. The mechanism for charge transport through the TiO_2 has been proposed to be diffusion [30], electron tunnelling [30], trapping/detrapping [31], or insulator-metal (Mott) transition [32]. If the dark current reaction was dominant the DSC would not work so the rate of reaction must be slower than that of charge transfer and has been estimated to be around 0.1 - several seconds [33].

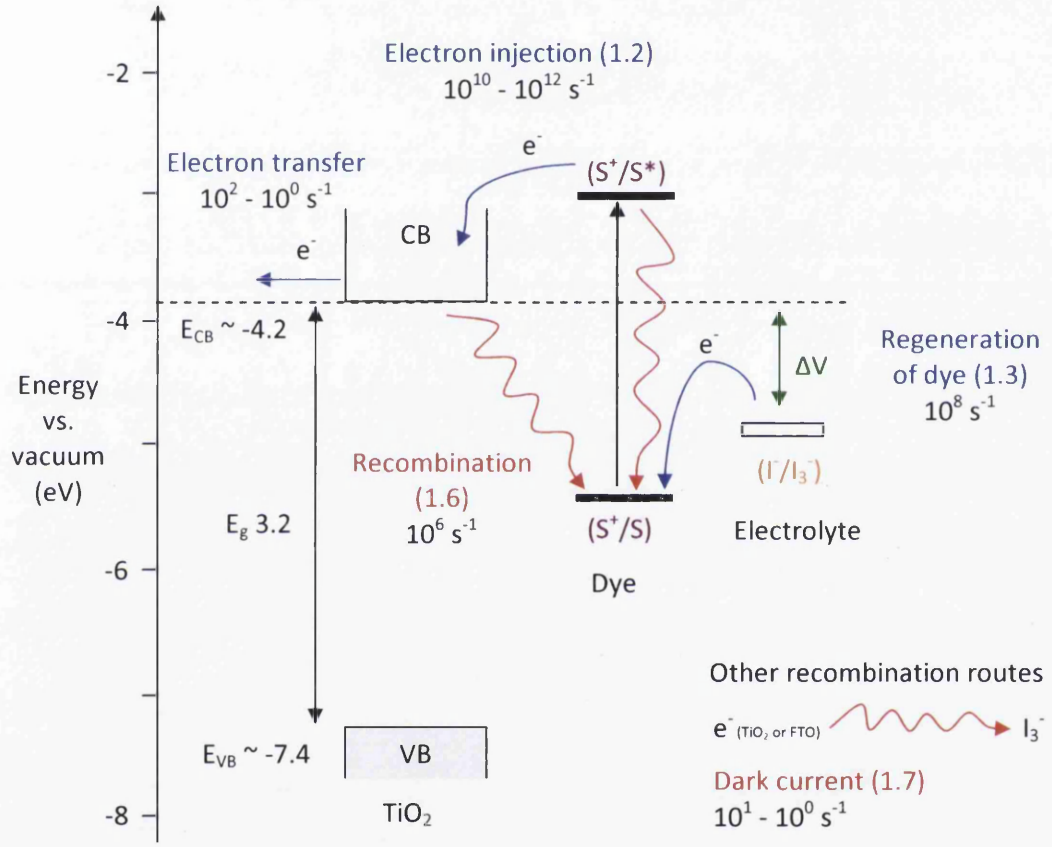

Figure 1.7: Schematic diagram of the energy levels and electron transfer processes in a DSC with typical rates for an Ru based dye and I^-/I_3^- electrolyte obtained from [28]

1.2.2 Substrate

1.2.2.1 Conductive glass

The most common substrate for a DSC is fluorine-doped tin oxide (FTO) coated glass. This is the substrate that the highest efficiencies have been achieved on [34]. Although FTO glass is rigid and heavy which doesn't make use of a DSC's potential for flexible substrates it boasts quite a few advantages. The first requirement for a substrate is that it can withstand the high processing temperatures required to manufacture a DSC. The sintering of the TiO_2 film

requires a temperature of 450-500°C [27][35] and FTO glass remains stable at and above this temperature [36]. FTO glass is easy to fabricate on compared to other substrates due to its superior robustness and chemical and thermal stability. It has good transparency in the visible region allowing for illumination directly into the dyed TiO_2 film without absorbing too many photons, and allows for use as a window if desired in conjunction with a range of different colours offered by the dyes [37] (such as that on the SwissTech Convention Centre of EPFL's campus in Switzerland [38], figure 1.8). Tin-doped indium oxide (ITO) glass has also been used for DSCs but it suffers significant resistivity rise at temperatures above 300°C due to oxygen diffusion into its vacancies reducing the carrier concentration and mobility [39]. This results in low efficiencies for sintered TiO_2 working electrodes although there is slight discrepancy in the literature to the extent of the impediment [40][41]. This issue will be addressed in Chapter 6 of this work. FTO and ITO coated glasses will be discussed further in section 1.3. While the traditional atmospheric pressure chemical vapour deposited (APCVD) FTO coated float glass is rigid ultra slim flexible glass has been developed by Corning Willow which may facilitate roll-to-roll production and has been demonstrated for use in electronic displays [42].

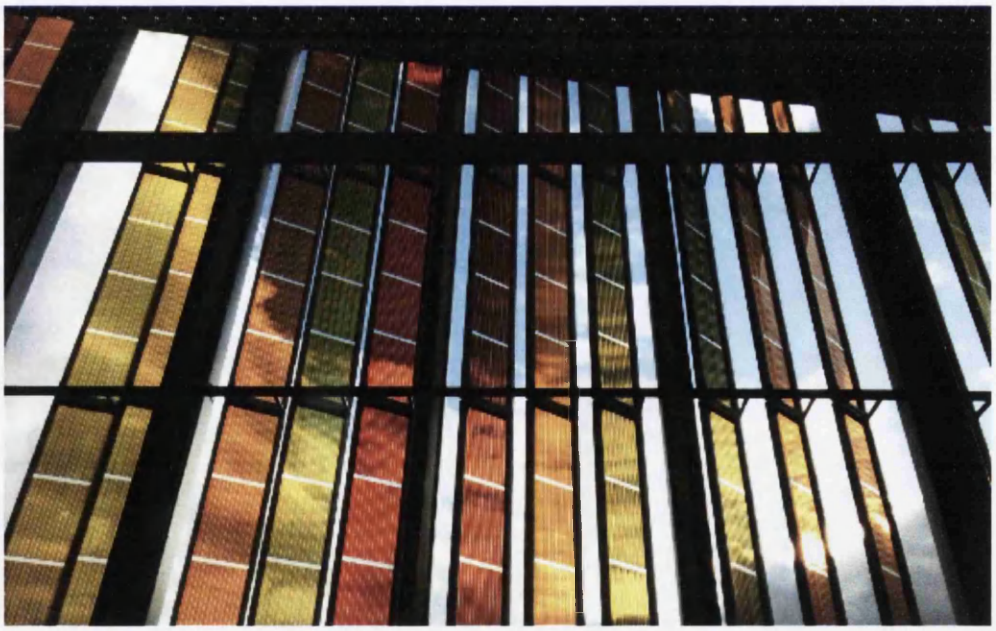

Figure 1.8: Solar façade on the SwissTech Convention Centre, EPFL, Switzerland

1.2.2.2 Metal

One of the advantages of using a thin film semiconductor for a solar cell is that flexible substrates can be feasible. For DSCs metal substrates offer a few benefits over glass. They can be flexible which allows greater freedom for roll-to-roll production as well as the use of

thinner substrates consequently weighing less. They are conductors so won't have as many resistive losses over large areas. They can be less expensive, stainless steel for example is cheaper than FTO glass [43]. As with glass they can withstand the temperatures required for sintering. However the choice of metal substrates is slightly restricted in terms of their compatibility with the iodide/triiodide electrolyte. For example zinc coated carbon, which is a common roofing material and would be ideal for building integrated photovoltaics, cannot be used for this reason. The corrosion of electrolytes on metallic substrates for the purpose of DSCs has been reviewed here [44]. Titanium and stainless steel the most stable metals for a DSC [45].

DSCs using a metallic working electrode have not reached as high efficiencies as FTO glass but 7.2% has been reached using titanium [35] and 8.6% using stainless steel [46]. The opacity of the metallic substrate means the DSC has to be illuminated through the counter electrode, reverse illumination rather than forward illumination. This direction of illumination is a significant impairment to the efficiency. The main reason is a change in the photons that contribute to photocurrent. Generation of current is most efficient closest to the back-collector contact [47]. Under forward illumination the photons of wavelengths most preferential to the dye, those closest the maximum absorption range, are absorbed first. For N719 this is 522-530 nm (green). These are absorbed by the dye closest to the back contact because they are exposed to this first and have a relatively short distance to travel which decreases the chance of recombination. The longer wavelengths such as red have to travel further through the film to be absorbed so the injected electron takes longer to reach the back contact, increasing the rate of recombination and lowering the incident photon-to-current conversion efficiency (IPCE). The same is true in reverse that the photons of wavelength closest to the maximum are absorbed first but in this case these injected electrons are now furthest away from the back contact. The red photons are absorbed nearest the back contact so in reverse illumination the IPCE is lower for most wavelengths but higher for red [48]. Additional increases in the rate of recombination is from photons lost on the way to the dye molecules absorbed by the electrolyte (iodide absorbs highly around 400-600 nm) and the platinum [46][49]. As a result of both of these factors current density [49] and subsequently efficiency is lower for metal working electrodes [46].

Using metal as a counter electrode would allow for forward illumination into the cell. Titanium was used as counter electrode for an impressively large 151 cm^2 active area cell

with an efficiency of 7.4% performing better than an equivalent FTO glass counter electrode [50]. The lower sheet resistance of the titanium allowed for less resistive losses across the large area. However in this case the platinum was sputtered and they used silver grids to enhance electron collection. Sputtering requires a vacuum so would not be suitable for roll-to-roll production of metal flexible substrates. Thermal decomposition of platinum was performed by Ma et al. on stainless steel via heating of chloroplatinic acid for 15 min at 385°C [51]. A slightly lower efficiency was obtained than for the equivalent sputtered DSC due to a lower fill factor of 46%, they cite this reduction to be due to a poorer adhesion of the Pt to the substrate. Toivola et al. thermally platinised stainless steel and carbon steel using a solution of $PtCl_4$ and heating at 385°C for 10-15 min [45]. Again they noticed a drop in fill factor and so efficiency and they postulate that the chemical composition and crystal structure of FTO may be more favourable for platinum physi- and/or chemisorptions. They noticed during sealing of the cells that platinum flakes stuck to the Surlyn if it was pulled off whereas platinum could not be removed from the FTO glass surface, agreeing with Ma et al. that adhesion was poorer on metallic substrates. This may be due to an oxide layer that has formed on the stainless steel and will be the subject of investigation in Chapter 7 of this work.

1.2.2.3 Plastic

Like metal, plastic presents an option as a flexible substrate for DSCs. This enables the feasibility of roll-to-roll production. Unlike metal they are transparent so are not restricted to reverse configuration illumination. They are extremely lightweight, lighter than metal or glass and inexpensive [52]. However they have a major drawback, their melting temperature. The two most common plastic substrates for DSCs are ITO PET (polyethylene terephthalate) and ITO PEN (polyethylene naphthalate). The maximum temperature these plastics can withstand is about 150°C. ITO is the transparent conducting oxide in this case because FTO requires high temperature to deposit. The advantage of ITO is that it is slightly more transparent and has a higher conductivity than FTO [53] and is also smoother as it would be sputtered for this purpose. However ITO coated plastic has a higher sheet resistance than ITO glass due to the restriction of preparation conditions, annealing ITO during deposition achieves a better film, and the plastic may be permeable to humidity over extended outdoor exposure. Coupled with the expensive cost of ITO offsetting the savings slightly [54] a popular area of research is ITO free plastic substrates.

For plastic working and counter electrode low temperature methods of TiO_2 deposition and platinisation need to be utilised. Low temperature heating methods for the working electrode include simply heating in an oven at 150°C to drive off the solvent with a binder free paste [55], spray deposition [52], using hydrothermal crystallisation from $TiCl_4$, $TiOSO_4$, or Ti-tetraisopropoxide mixed with TiO_2 [56], chemical vapour deposition of Ti alkoxides [57], and turning these to TiO_2 with microwaves [58] or UV light irradiance [57]. Localised heating was used to heat TiO_2 without damaging the plastic substrate by electron bombardment [59] and laser sintering [60]. It would be intriguing to see if near infrared radiation (see section 1.4) could also achieve this, as investigated in Chapter 7 of this work. The highest performing working electrodes on ITO PEN were obtained using a highly optimised pressed TiO_2 technique by Yamaguchi et al. who achieved 7.4% on plastic [61] with an equivalent FTO glass cell of 10.2% [62], narrowing the gap between plastic and glass. Most of the methods here yielded efficiencies of over 6% so viable alternatives to sintering are indeed possible.

Plastic counter electrodes for DSCs have been prepared with chemical platinisation [49] (poor crystallinity in the case of [63]), Pt-enriched $Sb:SnO_2$ suspension [64], and sputtering [65], with the latter yielding the highest results. Alternative catalysts such as carbon based ones are often employed for plastic counter electrodes; these are discussed in section 1.2.6.

1.2.3 Metal oxide layer

Wide band gap semiconductors are used as the electron acceptor and charge transport layer in DSCs. They require high transport mobility, preparation into a large surface area, and the ability to accept an electron from the sensitizer. The oxide film does not require doping because the injection of an electron from the sensitizer into the nanoparticle turns it from an insulating to a conducting state [30][66]. The presence of an electron already in the conduction band is undesirable for a DSC because it may quench the excited state sensitizer so wide band gap insulating semiconductors are used. Additionally they need to be extremely stable, especially in the presence of corrosive I^-/I_3^- electrolyte, and ideally abundant, low cost and non-toxic.

SnO_2 has a band gap of 3.8 eV but does not perform well in DSCs [67] due to problems of poor electron transport across the film and recombination being more favourable [68]. The highest efficiency for SnO_2 alone has been 2.8% sensitised with the indoline based dye D149 [69], it can be coupled with other semiconductors to improve its electron injection and open

circuit voltage such as TiO_2 [70] and ZnO coated SnO_2 [71]. Zinc oxide has a similar band gap and band edge position to TiO_2 and a higher electron mobility [72]. Unfortunately it is amphoteric and less chemically stable than TiO_2 [73]; Ru based dyes can dissolve ZnO and generate Zn_2^+/dye aggregates [74]. 6.6% efficiency has been achieved with a mesoporous ZnO film [75]. The vast majority of research efforts are focused on titanium dioxide as it is very well suited to DSCs.

1.2.3.1 Titanium dioxide

There are three naturally occurring polymorphs of titanium dioxide; rutile, anatase and brookite. Rutile and anatase are the most common, they are both based on the tetragonal crystal structure but have slightly different packing which influences their electronic properties, altering their band gaps of 3 eV and 3.2 eV respectively [76]. Titanium dioxide is naturally slightly oxygen deficient, TiO_{2-x} (x = 0.01), which causes it to be self doped n-type but as mentioned previously it is relatively insulating until electron injection [30].

Single crystal rutile TiO_2 was used in earlier investigations during the development of a dye-sensitised solar cell [22] but as surface area was discovered to be crucial to the performance of a DSC fractal films of TiO_2 on titanium were used in 1985 [24] and then colloidal mesoporous films from 1990 onwards [26][27]. $TiCl_4$ treated films were demonstrated in 1993 increasing surface area and consequently efficiency even further by introducing smaller nanoparticles within the existing mesoporous film [77] (figure 1.9).

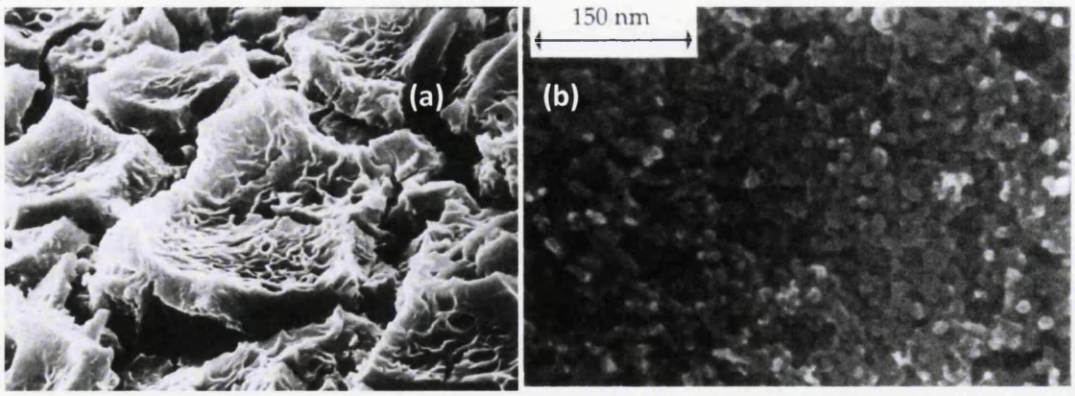

Figure 1.9: SEM images outlining two of the developments of the film structure for a DSC; (a) fractal TiO_2 [66], (b) mesoporous TiO_2, $TiCl_4$ treated [77]

There is an extremely large difference in surface area between fractal TiO_2 and the mesoporous nanoparticles of anatase, enabling the mesoporous film to adsorb a much

larger number of dye molecules than the latter. Rutile is usually the more thermodynamically stable phase of TiO_2 [78] but this is not the case for small crystals around 10-20 nm in size where anatase is the most stable [79]. Therefore the nanoparticles of TiO_2 synthesised for mesoporous films are more likely to be anatase.

For the working electrode of a DSC the TiO_2 can be synthesised directly onto the substrate such as by pyrolysis of titanium alkoxides onto titanium metal [80], anodic or thermal oxidation of Ti, sputtering, or aerosol pyrolysis [81]. However the most common method to create the mesoporous TiO_2 layer is to combine nanoparticles of TiO_2 (usually 15-20 nm) into a paste or slurry which is then deposited onto the substrate via doctor blading or screen printing and fired at around 450°C-500°C to remove the paste components and sinter the TiO_2 particles to achieve interconnectivity [27]. One of the main challenges for creating a mesoporous TiO_2 layer is preventing the particles from aggregating together so that sufficient porosity can be achieved. This is usually obtained by either electrostatic stabilisation, steric stabilisation, or both [82]. The nanoparticles aggregate together because of the phenomena Brownian motion; colloidal particles suspended in a fluid are in constant motion and may randomly collide with other particles in the surrounding medium. When they collide Van der Waal forces act and stick them together causing them to aggregate. These aggregations are undesirable because it effectively increases the particle size therefore decreasing the surface area.

Electrostatic stabilisation involves applying an identical charge to the particles so that as the particles approach each other they repel each other at a distance before Van der Waal forces can act. Charge can be applied by adding a low pH acid (e.g. HNO_3) or a high pH base (e.g. NH_4OH) to the paste (figure 1.10). At low pH concentrations the H^+ protons present result in an OH_2^+ charge on the titanium atoms, at high pH a proton from the TiO_2 is lost resulting in an O^- charge. Electrostatic stabilisation also causes an electroviscous effect which limits the particle concentration so only a limited amount of acid or base can be added without rendering the paste too viscous to use. The first sol-gel method mesoporous TiO_2 by Grätzel's group used this electrostatic stabilisation [27].

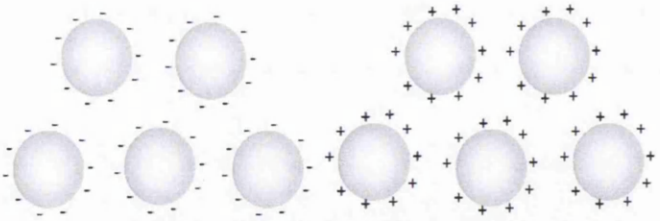

Figure 1.10: Electrostatic stabilisation of TiO_2 particles charged negatively using a base (left) and positively using an acid (right)

The steric stabilisation method involves adding a water soluble polymer to the paste. If a TiO_2 particle carries a layer of polymer as it approaches another particle to potentially collide the polymer chains prevent this because it is unfavourable for the concentration of polymer to be higher (figure 1.11). This has advantages over electrostatic stabilisation in that it is insensitive to ionic solutions. However the polymer needs to be burnt off so it is unsuitable for low temperature processing of DSCs but if temperature is not an issue it can create a very porous film either as the only form of stabilisation or combined with electrostatic stabilisation.

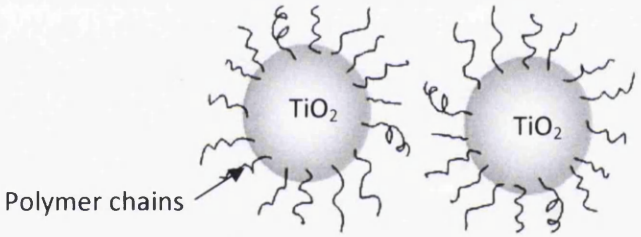

Figure 1.11: Steric stabilisation preventing two TiO_2 particles from colliding

Conventionally the TiO_2 paste is heated in an oven for 30 min at 450°C-500°C. The conversion of anatase to rutile occurs at around 610-1000°C depending on crystal size [83] and impurities [84]. This is an undesirable temperature for the sintering of TiO_2 not only because crystals of rutile are larger but also because there will be more energy for Ostwald ripening which will reduce the pore size and reduce the surface area further. So although sintering would occur faster at a higher temperature it would also encourage uncontrolled growth of the nanoparticles therefore a long heating time is used. Alternative heating processes have been applied to TiO_2 films and will be discussed in section 1.4 as well as being the subject of Chapter 5 of this work. As thickness increases there is more TiO_2 surface area for dye adsorption and so photocurrent increases. However recombination also increases because there is further for the electrons to travel and more grain boundaries to transgress. At least 10-15 μm is an optimal thickness for the mesoporous TiO_2.

1.2.4 Sensitizer

The sensitizer for a DSC has three main roles; absorbing photons to promote itself to an excited state, anchoring itself to the TiO_2 particle, and injecting an electron into the conduction band of the TiO_2 particle. Therefore it requires the following:

- Good light absorption in the visible and near IR region for light harvesting (as the solar spectrum emits well in both these regions)
- Good solubility in organic solvents (for facile deposition from stock solutions in a few hours or less)
- The presence of suitable peripheral anchoring ligands such as –COOH (to provide the effective interactions of the dye with oxide surface, thus coupling of donor and acceptor levels)
- Suitable disposition of the highest occupied molecular orbital (HOMO) and lowest unoccupied molecular orbital (LUMO) of the dye molecule (to permit quantitative injection charges from the electronically excited state)
- Good thermal stability and good chemical stability (to retain the chemical identify over repetitive oxide-reduction cycles)

Metal complex sensitizers based on ruthenium have been extensively studied throughout the development of DSCs and remain one of the most efficient in terms of photovoltaic yield and stability. The first dye to achieve over 10% was Ru(2,2'-bipyridyl-4,4'-dicarboxylic acid)2(NCS)2, known red dye (N3) [77], with the similar black dye (N749) [85] and N719 [86][87] (the dye used for the work in this thesis) succeeding this (shown in figure 1.12).

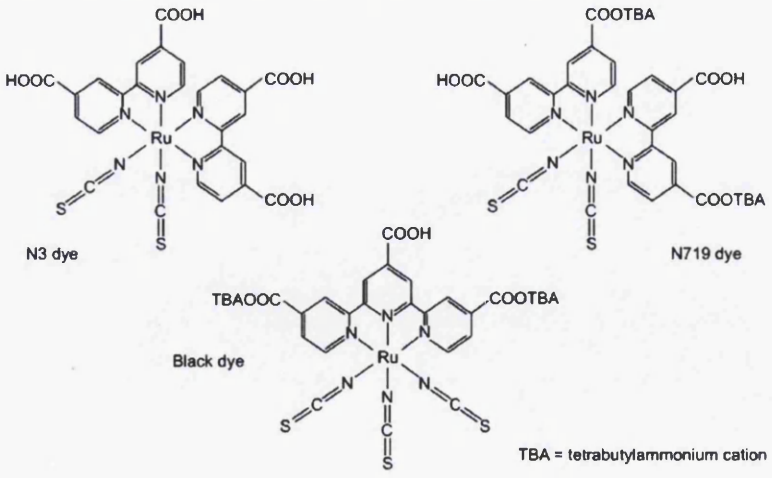

Figure 1.12: Structures of N3 (red dye), N749 (black dye), and N719 [88]

They have a broad absorption spectrum in the visible range peaking at around 530 nm, suitable excited and ground state energy levels for electron transfer with TiO_2 and iodide, relatively long excited-state lifetime (so that injection into the TiO_2 occurs faster than decaying to ground state), and good electrochemical stability. Until recently the record for most efficient DSC was one sensitized with a Ru based sensitizer and I^-/I_3^- redox couple [89], now succeeded by a zinc porphyrin dye and $Co^{(II/III)}$tris(bipyridyl) redox electrolyte [90].

Generally dyeing the TiO_2 film can take up to 24 hours particularly for N719 and related ruthenium based dyes (which take longer than organic dyes due to their larger molecules). For the conventional method of dyeing used in this work, which is immersion in a 0.3 mM N719 solution either in ethanol or 1:1 acetonitrile/tert-butanol in the dark at room temperature, the first stage of dyeing is an initial rapid dyeing where dye uptake is about 90% complete and takes 1.7 hours, stage 2 is when the film is saturated with dye (uptake >99.5%) and occurs at around 16 hours [91]. This is unfeasible for the commercialisation of DSCs because it is extremely time consuming and restricts production output. Dyeing time can be reduced by an increase in temperature [92], pressure [93][94], and concentration [91][92]. Dyeing in 30 min and 10 min can be achieved using pressurised CO_2 treatment [93] and dipping in a concentrated solution [92] respectively but this can be reduced further to under 5 min using a pumping technique developed by Holliman and co-workers [95] (figure 1.13).

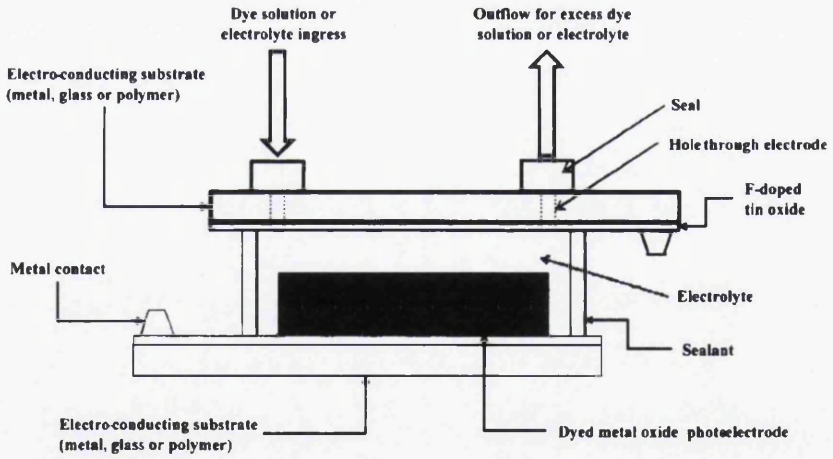

Figure 1.13: Diagram of the pump dyeing technique cell, the dye is pumped through one of the holes as shown using a pump or syringe [95]

A working and counter electrode (with two holes rather than one) are sealed together as standard for a DSC device except the TiO_2 is left undyed. Then a dye solution is pumped through one of the holes at an extremely high pressure that keeps the TiO_2 surface exposed

to fresh dye solution, this is usually performed at around 60°C to aid the adsorption further. This technique will be utilised in Chapter 8 of this work. Another benefit of this technique aside from time saving is the ease of co-sensitisation (using more than one dye). Co-sensitisation has traditionally been difficult to achieve as the uptake of different dyes needs to be controlled, selectively dyed, to achieve the desired absorption spectra. This has previously been achieved with slow dyeing, supercritical CO_2 and multi-phase photoelectrodes. However the pump dyeing technique can combine fast dyeing with co-sensitisation easily with two [96] or even three different dyes [97], which increases the efficiency by increasing the absorption spectra.

1.2.5 Electrolyte

Between the working electrode and the counter electrode is a redox couple. The function of the redox couple is to reduce the dye cation after it has injected an electron into the TiO_2 (dye regeneration, equation 1.3) and to then retrieve an electron from the counter electrode so that the cycle can continue (equation 1.4). It is usually contained in a liquid electrolyte and aside from the properties of the redox couple it should also be:

- Chemically stable
- Low viscosity (to penetrate the mesoporous film and reach the dye molecules)
- Contained in a suitable solvent that doesn't cause dissolution of the adsorbed dye and is compatible with the sealing material
- As transparent as possible (particularly for reverse illumination)

The I^-/I_3^- redox couple has been heavily used during the development of DSCs and was used in the first high efficiency DSC [27]. It has been used in all record efficiency cells until recently when $Co^{(II/III)}$tris(bipyridyl) redox couple was used in conjunction with zinc porphyrin dyes [90]. Although I^-/I_3^- is an efficient redox couple but has a few drawbacks. The maximum voltage of a DSC with a standard Ru-based sensitizer and I^-/I_3^- electrolyte is 0.7-0.8 V due to internal losses caused by TiO_2 and triiodide recombination (equation 1.7) [98], which has been one of the main factors that was stunting the growth of DSC efficiency in the last 15 years. Also as previously mentioned it is corrosive to most metallic substrates [44] and if a cell is reverse illuminated it will absorb some photons reducing the light entering the cell. A problem with all liquid electrolytes is encapsulation. Over time solvent usually escapes the sealant so electrolyte is lost and the efficiency slowly declines. This is the biggest lifetime issue for DSCs. It is also problematic to upscale a solar cell containing liquid, especially on

flexible substrates. Therefore replacing liquid electrolyte has been a key goal for DSCs. Organic solvents can be gelated, polymerised or dispersed with polymers to transform to quasi-solid state electrolytes [99] but the charge transport resistance is higher due to their viscosity and they remain at about 5% efficiency. This has been the main motivation for the development of solid state DSCs using hole transport materials as discussed in section 1.2.7.

1.2.6 Catalyst

The counter electrode of a DSC requires a catalyst so that the redox reaction of the electrolyte (triiodide reduction or equivalent, equation 1.4) can occur at a high rate to keep the reduced iodide available for dye oxidation [100]. The catalyst requires good adhesion, affinity for catalysing the redox couple and chemical stability. Possible catalysts include platinum, carbon, conducting polymers, and cobalt sulphide. Cost is a major drawback of platinum so if a low cost alternative reached the same efficiency and stability it would be highly desirable. Carbon has potential as a low cost and low temperature catalyst with many forms investigated such as graphene [101], carbon black [102], and a multiwall of carbon nanotubes achieving 7.7% [103], obtaining a good conductivity and stability are the main areas to improve. PEDOT:PSS was also used successfully as a triiodide reducing catalyst [104] and electrodeposited CoS on ITO PEN has been used as a suitable catalyst [105]. So far there are promising advancements for alternative catalysts but platinum remains the most widely used in research.

1.2.6.1 Platinum

Platinum is a very efficient catalyst; it has a high affinity and low overpotential for the reduction of iodine species (and $Co^{(II/III)}$tris(bipyridyl) electrolyte [106]) and good chemical stability (more so than carbon alternatives). It has been used since the first embodiment of a DSC and has always remained the highest performing catalyst. The drawback of platinum is its high expense which is not desirable for commercialisation. However it continues to be researched heavily and is the catalyst used in this work. To be an effective catalyst the platinum has a few requirements. It should have a large surface area to maximise the available sites for triiodide reduction; this can be achieved by having a small particle size, with 5 nm reported as the average cluster size with the best catalytic activity [107]. Good adhesion is extremely important, poor adhesion may lead to Pt adsorbing onto the TiO_2 surface and accelerating recombination at the TiO_2/electrolyte interface (equation 1.7) [108] and so reducing performance.

There are a few different methods suitable for platinum deposition; one of the original methods of platinisation was electrodepositon. An anode and a cathode are submerged in an aqueous solution of the source of platinum usually a chloride, sulphate-nitrite or hydroxyl complex [109]. DC electricity is supplied to the anode and cathode driving a reduction potential for platinum to be deposited onto the cathode. This technique can be performed at room temperature so is suitable for polymeric substrates [49], the thickness of the platinum layer can be controlled with a tolerance of a few μm [110], it has a fine structure which is continuous, and can achieve efficiencies close to that of other platinisation methods [111]. However it is reported to have poorer adhesion to the substrate than thermal and sputtered platinum [107] which contributes to its lower efficiencies and is also not a very fast process which limits its scalability. Another electrochemical method is electroless deposition which does not use an applied potential but rather the reaction occurs between the solution and the workpiece, it is also performed a low temperatures and creates a porous layer with large surface area [112]. Platinum can also be deposited by sputtering which also allows for a control of layer thickness and a continuous layer with good adhesion, 2 nm is reported as optimum thickness [108] and is one of the highest performing methods. It is another room temperature method but costs more than the electrochemical method, requires a vacuum making it unsuitable for roll-to-roll mass production, and has a high platinum loading wasting a lot of material because deposition is not strongly directional meaning the entire chamber is coated and due to the concave shape that develops in sputtering targets some of the target cannot be utilised although they can be melted down and reshaped into a new target.

Thermally decomposed platinum involves the conversion of a platinum chloride precursor, normally in the form of H_2PtCl_6, chloroplatinic acid, to catalytic platinum. There are three main reactions associated with the conversion of chloroplatinic acid to platinum, all reversible, which occur around these temperatures [113]:

125-220°C $(H_3O)_2PtCl_6.xH_2O \rightleftharpoons PtCl_4 + 2\,HCl + (x+2)\,H_2O$

300-375°C $PtCl_4 \rightleftharpoons PtCl_2 + Cl_2$

Above 375°C $PtCl_2 \rightleftharpoons Pt + Cl_2$

The optimum conditions for this were found to be at a temperature of 385°C heated for 30 minutes, with 375°C - 410°C the outer limits that achieve almost similar exchange current [107]. The conventional heating method is slow and low energy; it takes up to 30 minutes for

all of Pt-Cl bonds to be broken and fully converted to platinum. Residual $PtCl_2$ can impair the performance of the counter electrode as it is inactive and reduces the available number of sites for triiodide reduction. The focus of Chapter 4 will be reducing the heating time required for thermal platinisation using a near infrared heating method discussed in section 1.4. Aside from the high temperature requirement thermal platinisation does have a few advantages. It is a popular method used in literature and the most effective in terms of balancing efficiency and practicality [107][90]. It does not require a vacuum like sputtering and is less expensive because it only requires a low platinum loading of 5-10 $\mu m/cm^2$ which results in finely dispersed nanoparticles with an average cluster size of around 5 nm [107] (figure 1.14).

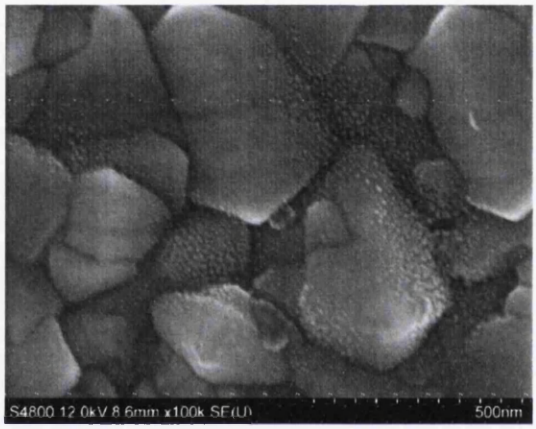

Figure 1.14: SEM of thermally decomposed platinum nanoparticles finely dispersed on FTO glass

1.2.7 Solid state analogues

Research on dye-sensitised solar cells has led to a solid state variation and another solar cell based on a slightly different concept. Solid state solar cells are more feasible to commercialise than the traditional liquid electrolyte DSC as mentioned in section 1.2.5 and although the content of this thesis is addressing the latter many of the concepts should be applicable to solid state solar cells.

1.2.7.1 Solid state DSCs

Following efforts to prevent leakage and corrosion issues from the traditional liquid electrolyte DSCs solid hole conductors have been employed in dye-sensitised solar cells, these are termed solid state DSCs (ss-DSCs) [114]. They function similarly to a liquid state cell but the regeneration of dye molecules after they have injected an electron into the TiO_2 occurs differently. Holes are transferred from the oxidised dye to the HOMO level of the

hole transporter then via hopping between electronic states on the organic molecules to the counter electrode [115][116]. They are capable of higher V_{OC}s than I^-/I_3^- electrolyte, over 1 V has been demonstrated thus far [117]. Dye regeneration is also several of orders of magnitude faster than with a I^-/I_3^- redox couple [115] which together gives a potential attainable efficiency of over 20% [118]. The hole transport material (HTM) is usually made either from wide band gap small molecules (such as spiro-OMeTAD) or semiconducting polymers (such as PEDOT or P3HT). Due to insufficient pore filling by the relatively large HTM molecules and a fast back electron recombination rate (1-2 orders of magnitude faster than liquid electrolyte) the effective electron diffusion length is reduced to only a few μm so currently the TiO_2 layer works best at only 2-3 μm thick (about a fifth of what is used for a liquid state DSC) [119]. A blocking layer of compact TiO_2 is also required to prevent pinholes. Therefore D-π-A organic dyes with very strong light absorption are generally used for these thinner films.

1.2.7.2 Perovskite based solar cells

Since 2009 $(CH_3NH_3)PbI_3$ and related halide perovskite nanocrystals have attracted substantial attention as an absorbing material for solar cells where 3.8% efficiency was demonstrated as a sensitizer in a liquid electrolyte "DSC" [120]. They were unsuitable with the I^-/I_3^- electrolyte due to rapid dissolution of the perovskite so were employed into the structure of a ss-DSC (figure 1.15) with a mesoporous TiO_2 film. It was found that the perovskite can act both as the absorber and the charge carrier enabling different architectures such as an insulating mesoporous Al_2O_3 scaffold and a perovskite planar heterojunction. Perovskite solar cells have developed very quickly with heavy contributions from Snaith's and Grätzel's groups; 9.7% was reported in mid 2012 [121] and over 15% in early 2013 [122][123]. Although the efficiency of perovskites is rising explosively a big challenge lies in their poor stability and lead content.

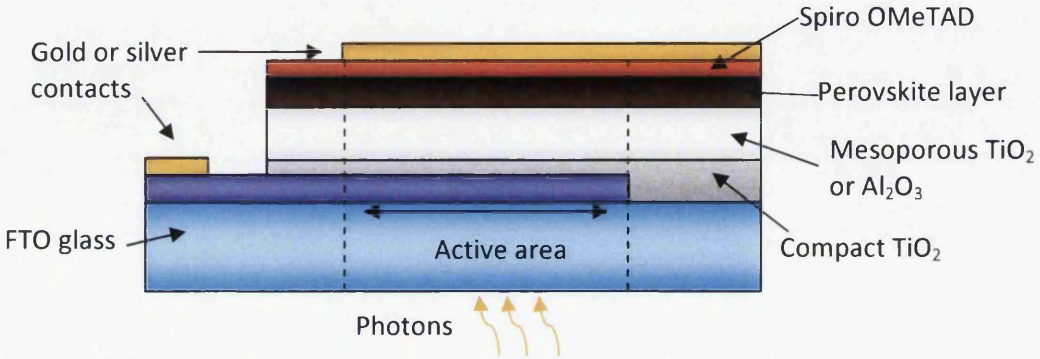

Figure 1.15: Generic architecture of a perovskite solar cell

1.2.8 Feasibility of dye-sensitised solar cells and industrial motivations

Dye-sensitised solar cells are an attractive solar candidate for commercialisation due to the relatively low cost of materials and ease of processing. DSCs are less efficient than traditional solar technology like silicon but have advantages such as cost, the ability to be lightweight and flexible, and superior performance in diffuse sunlight and indoors. This would potentially enable DSCs to have a lower price per watt ratio than silicon but unfortunately DSCs have not yet broken into the market. One of the bottlenecks in the commercialisation of DSCs is the time intensive heating steps which restrict process output both in terms of heating time and oven space. Another issue is the sealing of the liquid electrolyte which limits the lifetime to about 10 years at best whereas silicon is stable for over 25 years.

However a very viable use for DSCs is in portable applications such as personal electronics and cheap remote power in isolated areas where this shorter lifetime would not be an issue and the lightweight and low light and strong absorption in the visible range (for indoor lighting) becomes a huge benefit. Other solar cells such as perovskites also could become a future candidate in this area if their rapid development continues with similar advantages and superior performance. Crucially though DSCs are more likely to be accepted for these functions because it does not contain toxic materials and would be "safer" for indoor use than perovskites (which contain lead). Additionally perovskites may have difficulties reaching the market if tighter regulations regarding their lead content are imposed and at present they have a poorer lifetime than DSCs with extremely poor stability to moisture; both of these are of great importance and will become extensively researched in the field of perovskite solar cells.

Industries such as Tata Steel and NSG Pilkington are heavily linked to the motivations of this thesis through the SPECIFIC project (a Swansea University and multiple industry consortium) which in a wider sense aims to conduct research to aid the industrialisation of functionalised coatings, including photovoltaics, for applications related to buildings. The work in this thesis focuses on using the rapid heating technique NIR radiation for the application of components for DSCs. This is a first for glass substrates and significantly widens the potential application areas (NIR heating was previously only investigated for use on metallic substrates). The methods used in this thesis are extremely applicable and versatile because some of the DSC fabrication steps share strong similarity to other technologies. In particular

the sintering of a mesoporous TiO_2 film which could also be used in solid state DSCs, perovskite solar cells and photocatalysts.

1.3 Transparent conducting oxides

1.3.1 Electrical conductivity

Electrical conductivity describes a material's ability to transmit an electric current. Ohm's law relates current, I, to the applied voltage, V, as follows:

$$V = IR \tag{1.8}$$

Where R is the electrical resistance (Ω) of the material which is related to resistivity, ρ, (a size independent property) by:

$$\rho = \frac{RA}{l} \tag{1.9}$$

A is the cross-sectional area perpendicular to the direction of current and l is the distance between two points at which the voltage is measured. Resistivity is a common measure for characterising conducting materials and has the units Ωm. Conductivity, σ, can also be used to characterise a material's current carrying ability and is the reciprocal of resistivity:

$$\sigma = \frac{1}{\rho} \tag{1.10}$$

In most solid materials current arises from the flow of electrons (electronic conduction) and the magnitude of this is dependent upon the number of electrons available to participate. Metals are conductors and so have many free electrons that are delocalised from the lattice and able to contribute. Insulators and semiconductors have a band gap between their valence band and conduction band (section 1.1.3); the size of this gap (in eV) dictates the probability a valence electron will be promoted into an energy state within the conduction band so that it can contribute to electronic conduction. A larger band gap results in a lower electrical conductivity. Assuming the free carriers are electrons, conductivity can be expressed as a product of a material's free carrier concentration, n_e, and its carrier mobility, μ_e, by:

$$\sigma = n_e|e|\mu_e \tag{1.11}$$

Where |e| is the magnitude of electron charge which is a constant (1.6×10^{-19} C). For thin films of conducting material a common property to define them is sheet resistance, R_{sh} (Ω/□), which takes into account the thickness (t) of the conducting layer:

$$R_{sh} = \frac{\rho}{t} \tag{1.12}$$

1.3.2 Introduction and applications

A transparent conducting oxide (TCO) is a material that is both optically transparent and electrically conductive when deposited as a thin layer. In 1907 it was discovered that CdO films possess these properties [124] with ZnO, SnO_2, In_2O_3 and their alloys later also demonstrating transparency and conductivity [125]. These materials are wide band gap oxides and are transparent in the visible region due to their E_g of over 3 eV. Conductivity is achieved by either producing the oxide with a non-stoichiometric composition or by introducing dopants. Ternary compounds and quaternary compounds are self-doped due to their non-stoichiometric composition, for example cadmium stannate ($CdSnO_4$) which has achieved relatively low resistivity [126], but currently they are not used in commercial applications and are harder to control than binary compounds so will not be discussed further. Some free carriers do exist in the intrinsic binary oxides; e.g. In_2O_3, which has a cubic bixbyite structure, has an oxygen deficiency with oxygen atoms missing from each cube either along the face or body diagonal [127] creating some free carriers but an insufficient contribution for significant electrical conduction. Therefore doping is used to increase the carrier concentration, and consequently conductivity, of binary oxides. Nearly all TCOs are n-type so their free carriers are electrons, p-type TCOs have only been discovered relatively recently and require great development [128]. Common doping elements for n-type TCOs include fluorine, tin, aluminium, gallium, and boron. Most TCOs are based on ZnO, SnO_2 and In_2O_3 and are crystalline; CdO also has very low resistivity but is not used due to its toxicity. General properties for transparent conductors are shown in Table 1.1.

Table 1.1: Choice of transparent conductors, general properties [36]

Property	Material
Highest transparency	ZnO:F, Cd_2SnO_4
Highest conductivity	In_2O_3:Sn
Lowest plasma frequency	SnO_2:F, ZnO:F
Highest plasma frequency	In_2O_3:Sn
Highest work function, best contact to p-Si	SnO_2:F, $ZnSnO_3$
Lowest work function, best contact to n-Si	ZnO:F
Best thermal stability	SnO_2:F, Cd_2SnO_4
Best mechanical stability	SnO_2:F
Best chemical durability	SnO_2:F
Easiest to etch	ZnO:F
Best resistance to H plasmas	ZnO:F
Lowest deposition temperature	In_2O_3:Sn, ZnO:B
Least toxic	ZnO:F, SnO_2:F
Lowest cost	SnO_2:F

As well as the obvious desirable properties such as transparency and conductivity, there are many others that are important such as thermal stability, chemical stability, cost and method of processing. Plasma frequency is the frequency at which the material changes from a metallic to a dielectric response which affects the optical properties of a TCO in the IR region and is discussed in section 1.3.4. Work function is the energy required to remove an electron from the Fermi level at the surface to the vacuum, it can vary significantly for a material depending upon factors such as crystal alignment and surface chemistry. To form an ohmic contact (a junction where charge can flow easily in both directions) between two different materials the Schottky barrier height (potential energy between a metal and semiconductor interface) should be small, if too large then charge may flow in only one direction. A better ohmic contact is formed if the barrier height is small across the entire interface so it is desirable to match a semiconductor to a metal/TCO of specific work function to decrease resistive losses.

The most widely used TCOs are tin-doped indium oxide (ITO), In_2O_3:Sn, fluorine-doped tin oxide (FTO), SnO_2:F, and doped zinc oxides (Al, Ga). General applications of TCOs include transparent electrodes for flat panel displays, gas sensors, low emissivity windows, IR shielding, and transparent electrodes for solar cells. Zinc oxide is amphoteric and generally has poor chemical stability due to its low enthalpy of formation. However it does have good resistance to hydrogen plasma making it a suitable TCO for nanocrystalline silicon solar cells where this treatment is used in the manufacturing process. Low resistivity and 85% optical transmittance can be achieved with Al or Ga doped ZnO films. AZO is used in CIGS and amorphous silicon solar cells where high temperatures are not required. The resistivity of AZO rapidly increases at temperatures above 300°C [129]. For tandem solar cells (such as a DSC/CIGS stack) where extremely high transparency is needed to prevent optical losses alternative TCOs such as ITiO have been used [130]. ITO is heavily used for flat panel displays and OLEDs [131]. It has the highest conductivity of a TCO [53], its high carrier concentration is due to the good solubility of Sn in In_2O_3 [53] where 10 wt% SnO_2 in In_2O_3 is a common doping ratio. It is used in a few solar cells such as OPVs and some silicon. ITO is the most successful TCO to be coated onto polymeric substrates which is advantageous for flexible solar cells. However due to the scarcity and cost of indium [54], as well as the high demand in the electronic display market, there are efforts to replace it in solar cells. ITO also rapidly increases in resistivity at temperatures above 300°C [39]. This is due to its natural oxygen deficiency sites becoming filled with oxygen which significantly lowers its free carrier

concentration. It can be reversed by annealing the ITO in hydrogen to remove the excess oxygen and regain the natural deficiencies [41]. FTO is the lowest cost TCO and is produced in high quantities on glass during float glass production (see below). It has very good thermal stability and is used mostly for energy efficient windows and solar cells such as amorphous silicon, CIGS, CdTe and DSCs.

The optical, electrical and surface properties of TCOs are largely affected by the deposition method and parameters. For large scale production of TCOs the dominant technologies are sputtering and chemical vapour deposition (CVD). Sputtering involves bombarding a target with Ar+ ions to eject atoms from the material. The sputtered atoms then coat the substrate (and surrounding chamber). Different methods of sputtering exist as well as different power sources for the targets, where radio frequency (RF) is generally used for ceramic targets and direct current (DC) or mid frequency (MF) use for metallic and ceramic targets. Magnetron sputtering is the most suitable for cost-effective large scale TCO production. A tunnel of magnetic field lines is formed over the target using permanent magnets to confine the secondary electrons, increasing the plasma density and deposition rate. TCOs can be deposited from ceramic targets or by reactively sputtering metallic targets in the presence of oxygen. ITO is usually deposited by magnetron sputtering to achieve high quality low roughness films. AZO films are also usually sputtered. Attempts to deposit FTO by sputtering have been made but achieving an electrically conducting film by this method has proven difficult. For this reason FTO cannot be deposited onto a plastic substrate (as a high temperature technique is needed). ITO can be deposited onto plastic but at a lower quality of film because ideally the substrate should be heated to 200°C during sputtering deposition for desired grain orientation [131].

For CVD, precursors in the form of a vapour are decomposed into atoms or molecules which chemically react with each other on a hot substrate. Different pressures, activation methods, and precursors can be used. For TCOs atmospheric pressure CVD (APCVD), low pressure CVD (LPCVD), and metalorganic CVD (MOCVD) are the most common. LPCVD is used to deposit ZnO:B films and MOCVD has been used to grow complex TCOs of ternary or quaternary compounds. FTO glass is usually produced by APCVD. This process boasts a high deposition rate (~10 nm/s), no requirement for a vacuum and high throughput due to compatibility with the continuous processing of glass. For commercial producers of FTO glass, such as Pilkington NSG, the TCO layer is deposited during the latter stages of flat glass production; as

the float glass exits the tin bath (at a temperature of around 590-650°C) it is directly coated with SnO_2:F during cooling. A SiO_2 passivation layer is coated first to prevent leaching of fluorine into the glass at high temperature [36]. Commonly the produced film is textured and rough which helps promote light trapping.

1.3.3 Electrical properties

As mentioned in section 1.3.2 binary compound oxides require doping to achieve significant electrical conduction. In equation 1.11 (repeated below) it was shown that the conductivity of an n-type TCO can be expressed as a product of its electron concentration, n_e, and electron mobility, μ_e, where $|e|$ is the magnitude of electron charge:

$$\sigma = n_e|e|\mu_e \tag{1.11}$$

Increasing the level of doping raises the carrier concentration but there are drawbacks to heavy doping. Firstly a high electron concentration increases the optical absorption which, for a solar cell, results in a compromise between the amount of light entering a cell to generate photocurrent and the conductivity of the electrode. A figure of merit can be used to describe the relationship between conductivity and absorption as a method for comparing different TCOs for solar cells [36]:

$$\frac{\sigma}{\alpha} = -\{R_{sh}\ln(T+R)\}^{-1} \tag{1.13}$$

Where R_{sh} is sheet resistance, and transmittance and reflectance are defined for visible wavelengths. Secondly if the dopant concentration exceeds the solubility limit phase separation can occur. The solubility varies depending on the intrinsic oxide and dopant combination which limits the maximum carrier concentration. Finally the ionised dopant atoms act as scattering centres which reduce carrier mobility consequently there is a doping level after which conductivity no longer increases.

Free electrons in a lattice can be described as having an effective mass m_e* and feel a force in the presence of an electric field E:

$$eE = m_e^* \frac{dv}{dt} \tag{1.14}$$

Collisions with imperfections in the crystal slow down the electrons hence why dopant impurities reduce the electron mobility. The electrons acquire an average velocity component in the direction of the force known as drift velocity, v_d, to take this into account:

$$v_d = \frac{e\tau}{m_e *}E = \mu_e E \tag{1.15}$$

Electron mobility is proportional to the average time between collisions, τ (in the region of 5 x 10^{-15} to 1 x 10^{-14} s for a TCO):

$$\mu_e = \frac{e\tau}{m_e^*} \tag{1.16}$$

To keep conductivity high reducing the carrier mobility should be avoided. The major mechanisms that control electron mobility are scattering by ionised impurities, lattice vibrations, grain boundaries, and neutral impurities. A heavily doped TCO has a large number of ionised impurities which can be oxygen vacancies, dopants or excess metal atoms which can impede electrons. With increasing temperature the electron mobility also decreases because the atoms in the lattice vibrate more strongly causing acoustic phonon scattering (displacement of the atoms from their equilibrium position propagating like a wave). Grain boundaries can also trap electrons but for a typical TCO the free carrier concentration is sufficiently high that the mean free path for an electron is a few nm, less than the grain size, resulting in a low probability of this scattering. Neutral atoms and other electrons may also scatter the moving electrons but this is extremely unlikely. Generally for a heavily doped TCO impurity scattering is the dominant electron mobility loss mechanism.

1.3.4 Optical properties

The optical properties of a TCO are very strongly linked to its electrical properties. Generally a TCO absorbs in the ultraviolet region, transmits in the visible and reflects in the infrared. Heavily doped n-type TCOs are doped to such an extent that it causes the Fermi level to lie in the conduction band, more so than an n-type semiconductor where it would lie just below the conduction band (figure 1.16). This terms them as degenerate semiconductors. The lower states of the conduction band begin to fill when $n_e > N_c$ where n_e is carrier concentration and N_c is the effective density of states for the conduction band (the states available for electron occupancy). E is the energy and k is the wavevector (term for expressing the motion of the electrons and the nature of an electrostatic potential in the crystal lattice). The Fermi wavevector, k_F, is the radius of the "Fermi sphere" (where the electrons have occupied the lowest states of the conduction band and free electrons are modelled as a Fermi gas).

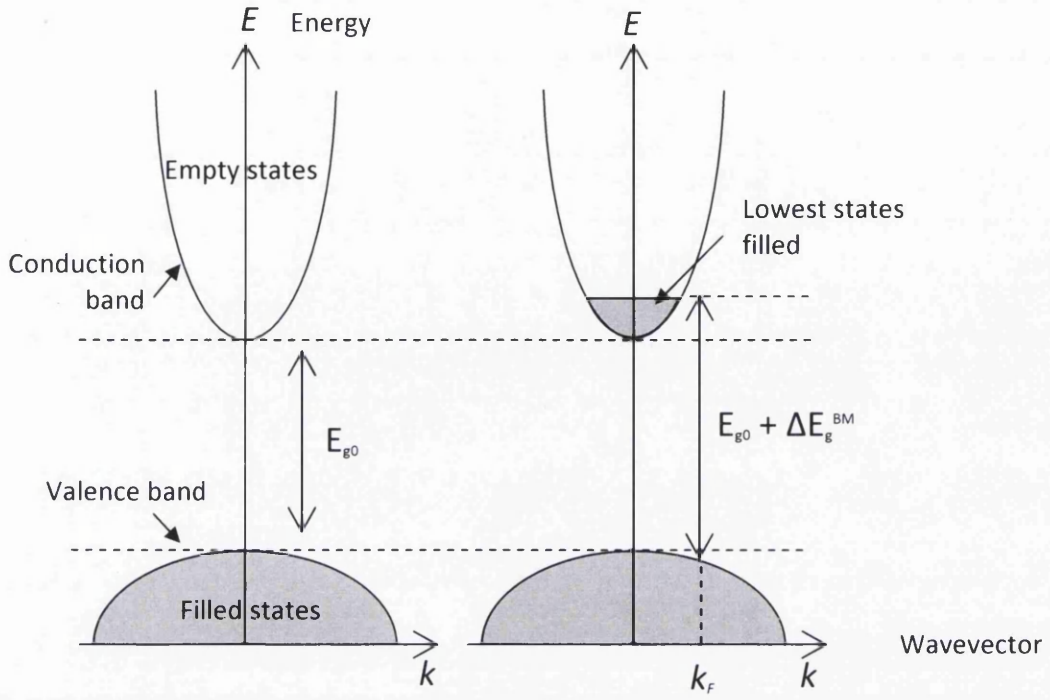

Figure 1.16: Schematic band structure of a semiconductor with VB and CB separated by E_{g0} (left) and a degenerative semiconductor where high doping has widened the optical band gap by an increment of energy, Burstein-Moss shift (right) redrawn from [132]

Because the lowest states of the conduction band are now filled photons need a larger energy than the fundamental band gap E_{g0} to excite a transition from the valence band to unoccupied states in the conduction band. This increment of energy is known as the Burstein-Moss shift, ΔE_g^{BM}, and given by [133]:

$$\Delta E_g^{BM} = \frac{\hbar^2 k_F^2}{2m_{vc}^*} = \left(\frac{h^2}{2m_{vc}^*}\right)\left(\frac{3n_e}{8\pi}\right)^{2/3} \quad (1.17)$$

Where h is Planck's constant, ħ is the reduced Planck's constant (ħ = h/2π), and m^*_{vc} is the reduced effective mass. The optical band gap, E_g, becomes:

$$E_g = E_{g0} + \Delta E_g^{BM} \quad (1.18)$$

Low energy transitions from the Fermi level into unoccupied states higher in the conduction band have a low probability for photons from the visible region because TCO cations have filled d-shells, $4d^{10}$ for Sn and In, thus the TCO is still transparent.

For the TCOs Drude theory is used to model the electrons as a classical gas; the interaction between light and free carriers occurs via an electric field and by introducing conductivity σ,

substitution for the drift velocity yields the complex frequency dependent conductivity of the TCO, hence:

$$\sigma(\omega) = \frac{n_e e^2 \tau}{m_e^*} \frac{1}{(1 - i\omega\tau)} = \varepsilon_0 \varepsilon_\infty \omega_p^2 \tau \frac{1 + i\omega\tau}{1 + \omega^2\tau^2} \tag{1.19}$$

At high frequencies, i.e. for shorter wavelengths such as ultraviolet, free carrier contribution becomes less important and other processes dominate (interband absorption) meaning the material acts as a perfect dielectric. At lower frequencies, i.e. for infrared wavelengths, the optical transmittance is determined by absorption and reflection of the free carrier plasma. In the low frequency regime ($\omega\tau << 1$) the free carrier term shows a $1/\omega$ dependence as $\omega \rightarrow 0$ this term dominates. Drude theory shows that at low frequency a material with a large concentration of free carriers is a perfect reflector. In the IR region where the reflectance of an insulator like glass begins to decrease, for a TCO it does not and continues to increase. Indeed the infrared reflectivity of ITO leads to its use as a heat shielding material [134]. From the equation 1.19 ω_p is the plasma frequency and given by:

$$\omega_p = \left(\frac{n_e e^2}{\varepsilon_0 \varepsilon_\infty m_e^*} \right)^{\frac{1}{2}} \tag{1.20}$$

The plasma frequency is the frequency at which the material changes from a metallic to a dielectric response. Drude theory predicts this to be in the NIR region for TCOs and in a frequency range where interband absorption is not important the ω_p occurs near the minimum in reflectivity, the plasma edge shift.

1.4 Heating techniques

1.4.1 Introduction

A material's ability to absorb heat from its external surroundings is known as its heat capacity, C, which represents the amount of energy required, dQ, to produce a unit temperature rise, dT:

$$C = \frac{dQ}{dT} \tag{1.21}$$

Heat capacity can be specified as per unit mole of material or specific heat, c, can be used for heat capacity per unit mass. Temperature is proportional to the average kinetic energy for all the atoms or molecules in a given system. When heat is absorbed thermal energy is transferred to increase the vibrational energy of the atoms or molecules in the lattice which are coupled together by bonding. The vibrations can be thought of as elastic waves with short wavelengths and high frequencies that propagate through the crystal, a single

quantum of vibrational energy is called a phonon and it has wave-particle duality. If there is a temperature gradient within the body the system will reach equilibrium, heat flows from the hot area to the cold area:

$$q = -k\frac{dT}{dx} \tag{1.22}$$

Where q (W/m^2) is the heat flow per unit time per area unit (heat flux), k is the thermal conductivity (W/mK), dT/dx is the temperature gradient through the conducting medium. Thermal conductivity is the ability of a material to transfer heat. Heat is transported within a solid material by phonons and free electrons. The total thermal conductivity is the sum of these:

$$k = k_l + k_e \tag{1.23}$$

Where k_l is the thermal conductivity of lattice vibration (phonons) and k_e is the thermal conductivity of electrons. Rather than the atoms or molecules vibrating, free electrons can transfer heat by gaining kinetic energy from hotter regions then migrating to colder areas and colliding with phonons or crystal defects to impart the energy, they have a higher velocity than phonons. The relative contribution of k_e increases with free electron concentration; as more electrons are present to participate in this heat transfer process it becomes predominant as it is more efficient. This is the case for metals and, to a lesser extent, degenerate semiconductors which have a high thermal conductivity. Insulating materials rely on phonons alone so tend to have a low thermal conductivity. Since free electrons are responsible for both thermal and electrical conductivity in metals the two can be related by the Wiedemann-Franz law:

$$L = \frac{k}{\sigma T} \tag{1.24}$$

Where σ is electrical conductivity, T is absolute temperature and L is a constant. Thermal conductivity is highest for pure metals; it diminishes with introduction of impurity atoms as they may act as scattering centres lowering the efficiency of electron motion (much as for electrical conductivity as discussed in section 1.3.3).

The heat transfer process discussed above occurs within the solid or between substances in direct contact with each other and is known as conduction. As well as conduction heat can also be transferred by convection and radiation. Convection is the thermal energy transfer that is predominant in liquid and gases. It is a combination of heat diffusion (random molecular motion) and advection (heat transfer by bulk fluid flow). Conventional heating (figure 1.17) in an oven heats an object via convection (the air in the oven transfers heat to the surface of the object) and conduction (by direct contact with the oven). Heat is

transferred through the object by thermal conduction from the surface inwards by phonons and free electrons if they are present.

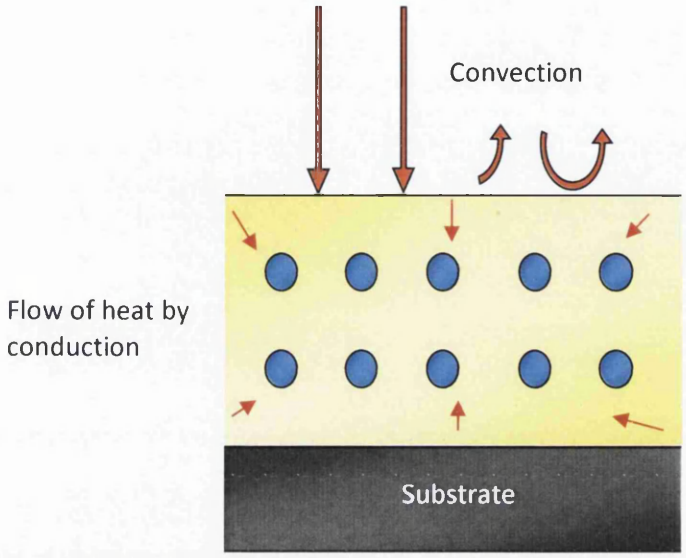

Figure 1.17: Diagram of conventional oven heating showing the heat transfer via conduction and convection

The process time is limited by the rate of heat flow into the body of the material from the surface as determined by its specific heat, thermal conductivity, density and viscosity so can be quite slow as is the case of DSC working electrode and counter electrode heating [27][107]. Additionally conventional heating is slow to respond to changes in temperature such as heating up and cooling down so it is difficult to control the temperature if quick changes are required. It is a low energy density process, about 2 kW for a lab scale oven, so heat transfer occurs slowly. Non-uniform heating could also be an issue, as the surface, edges and corners get hotter faster than the bulk of the material although once it reaches a steady state the temperature is uniform.

1.4.2 Electromagnetic radiation

Radiative heat transfer does not require contact between the heat source and the object hence can occur through a vacuum as the sun's energy does. Energy is transmitted via photons which also have wave-particle duality. The sun is often modelled as a black body, in that it absorbs all thermal radiation but does not transmit or reflect any. At room temperature it would appear black as it would emit in the infrared but at higher temperatures a black body would appear white hot. Emissivity, ε, is the ability of a surface to emit heat by radiation relative to a black body, with an emissivity of 1 corresponding to an

idealised black body and below 1 for a real object. Generally dull materials have a high emissivity and shiny materials have a low emissivity, highly polished silver has an $\varepsilon = 0.02$. The electromagnetic spectrum is shown in figure 1.17 with corresponding frequencies, energies and wavelengths (as photons can act as waves and particles).

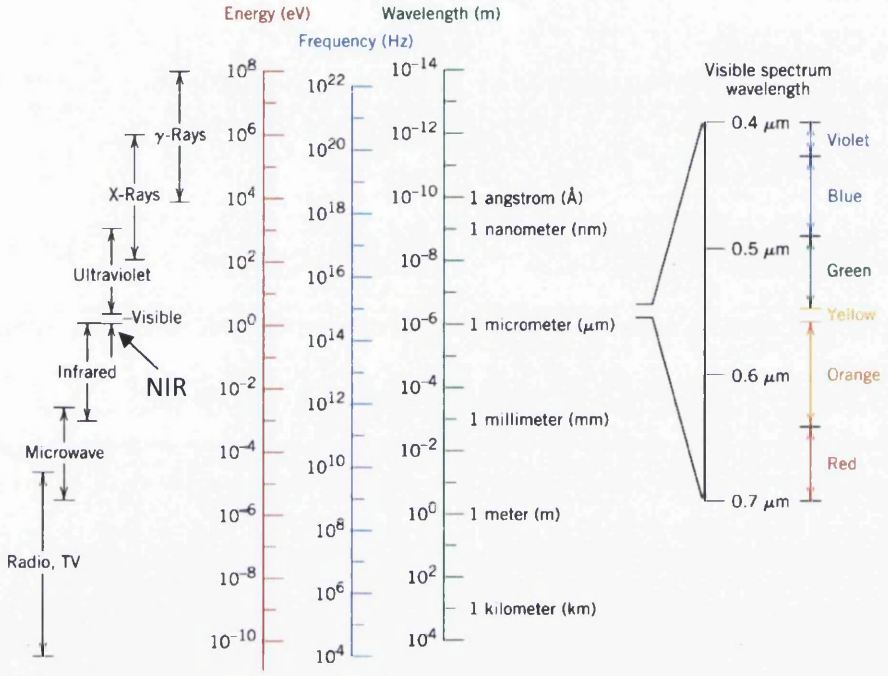

Figure 1.17: Electromagnetic radiation expressed as energy, frequency and wavelength [135]

Radiation that has been utilised for heating includes microwaves, infrared, ultraviolet and near infrared (NIR) and have the advantage of heating the sample directly rather than requiring time to warm up the surroundings. The ability of microwaves to heat materials was accidently discovered in 1950 while testing magnetrons in Raytheon's Microwave & Power Tube Division. They are now well established as a method of heating food and are also well used in industry. Microwaves interact with the material exciting the molecules or atoms causing them to vibrate rigorously heating the sample from the inside out. The most prominent characteristic of microwaves is known as volumetric heating since it is possible for entire volume of bulk to be heated [136]. This enables very fast heating times. Microwaves have a frequency range from around 0.3 GHz to 300 GHz corresponding to wavelengths from 1 m to 1 mm. Microwaves can be used for the sintering of ceramics and have been used to heat working electrodes for DSCs [58][137]. In this case 1 kW of 28 GHz frequency microwave radiation was used to achieve close to conventional method efficiency in 2-5 min. FTO absorbs microwaves well and heated to over 1000°C in 2 min, glass is transparent to microwaves, and TiO_2 absorbs moderately. Two concerns of microwaves have

been cost of electricity and uneven heating distribution. Similarly to other radiation techniques it is high energy so a sufficient reduction in heating time is required to offset the higher cost of the process itself. The nonuniformity of microwave heating can stem from an uneven distribution of electric field, differences in the absorbance of the materials, or heat loss on the boundary which can be significant at high temperature. It can be alleviated by the use of a variable frequency microwave furnace or hybrid heating solutions but these diminish the rapidness of the technique.

Infrared (IR) radiative heating is a common curing method in the powder coating industry; usually short wave (1.2-2 μm) or medium wave (2-3 μm) wavelengths are used due to their higher energies, long wave IR stretches beyond 3 μm and merges with microwaves at around 1 mm. Beneath 1.2 μm is the NIR region which merges into the red end of the visible and will be discussed shortly. Infrared radiation causes the bonds of functional groups to vibrate generating thermal energy. This phenomenon is also used in IR spectroscopy to detect organic molecules. Rather than the entire substrate needing to be heated the coating can absorb the radiation and so cure much faster with less than 2 min possible for specially formulated coatings and under 10 min in other cases [138]. IR heating is a suitable technique for heating organic coatings of a finite thickness but absorption of the molecules in this range is required. Also due to the nature of photons where wavelength is inversely proportional to energy (eV) IR has a lower energy density than NIR radiation so the photons absorbed transfer less energy thus limiting it to lower temperatures than NIR heating [139].

When NIR radiation is emitted it mostly transmits through the coating (organic molecules tend not to absorb in this region) allowing it to be absorbed and reflected by the substrate (figure 1.18). The NIR photons can excite the atoms to higher energy levels releasing thermal energy and rapidly heating the substrate. Due to the high thermal gradient created (equation 1.22) the coating on the substrate is heated very quickly by thermal conduction (equation 1.23). Particles that absorb well in the NIR can be added to aid heating but the main difference between the mechanisms of IR and NIR heating is that most of the radiation should pass through the coating rather than be absorbed by it so that it can instead be absorbed by the substrate. This allows for thicker coatings, higher temperatures and faster heating times, NIR radiation is capable of 30 s or less.

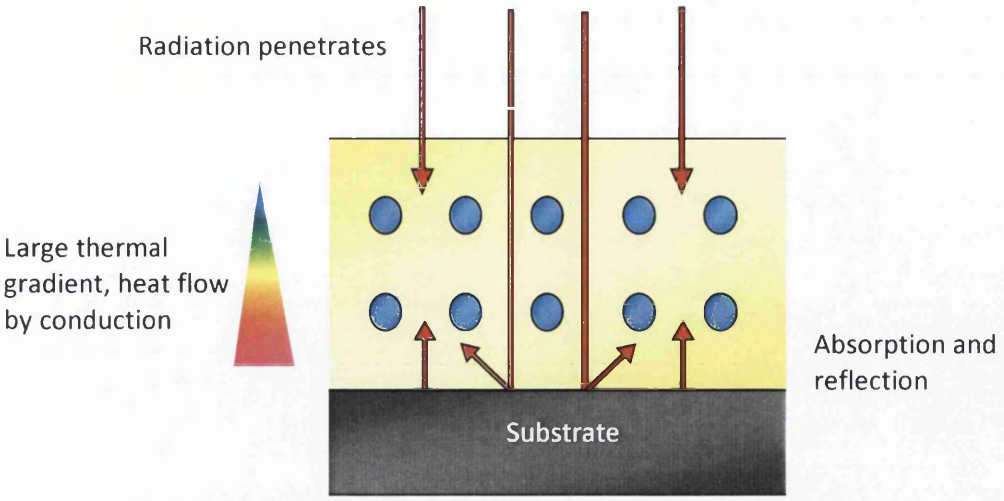

Figure 1.18: Diagram of NIR radiative heating; heat transfer occurs primarily by radiation absorbed by the substrate and conduction of this heat by the coating

NIR heating is extremely suited to industry due to the speed of heating (which could be combined with a roll-to-roll process at certain line speed) and the availability of large equipment. For example one supplier, Adphos (Bruckmühl-Heufeld, Germany), produces NIR units in a range of sizes including large industrial sized installations using emitters capable of up to 1 MW/m^2. Adphos equipment uses tungsten halogen emitters which have a very large spectral distribution (figure 1.19) from the visible to the infrared with a peak at around 1200 nm. The NIR equipment used in this work is an Adphos NIR Coil Lab LV2 unit which has a maximum power density of 25 kW/m^2.

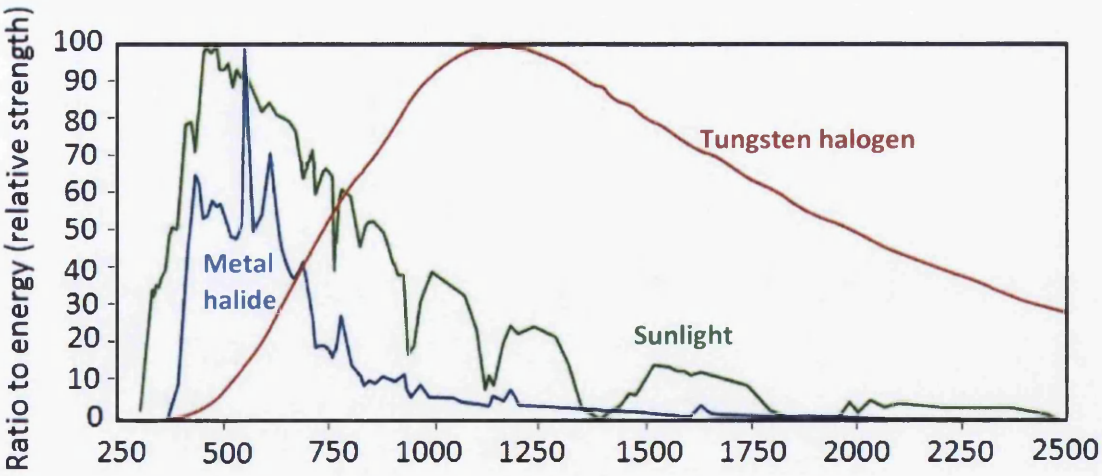

Figure 1.19: Comparison of the spectral distribution of different light sources (sunlight, metal halide and tungsten halogen) adapted from [140]

All substrates will heat to a certain extent when exposed to the NIR emitter, which covers a very wide range including some visible up to mid-IR but some transmit more in the NIR

range than others. Metal absorbs highly in this region so can reach very high temperatures in seconds. Substrates such as glass do heat but to a lesser degree and the main task of this project is to investigate if TCO coated glass (which was discussed in section 1.3) will heat sufficiently upon NIR exposure.

NIR radiation is conventionally used for drying organic coatings such as paints onto metal [141]. Following on from this idea it was applied to the heating of TiO_2 pastes on titanium metal which enabled DSC working electrodes to be constructed [142] with identical photovoltaic properties [143] to oven heated working electrodes and reduced the heating time from 30 minutes in a conventional oven to just 12.5 s with NIR exposure. The NIR radiation transmitted through the TiO_2 paste and was absorbed by the metal causing rapid release of thermal energy which then resulted in a huge temperature gradient directionally heating the TiO_2 paste on metal, burning off the binder and sintering the TiO_2 particles together. The free carriers in metals are extremely efficient at distributing this heat so facilitate the thermal transfer extremely quickly. This demonstrated application to DSCs will be explored in this thesis for the heating of both the working and counter electrode of a DSC device on various substrates.

Lasers can be used to heat the surface of a material which then heats the subsurface via thermal conduction. Laser sintering [60][144] has also been used to sinter TiO_2 for DSCs. In the latter a Nd:YVO_4 laser of wavelength 355 nm was raster scanned to generate high local temperatures.

1.5 Characterisation techniques

1.5.1 IV curves

Air Mass (AM) is a measure of how much absorption in the atmosphere affects the spectral content and intensity of the solar radiation reaching the Earth's surface. Just above the Earth's atmosphere the radiation intensity is about 1.353 kW/m^2 which is known as AM 0 as there is no atmosphere. It is at least 1 on Earth at sea level, the standard illumination used to characterise solar cells is the AM 1.5 spectrum which equates to the average annual solar irradiance for mid latitude countries and has a power density of 1 kW/m^2 (also known as 1 sun). Additionally sunlight at the Earth's surface has a diffuse component owing to scattering and refection in the atmosphere and surrounding landscape which can account for up to

20% of the light incident on a solar cell, it is standard to include this component further defining the spectrum as AM 1.5g (global), AM 1.5d (direct) does not include it.

Solar simulators are used to obtain IV curves of a solar cell with a lamp that emits AM 1.5g and are ranked according to their ability to match the spectrum perfectly [145]. Solar cells are modelled as a current source in parallel with a diode. In the dark the cell behaves like a diode and in the presence of light, current is generated. Figure 1.20 shows an IV curve for a DSC obtained under standard 1 sun illumination conditions.

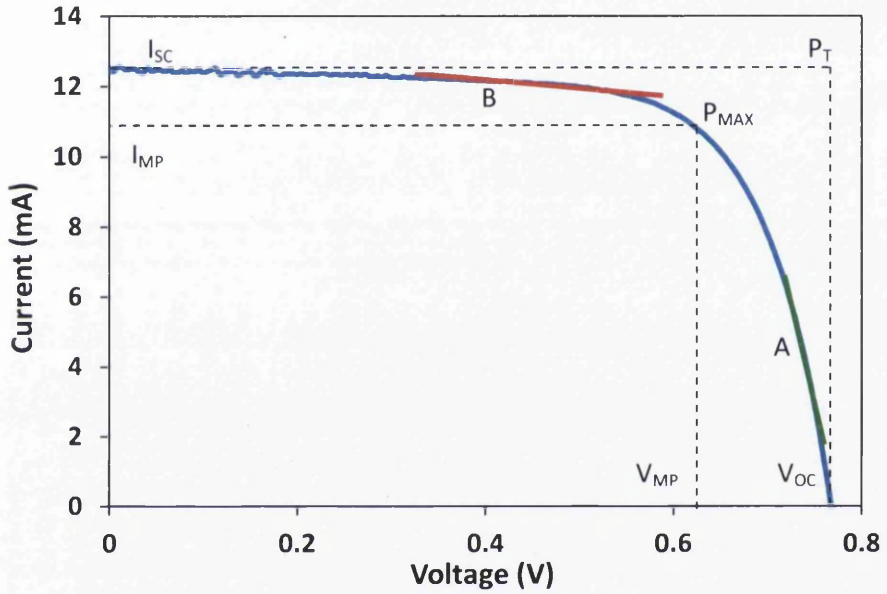

Figure 1.20: IV curve for a typical DSC showing obtained parameters

The open circuit potential of the cell, V_{OC}, is the voltage at which the resistance becomes too high for current to pass through. The maximum voltage of a DSC with a standard Ru-based sensitizer and I^-/I_3^- electrolyte is 0.7-0.8 V [98]. I_{SC} is the current at short circuit where the voltage is 0 and is the maximum current value. Commonly short circuit current density, J_{SC}, is quoted instead which is the current over area so that the area can be taken into account. For the majority of cells constructed in this thesis the active area is 1 cm^2 so the J_{SC} is equal to the I_{SC}. The photocurrent is largely dependent upon the working electrode of a DSC, both the generation of electrons by the dye and the transport of electrons by the TiO_2. The power (Watts) produced by the cell can be calculated along the IV curve by P = IV. The maximum power as shown in figure 1.20:

$$P_{MAX} = I_{MP}.V_{MP} \tag{1.25}$$

I_{MP} and V_{MP} are the current and voltage at maximum power respectively.

As well as a high current and voltage the squareness of the IV sweep is important. P_T is the theoretical power, the output at both V_{OC} and I_{SC} together and is equal to the product of these. The area under the IV curve is known as the fill factor, FF, and is equal to:

$$FF = \frac{P_{MAX}}{I_{SC}.V_{OC}} \tag{1.26}$$

That is the maximum power divided by the theoretical one. For a DSC FF is affected by series resistance and sluggish electron transfer kinetics at the cathode. It can also reflect intrinsic non-ideality behaviour of the DSC. It is typically 50-80% for a solar cell (also represented as a decimal, 0.5-0.8). The electron conversion efficiency of a solar cell, η, is equal to:

$$\eta = V_{OC}.J_{SC}.FF \tag{1.27}$$

It is the ratio of electrical power output compared to solar power input.

The efficiency of a solar cell is reduced by the dissipation of power across internal resistances described as shunt resistance and series resistance. The slope labelled A in figure 1.20 has a lower gradient than an ideal solar cell as a result of a decrease in the shunt resistance (which is ideally infinite so that there is no alternative path for current to flow). This manifests as a drop in P_{MAX} and FF, and also a drop in V_{OC} if shunt resistance is decreased dramatically. Slope B (figure 1.20) has a higher gradient than an ideal solar cell due to the series resistance (which would be be 0 to achieve the maximum voltage), an excessive increase in series resistance also results in a drop in I_{SC}.

1.5.2 Incident photon-to-current conversion efficiency

The incident photon-to-current conversion efficiency (IPCE) measures the spectral responsiveness of a photovoltaic device:

$$IPCE(\lambda) = \frac{j_{sc}}{qI_0} \tag{1.28}$$

Where j_{SC} is the current density of the cell under monochromatic light at wavelength λ and photon flux I_0 and q is the elementary charge. It is also known as the external quantum efficiency (EQE):

$$EQE = \frac{electrons/sec}{photons/sec} \tag{1.29}$$

The internal quantum efficiency (IQE) is related to EQE as follows:

$$IQE = \frac{EQE}{Total\ absorption} \tag{1.30}$$

A typical EQE for a DSC sensitised with N719 dye is shown in figure 1.21.

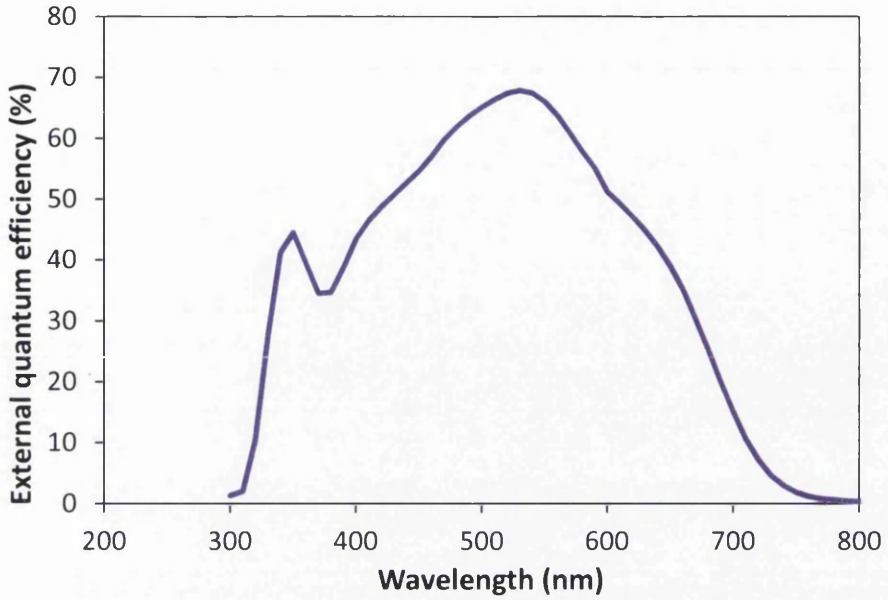

Figure 1.21: IPCE spectrum of an N719 dye-sensitised solar cell, showing peak efficiency at 530 nm

IPCE can also be expressed as the product of the efficiencies of three separate processes:

$$IPCE(\lambda) = n_{lh}(\lambda).n_{inj}(\lambda).n_{col}(\lambda) \quad (1.31)$$

η_{lh} is the wavelength dependent light harvesting efficiency, in a DSC this is usually the absorption and loading of dye but light scattering can also increase it. η_{inj} is the injection efficiency which is based on the match between energy levels of photoexcited dye and conduction band of TiO_2, the degree of electronic coupling between excited state of dye and CB states, and competition with other decay processes involving the excited state of dye. η_{col} is the collection efficiency and is sensitive to key loss processes such as trapped states in the TiO_2, and back electron transfer to I_3^- as well as oxidised species.

1.5.3 Electrochemical impedance spectroscopy

Electrochemistry is the study of the processes and factors that affect the transport of charge across the interfaces of chemical phases. The system is studied by imposing a controlled potential or a controlled current and monitoring its response. Electrochemical measurements can be used to characterise processes in a DSC such as ionic transport in the redox electrolyte, and electron transfer at both the counter electrode and working electrode. The most widely used techniques for DSCs are cyclic voltammetry (see section 1.5.4), intensity modulated photovoltage/photocurrent spectroscopy (IMVS/IMPS) which has not been used in this work, and electrochemical impedance spectroscopy (EIS). Rather

than driving the electrode far from equilibrium with large perturbations on the system, EIS perturbs the cell with an alternating signal of small magnitude to observe its response at steady state.

In EIS a DC bias potential applied to a system and perturbed by a small AC sine wave modulation (± 5-10 mV relative to bias potential). This modulation signal as a function of time can be expressed as:

$$E_t = E_0 \sin(\omega t) \tag{1.32}$$

Where E_t is the potential at time t, ω is the radial frequency and E_0 is amplitude of signal. The resulting sinusoidal current response is measured as a function of modulation frequency, in a linear system it is represented by:

$$I_t = I_0 = \sin(\omega t + \phi) \tag{1.33}$$

Where the system is by magnitude ϕ, I_t is the current response and I_0 is the amplitude.

Impedance is AC equivalent of resistance, describing the opposition a circuit presents to a current when a voltage is applied and can be substituted into Ohm's law which describes the resistance in a DC circuit (R = V/I) as $Z = E_t/I_t$. Impedance can be expressed in terms of magnitude Z_0 and phase shift ϕ by:

$$Z = \frac{E_t}{I_t} = \frac{E_0 \sin(\omega t)}{I_0 \sin(\omega t + \phi)} = Z_0 \frac{\sin(\omega t)}{\sin(\omega t + \phi)} \tag{1.34}$$

There are two additional mechanisms besides normal resistance for an AC circuit which are inductance and capacitance, collectively referred to as reactance and these are represented by the imaginary part of impedance. The resistance forms the real part of impedance. To analyse the impedance of a circuit it is represented as a complex function. Euler's formula is used:

$$e^{j\phi} = \cos\phi + j\sin\phi \tag{1.35}$$

Where the potential of imaginary unit j is given by:

$$E_t = E_0 e^{j\omega t} \tag{1.36}$$

And the current response of imaginary unit j is given by:

$$I_t = I_0 e^{(j\omega - \phi)} \tag{1.37}$$

So impedance as a complex function is expressed as:

$$Z(\omega) = \frac{E}{I} = Z_0 e^{j\phi} = Z_0(\cos\phi - j\sin\phi) \tag{1.38}$$

A Nyquist plot (figure 1.22) is obtained by plotting the real part on the x-axis and the imaginary part on the y-axis and is the most common way to present impedance data. Impedance can also be presented by Bode phase and magnitude plots with impedance is plotted with log ω on the x-axis, and phase shift ϕ on the y-axis for the phase plot, absolute impedance |Z| on the y-axis for the magnitude plot.

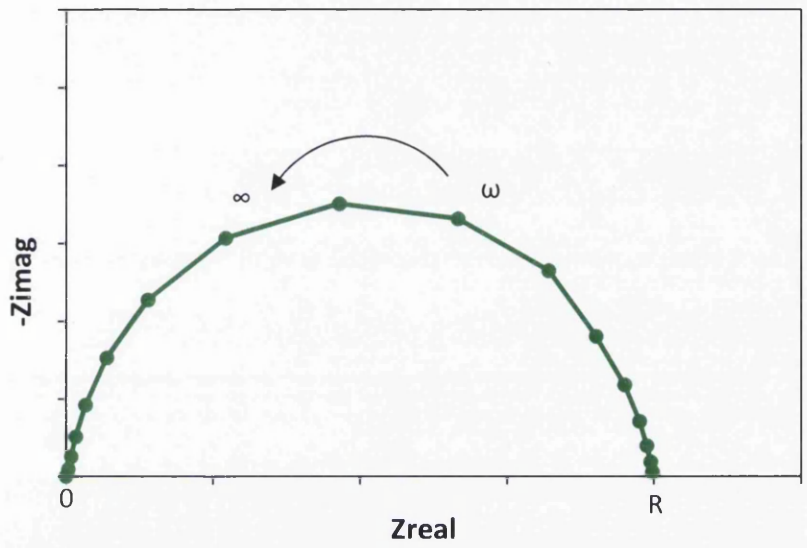

Figure 1.22: Nyquist plot of a resistor and capacitor in parallel

Each point represents impedance at a different value of frequency with the lowest frequencies on the right and the highest frequencies on the left. A resistor is a component which implements an electrical resistance to the circuit and is represented in a diagram by:

A capacitor is an electric circuit element composed of two metal sheets separated by a dielectric material; its behaviour is governed by the equation:

$$C = \frac{q}{E} \tag{1.39}$$

Where C is capacitance (in farads, F), q is charge stored on the capacitor (in coulombs, C) and E is the potential across the capacitor (V), it is represented in a circuit by:

A Nyquist plot of a typical DSC is shown in figure 1.23.

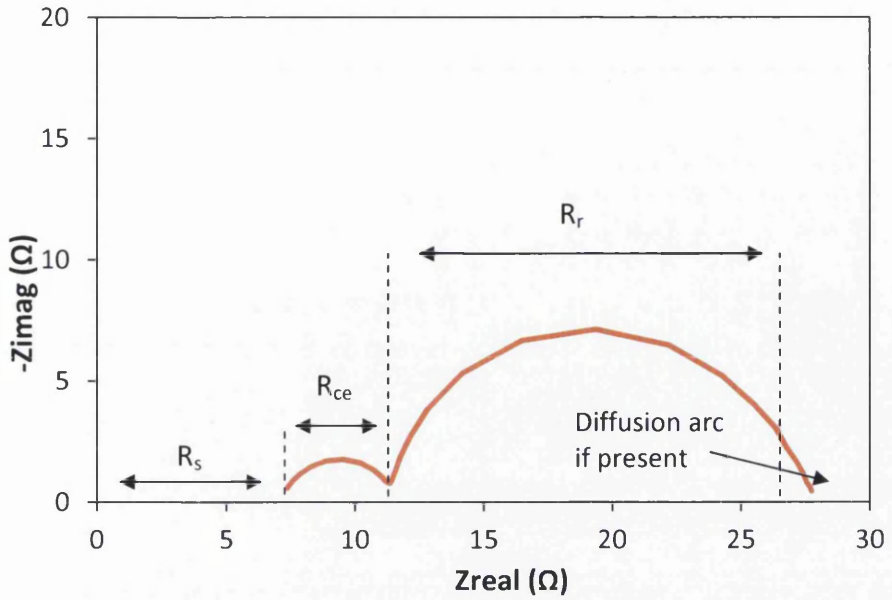

Figure 1.23: Nyquist plot of a typical DSC at bias potential near V_{MAX}

R_s is the series resistance which is the resistance across the TCO and contacts. R_{ce} is the resistance across the counter electrode/electrolyte interface and R_r is the resistance across the TiO_2/electrode. At the lower frequency end a third arc may be seen but is mostly obstructed in figure 1.25 by R_r. The arc represents the Nernst diffusion impedance of the electrolyte but can be ignored if just interested in the other two interfaces. Fast reactions are characterised by small resistance and slower reactions by high resistances. The differences in reaction speeds between iodide reduction by the Pt and recombination of TiO_2 with electrolyte species (see section 1.2.1) helps with the interpretation of a liquid electrolyte DSC because usually the arcs are clearly visible and identifiable. If ignoring the Nernst diffusion impedance a DSC can be modelled simply as where the two arcs are represented by a resistor/capacitor pair (figure 1.24).

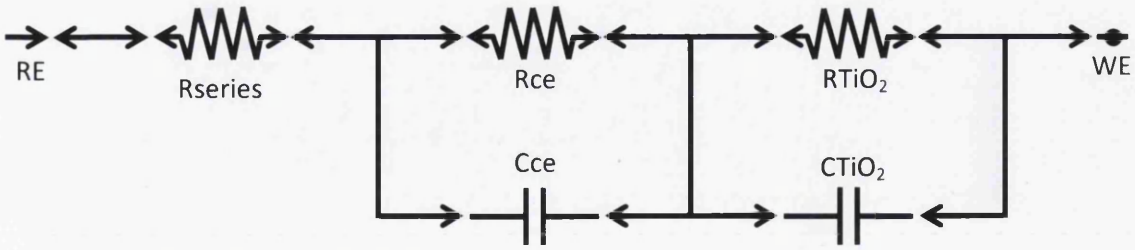

Figure 1.24: Simple equivalent circuit model of a dye-sensitised solar cell

The impedance of a resistor is:

$$Z(\omega) = Z_0 e^{j\phi} \tag{1.40}$$

And the impedance of a capacitor is:

$$Z = \frac{1}{j\omega C} \tag{1.41}$$

The capacitance of a system is not always ideal, which is shown by a depressed semicircle, so constant phase elements (CPEs) are introduced. The impedance of a CPE is:

$$\frac{1}{Z} = Q^{\circ}(j\omega)^{\beta} \tag{1.42}$$

The equivalent capacitance can then be represented by:

$$C_{eq} = \frac{(R\ x\ Q^{\circ})^{1/\beta}}{R} \tag{1.43}$$

1.5.4 Cyclic voltammetry

Cyclic voltammetry is a widely used electrochemical analysis technique that is very useful for obtaining qualitative and kinetic information about the redox reactions of electroactive species in a system. It involves using a potentiostat to apply a potential to an electrode between certain intervals, sweeping in both forward and reverse directions, and measuring the current response (figure 1.25). At a potential where no reactions occur no current will flow. At a more reducing potential it induces a reduction of oxidation species [O] to reduction species [R] and current starts to pass. It gets to a certain potential and current falls off and maximum is reached. The peak represents a balance between the rate of electron transfer reaction and the rate of O diffusion towards the electrode surface. Maximum current is called peak current (i_p), indicating a diffusion controlled reaction. Thickness of the diffusion layer increases so O has to cross longer distance to electrode surface. The electrode potential governs its reaction and rate. The current generated by the transfer of electrons is governed by Faraday's law; the amount of chemical reaction caused by the flow of current is proportional to the amount of electricity passed.

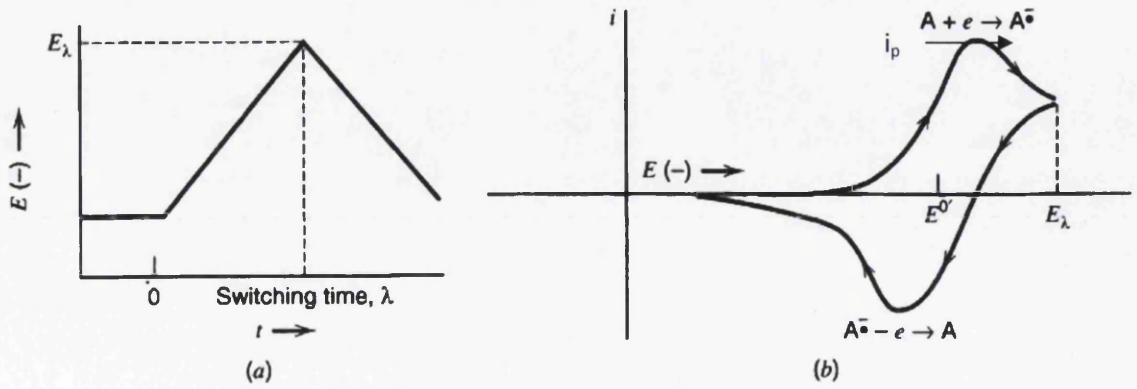

Figure 1.25: (a) Cyclic potential sweep and (b) resulting cyclic voltammogram [146]

The electrode reaction may be reversible or irreversible, which is determined by its ability to follow the Nernstian equilibrium. In a reversible system the electrons transfer back and forth according to the Nernst equation and match criteria according to this which means the reaction is efficient and sustainable. The Nernst equation expressed with a base 10 logarithm for a cell at 25°C is:

$$E = E^0 - \frac{0.05916\,V}{z}\log_{10}\frac{[O]}{[R]} \tag{1.44}$$

Where E is the electrode potential, E^0 is the standard electrode potential, z is the number of moles of electrons transferred in the reaction, and [O] and [R] is the chemical activity of the oxidation species and reduction species respectively.

The peak potential (E_p) is constant and independent of scan rate, the peak current i_p will increase with increasing scan rate because there is less time for diffusion to occur which as previously discussed limits the peak. Diagnostic equations derived from the Nernst equation (1.44) to validate the reversibility of a cyclic voltammogram include [146]:

$$\Delta E_p = E^a_p - E^c_p = 59/n \text{ mV}$$

$$|E_p - E_{p/2}| = 59/n \text{ mV}$$

$$|i^a_p/i^c_p| = 1$$

$$I_p \alpha v^{1/2}$$

Where c is the cathodic peak, where reduction occurs, and a is the anodic peak, where oxidation occurs and ΔE_p is the peak potential separation. In an irreversible electrode reaction the rate of electron transfer is insufficient to maintain the Nernstian equilibrium. In a more irreversible reaction peak current will appear at more negative potential than that of reversible reaction; it has a higher over-potential. The scan rate can illustrate if a system is irreversible, at a low scan rate the system may behave reversibly because the sluggish electron transfer has enough time to occur, but as the scan rate is increased there is peak separation and the E_p will drift to a further over-potential with increasing scan rate. For a totally irreversible reaction the reverse peak is absent in the reverse sweep. The diagnostic criteria for an irreversible system include:

$$i^c_p \alpha v^{1/2}$$

$$E^c_p \text{ shifts by } -30/\alpha_c n_\alpha \text{ mV for each decade increase in v}$$

$$|E_p - E_{p/2}| = 48/\alpha_c n_\alpha \text{ mV}$$

In DSCs cyclic voltammetry can be used to study the redox potentials of reactions occurring between the dye, TiO_2 and electrolyte, and is commonly used for the triiodide reaction in

evaluating the catalyst for the counter electrode [147][148][108]. A typical three electrode cyclic voltammogram of platinum in I^-/I_3^- electrolyte is shown in figure 1.26.

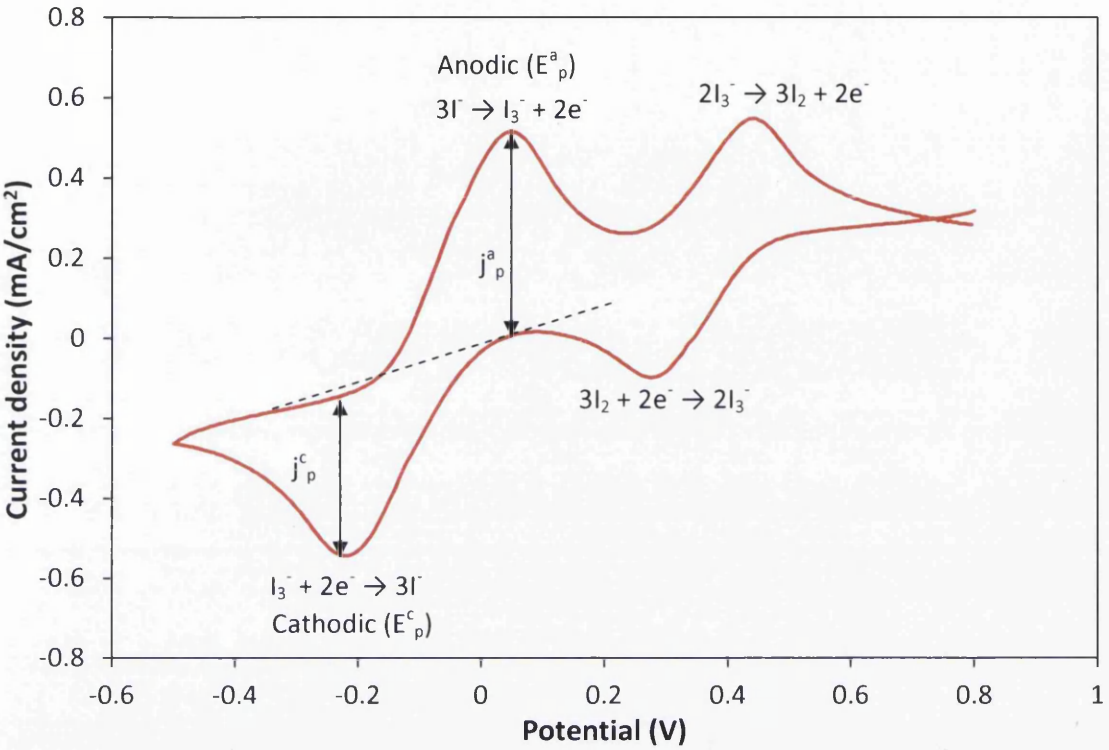

Figure 1.26: Cyclic voltammogram of platinum in a I^-/I_3^- system

This reaction is quasi-reversible; it is slower in the reverse direction than the forward direction. The redox reactions of greatest interest in evaluating the catalyst for a DSC are between I^- and I_3^- and these have been labelled E^a_p and E^c_p. It should meet close to the reversible criteria described above if the catalyst performs well and facilitates the charge transfer effectively.

1.5.5 Transient photovoltage and photocurrent decay

Charge transport and recombination in the TiO_2 film of a DSC can be measured at open circuit conditions from the rise and decay times associated with small perturbations of photovoltage transients [149]. The bias light intensity can be varied so that parameters such as the effective electron diffusion coefficient, D_n, and effective electron lifetime, τ_n, can be determined as functions of photovoltage and electron trap occupancy. These can then be used to calculate the effective electron diffusion length, L_n:

$$L_n = (D_n \tau_n)^{1/2} \qquad (1.45)$$

Studying the transport and recombination close to open circuit conditions is useful because the electron concentration is high. It is also possible to compare between cells at open circuit because the quasi-Fermi level is approximately uniform across the mesoporous TiO_2 film and measurable unlike at short circuit. Then by measuring at different light bias intensities the V_{OC} can be varied so that the position of the quasi-Fermi level can be equalised between devices [149]. For photocurrent decay measurements the cell is illuminated for a few seconds to obtain a constant photocurrent at short circuit conditions. Then the light is switched off and the cell is switched to open circuit simultaneously; the resulting voltage gives an indication of the electrochemical potential under short circuit conditions [98]. For the work in this thesis a set up was used similarly to described here [150] where photovoltage and photocurrent decay were both obtained.

1.5.6 Fourier transform infrared spectroscopy

Infrared spectroscopy involves the absorption of infrared radiation causing chemical bonds to bend and stretch so it is very useful for identifying organic molecules. It uses the vibrational portion of the infrared spectrum which lies between the wavelengths (λ) of 2.5 μm and 25 μm. Wavelength is related to wavenumber ($\bar{\upsilon}$) by:

$$\bar{\upsilon}\ (cm^{-1}) = \frac{1}{\lambda\ (cm)} \tag{1.46}$$

This corresponds to a range of 4000 to 400 cm^{-1}. Wavenumbers are the preferable unit because they are directly proportional to energy (a higher wavenumber has higher energy). In Fourier transform infrared spectroscopy the optical pathways produce a pattern called an interferogram which contains all frequencies of the infrared spectrum. An interferogram is essentially a plot of intensity vs. time. To convert this to intensity vs. frequency a Fourier transform is used to separate the individual absorption frequencies from the interferogram producing a spectrum virtually identical to that of the older dispersive spectrometer technique with greater speed and sensitivity. Attenuated total reflectance (ATR), see figure 1.27, is a different sampling method for FTIR which simplifies the preparation of solid and liquid samples and improves spectral reproducibility. When the infrared beam comes into contact with the sample, energy is absorbed and the beam is altered. The ATR crystal measures the changes in the internally reflected beam [151].

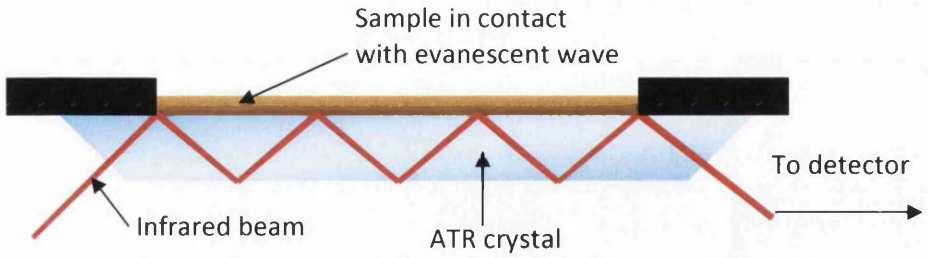

Figure 1.27: Diagram of an ATR crystal used in FTIR spectroscopy

1.6 Aims and objectives

This thesis aims to investigate methods to reduce the time intensive steps associated with the fabrication of a dye-sensitised solar cell (DSC) (shown in figure 1.28) which are currently a bottleneck for translating this technology from the laboratory to an industrial scale. DSCs have the potential to be a low cost solar cell candidate due to the relatively low cost of materials and ease of processing. In addition some steps associated with the fabrication of a DSC share similarity to other technologies so these methods could be extremely applicable and versatile.

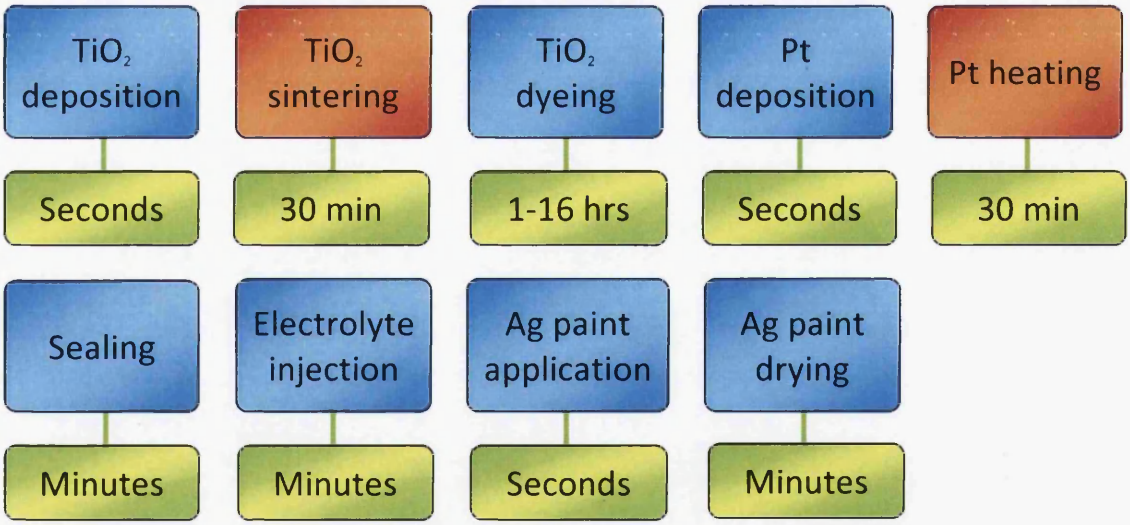

Figure 1.28: Traditional lab process and associated times for the construction of a DSC

The main focus was using near infrared (NIR) radiation to rapidly heat components for a DSC. In Chapter 3 the effect of NIR radiation on transparent conducting oxide coated glass was quantified to estimate if suitable temperatures for DSC processing could be reached on those substrates. The resistivity changes of tin-doped indium oxide (ITO) and fluorine-doped tin oxide (FTO) coated glasses were also studied upon exposure to NIR heating as it is crucial for conductivity to be maintained for applications in electronic devices.

In Chapters 4 and 5 NIR radiation was used on FTO glass, the most widely used substrate for DSCs, to thermally platinise counter electrodes and to heat TiO_2 paste to create a mesoporous TiO_2 working electrode. The aim was complete these heating steps as quickly as possible with the same or superior performance when implemented into a DSC device. Samples were directly compared to conventionally heated platinum and TiO_2 to compare their structure and behaviour. In Chapter 8 these components were combined into a device using only rapid NIR heating with other time saving methods such as fast dyeing to remove all time intensive steps from the lab fabrication procedure and make suggestions to how this would translate to industrial scale.

In Chapter 6 ITO glass substrates were subjected to NIR heating in an attempt to create counter electrodes and working electrodes for DSCs. The aim was to investigate if high temperature platinisation and TiO_2 sintering can be achieved without rapidly increasing the resistivity of the substrate which is a current problem for ITO glass. Although not directly relevant to DSC fabrication this would demonstrate a high temperature application of ITO glass not possible with conventional heating; thus supporting the merit of using NIR heating for technologies that require ITO glass.

Titanium has been used previously with NIR radiation to rapidly produce a working electrode for DSCs and is a suitable metallic substrate in this configuration due to its compatibility with I^-/I_3^- electrolyte and semiconducting oxide layer of TiO_2 created during heating. However for thermal platinisation of counter electrodes the oxide growth hinders performance which has led to a less than optimal heating time used for conventional heating in an attempt to balance preventing oxide growth with time required for platinum conversion. In Chapter 7 NIR heating was used to rapidly heat a counter electrode for DSC devices on titanium to see if oxide growth could be prevented and high catalytic performance achieved. NIR heating of flexible polymeric substrates was also investigated in Chapter 7 to see if short repetitive exposures of radiation could achieve any level of thermal platinisation or mesoporous TiO_2 film creation.

1.7 References

[1] BP, BP Statistical Review of World Energy June 2013, 2013.

[2] BP, [Online]. Available at: http://www.bp.com/en/global/corporate/about-bp/statistical-review-of-world-energy-2013/review-by-energy-type/renewable-energy/renewable-power-.html. [Accessed: 30-Aug-2013].

[3] Department of Energy & Climate Change, DUKES 2013 Chapter 6: Renewable sources of energy, 2013.

[4] Viridian Solar, [Online]. Available at: http://www.viridiansolar.co.uk/Solar_Energy_Guide_5_2.htm. [Accessed: 25-Sep-2013].

[5] J. Zhao, A. Wang, P.P. Altermatt, S.R. Wenham, M.A. Green, 24% Efficient perl silicon solar cell: Recent improvements in high energy silicon cell research, Sol. Energy Mater. Sol. Cells. 41/42 (1996) 87–99.

[6] D. Chapin, C. Fuller, G. Pearson, A New Silicon p-n Junction Photocell for Converting Solar Radiation into Electrical Power, J. Appl. Phys. 25 (1954) 676–678.

[7] US Department of Energy, [Online]. Available at: http://www.nrel.gov/docs/fy12osti/51847.pdf. [Accessed: 21-Sep-2013].

[8] First Solar, [Online]. Available at: http://investor.firstsolar.com/releasedetail.cfm?ReleaseID=833971. [Accessed: 17-May-2014].

[9] First Solar, [Online]. Available at: http://investor.firstsolar.com/releasedetail.cfm?ReleaseID=755244. [Accessed: 25-Sep-2013].

[10] PV-Tech, [Online]. Available at: http://www.pv-tech.org/guest_blog/top_10_pv_module_suppliers_in_2012. [Accessed: 25-Sep-2013].

[11] V. Fthenakis, Sustainability of photovoltaics: The case for thin-film solar cells, Renew. Sustain. Energy Rev. 13 (2009) 2746–2750.

[12] V.M. Fthenakis, M. Fuhrmann, J. Heiser, a. Lanzirotti, J. Fitts, W. Wang, Emissions and encapsulation of cadmium in CdTe PV modules during fires, Prog. Photovoltaics Res. Appl. 13 (2005) 713–723.

[13] L. Kranz, C. Gretener, J. Perrenoud, R. Schmitt, F. Pianezzi, F. La Mattina, et al., Doping of polycrystalline CdTe for high-efficiency solar cells on flexible metal foil, Nat. Commun. 4 (2013).

[14] EMPA, [Online]. Available at: http://www.empa.ch/plugin/template/empa/1/131438/---/l=2. [Accessed: 25-Sep-2013].

[15] G. Yu, J. Gao, J.C. Hummelen, F. Wudl, a. J. Heeger, Polymer Photovoltaic Cells: Enhanced Efficiencies via a Network of Internal Donor-Acceptor Heterojunctions, Science (80-.). 270 (1995) 1789–1791.

[16] Osa Direct, [Online]. Available at: http://www.osa-direct.com/osad-news/323.html. [Accessed: 01-Nov-2010].

[17] Heliatek, [Online]. Available at: http://www.heliatek.com/newscenter/latest_news/neuer-weltrekord-fur-organische-

solarzellen-heliatek-behauptet-sich-mit-12-zelleffizienz-als-technologiefuhrer/?lang=en. [Accessed: 15-Oct-2013].

[18] NREL, [Online]. Available at: http://www.nrel.gov/ncpv/images/efficiency_chart.jpg. [Accessed: 17-May-2014].

[19] J. Moser, Notiz uber Verstarkung photoelektrischer Strome durich optische Sensibilisirung, Monatshefte Fur Chemie. 8 (1887) 373.

[20] A. Terenin, I. Akimov, Some Experiments on the Photosensitization Mechanism of Semiconductors by Dyes, 69 (1965) 730–738.

[21] H. Gerischer, H. Tributsch, Electrochemistry of ZnO monocrystal spectral sensitivity, Berichte Der Bunsen-Gesellschaft Fur Phys. Chim. 72 (1968) 437.

[22] W.D.K. Clark, N. Sutin, Spectral Sensitization of n-Type TiO_2 Electrodes by Polypyridineruthenium(II) Complexes, J. Am. Chem. Soc. 19 (1977) 4676–4682.

[23] J. Moser, M. Grätzel, Photoelectrochemistry with Colloidal Semiconductors; Laser Studies of Halide Oxidation in Colloidal Dispersions of TiO_2 and a-Fe_2O_3, Helv. Chim. Acta. 65 (1982) 1436–1444.

[24] J. Desilvestro, M. Grätzel, L. Kavan, J. Moser, Highly Efficient Sensitization of Titanium Dioxide, J. Am. Chem. Soc. 107 (1985) 2988–2990.

[25] K. Kalyanasundaram, N. Vlachopoulos, V. Krishnan, A. Monnier, M. Grätzel, Sensitization of TiO_2 in the visible light region using zinc porphyrins, J. Phys. Chem. 91 (1987) 2342–2347.

[26] B. O'Regan, J. Moser, M. Anderson, M. Grätzel, Vectorial electron injection into transparent semiconductor membranes and electric field effects on the dynamics of light-induced charge separation, J. Phys. Chem. 94 (1990) 8720–8726.

[27] B. O'Regan, M. Grätzel, A low-cost, high-efficiency solar cell based on dye-sensitized colloidal TiO2 films, Nature. 353 (1991) 737–740.

[28] K. Hara, H. Arakawa, Dye-sensitised Solar Cells, in: A. Luque, S. Hegedus (Eds.), Handb. Photovolt. Sci. Eng., 1st ed., John Wiley & Sons, 2003: pp. 663–700.

[29] S.A. Haque, Y. Tachibana, D.R. Klug, J.R. Durrant, Charge Recombination Kinetics in Dye-Sensitized Nanocrystalline Titanium Dioxide Films under Externally Applied Bias, J. Phys. Chem. B. 102 (1998) 1745–1749.

[30] P.M. Sommeling, H.C. Rieffe, J.A.M. Van Roosmalen, A. Schonecker, J.M. Kroon, J.A. Wienke, et al., Spectral response and IV-characterization of dye-sensitized nanocrystalline TiO solar cells, Sol. Energy Mater. Sol. Cells. 62 (2000) 399–410.

[31] P. de Jongh, D. Vanmaekelbergh, Investigation of the Electronic Transport Properties of Nanocrystalline Particulate TiO_2 Electrodes by Intensity-Modulated Photocurrent Spectroscopy, J. Phys. Chem. B. 101 (1997) 2716–2722.

[32] A. Wahl, J. Augustynski, Charge Carrier Transport in Nanostructured Anatase TiO_2 Films Assisted by the Self-Doping of Nanoparticles, J. Phys. Chem. B. 102 (1998) 7820–7828.

[33] J.S. Salafsky, W.H. Lubberhuizen, E. Van Faassen, R.E.I. Schropp, Charge Dynamics following Dye Photoinjection into a TiO_2 Nanocrystalline Network, J. Phys. Chem. B. 102 (1998) 766–769.

[34] A. Yella, H.-W. Lee, H. Tsao, C. Yi, A. Chandiran, M.K. Nazeeruddin, et al., Porphyrin-Sensitised Solar Cells with Cobalt (II/III)-Based Redox Electrolyte Exceed 12 Percent Efficiency, Science (80-.). 334 (2011) 629–634.

[35] S. Ito, N.-L.C. Ha, G. Rothenberger, P. Liska, P. Comte, S.M. Zakeeruddin, et al., High-efficiency (7.2%) flexible dye-sensitized solar cells with Ti-metal substrate for nanocrystalline-TiO2 photoanode., Chem. Commun. (2006) 4004–6.
[36] R.G. Gordon, Criteria for Choosing Transparent Conductors, MRS Bull. (2000) 52–57.
[37] Scientific American, [Online]. Available at: http://www.scientificamerican.com/article.cfm?id=more-efficient-dyed-cells-offer-hope-for-cheap-solar-windows. [Accessed: 27-Sep-2013].
[38] EPFL, [Online]. Available at: http://actu.epfl.ch/news/epfl-s-campus-has-the-world-s-first-solar-window/. [Accessed: 02-Jun-2014].
[39] K. Goto, T. Kawashima, N. Tanabe, Heat-resisting TCO films for PV cells, Sol. Energy Mater. Sol. Cells. 90 (2006) 3251–3260.
[40] C. Sima, C. Grigoriu, S. Antohe, Comparison of the dye-sensitized solar cells performances based on transparent conductive ITO and FTO, Thin Solid Films. 519 (2010) 595–597.
[41] S. Lee, J. Noh, S. Bae, I. Cho, Indium-Tin-Oxide-Based Transparent Conducting Layers for Highly Efficient Photovoltaic Devices, J. Phys. Chem. C. 113 (2009) 7443–7447.
[42] S. Garner, M. He, P.-Y. Lo, C.-F. Sung, C.-W. Liu, Y.-M. Hsieh, et al., Electrophoretic Displays Fabricated on Ultra-Slim Flexible Glass Substrates, J. Disp. Technol. 8 (2012) 590–595.
[43] A. Payne, R. Duke, R.H. Williams, Accelerating residential PV expansion: supply analysis for competitive electricity markets, Energy Policy. 29 (2001) 787–800.
[44] T. Watson, G. Reynolds, D. Wragg, G. Williams, D. Worsley, Corrosion Monitoring of Flexible Metallic Substrates for Dye-Sensitized Solar Cells, Int. J. Photoenergy. 2013 (2013) 1–8.
[45] M. Toivola, F. Ahlskog, P. Lund, Industrial sheet metals for nanocrystalline dye-sensitized solar cell structures, Sol. Energy Mater. Sol. Cells. 90 (2006) 2881–2893.
[46] J. Park, Y. Jun, H. Yun, S.-Y. Lee, M. Kang, Fabrication of an Efficient Dye-Sensitized Solar Cell with Stainless Steel Substrate, J. Electrochem. Soc. 155 (2008) 145–149.
[47] A. Hagfeldt, U. Björkstén, S.-E. Lindquist, Photoelectrochemical studies of colloidal TiO_2-films: the charge separation process studied by means of action spectra in the UV region, Sol. Energy Mater. Sol. Cells. 27 (1992) 293–304.
[48] H. Lindström, H. Rensmo, S. Södergren, A. Solbrand, S.-E. Lindquist, Electron Transport Properties in Dye-Sensitized Nanoporous - Nanocrystalline TiO_2 Films, J. Phys. Chem. 100 (1996) 3084–3088.
[49] M. Kang, N. Park, K. Ryu, S. Chang, K. Kim, A 4.2% efficient flexible dye-sensitized TiO_2 solar cells using stainless steel substrate, Sol. Energy Mater. Sol. Cells. 90 (2006) 574–581.
[50] G.R. a. Kumara, S. Kawasaki, P.V.V. Jayaweera, E.V. a. Premalal, S. Kaneko, Large area dye-sensitized solar cells with titanium based counter electrode, Thin Solid Films. 520 (2012) 4119–4121.
[51] T. Ma, X. Fang, M. Akiyama, K. Inoue, H. Noma, E. Abe, Properties of several types of novel counter electrodes for dye-sensitized solar cells, J. Electroanal. Chem. 574 (2004) 77–83.
[52] M. Toivola, J. Halme, K. Miettunen, K. Aitola, P.D. Lund, Nanostructured dye solar cells on flexible substrates — Review, Int. J. Energy Res. 33 (2009) 1145–1160.

[53] H. Kostlin, Application of thin semiconductor metal films in energy technology, in: Aachen P.G. (Ed.), Festkorperprobleme 22, Springer Berlin Heidelberg, 1982: pp. 229–254.

[54] I. Forbes, L. Peter, Chapter 17 Materials for Photovoltaics, in: T. Letcher, J. Scott (Eds.), Mater. a Sustain. Futur., RSC Publishing, 2012.

[55] T. Miyasaka, M. Ikegami, Y. Kijitori, Photovoltaic Performance of Plastic Dye-Sensitized Electrodes Prepared by Low-Temperature Binder-Free Coating of Mesoscopic Titania, J. Electrochem. Soc. 154 (2007) A455.

[56] W. Tan, J. Chen, X. Zhou, J. Zhang, Y. Lin, X. Li, et al., Preparation of nanocrystalline TiO_2 thin film at low temperature and its application in dye-sensitized solar cell, J. Solid State Electrochem. 13 (2009) 651–656.

[57] T.N. Murakami, Y. Kijitori, N. Kawashima, T. Miyasaka, Low temperature preparation of mesoporous TiO_2 films for efficient dye-sensitized photoelectrode by chemical vapor deposition combined with UV light irradiation, J. Photochem. Photobiol. A Chem. 164 (2004) 187–191.

[58] S. Uchida, M. Tomiha, H. Takizawa, M. Kawaraya, Flexible dye-sensitized solar cells by 28GHz microwave irradiation, J. Photochem. Photobiol. A Chem. 164 (2004) 93–96.

[59] T. Kado, M. Yamaguchi, Y. Yamada, S. Hayase, Low temperature preparation of nano-porous TiO_2 layers for plastic dye-sensitized solar cells, Chem. Lett. 32 (2003) 1056–1057.

[60] H. Pan, S. Ko, N. Misra, C. Grigoropoulos, Laser annealed composite titanium dioxide electrodes for dye-sensitized solar cells on glass and plastics, Appl. Phys. Lett. 94 (2009) 071117.

[61] T. Yamaguchi, N. Tobe, D. Matsumoto, H. Arakawa, Highly efficient plastic substrate dye-sensitized solar cells using a compression method for preparation of TiO_2 photoelectrodes, Chem. Commun. (2007) 4767–9.

[62] Z. Wang, H. Kawauchi, T. Kashima, H. Arakawa, Significant influence of TiO_2 photoelectrode morphology on the energy conversion efficiency of N719 dye-sensitized solar cell, Coord. Chem. Rev. 248 (2004) 1381–1389.

[63] S.-S. Kim, Y.-C. Nah, Y.-Y. Noh, J. Jo, D.-Y. Kim, Electrodeposited Pt for cost-efficient and flexible dye-sensitized solar cells, Electrochim. Acta. 51 (2006) 3814–3819.

[64] H. Lindström, A. Holmberg, E. Magnusson, L. Malmqvist, A. Hagfeldt, A new method to make dye-sensitized nanocrystalline solar cells at room temperature, J. Photochem. Photobiol. A Chem. 145 (2001) 107–112.

[65] X. Fang, T. Ma, M. Akiyama, G. Guan, S. Tsunematsu, E. Abe, Flexible counter electrodes based on metal sheet and polymer film for dye-sensitized solar cells, Thin Solid Films. 472 (2005) 242–245.

[66] M. Grätzel, Conversion of sunlight to electric power by nanocrystalline dye-sensitized solar cells, J. Photochem. Photobiol. A Chem. 164 (2004) 3–14.

[67] B. V Bergeron, A. Marton, G. Oskam, G.J. Meyer, Dye-sensitized SnO_2 electrodes with iodide and pseudohalide redox mediators, J. Phys. Chem. B. 109 (2005) 937–43.

[68] A.N.M. Green, E. Palomares, S. a Haque, J.M. Kroon, J.R. Durrant, Charge transport versus recombination in dye-sensitized solar cells employing nanocrystalline TiO_2 and SnO_2 films, J. Phys. Chem. B. 109 (2005) 12525–33.

[69] B. Onozawa-Agyeman, S. Kaneko, A. Kumara, M. Okuya, K. Murakami, A. Konno, et al., Sensitization of Nanocrystalline SnO_2 Films with Indoline Dyes, Jpn. J. Appl. Phys. 44 (2005) L731–L733.

[70] C. Nasr, P. V Kamat, S. Hotchandani, Photoelectrochemistry of Composite Semiconductor Thin Films. Photosensitization of the SnO_2/TiO_2 Coupled System with a Ruthenium Polypyridyl Complex, J. Phys. Chem. B. 102 (1998) 10047–10056.

[71] A. Kay, M. Grätzel, Dye-Sensitized Core - Shell Nanocrystals: Improved Efficiency of Mesoporous Tin Oxide Electrodes Coated with a Thin Layer of an Insulating Oxide, Chem. Mater. 14 (2002) 2930–2935.

[72] M. Matsumura, S. Matsudaira, H. Tsubomura, M. Takata, H. Yanagida, Dye Sensitization and Surface Structures of Semiconductor Electrodes, Ind. Eng. Chem. Prod. Res. Dev. 19 (1980) 415–421.

[73] T.P. Chou, Q. Zhang, G. Cao, Effects of Dye Loading Conditions on the Energy Conversion Efficiency of ZnO and TiO_2 Dye-Sensitized Solar Cells, J. Phys. Chem. C. 111 (2007) 18804–18811.

[74] K. Keis, J. Lindgren, S. Lindquist, A. Hagfeldt, Studies of the Adsorption Process of Ru Complexes in Nanoporous ZnO Electrodes, Langmuir. 16 (2000) 4688–4694.

[75] M. Saito, S. Fujihara, Large photocurrent generation in dye-sensitized ZnO solar cells, Energy Environ. Sci. 1 (2008) 280.

[76] L. Kavan, M. Grätzel, S.E. Gilbert, C. Klemenz, H.J. Scheel, Electrochemical and Photoelectrochemical Investigation of Single-Crystal Anatase, J. Am. Chem. Soc. 118 (1996) 6716–6723.

[77] M.K. Nazeeruddin, A. Kay, I. Rodicio, R. Humphry-Baker, E. Muller, P. Liska, et al., Conversion of Light to Electricity by cis-X_2Bis(2,2'-bipyridyl-4,4'-dicarboxylate)ruthenium(II) Charge-Transfer Sensitizers (X = Cl^-, Br^-, CN^-, and SCN^-) on Nanocrystalline TiO_2 Electrodes, J. Am. Chem. Soc. 115 (1993) 6382–6390.

[78] A. Fahmi, C. Minot, B. Silvi, M. Causa, Theoretical analysis of the structures of titanium dioxide crystals, Phys. Rev. B. 47 (1993) 11717–11724.

[79] P. Badziag, W. Verwoerd, W. Ellis, N. Greiner, Nanometre-sized diamonds are more stable than graphite, Nature. 343 (1990) 244–245.

[80] N. Vlachopoulos, P. Liska, J. Augustynski, M. Grätzel, Very Efficient Visible Light Energy Harvesting and Conversion by Spectral Sensitization of High Surface Area Polycrystalline Titanium Dioxide Films, J. Am. Chem. Soc. 110 (1988) 1216–1220.

[81] L. Kavan, M. Grätzel, Highly Efficient Semiconducting TiO_2 Photoelectrodes Prepared by Aerosol Pyrolysis, Electrochim. Acta. 40 (1995) 643–652.

[82] S. Hejiman, H. Stein, Electrostatic and Sterical Stabilization of TiO_2 Dispersions, Langmuir. 11 (1995) 422–427.

[83] J. Banfield, B. Bischoff, M. Anderson, TiO_2 accessory minerals: coarsening, and transformation kinetics in pure and doped synthetic nanocrystalline materials, Chem. Geol. 110 (1993) 211–231.

[84] K. MacKenzie, Calcination of titania: IV, Effect of additives on the anatase-rutile transformation, Trans. J. Br. Ceram. Soc. 74 (1975) 29–34.

[85] M.K. Nazeeruddin, P. Péchy, T. Renouard, S.M. Zakeeruddin, R. Humphry-Baker, P. Comte, et al., Engineering of Efficient Panchromatic Sensitizers for Nanocrystalline TiO_2-based Solar Cells, J. Am. Chem. Soc. 123 (2001) 1613–24.

[86] M.K. Nazeeruddin, F. De Angelis, S. Fantacci, A. Selloni, G. Viscardi, P. Liska, et al., Combined experimental and DFT-TDDFT computational study of photoelectrochemical cell ruthenium sensitizers, J. Am. Chem. Soc. 127 (2005) 16835–47.

[87] C. Klein, M.K. Nazeeruddin, D. Di Censo, P. Liska, M. Grätzel, Amphiphilic ruthenium sensitizers and their applications in dye-sensitized solar cells, Inorg. Chem. 43 (2004) 4216–26.

[88] M. Ryan, Ruthenium Complexes for Dye Sensitised Solar Cells, Platin. Met. Rev. 53 (2009) 216–218.

[89] C.-Y. Chen, M. Wang, J.-Y. Li, N. Pootrakulchote, L. Alibabaei, C. Ngoc-le, et al., Highly Efficient Light-Harvesting, ACS Nano. 3 (2009) 3103–3109.

[90] A. Yella, H.-W. Lee, H.N. Tsao, C. Yi, A.K. Chandiran, M.K. Nazeeruddin, et al., Porphyrin-sensitized solar cells with cobalt (II/III)-based redox electrolyte exceed 12 percent efficiency, Science (80-.). 334 (2011) 629–34.

[91] T. Watson, P. Holliman, D. Worsley, Rapid, continuous in situ monitoring of dye sensitisation in dye-sensitized solar cells, J. Mater. Chem. 21 (2011) 4321–4325.

[92] M.K. Nazeeruddin, R. Splivallo, P. Liska, P. Comte, M. Grätzel, A swift dye uptake procedure for dye sensitized solar cells., Chem. Commun. (2003) 1456–7.

[93] Y. Ogomi, S. Sakaguchi, T. Kado, M. Kono, Y. Yamaguchi, S. Hayase, Ru Dye Uptake under Pressurized CO_2 Improvement of Photovoltaic Performances for Dye-sensitized Solar Cells, J. Electrochem. Soc. 153 (2006) A2294–A2297.

[94] Y. Ogomi, Y. Kashiwa, Y. Noma, Y. Fujita, S. Kojima, M. Kono, et al., Photovoltaic performance of dye-sensitized solar cells stained with black dye under pressurized condition and mechanism for high efficiency, Sol. Energy Mater. Sol. Cells. 93 (2009) 1009–1012.

[95] P. Holliman, M. Davies, A. Connell, Solar cells with multiple dyes, US 2013/0167900 A1, 2013.

[96] P.J. Holliman, M.L. Davies, A. Connell, B. Vaca Velasco, T.M. Watson, Ultra-fast dye sensitisation and co-sensitisation for dye sensitized solar cells., Chem. Commun. 46 (2010) 7256–8.

[97] P.J. Holliman, M. Mohsen, A. Connell, M.L. Davies, K. Al-Salihi, M.B. Pitak, et al., Ultra-fast co-sensitization and tri-sensitization of dye-sensitized solar cells with N719, SQ1 and triarylamine dyes, J. Mater. Chem. 22 (2012) 13318.

[98] G. Boschloo, A. Hagfeldt, Characteristics of the iodide/triiodide redox mediator in dye-sensitized solar cells, Acc. Chem. Res. 42 (2009) 1819–26.

[99] W. Kubo, K. Nurakoshi, T. Kitamura, Y. Wada, K. Hanabusa, S. Hirofusa, et al., Fabrication of Quasi-solid-state Dye-sensitized TiO_2 Solar Cells using Low Molecular Weight Gelators, Chem. Lett. 12 (1998) 1241–1242.

[100] K. Suzuki, M. Yamaguchi, M. Kumagai, S. Yanagida, Application of Carbon Nanotubes to Counter Electrodes of Dye-sensitized Solar Cells, Chem. Lett. 32 (2003) 28–29.

[101] J.D. Roy-mayhew, D.J. Bozym, C. Punckt, I.A. Aksay, Functionalized Graphene as a Catalytic Solar Cells, ACS Nano. 4 (2010) 6203–6211.

[102] A. Kay, M. Grätzel, Low cost photovoltaic modules based on dye sensitized nanocrystalline titanium dioxide and carbon powder, Sol. Energy Mater. Sol. Cells. 44 (1996) 99–117.

[103] W.J. Lee, E. Ramasamy, D.Y. Lee, J.S. Song, Efficient dye-sensitized solar cells with catalytic multiwall carbon nanotube counter electrodes, Appl. Mater. Interfaces. 1 (2009) 1145–9.

[104] L. Bay, K. West, B. Wintherjensen, T. Jacobsen, Electrochemical reaction rates in a dye-sensitised solar cell—the iodide/tri-iodide redox system, Sol. Energy Mater. Sol. Cells. 90 (2006) 341–351.

[105] M. Wang, A.M. Anghel, B. Marsan, N.-L. Cevey Ha, N. Pootrakulchote, S.M. Zakeeruddin, et al., CoS supersedes Pt as efficient electrocatalyst for triiodide reduction in dye-sensitized solar cells, J. Am. Chem. Soc. 131 (2009) 15976–7.

[106] A. Yella, [Online]. Available at: http://www.sciencemag.org/content/suppl/2011/11/03/334.6056.629.DC1/Yella-SOM.revision.1.pdf. [Accessed: 03-Oct-2013].

[107] N. Papageorgiou, W. Maier, M. Grätzel, An Iodine/Triiodide Reduction Electrocatalyst for Aqueous and Organic Media, J. Electrochem. Soc. 144 (1997) 876–884.

[108] A. Hauch, A. Georg, Diffusion in the electrolyte and charge-transfer reaction at the platinum electrode in dye-sensitized solar cells, Electrochim. Acta. 46 (2001) 3457–3466.

[109] M.E. Baumgartner, C.J. Raub, The Electrodeposition of Platinum and Platinum Alloys, Platin. Met. Rev. 32 (1988) 188–197.

[110] C. Rao, D. Trivedi, Chemical and electrochemical depositions of platinum group metals and their applications, Coord. Chem. Rev. 249 (2005) 613–631.

[111] C.H. Yoon, J. Lee, W.-S. Chae, K.-J. Kim, Enhanced performance of a dye-sensitized solar cell with an electrodeposited-platinum counter electrode, Electrochim. Acta. 53 (2008) 2890–2896.

[112] C.-M. Chen, C.-H. Chen, S.-J. Cherng, T.-C. Wei, Electroless deposition of platinum on indium tin oxide glass as the counterelectrode for dye-sensitized solar cells, Mater. Chem. Phys. 124 (2010) 173–178.

[113] A. Schweizer, G. Kerr, Thermal Decomposition of Hexachloroplatinic Acid, Inorg. Chem. 17 (1978) 8–9.

[114] U. Bach, D. Lupo, P. Comte, J.E. Moser, F. Weissortel, J. Salbeck, et al., Solid-state dye-senitized mesoporous TiO_2 solar cells with high photon-to-electron conversion efficiencies, Nature. 395 (1998) 583–585.

[115] U. Bach, Y. Tachibana, J. Moser, S.A. Haque, J.R. Durrant, M. Gra, Charge Separation in Solid-State Dye-Sensitized Heterojunction Solar Cells, J. Am. Chem. Soc. 121 (1999) 7445–7446.

[116] H.J. Snaith, A.J. Moule, C. Klein, K. Meerholz, R.H. Friend, M. Grätzel, Efficiency enhancements in solid-state hybrid solar cells via reduced charge recombination and increased light capture, Nano Lett. 7 (2007) 3372–6.

[117] P. Chen, J.H. Yum, F. De Angelis, E. Mosconi, S. Fantacci, S. Moon, et al., High Open-Circuit Voltage Solid-State Dye-Sensitized Solar Cells with Organic Dye, Nano Lett. 9 (2009) 2487–2492.

[118] B.E. Hardin, H.J. Snaith, M.D. McGehee, The renaissance of dye-sensitized solar cells, Nat. Photonics. 6 (2012) 162–169.

[119] L. Schmidt-mende, J.E. Kroeze, J.R. Durrant, K. Nazeeruddin, M. Grätzel, Effect of Hydrocarbon Chain Length of Amphiphilic Ruthenium Dyes on, Nano Lett. 5 (2005) 1315–1320.

[120] A. Kojima, K. Teshima, Y. Shirai, T. Miyasaka, Organometal halide perovskites as visible-light sensitizers for photovoltaic cells, J. Am. Chem. Soc. 131 (2009) 6050–1.

[121] H.-S. Kim, C.-R. Lee, J.-H. Im, K.-B. Lee, T. Moehl, A. Marchioro, et al., Lead iodide perovskite sensitized all-solid-state submicron thin film mesoscopic solar cell with efficiency exceeding 9%., Sci. Rep. 2 (2012) 591.

[122] M. Liu, M.B. Johnston, H.J. Snaith, Efficient planar heterojunction perovskite solar cells by vapour deposition, Nature. 501 (2013) 395–398.

[123] J. Burschka, N. Pellet, S.-J. Moon, R. Humphry-Baker, P. Gao, M.K. Nazeeruddin, et al., Sequential deposition as a route to high-performance perovskite-sensitized solar cells, Nature. 499 (2013) 316–319.

[124] K. Baedeker, Electrical conductivity and thermoelectric power of some heavy metal compounds, Ann. Der Phys. 22 (1907) 749.

[125] G. Haacke, Transparent Conducting Coatings, Annu. Rev. Mater. Sci. 7 (1977) 73–93.

[126] X. Wu, W.P. Mulligan, T.J. Coutts, Recent developments in RF sputtered cadmium stannate films, Thin Solid Films. 286 (1996) 274–276.

[127] I. Hamberg, C.G. Granqvist, Evaporated Sn-doped In_2O_3 films: Basic optical properties and applications to energy-efficient windows, J. Appl. Phys. 60 (1986) 123.

[128] S. Sheng, G. Fang, C. Li, S. Xu, X. Zhao, P-Type Transparent Conducting Oxides, Phys. Status Solidi. 203 (2006) 1891–1900.

[129] K. Gao, S. Zhou, X. Zhao, Thermal Stability of Aluminum Doped Zinc Oxide Thin Films, Mater. Sci. Forum. 685 (2011) 147–151.

[130] J.W. Bowers, H.M. Upadhyaya, T. Nakada, A.N. Tiwari, Effects of surface treatments on high mobility ITiO coated glass substrates for dye sensitized solar cells and their tandem solar cell applications, Sol. Energy Mater. Sol. Cells. 94 (2010) 691–696.

[131] U. Betz, M. Kharrazi Olsson, J. Marthy, M.F. Escolá, F. Atamny, Thin films engineering of indium tin oxide: Large area flat panel displays application, Surf. Coatings Technol. 200 (2006) 5751–5759.

[132] B. Sernelius, K.-F. Berggren, Z.-C. Jin, I. Hamberg, C. Granqvist, Band-gap tailoring of ZnO by means of heavy Al doping, Phys. Rev. B. 37 (1988) 10244–10248.

[133] E. Burstein, Anomalous Optical Absorption Limit in InSb, Phys. Rev. 93 (1954) 632–633.

[134] A. Hjortsberg, I. Hamberg, C. Granqvist, Transparent and heat-reflecting indium tin oxide films prepared by reactive electron beam evaporation, Thin Solid Films. 90 (1982) 323–326.

[135] W. Callister, ed., Materials Science and Engineering: An Introduction, 7th ed., John Wiley & Sons, 2007.

[136] E.T. Thostenson, T.-W. Chou, Microwave processing: fundamentals and applications, Compos. Part A Appl. Sci. Manuf. 30 (1999) 1055–1071.

[137] S. Uchida, M. Tomiha, N. Masaki, A. Miyazawa, H. Takizawa, Preparation of TiO_2 nanocrystalline electrode for dye-sensitized solar cells by 28GHz microwave irradiation, Sol. Energy Mater. Sol. Cells. 81 (2004) 135–139.

[138] M. Stuhldreher, Near-infrared curing: What it is; what it isn't, Powder Coat. 13 (2002) 25–29.
[139] Adphos, [Online]. Available at: http://www.adphosna.com/nirtechnology.html. [Accessed: 15-Oct-2013].
[140] Public Lab, [Online]. Available at: http://publiclab.org/wiki/uv-spectrometry. [Accessed: 26-Oct-2014].
[141] K.K.O. Bär, J. Anderson, N. Frederiksen, New Opportunities for Inline Paint Applications in Galvanizing Lines, AIST Conf. May (2004).
[142] T. Watson, I. Mabbett, H. Wang, L. Peter, D. Worsley, Ultrafast near infrared sintering of TiO_2 layers on metal substrates for dye-sensitized solar cells, Prog. Photovoltaics Res. Appl. 19 (2010) 482–486.
[143] M.J. Carnie, C. Charbonneau, P.R.F. Barnes, M.L. Davies, I. Mabbett, T.M. Watson, et al., Ultra-fast sintered TiO_2 films in dye-sensitized solar cells: phase variation, electron transport and recombination, J. Mater. Chem. A. 1 (2013) 2225.
[144] G. Mincuzzi, L. Vesce, M. Liberatore, A. Reale, A. Di Carlo, T.M. Brown, Laser-Sintered TiO_2 Films for Dye Solar Cell Fabrication: An Electrical, Morphological, and Electron Lifetime Investigation, IEEE Trans. Electron Devices. 58 (2011) 3179–3188.
[145] H.J. Snaith, The perils of solar cell efficiency measurements, Nat. Photonics. 6 (2012) 337–340.
[146] A. Bard, L. Faulkner, Electrochemical Methods: Fundamentals and Applications, 2nd ed., John Wiley & Sons, 2001.
[147] P. Li, J. Wu, J. Lin, M. Huang, Z. Lan, Q. Li, Improvement of performance of dye-sensitized solar cells based on electrodeposited-platinum counter electrode, Electrochim. Acta. 53 (2008) 4161–4166.
[148] K.-C. Huang, Y.-C. Wang, P.-Y. Chen, Y.-H. Lai, J.-H. Huang, Y.-H. Chen, et al., High performance dye-sensitized solar cells based on platinum nanoparticle/multi-wall carbon nanotube counter electrodes: The role of annealing, J. Power Sources. 203 (2012) 274–281.
[149] B.C. O'Regan, K. Bakker, J. Kroeze, H. Smit, P. Sommeling, J.R. Durrant, Measuring charge transport from transient photovoltage rise times. A new tool to investigate electron transport in nanoparticle films., J. Phys. Chem. B. 110 (2006) 17155–17160.
[150] P.R.F. Barnes, K. Miettunen, X. Li, A.Y. Anderson, T. Bessho, M. Grätzel, et al., Interpretation of optoelectronic transient and charge extraction measurements in dye-sensitized solar cells, Adv. Mater. 25 (2013) 1881–922.
[151] Perkin Elmer, [Online]. Available at: http://www.utsc.utoronto.ca/~traceslab/ATR_FTIR.pdf. [Accessed: 11-Jan-2013].

Further reading

M. S. Dresselhaus "Optical properties of solids." Proceedings of the International School of Physics" Enrico Fermi," J. Tauc, Editor (Academic Press. NY. 1966) (1966).
D. Pavia, G. Lampman, and G. Kriz, *Introduction to Spectroscopy*, 2nd ed. Saunders College Publishing, 1996.

A. Delahoy and S. Guo, "Transparent Conducting Oxides for Photovoltaics," in *Handbook of Photovoltaic Science and Engineering*, 2nd ed., A. Luque and S. Hegedus, Eds. John Wiley & Sons, 2011, pp. 716–796.
K. Kalyanasundaram, Ed., *Dye-sensitized Solar Cells*, 1st ed. Lausanne: EPFL Press, CRC Press, 2010.
M. N. Rahanan, Ed., *Ceramic Processing and Sintering*, 2nd ed. New York: Marcel Dekker Inc., 2003.
A. Luque and S. Hegedus, Eds., *Handbook of Photovoltaic Science and Engineering*, 1st ed. John Wiley & Sons, 2003.
J. Poortmans and V. Arkhipov, Eds., *Thin Film Solar Cells: Fabrication, Characterisation and Applications*, 1st ed. John Wiley & Sons, 2006.
F. Krebs, *Polymer Photovoltaics: A Practical Approach*. Society of Photo-Optical Instrumentation Engineers, 2008.
A. Bard and L. Faulkner, *Electrochemical Methods: Fundamentals and Applications*, 2nd ed. John Wiley & Sons, 2001, p. 240.
W. Callister, Ed., *Materials Science and Engineering: An Introduction*, 7th ed. John Wiley & Sons, 2007.
I. Grant and W. Phillips, Eds., *The Elements of Physics*, 1st ed. Oxford University Press, 2001.

2. Experimental Procedures

2.1 Near infrared radiative heating

2.1.1 Introduction and operation

Near Infrared (NIR) heating involves using high intensity NIR radiation to heat a substrate rapidly (see section 1.4.2). A portion of the radiation is absorbed by the substrate which causes the atoms to vibrate vigorously releasing energy as heat. This results in a huge temperature gradient between the substrate and the coating so the heat will rapidly transfer to the coating upwards from the inside out by thermal conduction. A material will predominantly transmit, absorb or reflect in the NIR region. If the material mostly transmits then the radiation will pass through and only a small portion will be absorbed or reflected resulting in a small rise in temperature; the amount the material absorbs determines its temperature gain. The emitters are encased in a reflective metallic box that will direct any radiation not absorbed inwardly. Typical materials used in coatings such as paints do not tend to absorb in the NIR region allowing the radiation to pass through and be absorbed by the substrate. Any radiation that is absorbed by the coating will aid the heating but the objective of NIR heating is for the substrate to heat up rather than the coating so that directional heating can be achieved which is more rapid than if the coating absorbed all the radiation (as usually occurs for IR heating which is a slower process) so it is desirable for most radiation to pass through the coating. All real materials will experience some heat gain upon exposure as no material is 100% transparent. Additionally NIR equipment usually emits in a wide range including the visible and short infrared region increasing the range of electromagnetic photons to be absorbed and has a high energy density compared to conventional and IR heating (25 kW for the lab model) enabling high temperatures of over 500°C in seconds for highly absorbing substrates.

The NIR heating equipment used in this work was an AdPhos NIR Coil Lab LV2 unit (figure 2.1). It primarily consists of a heater module, conveyor belt, platform and a control panel. Contained in the heater module are tungsten filament halogen lamps which have a combined power density of 25 kW. They emit from the visible range to the infrared range and peak between 800 and 1200 nm (figure 2.2). The intensity of the lamps can be varied on a non-linear percentage scale from 0-100% so that the amount of radiation emitted can be controlled. The sample is placed on a platform which moves under the lamp; the exposure time for the substrate is determined by the speed of the conveyor belt in m/min.

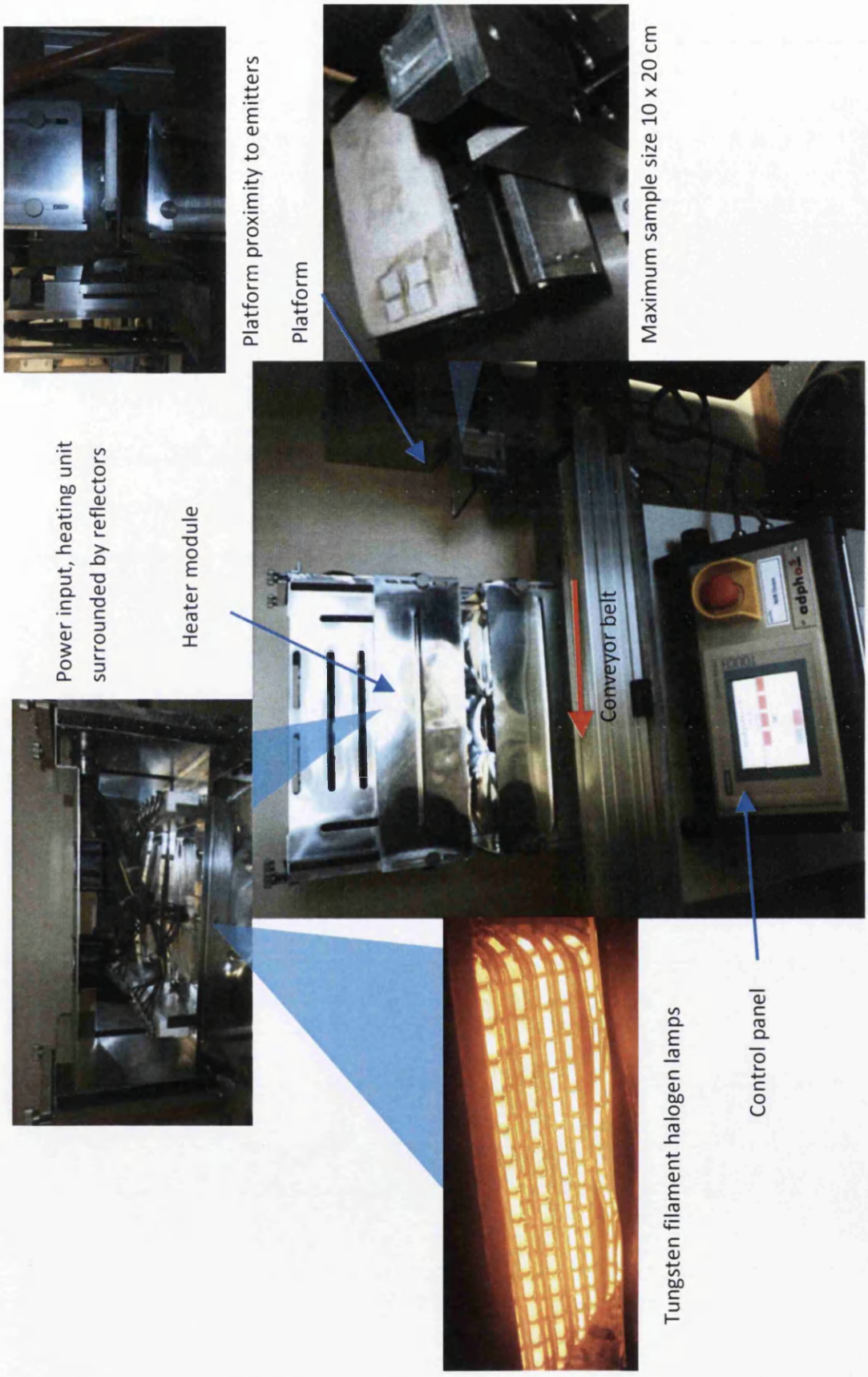

Figure 2.1: The NIR oven and its components

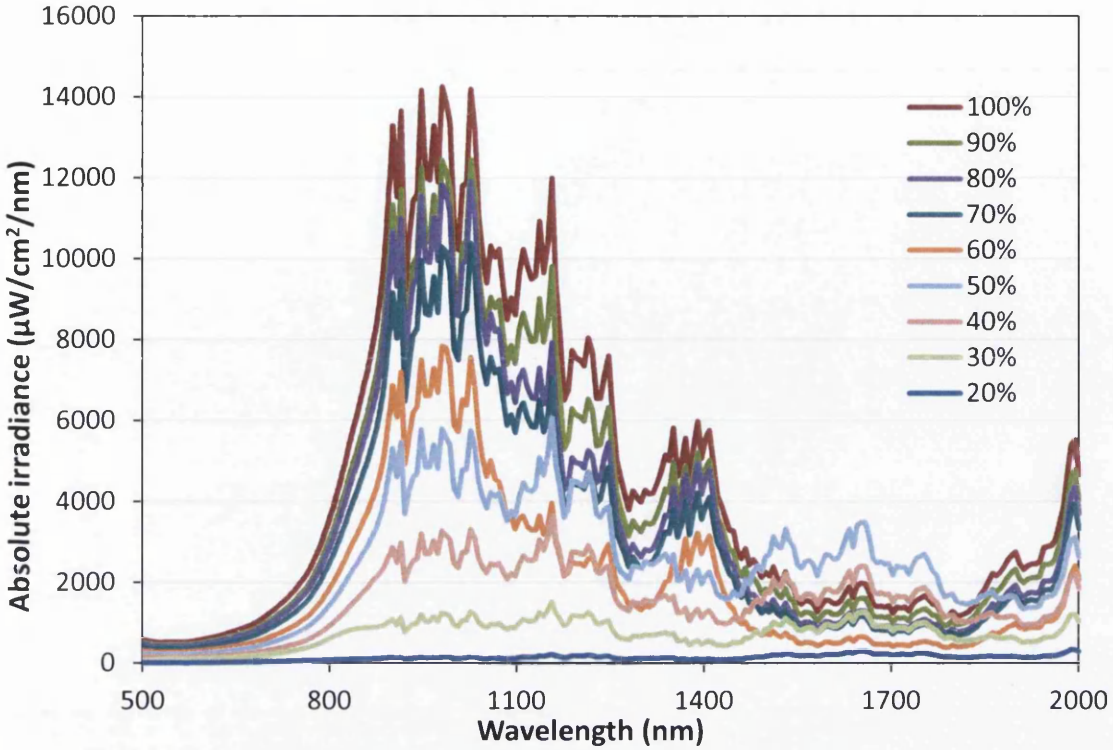

Figure 2.2: Measured absolute irradiance vs. wavelength per intensity of NIR lamp power [1]

The spectral emittance plotted in figure 2.2 was measured empirically using two portable Ocean Optics spectrometers, an HR2000+ UV/VIS (range 200-1100 nm) and NIRQUEST256 NIR (range 900-2500 nm); the input fibre with cosine corrector was positioned 5 cm away and 10 cm above the exit of the lamps to avoid thermal damage and data was collected for each power setting at 1 m/min speed (25 s exposure) [1]. This means the output spectra is not necessarily the energy density that the samples are exposed to but it gives a comparative assessment between different intensities of lamp power and an idea of the peak wavelengths.

The samples for NIR heating were placed on the platform on a block of polytetrafluoroethylene (PTFE) (10 x 20 cm) which will henceforth be referred to as the platform. This material was used because it does not absorb strongly in the NIR which minimises additional heating from below and because it has a fairly good heat resistance, low thermal conductivity and toughness to withstand the thermal shock of rapid heating and cooling. The substrates used in these experiments do sometimes exceed PTFE's melting point which results in a slight marking of the platform as seen in figure 2.1 rather than substantial damage. The lamp intensity and speed of the conveyor belt are selected using the control panel; a typical speed used was 2 m/min which results in an exposure time of

12.5 s. Prior to experimentation on samples the NIR was run once at typical settings to warm up the emitters and between each use the platform was allowed to cool for a few minutes to room temperature to increase reproducibility. This was important to keep each substrate consistent as the starting temperature will influence the temperature reached during exposure.

2.1.2 Estimating the temperature of substrates exposed to NIR

The standard method for estimating the temperature of a metallic substrate under NIR radiation exposure is to weld a thermocouple to the substrate and log its temperature. For non-metallic substrates it was not possible to weld a thermocouple to the substrate or attach it in any other way to maintain the close contact needed to get a reading that could withstand high temperatures. Therefore a non-contact method was necessary to estimate the temperature of glass substrates. To estimate the temperatures reached by NIR radiation exposure firstly the emissivity of the substrates had to be calculated. Samples of ITO glass, FTO glass and uncoated glass were placed on a hot plate (PZ 28-3TD, Gestigkeit) at 100°C and the surface was photographed using an IR camera (thermoIMAGER TIM200, Micro-Epsilon) with a k-type thermocouple and TC-08 data logger to confirm the temperature of the hot plate surface (figure 2.3).

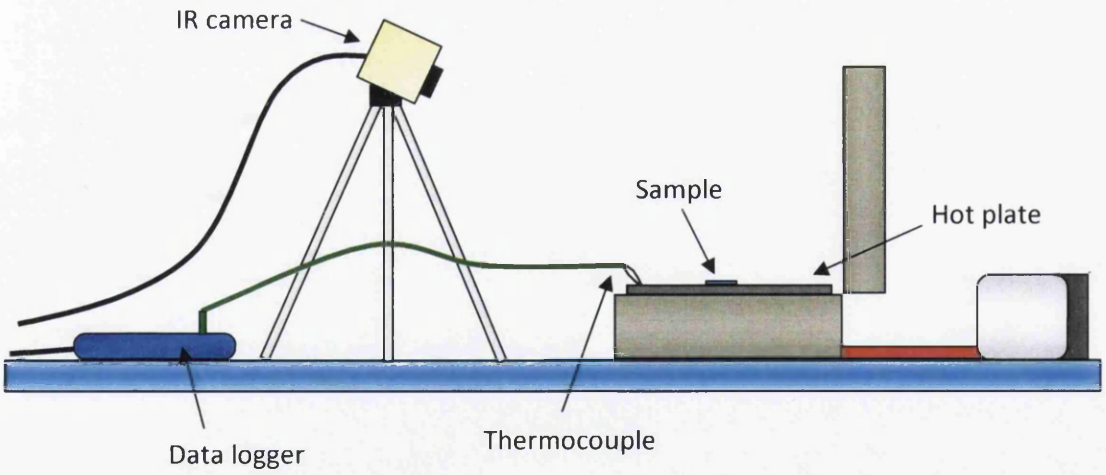

Figure 2.3: Diagram of the IR camera and hot plate positioning for true-IR temperature calibration

Using the USB IR CAM software the emissivity of a select area encompassing the substrate could be defined until the IR camera temperature matched the known temperature from the hot plate and thermocouple (figure 2.4). These calculated emissivities could then be used to

estimate the temperature for each substrate when filming the NIR oven in operation, which corresponded well to those in the literature.

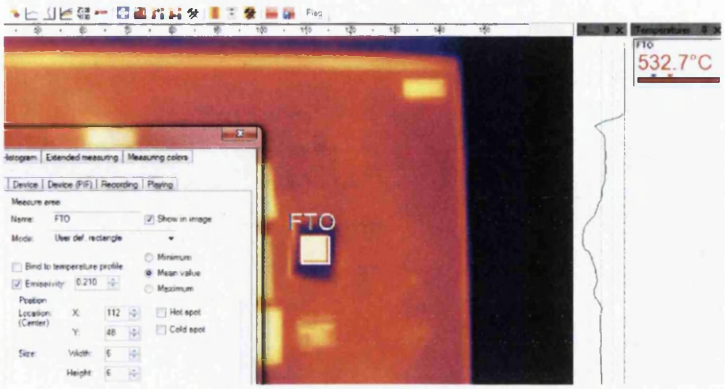

Figure 2.4: Defining an area to change the emissivity of an object for an IR camera snapshot

The same substrates were filmed with the IR camera after exiting the NIR oven as shown in figures 2.5 and 2.6. The camera angle was kept the same to minimise variations in emissivity as angle and temperature affect it. The camera had to be positioned to film the samples as they exited the heating module because it was not possible to film inside without dismantling the reflectors which would have altered temperatures measured from the normal operating conditions (figure 2.6.a). The field of view was restricted (figure 2.6.b) so temperatures were obtained from the same position immediately after exit and can be assumed to be lower than the peak temperature during heating as cooling would have occurred. Using the same software as above each power at 2 m/min speed was filmed and the emissivity values obtained from the hot plate calibration substituted for each different substrate to estimate the temperatures obtained after NIR exposure.

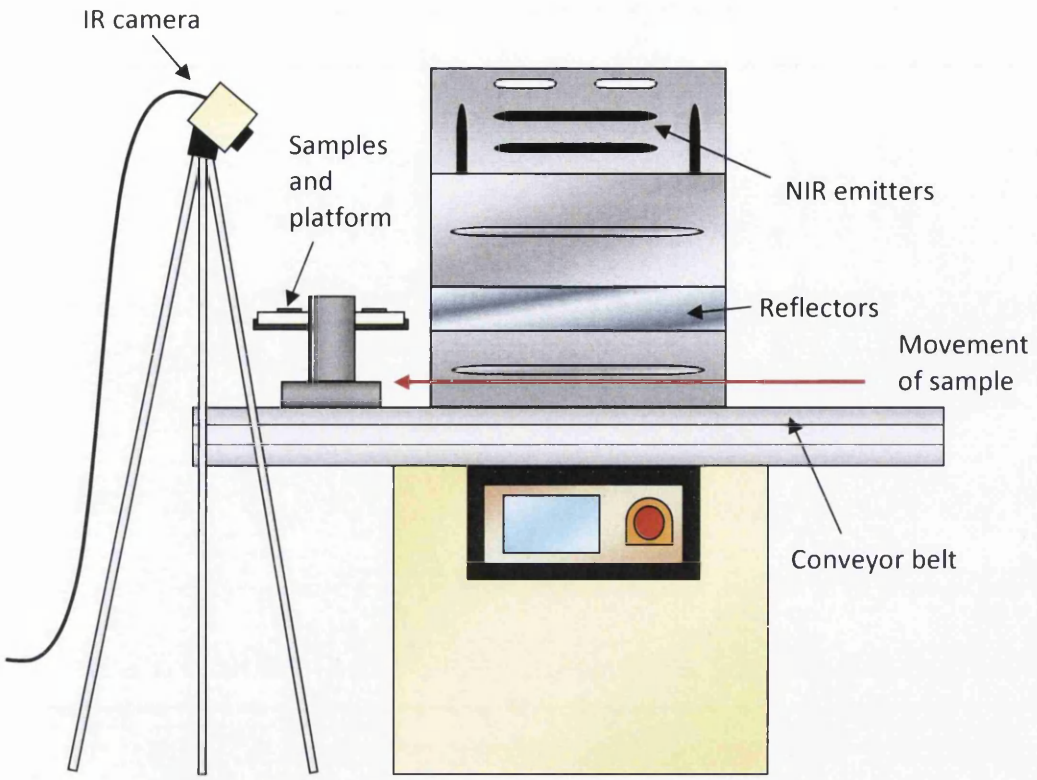

Figure 2.5: Diagram of the IR camera and the NIR equipment for estimating temperature

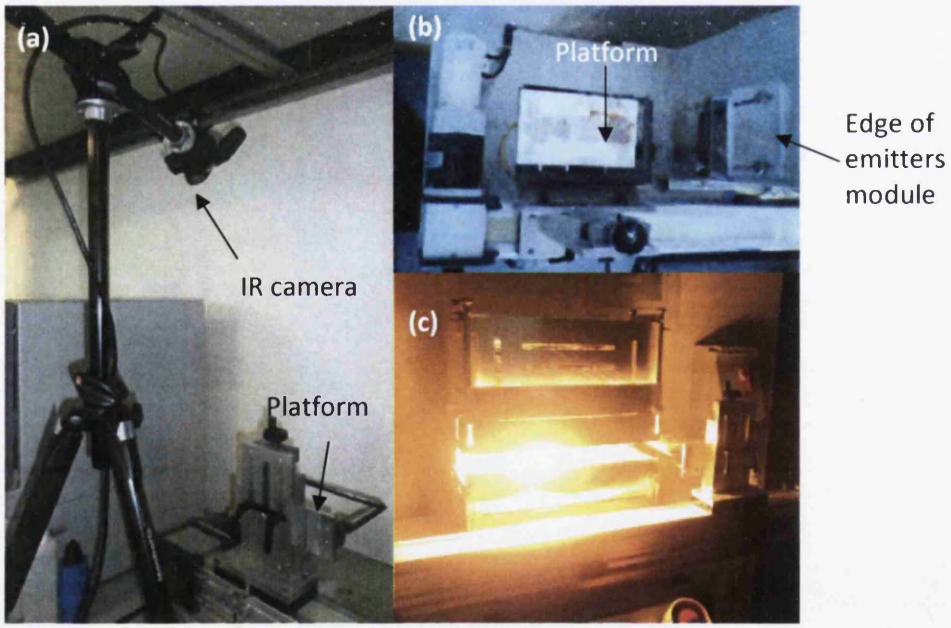

Figure 2.6: Photographs of the NIR equipment; (a) IR camera position, (b) view from the camera and (c) the NIR equipment in operation

2.2 Fabrication of a liquid electrolyte dye-sensitised solar cell

Dye-sensitised solar cells (DSCs) were fabricated according to the method shown here with variations specified for each chapter.

2.2.1 Materials and preparation

The fluorine-doped tin oxide glass (FTO glass) used was 7.5 Ω/□ (TEC 8) from NSG Pilkington and 2.2 mm thick. The tin-doped indium oxide glass (ITO glass) used was 13 Ω/□ from Sigma Aldrich and 1.1 mm thick. 1 mm thick titanium was obtained from Goodfellow pre-cut to 15 x 25 mm in size. Flexible ITO coated PET (EmiCare 15 Ω/□) was obtained from Optical Filters and a substrate consisting of a nickel grid mesh embedded in PET (Epimesh 300s) was from Epigem.

The TiO_2 pastes were 18NR-AO and 18NR-T from Dyesol, and Ti-Nanoxide D from Solaronix. TiO_2 paste was also made from P25 TiO_2 (Degussa), nitric acid, water and polyethylene glycol. $TiCl_4$ treatment solution was made from 1 g of titanium(IV) chloride tetrahydrofuran complex (Sigma Aldrich) dissolved in 100 ml of deionised water. The 0.3 mM dye solution used was N719 (Solaronix) in 1:1 acetonitrile/tert-butanol or ethanol when specified otherwise. The solution was sonicated for 1 hour in total with pauses if the solution rose above room temperature and kept in the dark once made. 5mM hexachloroplatinic acid in 2-propanol was prepared from hydrogen hexachloroplatinate(IV) hexahydrate (Sigma Aldrich). The electrolyte solution was made from 0.8 M 1-propyl-3-methylimidazolium iodide (PMII), 0.3 M benzimidazole, 0.1 M I_2 and 0.05 M guanidinum thiocyanate dissolved in 3-methoxypropionitrile. The sealing material used was 25 μm thick Surlyn (Solaronix) which was cut using a laser cutter into 1 cm^2 active area gaskets. Silver paint (Electrolube) was obtained from Farnell.

2.2.2 Standard glass based device

This is the standard DSC method upon which all others are based. It is used in this form for glass substrates, either FTO glass, ITO glass, or a combination of the two, which were built in Chapters 4, 5 and 6. TCO coated glass was cut into 15 x 25 mm sized pieces and cleaned thoroughly using detergent, deionised water and ethanol. The pieces were arranged conducting side up into 75 mm long sets with one layer of Scotch™ tape applied across the top and down both sides overlapping the glass by a few mm (figure 2.7). TiO_2 paste was deposited onto the tape at the top and using a glass rod the paste was firmly cast down in a

clean, continuous motion. The tape was then carefully removed and any excess paste cleaned away.

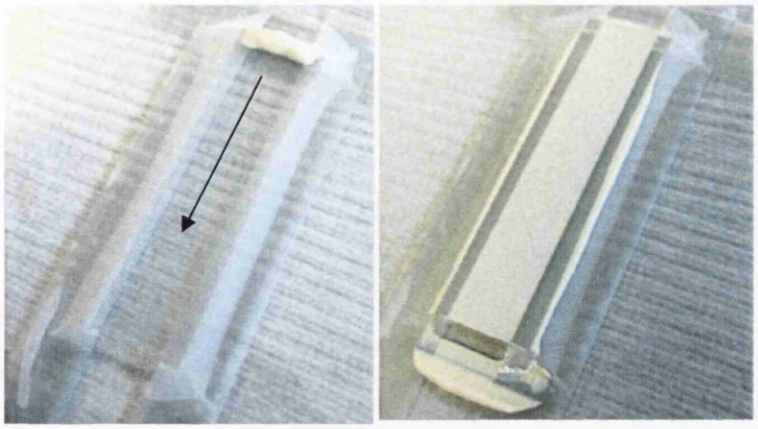

Figure 2.7: Doctor blading of strip before (left) and after (right) casting paste

The TiO_2 paste coated glass was sintered to create working electrodes. Two different heating techniques were used; conventional oven heating or NIR radiation. For conventional heating the samples were heated in an oven at 450°C for 30 minutes. For NIR heating (section 2.1) the TiO_2 paste coated glass was exposed to 12.5 s of radiation at lamp settings between 60 and 100%. Variations involving $TiCl_4$ treatment are discussed below in section 2.2.2.1. After sintering the TiO_2 films were shaped into 1 cm^2 square active areas using a glass coverslip. They were heated to 100°C to remove any water that may have adsorbed to the surface during rest before being immediately immersed into 0.3 mM N719 dye solution in acetonitrile/tert-butanol for 16-24 hours.

Counter electrodes were prepared from TCO coated glass of 15 x 25 mm in size and a 0.5 mm diameter hole was drilled to align with the corner of the TiO_2 square of the working electrode. These were then cleaned and coated evenly using a capillary tube with 3 drops of 5 mM hexachloroplatinic acid in 2-propanol. Again two different heating techniques were used; conventional oven heating and NIR radiation. For conventional heating the counter electrodes were heated in an oven at 385°C for 30 minutes. For NIR heating (section 2.1) they were exposed to 12.5 s of radiation at lamp settings between 60 and 90%.

The devices with an active area of 1 cm^2 were constructed by heat sealing the counter electrodes to the dyed TiO_2 film using 25 µm thick Surlyn gaskets (figure 2.8) in a heat press at 120°C for 30 s. The electrolyte solution was injected into the cell using a vacuum and

backfilling through the drilled hole of the counter electrode. The hole was sealed using Surlyn and a small microscope coverslip heated with a soldering iron and then silver paint was applied to the exposed conductive sides of the working and counter electrodes for measuring contacts (figure 2.9).

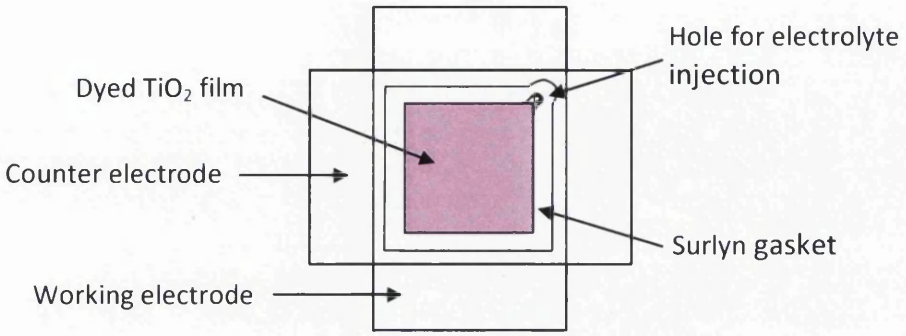

Figure 2.8: Schematic of DSC sealing assembly

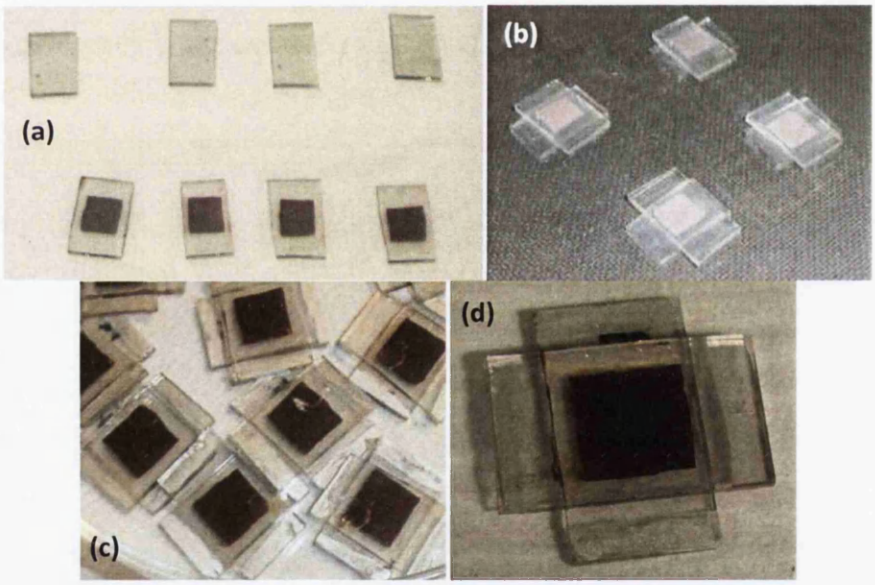

Figure 2.9: Latter stages of DSC construction (a) finished working and counter electrodes, (b) heat sealing, (c) batch of devices showing the sealed hole, (d) a finished cell forward illumination side up

2.2.2.1 $TiCl_4$ treatment variation

$TiCl_4$ treated films were first demonstrated in 1993 [2], they improve the surface area of the mesoporous TiO_2 film by introducing smaller nanoparticles within its pores allowing for more dye adsorption and improve the interconnectivity of any poorly sintered regions by bridging the TiO_2 particles together to transfer charge. Consequently this method improves the efficiency of a DSC by increasing the photocurrent without the need to deposit a thicker layer of TiO_2. For DSC devices where the counter electrode was being investigated (Chapter

4, and parts of Chapters 6 and 7), $TiCl_4$ treated oven heated TiO_2 working electrodes were used. This would create higher efficiency devices with as little variation being introduced by the working electrode as possible so that the performance and conclusions drawn could be solely influenced by the counter electrode. The traditional $TiCl_4$ treatment method (figure 2.10) is to sinter the layer of TiO_2 paste at 450°C for 30 min in an oven and then submerge the films in a 1 wt% $TiCl_4$ in deionised water solution at a temperature of 80°C for 30 min. This allows the precursor to soak into the mesoporous film. This is then rinsed off with deionised water, dried and the films are again heated to 450°C for 30 min in an oven so that the TiO_2 nanoparticles can be formed, adhered and sintered.

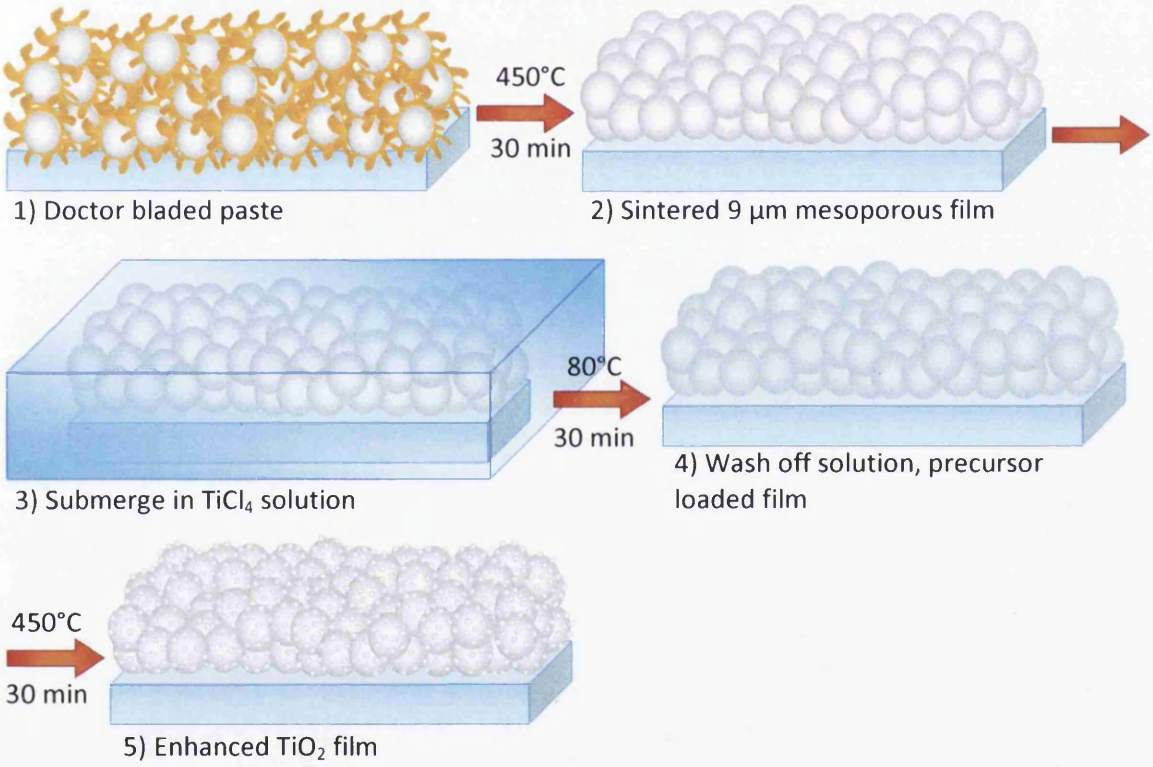

Figure 2.10: $TiCl_4$ treating steps; 1) Wet TiO_2 paste, 2) Paste is sintered into mesoporous TiO_2 film, 3) Film submerged in $TiCl_4$ solution at 80°C, 4) Precursor loaded film is heated again at 450°C, 5) $TiCl_4$ treated mesoporous TiO_2 film has superior coverage and surface area

A variation on this technique involving using NIR radiation instead of the high temperature oven heating steps was investigated in Chapters 6 and 8. This is described in Table 2.1 and figure 2.11. It was performed for both FTO and ITO glass with the optimum NIR settings used for each substrate, more detail in the relevant chapters. For the fast $TiCl_4$ method the 1 wt% $TiCl_4$ solution was dabbed onto the sintered TiO_2 with a cotton bud to cover the entire film and then exposed to NIR as soon as it had dried (at room temperature). For the slow $TiCl_4$

method the sintered films were submerged in $TiCl_4$ solution at 80°C for 30 min in an oven as normal, washed off, dried and then subjected to a second run of NIR.

Table 2.1: Description of different NIR $TiCl_4$ variations and their relation to figure 2.11

Schematic	Method name	No. of NIR runs	$TiCl_4$ treatment
a	Single run	1	None
b	Double run	2	None
c	Fast $TiCl_4$	2	Dab with solution
d	Slow $TiCl_4$	2	Soak in solution (80°C, 30 min)

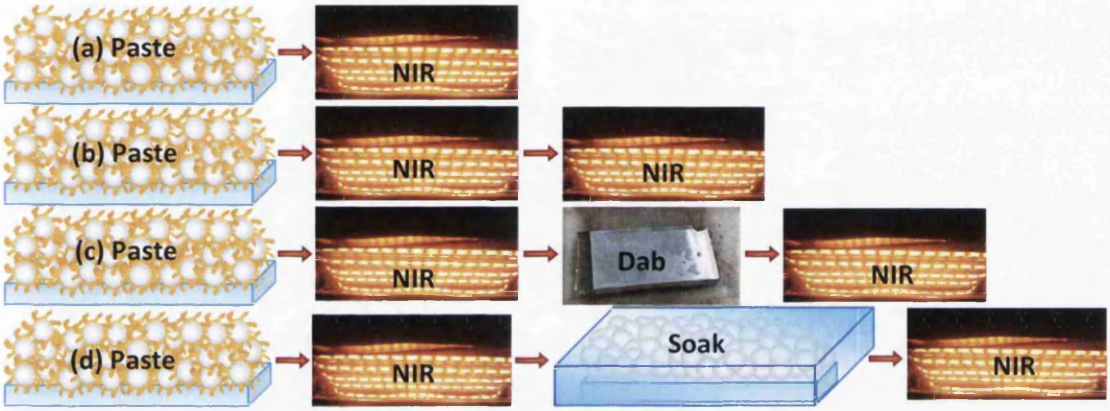

Figure 2.11: Schematic of different NIR $TiCl_4$ treatments methods used in this thesis; (a) Single, (b) Double, (c) Fast, (d) Slow

2.2.3 Metallic substrates

This concerns DSCs built in Chapter 7 where the working or counter electrode was metal and the other electrode was FTO glass. The method was the same as in section 2.2.2 except in the case of metallic counter electrode the electrolyte was injected through the FTO glass working electrode (figure 2.12).

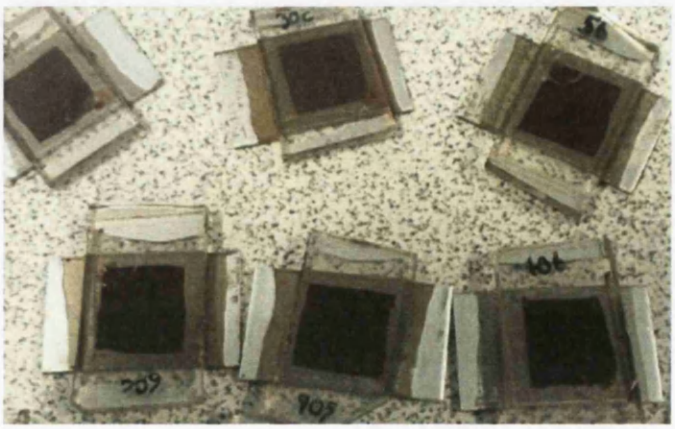

Figure 2.12: Metal counter electrodes DSCs with the working electrode drilled

2.2.4 Plastic substrates

This concerns DSCs built in Chapter 7 where the working or counter electrode was polymeric (ITO PET or Ni Epimesh grid) and the other electrode was FTO glass. The method was as section 2.2.2 but in the case of a plastic counter electrode the FTO glass working electrode was drilled for electrolyte injection. For a conventional method plastic counter electrode 4 nm of platinum was sputtered using a Quorum Q150 ES desktop sputterer/evaporator. Additionally to improve sealing 2 pieces of 25 μm Surlyn were melted to the working electrode (figure 2.13) prior to dyeing (to avoid damage to the dyed TiO_2), for both glass and plastic. When sealing the cell another Surlyn was placed between the working and counter electrode as normal using a fairly low pressure and 15 s hot press time. This was as an extra precaution to prevent electrolyte leakage but the sealing of plastic/FTO glass DSCs still proved problematic.

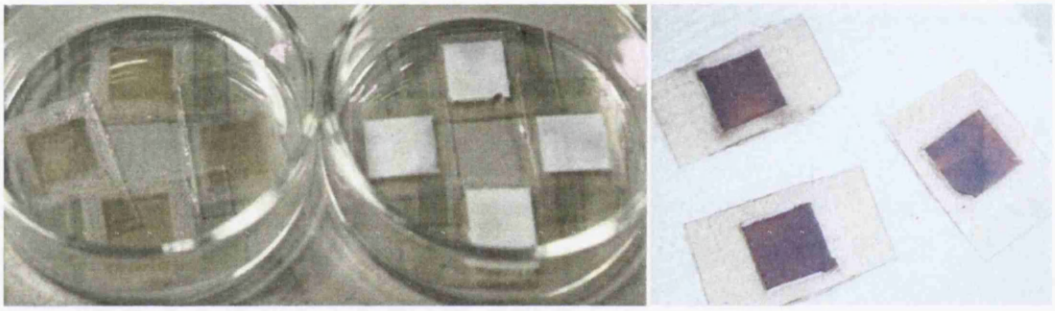

Figure 2.13: Working electrodes with Surlyn prior to dyeing (left) and after (right)

2.2.5 Fast dyeing

For DSCs built in Chapter 8 a pump dyeing technique was used as developed by Holliman and co-workers [3]. DSCs were made based on the method in section 2.2.2 but with different dimensions as to facilitate the fast dyeing method (15 x 30 mm pieces of glass), the TiO_2 film area was 0.5 x 2 cm (1 cm^2 active area), two holes were drilled in the counter electrode (in corners diagonally opposite), and the working and counter electrode were sealed prior to dyeing (known as a shell, figure 2.14.a). Dye was injected into the shells at 60°C on a hot plate using a pipette to force it through one hole and a glass pasteur pipette to collect dye that passes through (figure 2.14), with 3-4 passes the dyeing was complete in as little as 2 min. The ease of dyeing depended upon the sealing of the shell; if the shell was sealed too tightly (i.e. the 25 μm Surlyn spacer was melted for too long) dyeing would be difficult. Electrolyte was injected into one of the holes without the need to use a vacuum and then the holes sealed.

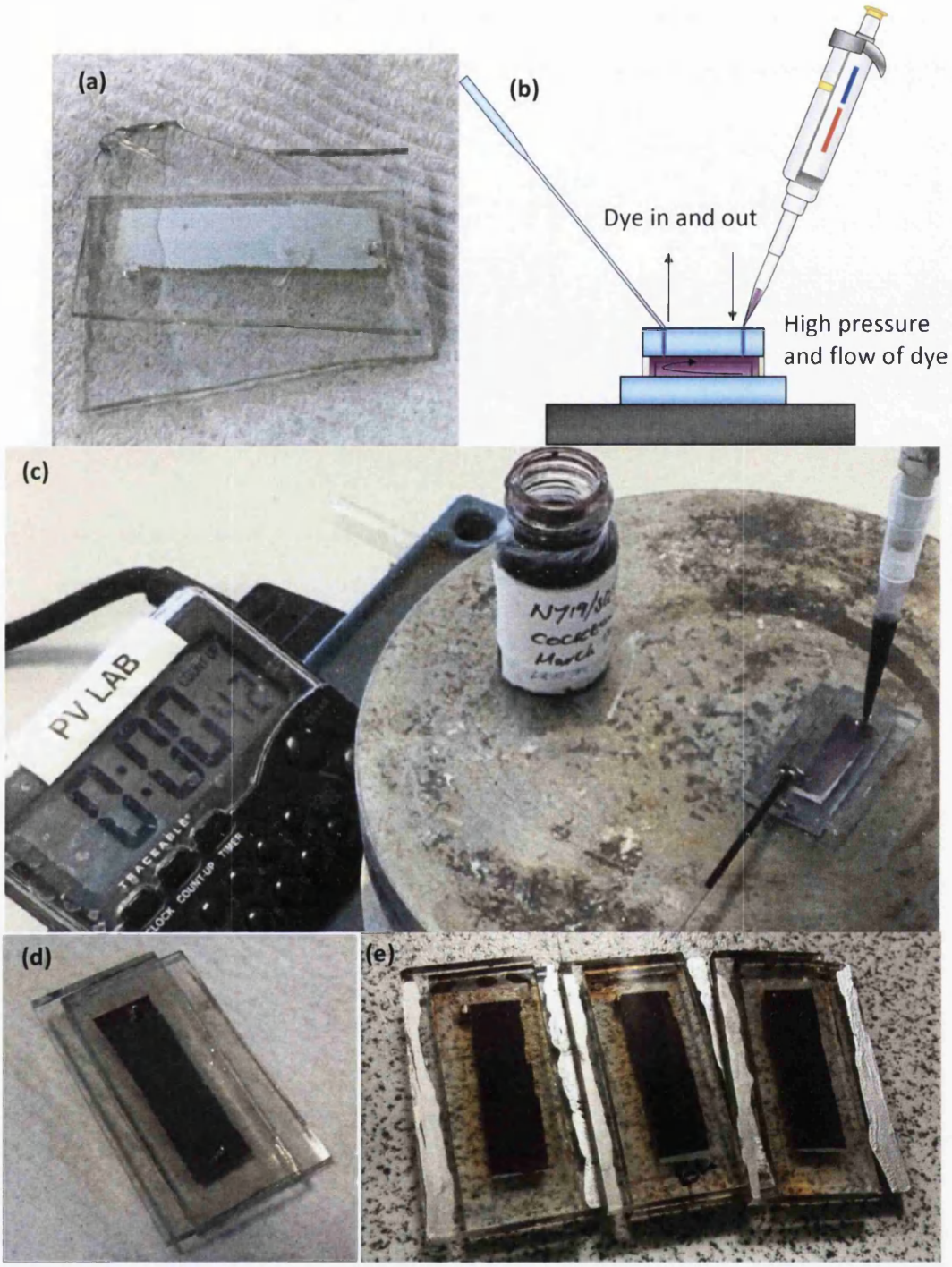

Figure 2.14: Various stages of pump dyeing technique; (a) shell, (b) diagram of dyeing, (c) dyeing in progress, (d) after dye and before electrolyte injection, and (e) finished devices

2.3 IV measurements

Current-voltage (IV) measurements were used to obtain the important parameters of a solar cell such as its open circuit voltage, current density, fill factor and efficiency (as discussed in section 1.5.1). Solar cells were measured using a Sol3A class AAA solar simulator (94023A, Newport Oriel) as shown in figure 2.15.a. The 450 watt xenon lamp has an AM 1.5 optical

filter to replicate the solar spectrum as experienced on Earth for mid latitude countries. It was used in conjunction with a Keithley sourcemeter and Universal Arc power supply. An irradiance of 1.00 sun was used for all measurements and the light source calibrated using a NREL certified monocrystalline silicon reference cell (91150V, Newport Oriel). DSCs were measured in a four electrode set up shown in figure 2.15.b.

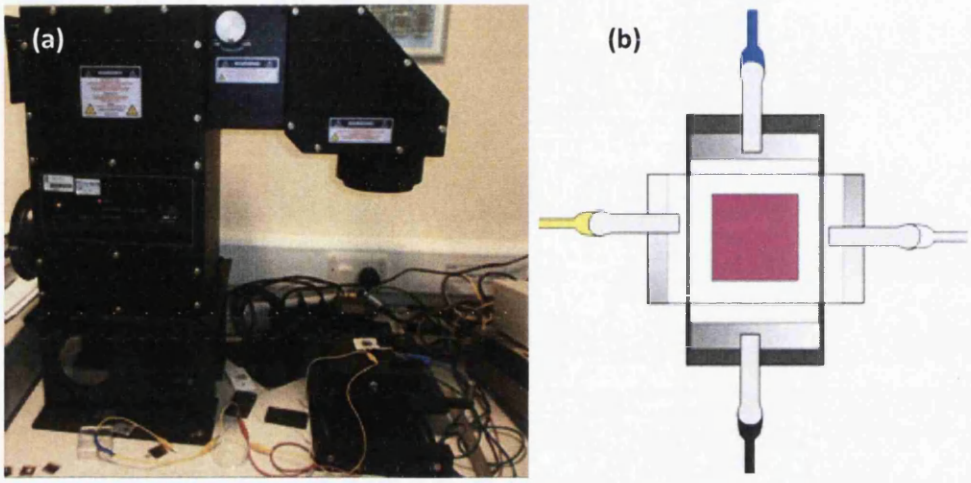

Figure 2.15: (a) The solar simulator and (b) electrical connections for a DSC

2.4 Incident photon-to-current conversion efficiency

An IPCE measurement system (QEX10, PV Measurements) was used to measure the external quantum efficiency (EQE) of a solar cell (theory in section 1.5.2). This allows the EQE of a cell to be plotted against wavelength.

2.5 Optoelectronic transient measurements

The theory of photovoltage and photocurrent decay transients is discussed in section 1.5.5. Optoelectronic transient measurements of solar cells (as described by Barnes et al. [4]) were performed by pulsing light at various conditions and measuring the decay of certain parameters once the circuit had been changed and light removed. The testing rig is shown in figure 2.16 and the testing software was written using Igor Pro. The light was provided by a bank of white LEDs with the cells kept at a fixed height.

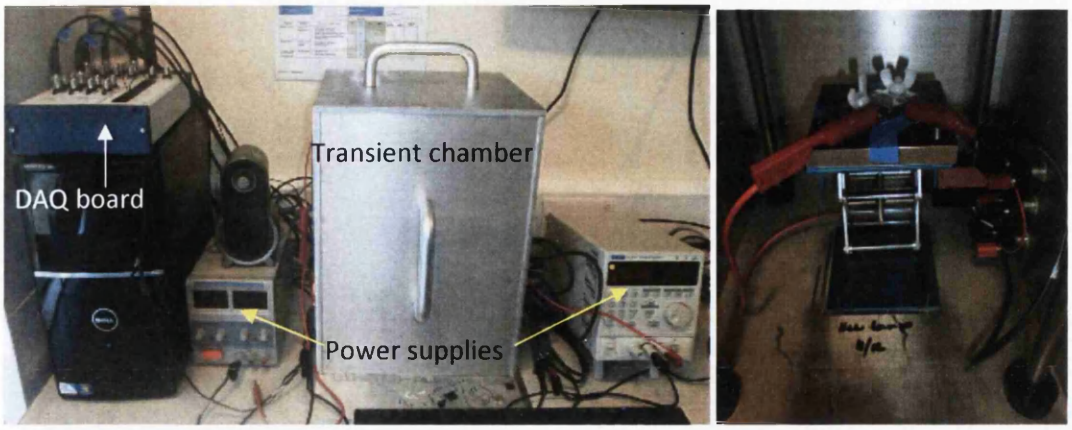

Figure 2.16: The transient testing rig (left) and inside the transient chamber with cell attached (right)

For each measurement the light source was kept at a constant voltage and the current was varied. There were 21 steps in total with the current varied from 2 to 0.011 A. The acquisition time for current and voltage decay increased with decreasing light current. At the end of the experiment each graph for voltage decay and current decay at various light levels was fitted using first order exponential decay equations. The modelling is not complex unlike impedance spectroscopy allowing for fast acquisition of data as the software both fits the curves and generates graphs automatically (figure 2.17), but adjustments can be made to the fit if necessary.

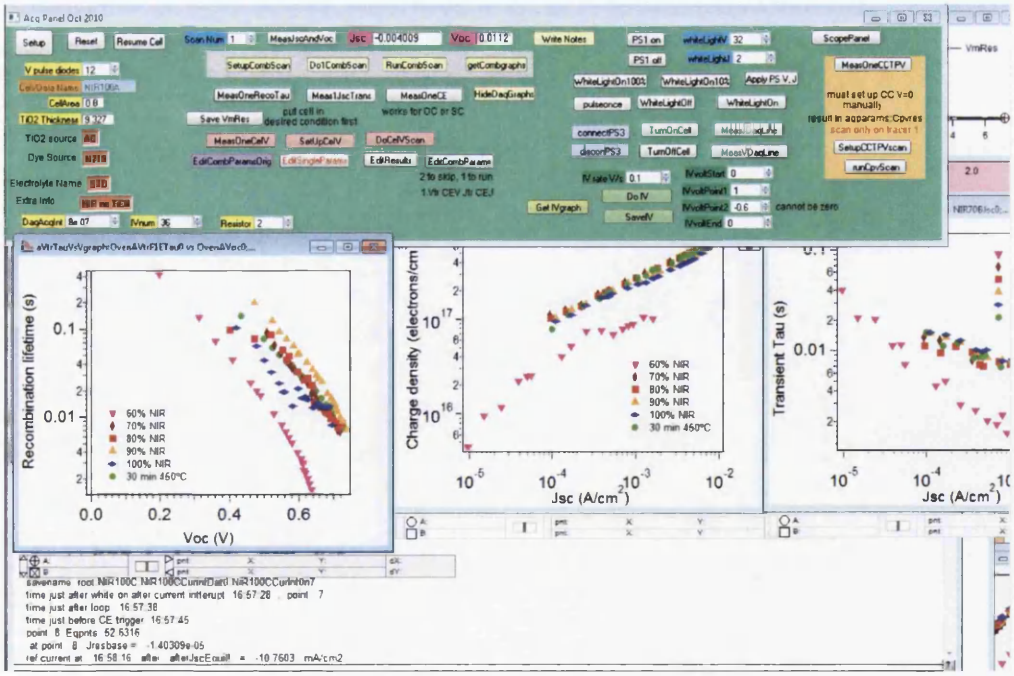

Figure 2.17: Interface of the transient rig software showing the graphs automatically generated

2.6 Electrochemical impedance spectroscopy

Electrochemical impedance spectroscopy (EIS) was performed on DSC devices using a Gamry Reference 600 potentiostat/galvanostat/ZRA and Gamry Framework software. All cells were measured using a two electrode set up under darkness for consistent steady state conditions. Bias voltages of between 540 and 780 mV were measured, the AC amplitude was ± 10 mV with a frequency range of 50 kHz to 0.1 Hz. The theoretical aspects of EIS and details of the simple equivalent circuit DSC model used are discussed in section 1.5.3.

2.7 Cyclic voltammetry

Cyclic voltammetry was performed using a CompactStat potentiostat (Ivium Technologies) in a three electrode setup (figure 2.18). The theory of cyclic voltammetry is discussed in section 1.5.4.

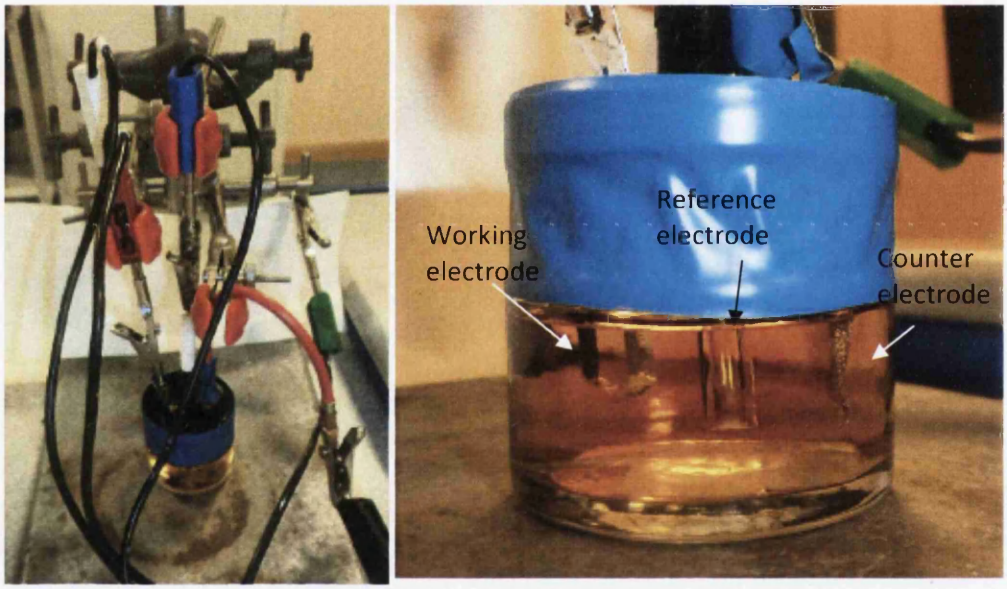

Figure 2.18: Overview of the three electrode setup (left) and close up of the working, reference and counter electrode in the electrolyte solution (right)

It was used to test the catalytic performance of the counter electrodes for DSCs. Platinised working electrodes (cyclic voltammetry terminology) were prepared on pieces of 3 x 1 cm sized FTO glass (TEC 7, NSG Pilkington) as per the method for DSC counter electrodes (section 2.2.2). A non-aqueous Ag/Ag^{+} reference electrode in acetonitrile (CHI112, CH Instruments Inc.) was used as the reference electrode and platinum mesh was used for the counter electrode. The spacing between each was kept equal as possible and the platinum side of the working electrode was positioned facing the reference electrode. The exposed

area was also kept as constant as possible for each set of experiments. The electrolyte used for these experiments was 0.033 g 5 mM LiI, 0.006 g 0.5 mM I_2, 0.532 g 0.1 mM $LiClO_4$ in a volumetric flask made up to 50 ml with acetonitrile. Cyclic voltammetry was performed between the potentials of 0.8 and -0.5 V with a step size of 5 mV, a scan rate of 50 mV/s, 20 s equilibrium time and 10 cycles run.

2.8 UV/Vis/NIR spectrophotometry

A Perkin Elmer Lambda 750S was used to measure the transmission, absorbance and reflectance of a material from the UV to NIR region of light. Both transmission/absorbance measurements and reflectance measurements were taken from 250 nm to 3000 nm on various substrates. Total reflectance measurements were taken using the integrating sphere accessory.

2.9 Fourier transform infrared spectroscopy

The theory of FTIR is discussed in section 1.5.6. Attenuated total reflectance (ATR) was used in conjunction with a Perkin Elmer Spectrum 100 FTIR to obtain IR spectra of TiO_2 pastes. The powders were placed on the ATR crystal and the spectra averaged over 5 scans.

2.10 Thermogravimetric analysis

Heated TiO_2 films (as per DSC manufacturing method in section 2.2.2) were removed from the FTO glass and placed in a platinum crucible for thermogravimetric analysis using a Pyris 1 TGA (Perkin Elmer) at between 30 and 600°C with a ramping rate of 20°C/min in a nitrogen atmosphere.

2.11 Scanning electron microscopy

Scanning electron microscope (SEM) images were obtained using a FEG-SEM (S-4800, Hitachi) with beam parameters of 10-12 eV and 10 μA and a 4-12 mm working distance.

2.12 Energy-dispersive X-ray spectroscopy

EDX analysis was performed with an Oxford instruments X Max detector which was an accessory to the FEG-SEM (section 2.11). This was used on counter electrode samples to image and detect the presence of platinum.

2.13 X-ray diffraction

X-ray diffraction (XRD) was performed using a PANalytical diffractometer at 45 kV and 35 mA using Ni-filtered Cu-$K_{\alpha 1}$ radiation (λ=1.5405˚A) between the angle positions of 4 and 80 with a step size of 0.033 2θ and a scan time of 50.8 s.

2.14 Profilometer

A profilometer (Veeco Dektak 150) was used to measure the thicknesses of film samples by obtaining the average step height. It was sat on a vacuum table to minimise vibrations and a probe force of 10 mg was used on TiO_2 films.

2.15 Four point probe

Four point probe measurements were taken with a RM3000 (Jandel) to obtain the resistivity of thin films in $\Omega/\square$.

2.16 Light box and image analysis

An Ortery Photosimile light box with Canon DSLR camera was used to take photographs in a set illumination so that image analysis could be used to compare samples with no variation in light. Sigma scan pro was used to obtain colour values.

2.17 References

[1] M. Cherrington, Printing technologies for current collectors for dye-sensitized solar cells, Swansea University, 2012.

[2] M.K. Nazeeruddin, A. Kay, I. Rodicio, R. Humphry-Baker, E. Muller, P. Liska, et al., Conversion of Light to Electricity by cis-X_2Bis(2,2'-bipyridyl-4,4'-dicarboxylate)ruthenium(II) Charge-Transfer Sensitizers (X = Cl^-, Br^-, CN^-, and SCN^-) on Nanocrystalline TiO_2 Electrodes, J. Am. Chem. Soc. 115 (1993) 6382–6390.

[3] P. Holliman, M. Davies, A. Connell, Solar cells with multiple dyes, US 2013/0167900 A1, 2013.

[4] P.R.F. Barnes, K. Miettunen, X. Li, A.Y. Anderson, T. Bessho, M. Grätzel, et al., Interpretation of optoelectronic transient and charge extraction measurements in dye-sensitized solar cells, Adv. Mater. 25 (2013) 1881–922.

3. Optical, Structural and Electronic Properties of ITO and FTO and their Suitability for Near Infrared Heating

3.1 Introduction

A transparent conducting oxide (TCO) is a material that is both optically transparent and electrically conductive when deposited as a thin layer and is discussed in detail in section 1.3. The combination of conductivity and transparency is usually achieved by doping a wide band gap binary oxide such as In_2O_3, SnO_2, or ZnO. Doping increases the conductivity of the oxide by increasing the concentration of free carriers; typically TCOs are n-type so these free carriers are electrons. A typical TCO for commercial applications has a high concentration of free electrons which results in a very low resistivity, in the region of 10^{-6} Ωm. TCOs are usually deposited onto a substrate such as glass or plastic and used for electronic applications or their optical properties (which differ to glass) as discussed in section 3.3.1.

Tin-doped indium oxide (ITO), In_2O_3:Sn, and fluorine-doped tin oxide (FTO), SnO_2:F, are two of the most commonly used TCOs. ITO is used in a wide range of applications such as flat panel displays [1], touch screens, organic light emitting diodes [2], energy efficient windows [3], gas sensors and some photovoltaics. ITO is a particularly desirable TCO for OLEDs [4] and flat panel displays due its very low roughness [5]. FTO is used mostly for solar cells such as amorphous silicon, CIGS and dye-sensitised, as well as energy efficient windows [6][7] and gas sensors [8]. ITO has a higher carrier concentration than FTO, almost by a factor of two, because the solubility of fluorine in SnO_2 is inferior to that of Sn in In_2O_3 [9]. Combined with its good carrier mobility of ~30 cm^2/Vs, ITO also has an extremely low resistivity of 2×10^{-6} Ωm [3] whereas FTO has a resistivity of $5\text{-}8 \times 10^{-6}$ Ωm. The lower resistivity of ITO allows less material to be used to achieve the same sheet resistance ($R_{sh} = \rho/t$ resistivity/thickness) as FTO which also results in a higher visible transparency. However ITO is still the highest cost TCO partly due to its demand in high cost electronics coupled with the scarcity of indium; its price has risen sharply in recent years [10]. Conversely FTO is the least expensive TCO [11] deposited with high throughput during float glass manufacture using atmospheric pressure chemical vapour deposition (APCVD).

As discussed in section 1.3.4, ITO and FTO are heavily doped degenerative semiconductors which results in a strong absorption in the infrared region. They undergo a transition from a dielectric (transmitting in the visible region) to a metallic (absorbing in the IR) response so it was hypothesised that this metallic behaviour in the IR region may be suitable for NIR

radiative heating. An issue for high temperature heating steps in the manufacture of electronic devices (such as solar cells) on TCOs is slow heating times which limit throughput and increase cost (heating techniques are discussed in section 1.4). Conventional heating relies on convection and conduction requiring the oven and entire substrate to heat up. Faster heating processes include microwaves [12], lasers [13], near infrared (NIR) [14] and far infrared [15]. Out of these techniques NIR radiation has achieved the highest reductions in heating times; it has previously been demonstrated on metallic substrates to dramatically reduce the processing time of a DSC working electrode from 30 min to 12.5 s [14][16]. NIR heating emits high energy density NIR radiation which is transmitted through most coatings (organic molecules tend not to absorb in this region) allowing it to reach the substrate where if absorbed the NIR photons interact with and excite the atoms to higher energy levels releasing thermal energy as phonons and rapidly heating the substrate. Due to the high thermal gradient the coating on the substrate is heated very quickly by thermal conduction. If TCO coated glass substrates could also rapidly heat with NIR radiation it would enable fast heating of transparent substrates rather than the restriction to opaque metal substrates, drastically increasing the range of possible applications for electronic devices.

An additional issue for TCOs is thermal degradation; one of the main disadvantages of ITO films is that they are not suitable for high temperature applications where conductivity is required (they are still used in high temperature applications for heat shielding where conductivity is not needed). Above a temperature of about 300°C the resistivity increases substantially with rising temperature [17] due to oxygen deficiency sites becoming filled. This limits their use in some photovoltaics such as dye-sensitised solar cells (DSCs) where high temperature heating steps (450°C) are required for the fabrication. There have been attempts to overcome the poor conductivity of ITO at high temperatures such as by combining ITO thin films with FTO [18] and annealing ITO after heating in a hydrogen atmosphere [19]. Although these approaches have had some success they are fairly complicated and time consuming severely limiting their feasibility especially when it would be easier to use an alternative TCO. It will be interesting to see how NIR radiation affects the conductivity of TCO coated substrates and if any time dependent kinetic diffusion of oxygen into ITO can be avoided.

3.2 Experimental

Scanning Electron Microscopy (SEM) (section 2.11) was used to obtain micrographs of 7.5 Ω/□ FTO glass (NSG Pilkington) and 13 Ω/□ ITO glass (Sigma Aldrich). The absorbance and reflectance of ITO and FTO glass was measured using a Perkin Elmer Lambda 750S spectrophotometer (section 2.8). Both glasses were also etched, FTO using zinc powder and 4 M HCl, and ITO using an aqueous solution of 20% HCl and 5% HNO_3 at 60°C for 30 min. The TCOs were removed so the absorbance and reflectance of the identical thickness and composition glass could be measured.

To estimate the temperature reached by exposing glass to NIR radiation a non-contact method had to be utilised because attaching a thermocouple to glass was not possible. The emissivity of ITO glass, FTO glass and uncoated glass was calculated by placing the substrates on a hot plate (PZ 28-3TD, Gestigkeit) at 100°C and using an IR camera's software (thermoIMAGER TIM200, Micro-Epsilon) to define the emissivity as described in section 2.1.2. The substrates were then exposed to 12.5 s of NIR radiation at power settings of between 10 and 100% using an AdPhos NIR Coil Lab LV2 unit (section 2.1.1) while filming with the IR camera (section 2.1.2) which was positioned to film the samples as they exited the NIR heating module (due to physical constraints). Using the IR camera software as above the emissivity values obtained from the hot plate calibration were substituted for each different substrate to estimate the temperatures obtained after NIR exposure, the maximum temperature was chosen, 2 s after exit from the NIR lamps (due to problems of reflection real values could not be obtained immediately at exit).

To investigate any change in the resistivity of the ITO glass and FTO glass substrates a four point probe (section 2.15) was used to measure their sheet resistance before and after various heating methods. The substrates were subjected to heating in a conventional oven at varying times and temperatures. They were also exposed to 12.5 s (2 m/min line speed) of NIR radiation varying the intensity of the NIR emitters.

3.3 Results and discussion

3.3.1 Optical and structural characterisation of TCO coated glass

The ITO glass used for this study was 13 Ω/□ from Sigma Aldrich and consisted of a ~150 nm layer of magnetron sputtered tin-doped indium oxide on 1.1 mm soda lime float glass with a SiO_2 passivation layer. The passivation layer is present to prevent leaching of alkali oxides

into the float glass during glass manufacture. The doping concentration was 10 wt% SnO_2 to In_2O_3. Indium oxide crystallises in the cubic bixbyite structure which has a slight oxygen deficiency introducing some carriers on its own but it is negligible compared to Sn doping. Figure 3.1 shows a micrograph of the ITO glass; the grains exhibit a bimodal microstructure typical of an ITO film sputtered at a temperature of around 200°C [4] and a small grain size resulting in a smooth film. The low roughness of ITO from this deposition method is very desirable for some applications, such as OLEDs [5], as it both helps maintain a high work function and prevents pinholes on subsequent layers which, in an electronic device such as a solar cell, would present alternative paths for the current to flow resulting in losses.

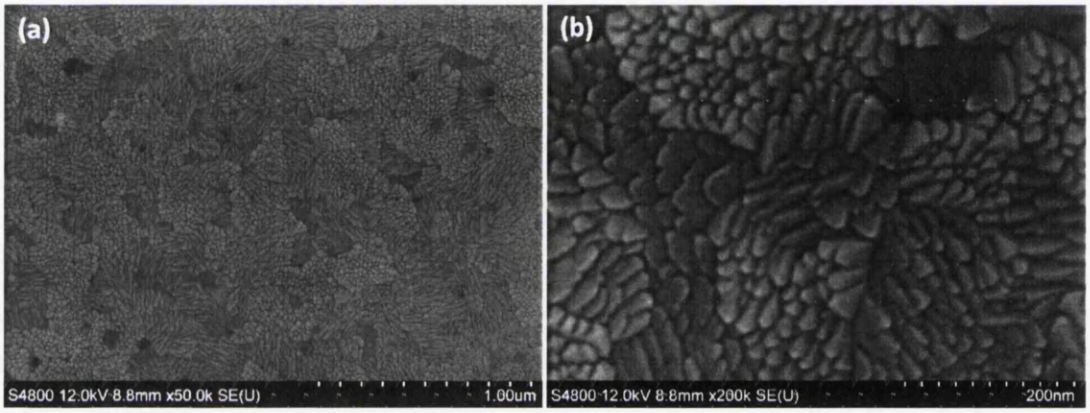

Figure 3.1: Scanning electron micrographs of ITO on glass at (a) 50k and (b) 200k magnification

The FTO glass used for this study was 7.5 Ω/□ (TEC 8) from NSG Pilkington. It consists of a ~600 nm layer of fluorine-doped tin oxide on 2.2 mm thick soda lime glass with a SiO_2 passivation layer. The transparent conducting oxide is deposited during the latter stages of flat glass production; as the float glass exits the tin bath (at a temperature of around 590-650°C) it is directly coated with SnO_2:F during cooling by atmospheric pressure chemical vapour deposition (APCVD). This process boasts a high deposition rate (~10 nm/s), no requirement for a vacuum and high throughput due to compatibility with the continuous processing of glass. Pilkington use $(CH_2)_2SnCl_2$, dimethyltin dichloride (DMT), as a precursor mixed with helium, water, oxygen and a dopant such as HF or organofluorine [20] and the deposited layer is textured to promote light trapping (although smooth layers can be coated using this process). Figure 3.2 shows an SEM of the APCVD coated FTO glass from NSG Pilkington.

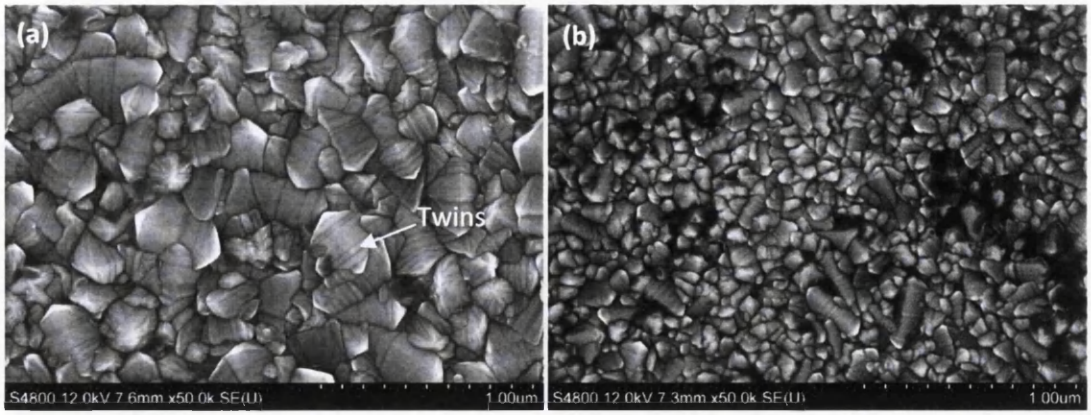

Figure 3.2: Scanning electron micrographs of (a) 7.5 Ω/□ FTO glass and (b) 15 Ω/□ FTO glass

FTO has a tetragonal crystal structure and the APCVD process introduces annealing twins (where there is mirror lattice symmetry between the atoms on each side of the boundary as a result of atomic displacement during the annealing) into the grains which help improve light scattering. Both grades of FTO glass shown in figure 3.2 have much larger grains than the ITO glass and thus a much higher roughness. The grain size of FTO corresponds to the thickness of the deposited layer as demonstrated in figure 3.2.b, 15 Ω/□ FTO glass, which has a thinner coating of FTO than the 7.5 Ω/□ FTO glass that was used in this work, 320 nm compared to 600 nm, and consequently smaller grains and higher optical transparency. The roughness of FTO glass is not an issue for liquid electrolyte DSCs where a thick layer of TiO_2 (several microns) is usually used, but for related solid state devices (such solid state DSCs and perovskite solar cells) where films of 1 μm or less are used a blocking layer becomes desirable to prevent pinholes.

The absorbance and reflectance of FTO and ITO coated glass was measured using a Perkin Elmer Lambda 750S spectrophotometer along with identical uncoated glass substrates that had had their TCO removed by chemical etching, the absorbance is shown in figure 3.3.

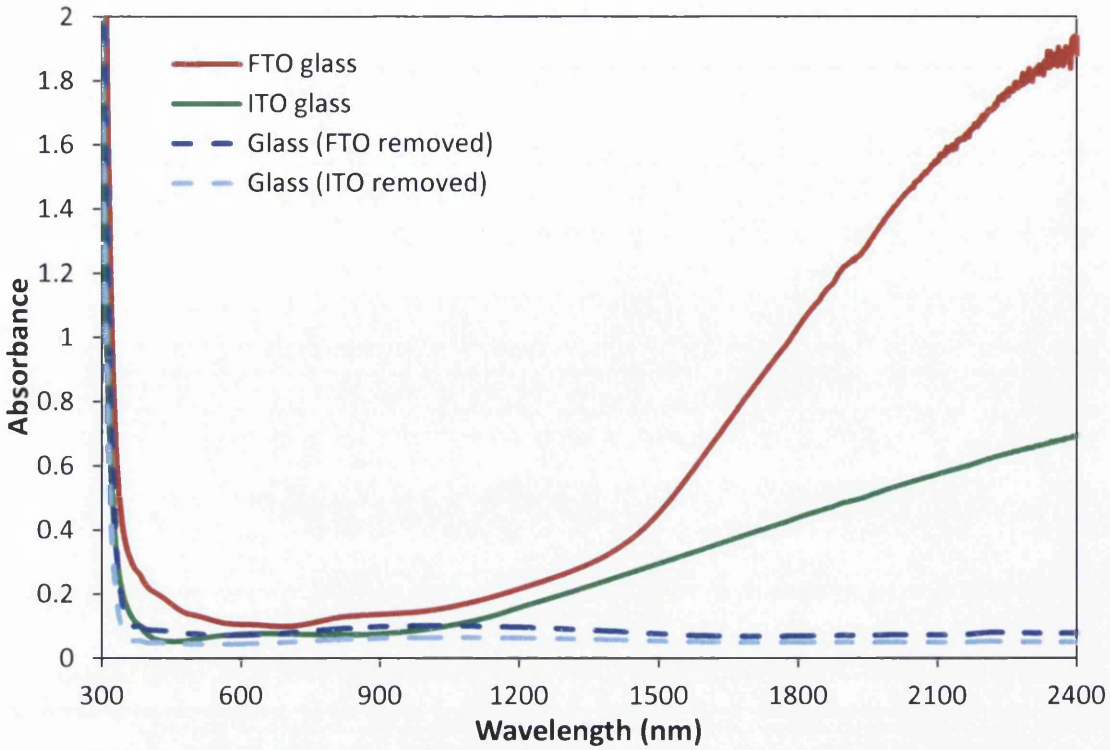

Figure 3.3: Absorbance of FTO glass, ITO glass, and the same glasses with their TCO removed between the wavelengths of 300 and 2400 nm

Each substrate absorbs in the UV region and transmits in the visible region. The TCO coated glasses absorb in the infrared region whereas glass continues to be transparent. The glass for the FTO is also 2.2 mm thick compared to 1.1 mm thick for the ITO glass explaining the slight difference between absorbance for the two glasses which are of identical composition. The FTO layer is 600 nm, thicker than the ITO layer's 150 nm meaning that it absorbs more, if the TCOs were of equal thickness it is likely the ITO would absorb more due to its higher carrier concentration. Fundamental absorption, a valence band (VB) to conduction band (CB) transition, depends upon:

$$\alpha(E) = \frac{A}{E}(E - E_g)^{1/2} \tag{3.1}$$

Where α is the absorption coefficient, E is the photon energy, E_g is the optical band gap and A is a fitting constant. This assumes that the conduction band is parabolic and unoccupied, such is the case for an intrinsic semiconductor and an insulator. For fundamental absorption to occur the energy of the photon must exceed the energy of the band gap. Glass absorbs in the ultraviolet light because the UV photons have sufficient energy to excite an electron from the valence band to an unoccupied state in the conduction band. Visible light photons do not have sufficient energy for this fundamental VB to CB transition so it transmits in that region and thus appears transparent.

For doped semiconductors (section 1.1.3) the conduction and valence band edges are perturbed by Coulomb interaction with ionised impurities (dopants) which results in the Fermi level being shifted towards either the valence band or conduction band. If doping exceeds a certain threshold a semiconductor is known as a degenerative semiconductor (as discussed section 1.3.4). ITO and FTO are such examples; they are heavily doped resulting in a very high free carrier concentration.

ITO and FTO appear transparent in the visible region because low energy transitions from the Fermi level into unoccupied states higher in the conduction band have a low probability, the TCO cations have filled d-shells, $4d^{10}$ for Sn and In. Similarly to the glass ITO and FTO are opaque in the UV region because the photons have sufficient energy to make a VB to CB transition (to states higher than the filled ones in the CB). Another type of absorption that can occur in a material is free carrier absorption. Figure 3.4 shows both fundamental absorption (from the valence band to the conduction band as a UV photon would in this case) and free carrier absorption illustrated for a degenerative semiconductor.

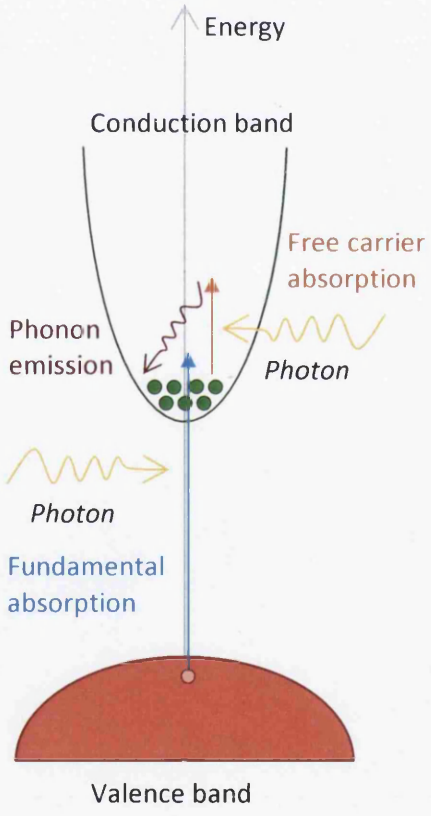

Figure 3.4: Schematic of fundamental and free carrier absorption for a degenerative semiconductor

Free carrier absorption allows the absorption of a photon to excite an electron by the absorption or emission of a phonon to accommodate the change in electron momentum. This occurs for ITO and FTO in the infrared region where they begin to absorb. An NIR photon can excite an electron from near the bottom of the conduction band where it is occupied to higher within the conduction band where it is empty emitting a phonon. Figure 3.5 shows the total reflectance of ITO and FTO glass with their respective TCOs removed.

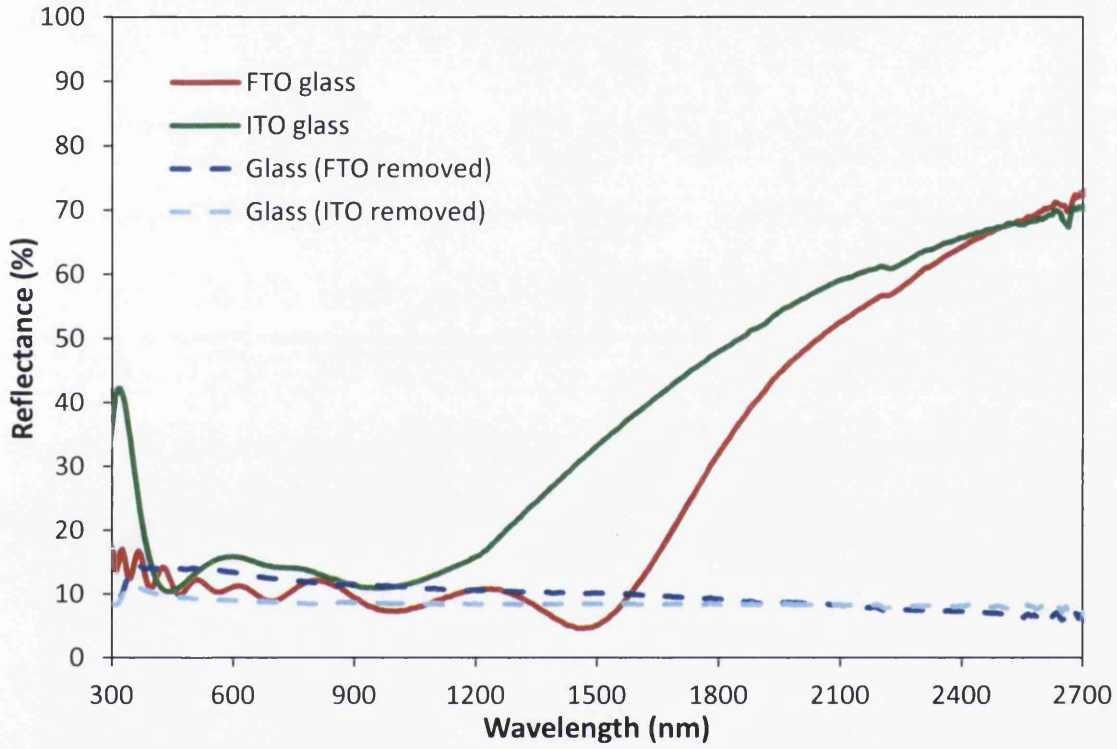

Figure 3.5: Reflectance of FTO glass and ITO glass and the same glass with their TCOs removed

Glass (without a TCO) has low reflectance throughout the ultraviolet, visible and near infrared range because in these regions it is highly transparent. The FTO and ITO glass also have low reflectance in the visible region but start reflecting highly in the near infrared region. Drude theory is used to explain the behaviour of the TCOs by modelling the electrons as a classical gas. The interaction between light and free carriers occurs via an electric field and by introducing conductivity σ; substitution for the drift velocity yields the complex frequency dependent conductivity of the TCO, hence:

$$\sigma(\omega) = \frac{n_e e^2 \tau}{m_e^*} \frac{1}{(1 - i\omega\tau)} = \varepsilon_0 \varepsilon_\infty \omega_p^2 \tau \frac{1 + i\omega\tau}{1 + \omega^2\tau^2} \qquad (3.2)$$

At high frequencies, i.e. for shorter wavelengths such as ultraviolet, free carrier contribution becomes less important and other processes dominate (interband absorption) meaning the material acts as a perfect dielectric just as the glass does. At lower frequencies, i.e. for infrared wavelengths, the optical transmittance is determined by absorption and reflection of the free carrier plasma. In the low frequency regime ($\omega\tau << 1$) the free carrier term shows a $1/\omega$ dependence as $\omega \rightarrow 0$ this term dominates. Drude theory shows that at low frequency a material with a large concentration of free carriers is a perfect reflector. In the IR region where the reflectance of glass begins to decrease for a TCO it does not and continues to increase. Indeed the infrared reflectivity of ITO leads to its use as a heat shielding material [21]. From the equation above ω_p is the plasma frequency and given by:

$$\omega_p = \left(\frac{n_e e^2}{\varepsilon_0 \varepsilon_\infty m_e^*}\right)^{\frac{1}{2}} \tag{3.3}$$

The plasma frequency is the frequency at which the material changes from a metallic to a dielectric response. Drude theory predicts this to be in the NIR region for ITO and FTO and in a frequency range where interband absorption is not important the ω_p occurs near the minimum in reflectivity, the plasma edge shift. Figure 3.6 shows the transmittance and reflectance of ITO and FTO glass against wavelength.

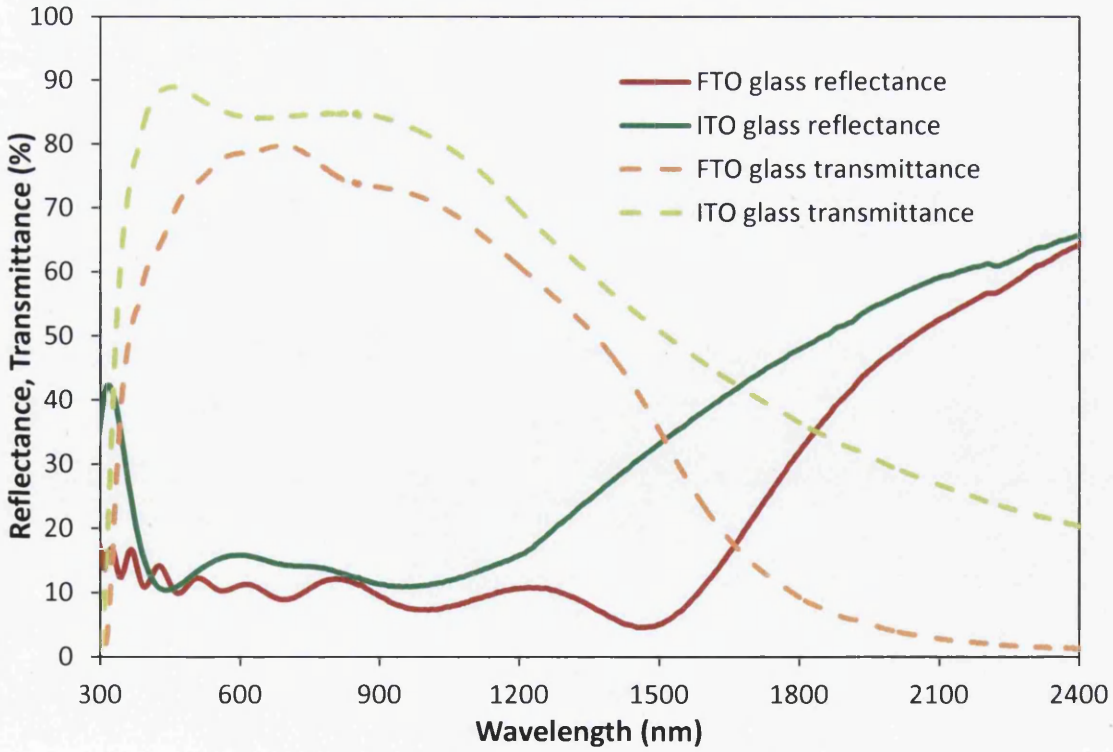

Figure 3.6: Transmittance and reflectance of ITO and FTO glass

It illustrates the crossover at which the transmittance decreases and the reflectance begins to increase, this is the high frequency dielectric constant ε_∞. This occurs at around 1650 nm for both substrates and this maximum absorption corresponds well to the output of the NIR heating technique.

The ratio of conductivity to optical transparency is considered a figure of merit for TCOs, where $\sigma/\alpha = -\{R_s \ln(T + R)\}^{-1}$ [11]. For the commercial substrates used here, calculating with the average T and R values for the range 390 to 700 nm, the figures of merit are 1.5 Ω^{-1} for the FTO glass and 2.49 Ω^{-1} for the ITO glass suggesting that the ITO has a better ratio of conductivity to transparency.

3.3.2 Estimating emissivity of ITO and FTO glass to predict temperature after NIR exposure

An NIR heater emits high energy density NIR radiation which causes a rapid release of thermal energy if the substrate absorbs in this region. The NIR equipment used in this work, an AdPhos NIR Coil Lab LV2 unit (described in section 2.1), consists of a module of NIR emitters which have a total energy density of 25 kW surrounded by reflectors, and a conveyor belt for the sample platform to move at a certain line speed under the NIR emitters to determine the exposure time. The intensity output of the NIR emitters is controlled on a scale of % power from 0 to 100. Figure 3.7 shows the spectral output for of the NIR unit which was measured empirically using two portable Ocean Optics spectrometers, an HR2000+ UV/VIS (range 200-1100 nm) and NIRQUEST256 NIR (range 900-2500 nm); the input fibre with cosine corrector was positioned 5 cm away and 10 cm above the exit of the lamps to avoid thermal damage and data was collected for each power setting at 1 m/min speed (25 s exposure) [22].

The peak of radiation is in the NIR region at around 800-1200 nm but as the lamp is based on tungsten halogen (shown in section 1.4.2) it emits a wide range from visible to mid-IR. As the intensity of the lamps increase more radiation is emitted per wavelength. The increase between increments of 10% power is not linear and also varies by wavelength. Since FTO and ITO absorb in the NIR region it is believed they may significantly heat when subjected to this NIR equipment as occurs with metal [14].

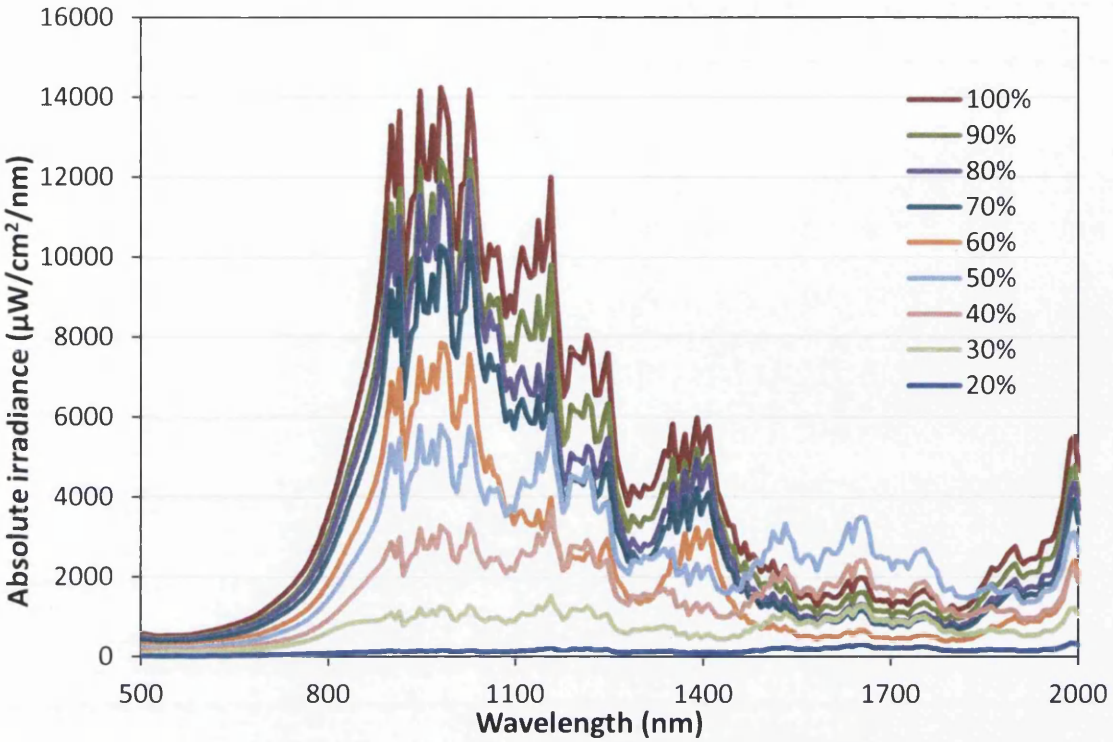

Figure 3.7: Measured absolute irradiance vs. wavelength per intensity of the NIR unit lamp power [22]

Due to the non-linear progression of the radiation emitted with lamp intensity it is difficult to predict the temperature. For metal samples the temperature can be measured by welding a thermocouple to the metal and plotting the heating profile with a data logger during the sample's exposure to the emitters. However this is infeasible for glass samples therefore a different approach is required. This involved using a thermal imaging camera to film the samples as they exited the NIR lamp after having been exposed for 12.5 s (resulting from a line speed of 2 m/min). This speed was chosen because it suits continuous manufacture and suitably high temperatures were obtained at 2 m/min previously on the same equipment for titanium substrates [14].

The IR camera was set to assume an emissivity of 1 for all objects, that of a black body which is heavily idealised: a black body is one that absorbs all thermal radiation but transmits and reflects none. Emissivity is the ability of a surface to emit heat by radiation relative to a black body. All real world materials will have an emissivity lower than 1 and to obtain the actual values of temperature from the IR camera footage of NIR exposure the emissivity of each substrate needed to be known. To calculate the emissivity of ITO glass, FTO glass and uncoated glass (2.2 mm thick) they were placed on a hot plate at 100°C, which was

confirmed using a thermocouple, and photographed with the IR camera. Using the IR camera's software an area encompassing each substrate was chosen in turn and the emissivity of that area was adjusted until the temperature displayed on the IR camera matched 100°C which the substrates should be. The obtained emissivities are shown in Table 3.1.

Table 3.1: Calculated emissivities for glass substrates by calibrating a hot plate with IR camera

Substrate	Emissivity
FTO glass	0.16
ITO glass	0.21
Glass	0.92

The emissivity of glass agrees well with values in literature where glass varies from around 0.9 - 0.94 [23]. The emissivity of FTO glass and ITO glass is markedly different to that of glass, where they would appear to look fairly similar, but FTO and ITO follow the trend of metals which tend to have low emissivities due to their high reflectivity in the IR. As the FTO glass has a thicker layer of TCO than the ITO glass, 600 nm compared to 150 nm, its emissivity is lower because it has a higher reflectivity with the glass underneath having a reduced impact on the optical properties. If the two TCOs were the same thickness the emissivity would probably fairly similar or slightly lower for ITO glass which would have higher reflectivity due to its higher carrier concentration. The surface properties also greatly influence emissivity, such as polished metals having lower emissivity than dull ones, so a smoother TCO of identical thickness may have a lower emissivity than a rougher one. The emissivity of a material can depend upon the temperature, emission angle and wavelength of light. By doing the NIR filming and IR camera/hot plate calibration without adjusting the camera angle and tripod these factors should hopefully been kept constant. The rise in temperature should not have a significant impact on the emissivity for the temperatures obtained here because the phenomenon is more prominent at high temperatures (e.g. an object reaching such high temperatures that the IR radiation emitted shifts towards the visible and it glows red-white). The emissivity of the FTO glass was also checked using an emissometer (Devices and Services) and found to be accurate to within ±0.01 (0.15, figure 3.8). Using the emissivity values in Table 3.1 the temperatures reached by the substrates after NIR exposure could be estimated by inputting them into the footage in the IR camera software. The peak temperature was chosen for each NIR intensity. The resulting graph is shown in figure 3.9

where temperature is plotted against NIR intensity after a fixed exposure time of 12.5 s for the FTO glass, ITO glass and 2.2 mm thick uncoated glass.

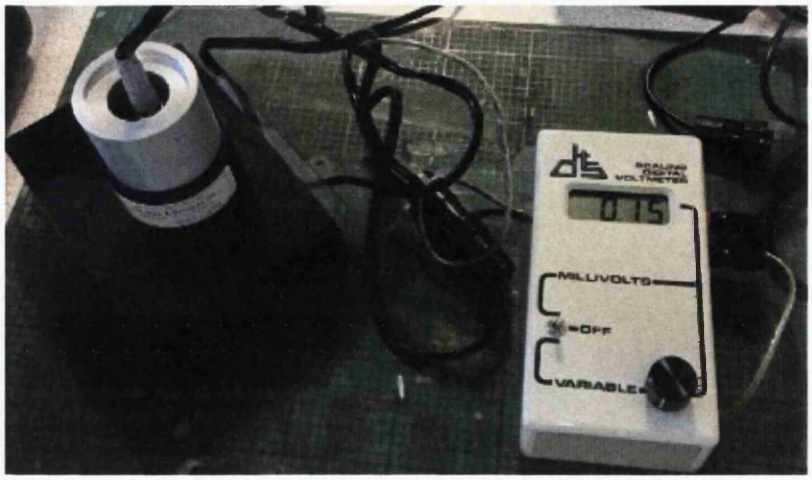

Figure 3.8: Emissometer measuring the emissivity of 7.5 Ω/□ FTO glass

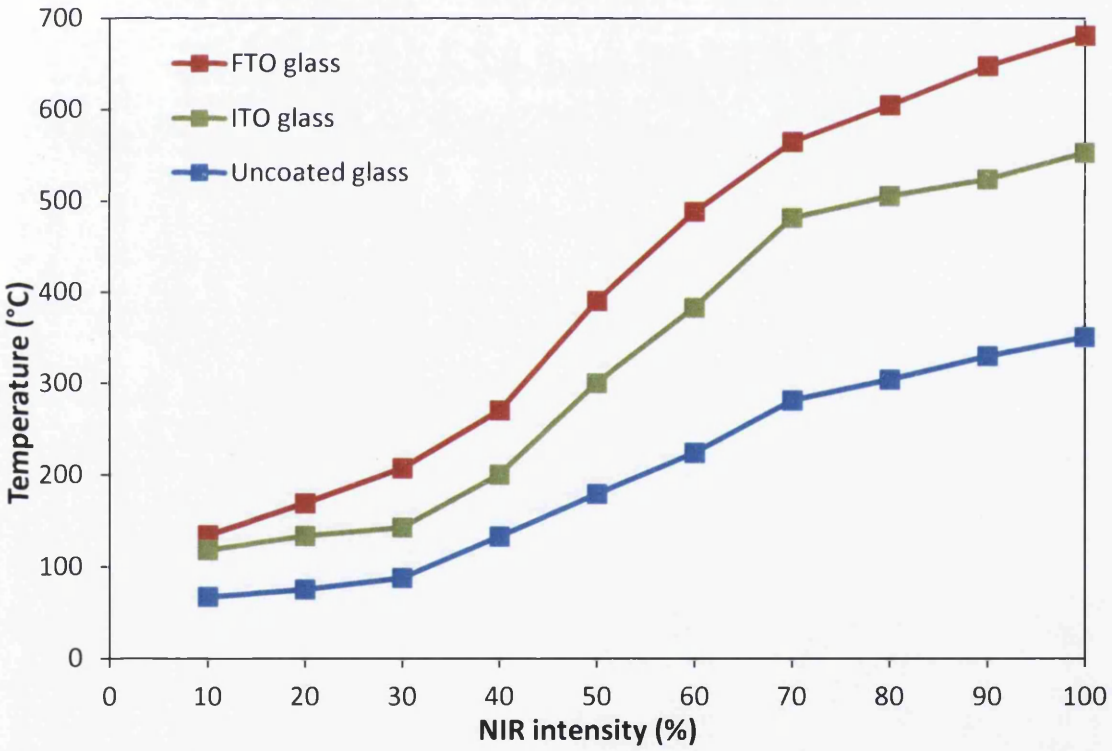

Figure 3.9: Estimated maximum temperature of glass based substrates after 12.5 s exposure of NIR radiation vs. intensity of NIR lamps

The substrates were room temperature prior to each 12.5 s NIR exposure and heated during the run reaching their maximum temperature immediately prior to exit from the emitter modules. The warming during heating is partly influenced by the thermal conductivity of the

material and partly due to the nature of the halogen emitters which get hotter while in operation. Therefore the temperatures shown in figure 3.9 are the maximum temperatures and the substrates would not have been those temperatures for the entire duration. Additionally due to the constraints of filming the substrates they would have begun to cool when the values were obtained and the maximum temperature may be higher but these temperatures give a good comparison between each substrate and NIR intensity and were taken at the same time, 2 s after exit, to maintain consistency. The progression of temperature is not linear because the NIR power intensity does not increase linearly as shown in figure 3.7 and it follows this same trend with high progressions in radiation and thus obtained temperatures at 50%, 60%, and 70% NIR. It should be noted that the spectra obtained in figure 3.8 was for a 25 s duration rather than 12.5 s but this would only affect the values of the irradiance rather than the positions of the peaks and relation between each NIR power.

Each substrate heats upon exposure to the NIR photons which interact with the substrate releasing thermal energy rapidly. The NIR module emits a large range of wavelengths including those into the mid-NIR (though not as much as in the NIR) which increase the chances of glass absorbing a photon as discussed previously. The lamps are also enclosed in a metal reflecting box causing the area around the samples to become hot which may contribute some heat. The TCO coated glasses heated significantly more than the glass alone due their enhanced absorption in the NIR region. A higher proportion of free carrier absorption occurred, when the photons are absorbed a phonon is emitted to conserve electron momentum and the associated energy of this is dissipated as heat. At maximum NIR power this results in the 600 nm FTO layer contributing an extra 300°C of heat compared to the glass and the 150 nm ITO layer contributing an extra 200°C of heat compared to the glass. Glass of 1.1 mm thick was also filmed but there was very little difference between the temperatures of 1.1 mm thick and 2.2 mm thick glass so it was not included. The increase in absorption of 2.2 mm thick glass over 1.1 mm thick (shown earlier in figure 3.3) is so miniscule that it has negligible difference in thermal energy gain as a result of photon interaction with the substrate. The TCO coated substrates, despite the difference in thermal expansion coefficients between the TCO and the glass, were undamaged by the rapid heating and cooling as a result of NIR exposure with no cracking or thermal stress induced.

During the experiment it was noted that the temperatures reached varied across the platform (see figure 3.10). Identical samples of 1.1 mm glass were spread around the platform at the extremes so that the variations could be mapped (figure 3.11). These variations would be down to the positioning of the NIR lamps and uneven distribution of electromagnetic radiation emitted.

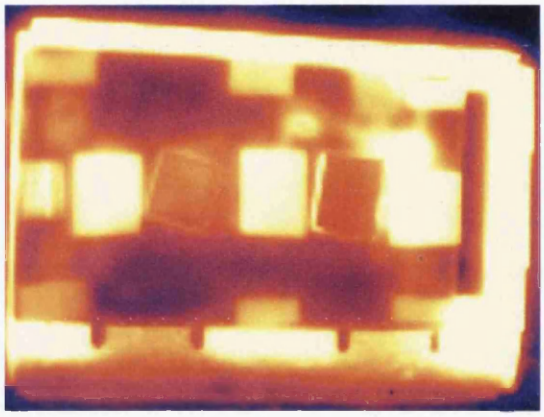

Figure 3.10: IR camera image at 100% lamp power of the platform after exiting

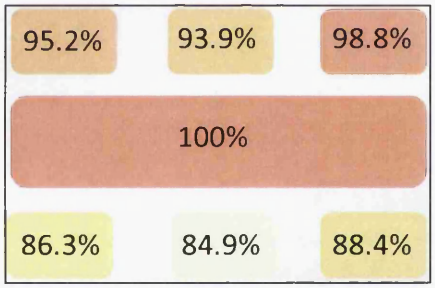

Figure 3.11: Mapping of the uneven radiation distribution within the platform by showing average temperature deviations of 1.1 mm thick glass from the centre of the platform by platform position

The average temperature reached for all powers was calculated and the deviation of this as a percent for the colder samples was plotted onto the diagram corresponding to the sample's position. The 1.1 mm thick glass near the centre of the platform was the hottest with the samples along the top deviating slightly, most prominently in the middle of the top, and the samples along the bottom deviating more, most significantly in the middle of the bottom. This is crucial to note so to avoid inconsistency during future heating of samples they will be placed along the middle of the platform.

It is extremely promising that the temperatures obtained for the FTO and ITO coated substrates for the higher power intensities at the line speed of 2 m/min (12.5 s exposure time) correspond to those required for the heating steps of dye-sensitised solar cell manufacture which should allow the same reduction in fabrication time that was achieved on metal to be achievable for the first time on TCO coated glass.

3.3.3 Effect of temperature on resistivity by conventional and NIR heating

In order to be suitable for high temperature applications a TCO needs to withstand the temperature without degradation of visible transparency or electrical conductivity. Unfortunately it is well known that ITO's conductivity drastically decreases after heating in air at temperatures above 300°C [17]. This is illustrated in figure 3.12 where ITO and FTO glass were heated for 30 minutes at various temperatures in a conventional oven with their sheet resistance, R_{sh}, measured before and after using a four point probe.

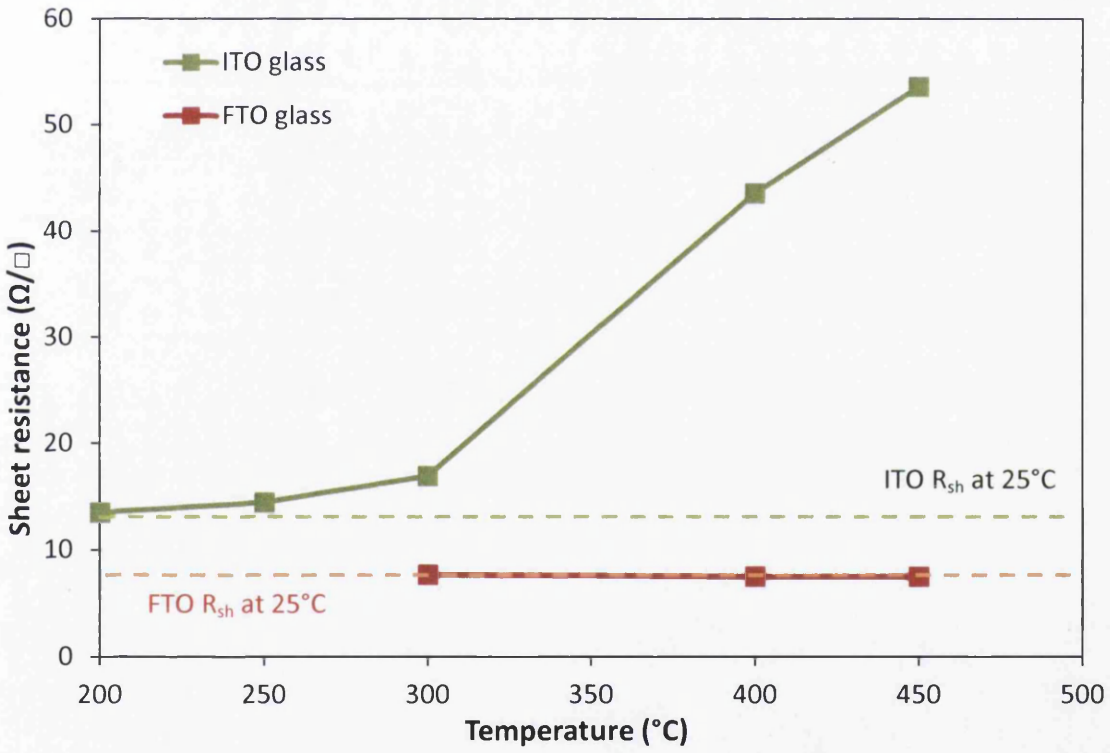

Figure 3.12: Sheet resistance of ITO and FTO glass vs. temperature after 30 min of heating in a conventional oven

At 200°C there was no change in the sheet resistance of the ITO glass. This is the temperature that ITO is deposited onto glass [4] and TCOs tend to be stable until just above their deposition temperature [11]. At this temperature no diffusion of oxygen into vacancies

will occur. At 250°C there is a small rise in sheet resistance of about 1.4 Ω/□ which indicates that some oxygen has diffused into the natural oxygen vacancies of ITO resulting in a reduced carrier concentration. This diffusion is accelerated at higher temperatures, with 300°C showing a 30% increase in R_{sh}, 400°C showing a 234% increase in R_{sh}, and 450°C showing a 312% increase in R_{sh}. This significant rise in sheet resistance is why ITO glass is incompatible with processes that require temperatures above 300°C. It may be worth noting that the ITO glass used in this work was supplied as "8-12 Ω/□" and yet no pieces were below 12.9 Ω/□ out of the packet (and for more than one batch) so this particular item of ITO glass is not of great quality and perhaps may degrade more easily than others reported in literature. ITO's increase in resistivity is reversible by heating the film in a reducing (H_2) atmosphere [19] but this is a fairly cumbersome compromise.

The sheet resistance of the FTO glass remains unaffected at these temperatures, the thermal stability of tin oxide films is more limited by the softening of the glass substrate than by thermal decomposition of the FTO film [11]. FTO glass is deposited via APCVD at temperatures up to 700°C. Figure 3.13 shows the sheet resistance of ITO and FTO films after heating at a temperature of 450°C in a conventional oven for shorter times. 450°C was chosen because this is the highest temperature required for DSC processing. Although for 30 min exposure at this temperature it results in a tripling of resistivity for ITO glass it was still useful to determine how long it took for a rise in R_{sh} to occur.

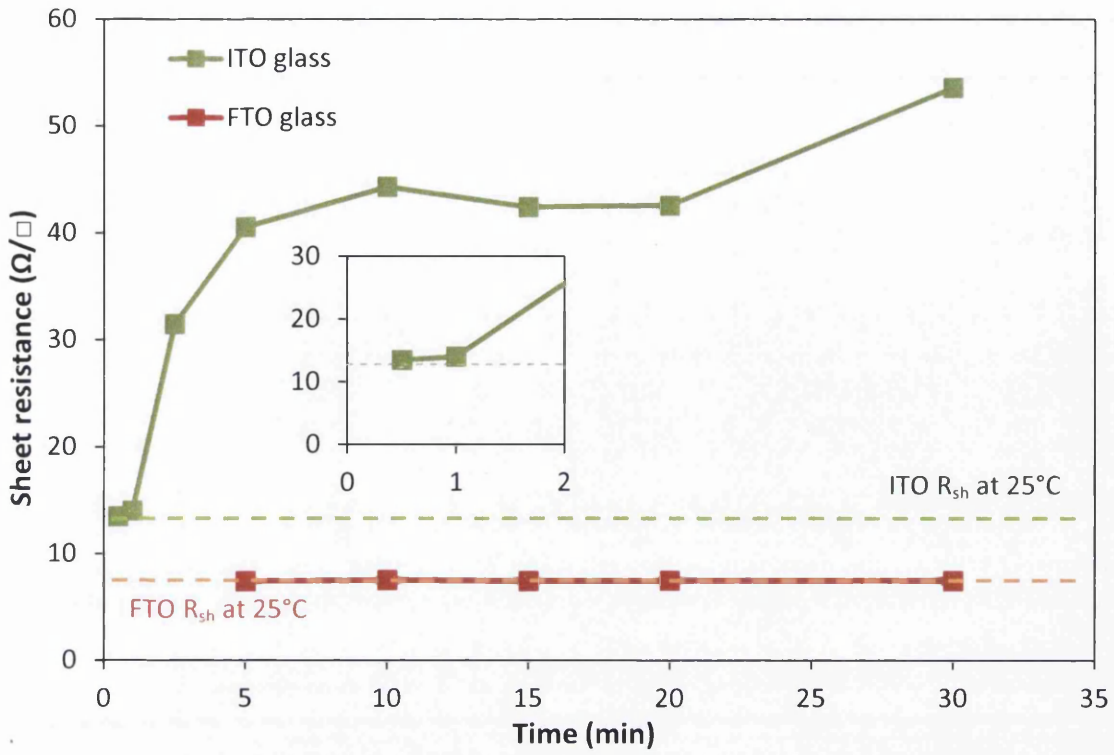

Figure 3.13: Sheet resistance of ITO and FTO glass vs. time in an oven at 450°C with detail for 0-2 minutes (inset)

There was no rise in sheet resistance after 30 s exposure in an oven at 450°C although the sample is unlikely to have reached 450°C in 30s. However after 1 min there was a 0.5 Ω/□ rise in R_{sh} which was surprisingly fast, the sample would have exceeded the temperature for oxygen diffusion to begin occurring. After 2.5 min there was a 138% rise in R_{sh} which suggests there is an extremely high rate of diffusion of oxygen into the vacancies at 450°C. This trend continues and seems to plateau at around 5 min where the sheet resistance rise is more linear because oxygen diffusion into vacancies rises at a slower rate with the initial more exposed vacancies already filled and so further filling of vacancies at less readily available lattice sites. There is some inconsistency for times between 10 min and 20 min because each sample was a fresh sample and the quality of the ITO films varied between samples with some more susceptible to oxygen diffusion than others. Nonetheless the trend would remain the same on average with a linear increase between 10 and 30 min. As expected the sheet resistance of FTO remained unaffected. ITO and FTO glass were also heated using NIR radiation in an identical fashion to that used in section 3.2 where they were exposed for 12.5 s. Figure 3.14 shows the sheet resistance of ITO and FTO glass vs. NIR lamp intensity.

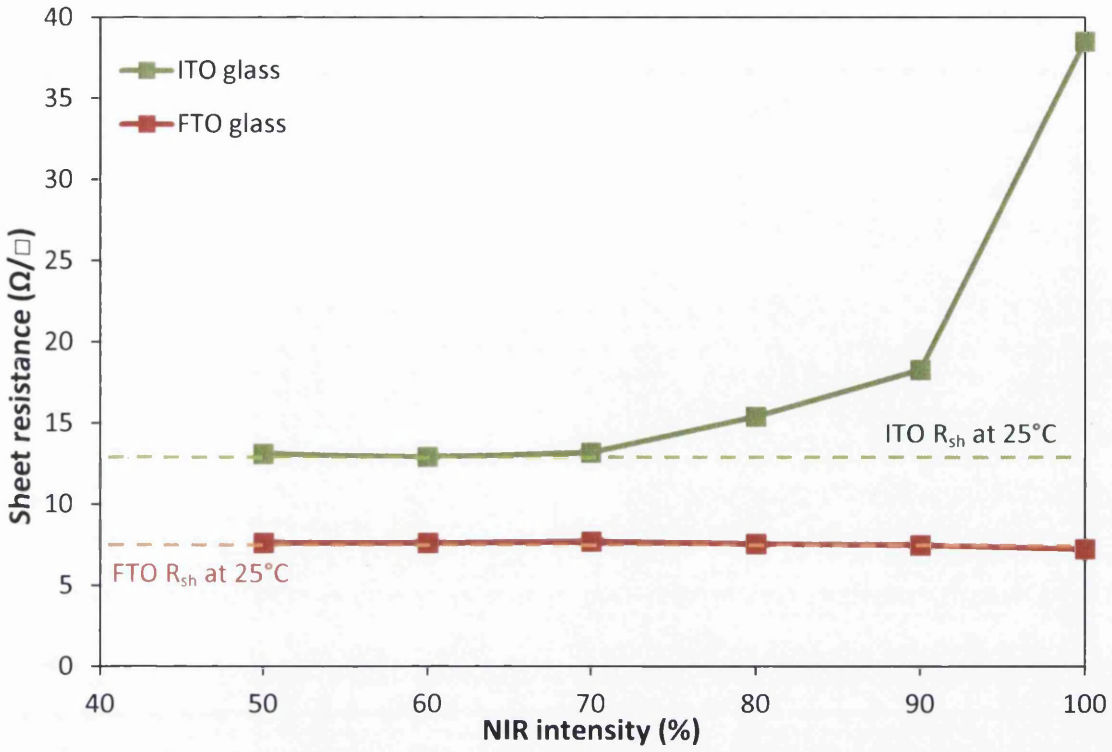

Figure 3.14: Sheet resistance of ITO and FTO glass vs. NIR lamp intensity for 12.5 s exposure

Again the FTO glass does not change in sheet resistance because it does not exceed the temperature necessary for its thermal degradation. The R_{sh} of ITO begins to increase at around 80% NIR lamp intensity after 12.5 s exposure with an increase of 18%, 38%, and 196% in R_{sh} for 80, 90 and 100% NIR intensity respectively. As was shown in figure 3.13 an increase in R_{sh} occurs after only 1 min at 450°C in an oven and that is with slow heating where the substrate would have risen from room temperature approaching the temperature of the air and would not have been close to 450°C for the entire duration. With the rapid heating of NIR radiation the temperature change would have been extremely sudden with a few seconds to allow some oxygen diffusion into the vacancies. To compare the effect of sheet resistance on ITO glass by the two heating processes more directly the NIR exposed samples could be plotted using the estimated temperature obtained at each lamp intensity from section 3.2 rather than the arbitrary NIR intensity. Shown in figure 3.15 are the oven heated samples and NIR heated samples against oven temperature and predicted maximum temperature after 12.5 s NIR exposure.

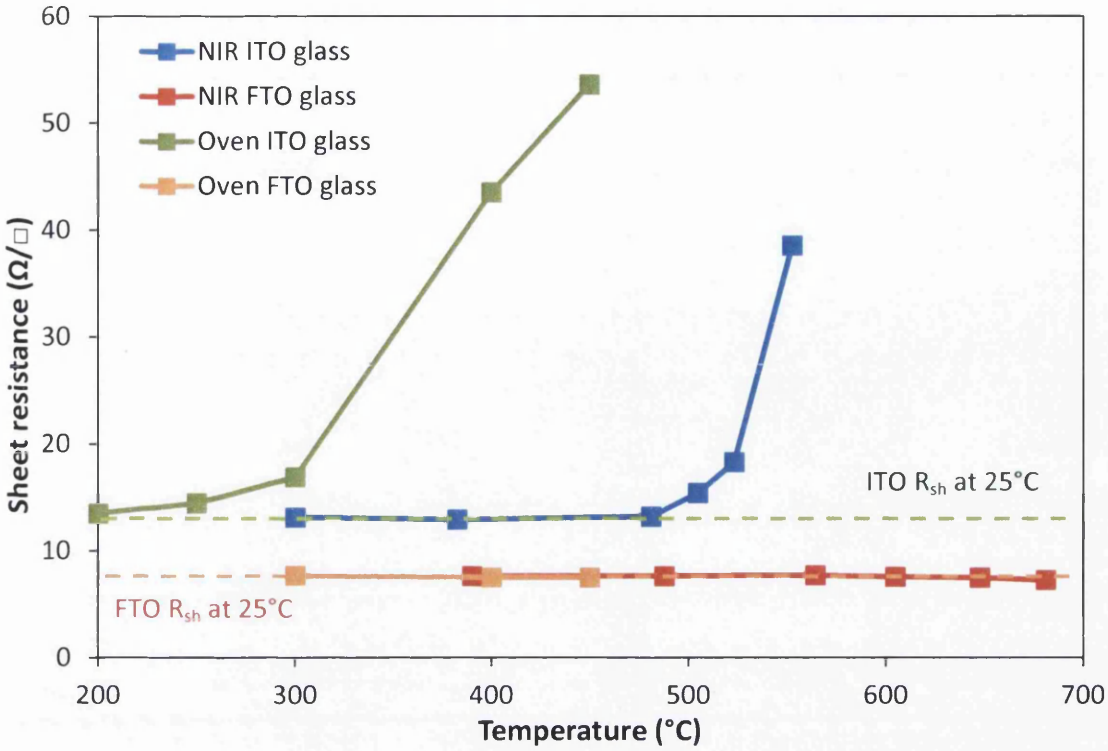

Figure 3.15: Sheet resistance vs. estimated average temperature for NIR heated substrates and temperature for oven heated substrates

The maximum temperature obtained for the NIR exposed ITO glass samples was 481°C for 70% NIR intensity with no change in R_{sh}. The NIR heating process was faster than the oxygen diffusion at this temperature or at least the time at which it peaked was faster. This is extremely significant if heating processes can be performed at this peak temperature with NIR radiation that are not possible without a rise in R_{sh} otherwise. With the speed at which NIR radiation can process heating steps that require much longer with conventional heating, such as the NIR sintering of TiO_2 onto titanium in 12.5 s [14], it does not matter that there is a still a short time constraint of less than a minute at which filling of vacancies and thus R_{sh} rise will occur. There is an 18% increase in R_{sh} when NIR exposure heats the ITO glass up to 505°C but this is a smaller increase than that of 300°C exposure in a conventional oven for 30 min. The former is a dramatically shorter timeframe than the latter so this comparison may seem unfair but in terms of raw heating power the 12.5 s NIR exposure will have achieved much higher and more effective heating than the oven with less of a rise R_{sh}. At 100% NIR exposure with a maximum temperature of 553°C there is a substantial increase in ITO's sheet resistance suggesting at this temperature the drive for oxygen diffusion into the film is so strong it can occur in 12.5 s albeit still not as much as for 30 min. Although the NIR heating technique cannot prevent oxygen diffusion altogether it still presents a further

200°C higher temperature range for processing on ITO substrates without causing significant degradation of the film's conductivity.

3.4 Conclusions

For the first time NIR radiation was shown to heat FTO and ITO coated glass to significantly high temperatures, high enough to be compatible with the fabrication processes associated with dye-sensitised solar cells (DSCs), in only 12.5 s of exposure. This dramatic time reduction is very attractive for industrial manufacture, especially if traditional heating steps can be replicated to the same efficacy with the NIR heating technique. Of additional significance is the compatibility of this technique for the heating of glass based substrates which will also enable a wider range of applications, especially where transparency is desired. Previously NIR radiation has only been demonstrated for reducing heating times on metallic substrates. Subsequent chapters will investigate the application of NIR heating on glass for the fabrication of DSCs.

A further benefit revealed when using NIR heating, particularly for ITO glass, was the ability to reach a higher temperature than conventional heating with no resistivity rise. A significant disadvantage of ITO is its resistivity increase at temperatures above 300°C which restricts its use, where conductivity is required, to processing below this temperature. However it was shown here that a maximum temperature of 505°C can be obtained using 12.5 s of NIR heating with no significant rise in sheet resistance (the same rise experienced for 30 min oven exposure at 300°C) which presents a further 200°C higher temperature range for processing on ITO substrates while preserving the conductivity. This potentially could widen the possible applications of ITO glass and will be investigated in Chapter 6 by demonstrating the DSC processing steps on ITO glass which by conventional heating are severely restrictive. It is believed that the short exposure of NIR limits the oxygen diffusion into ITO's vacancies, which are responsible for its reduction in carrier concentration and mobility, thereby reducing the severity of a high temperature.

3.5 References

[1] M. Katayama, TFT-LCD technology, Thin Solid Films. 341 (1999) 140–147.

[2] C.W. Tang, S.A. VanSlyke, Organic electroluminescent diodes, Appl. Phys. Lett. 51 (1987) 913.

[3] I. Hamberg, C.G. Granqvist, Evaporated Sn-doped In_2O_3 films: Basic optical properties and applications to energy-efficient windows, J. Appl. Phys. 60 (1986) 123.

[4] U. Betz, M. Kharrazi Olsson, J. Marthy, M.F. Escolá, F. Atamny, Thin films engineering of indium tin oxide: Large area flat panel displays application, Surf. Coatings Technol. 200 (2006) 5751–5759.

[5] A. Kloppel, J. Trube, U. Hoffman, J. Burroughes, S. Heeks, A. Gunner, et al., 46.3: Ultra-flat ITO Films for Light Emitting Polymer Applications, SID Symp. Dig. Tech. Pap. 31 (2000) 1084–1087.

[6] Bine, [Online]. Available at: http://www.bine.info/fileadmin/content/Publikationen/Englische_Infos/projekt_0509_engl_Internetx.pdf. [Accessed: 26-Jul-2013].

[7] Pilkington, [Online]. Available at: http://www.pilkington.com/resources/ats138dmultiplelowecoatingsinig20130115.pdf. [Accessed: 26-Jul-2013].

[8] D.D. Vuong, G. Sakai, K. Shimanoe, N. Yamazoe, Preparation of grain size-controlled tin oxide sols by hydrothermal treatment for thin film sensor application, Sensors Actuators B. 103 (2004) 386–391.

[9] H. Kostlin, Application of thin semiconductor metal films in energy technology, in: Aachen P.G. (Ed.), Festkorperprobleme 22, Springer Berlin Heidelberg, 1982: pp. 229–254.

[10] I. Forbes, L. Peter, Chapter 17 Materials for Photovoltaics, in: T. Letcher, J. Scott (Eds.), Mater. a Sustain. Futur., RSC Publishing, 2012.

[11] R.G. Gordon, Criteria for Choosing Transparent Conductors, MRS Bull. (2000) 52–57.

[12] S. Uchida, M. Tomiha, N. Masaki, A. Miyazawa, H. Takizawa, Preparation of TiO_2 nanocrystalline electrode for dye-sensitized solar cells by 28GHz microwave irradiation, Sol. Energy Mater. Sol. Cells. 81 (2004) 135–139.

[13] G. Mincuzzi, L. Vesce, M. Liberatore, A. Reale, A. Di Carlo, T.M. Brown, Laser-Sintered TiO_2 Films for Dye Solar Cell Fabrication: An Electrical, Morphological, and Electron Lifetime Investigation, IEEE Trans. Electron Devices. 58 (2011) 3179–3188.

[14] T. Watson, I. Mabbett, H. Wang, L. Peter, D. Worsley, Ultrafast near infrared sintering of TiO_2 layers on metal substrates for dye-sensitized solar cells, Prog. Photovoltaics Res. Appl. 19 (2010) 482–486.

[15] C.-T. Wu, H.-P. Kuo, H.-A. Tsai, W.-C. Pan, Rapid dye-sensitized solar cell working electrode preparation using far infrared rapid thermal annealing, Appl. Energy. 100 (2012) 138–143.

[16] M.J. Carnie, C. Charbonneau, P.R.F. Barnes, M.L. Davies, I. Mabbett, T.M. Watson, et al., Ultra-fast sintered TiO_2 films in dye-sensitized solar cells: phase variation, electron transport and recombination, J. Mater. Chem. A. 1 (2013) 2225.

[17] K. Goto, T. Kawashima, N. Tanabe, Heat-resisting TCO films for PV cells, Sol. Energy Mater. Sol. Cells. 90 (2006) 3251–3260.

[18] T. Kawashima, H. Matsui, N. Tanabe, New transparent conductive films: FTO coated ITO, Thin Solid Films. 445 (2003) 241–244.

[19] S. Lee, J. Noh, S. Bae, I. Cho, Indium-Tin-Oxide-Based Transparent Conducting Layers for Highly Efficient Photovoltaic Devices, J. Phys. Chem. C. 113 (2009) 7443–7447.

[20] M. Soubeyrand, A.C. Halliwell, Method for Forming Tin Oxide Coating on Glass, 5698262, 1997.

[21] A. Hjortsberg, I. Hamberg, C. Granqvist, Transparent and heat-reflecting indium tin oxide films prepared by reactive electron beam evaporation, Thin Solid Films. 90 (1982) 323–326.
[22] M. Cherrington, Printing technologies for current collectors for dye-sensitized solar cells, Swansea University, 2012.
[23] Omegascope, [Online]. Available at: http://www.monarchserver.com/TableofEmissivity.pdf. [Accessed: 26-Jul-2013].

Further Reading

M. S. Dresselhaus "Optical properties of solids." *Proceedings of the International School of Physics" Enrico Fermi," J. Tauc, Editor (Academic Press. NY. 1966)* (1966).
A. Delahoy and S. Guo, "Transparent Conducting Oxides for Photovoltaics," in *Handbook of Photovoltaic Science and Engineering*, 2nd ed., A. Luque and S. Hegedus, Eds. John Wiley & Sons, 2011, pp. 716–796.

4. Rapid Platinisation of Counter Electrodes on FTO glass for Dye-sensitised Solar Cells using Near Infrared Radiation

4.1 Introduction

A dye-sensitised solar cell (DSC) is a potentially low cost solar cell [1] that typically consists of a porous titanium dioxide layer coated onto a conducting substrate and sensitised with a dye. A DSC differs from a traditional solar cell (based on a p-n junction) in that excitons are generated rather than free electron-pairs, and the roles of absorber and charge transport are not both performed by the semiconductor (section 1.2.1). The dye extends the absorption into the visible (TiO_2 can only absorb in the UV) allowing injection of an electron into the conduction band of TiO_2, which transports the electron through the sintered TiO_2 particles and charge is collected at the conducting substrate. The electrons flow through the circuit transferring their energy and are returned to the conducting substrate of the counter electrode. Meanwhile the dye accepts an electron from an I^- ion in the electrolyte to reduce it back to ground state, this in turn oxidises the I^- to an I_3^- ion. To sustain this regenerative process the I_3^- ions are reduced to I^- ions at the counter electrode, catalysed by platinum which has a special affinity for the reduction of iodine and its related species.

Alternative catalysts can be used for DSC counter electrodes (see section 1.2.6) but platinum (section 1.2.6.1) is the most widely used and performs well both in conjunction with the I^-/I_3^- redox couple electrolyte [2]and $Co^{(II/III)}$ species [3] which is used in the currently highest efficiency DSC. To be an effective catalyst platinum has a few requirements. The platinum should have a large surface area to maximise the available number of sites for triiodide reduction. This can be achieved by having a small particle size, with 5 nm reported as the average cluster size with the best catalytic activity [4]. Good adhesion is required, poor adhesion may lead to Pt adsorbing at the TiO_2 surface and increasing recombination at the TiO_2/electrolyte interface [5] so reducing the photocurrent. Most other properties depend on the preparation method as the structure of platinum created varies with method.

Platinum can be electrochemically deposited which is a low cost method that can be performed at room temperature and allows control over layer thickness. However it is reported to be vulnerable to dissolution in the iodine electrolyte and easily damaged due to poor adhesion [4]. Sputtered platinum also allows control of the layer thickness and has strong adhesion resulting in good performance [5] but it is an expensive method due to the equipment required and amount of platinum used; it also requires a vacuum which is not

favourable for roll-to-roll continuous production. Thermal decomposition of $PtCl_x$ is commonly used in the literature and the most effective in terms of balancing efficiency and practicality [4]. Rather than creating a constant layer the thermal method results in clusters of platinum nanoparticles.

Thermally decomposed platinum involves the conversion of a platinum chloride precursor, normally in the form of H_2PtCl_6, chloroplatinic acid, to catalytic platinum. Thermal energy breaks the Pt-Cl bond at temperatures above 375°C [6]:

$$PtCl_{2(s)} \rightarrow Pt_{(s)} + Cl_{2(g)}$$

The optimum conditions for this reaction (with 5 mM H_2PtCl_6) were found to be at a temperature of 385°C heated for 30 minutes, with 375°C - 410°C the outer limits that achieve almost similar exchange current, and a platinum loading of 5-10 $\mu m/cm^2$ which results in an average cluster size of around 5 nm [4]. Residual $PtCl_2$ can impair the performance of the counter electrode as it is inactive and reduces the available number of sites for triiodide reduction.

Thermal platinisation is one of the slowest steps of DSC manufacture requiring 30 minutes with conventional oven heating at 385°C. This is unfeasible for the commercialisation of DSCs because it is time consuming, is a batch process (would require an impossibly long oven if it were inline), and restricts production output. Conventional heating (section 1.4.1) requires the entire oven and sample to heat up which wastes energy and heats the substrate with convection and conduction which is quite slow. Near infrared (NIR) radiative heating (section 1.4.2) is a fast heating process that involves high energy NIR radiation transmitting through a coating (since most do not absorb in the IR) and being absorbed by any free carriers in the substrate which rapidly releases thermal energy. It has previously been used to reduce the heating time of TiO_2 sintered working electrodes to 12.5 s on titanium [7] but has not been applied to a counter electrode thus far or to a non metallic substrate.

In Chapter 3 FTO and ITO coated glass were shown to heat significantly compared to uncoated glass when exposed to NIR radiation due to their high concentration of free carriers. The ability of FTO glass to reach a high temperature in seconds may enable rapid processing of a DSC component on FTO glass. In this chapter the possibility of using NIR radiation to thermally decompose chloroplatinic acid to platinum on FTO glass is investigated.

4.2 Experimental

Prior to manufacturing DSC devices the prospective NIR heated counter electrodes were characterised as follows. 7.5 Ω/□ FTO glass (NSG Pilkington) was coated with 3 drops of 5 mM chloroplatinic acid in propan-2-ol using a capillary tube (as per the DSC method in section 2.2.2). It was heated either in a conventional oven at 385°C for 30 min or using Near Infrared (NIR) radiation at a speed of 2 m/min for a 12.5 s lamp exposure (section 2.1.1). The absorbance of an unheated and a heated sample of chloroplatinic acid on FTO glass was measured using a UV/Vis/NIR spectrophotometer (section 2.8). Samples were also characterised with scanning electron microscopy (SEM) (section 2.11) and energy-dispersive X-ray spectroscopy (EDX) (section 2.12).

Cyclic voltammetry was performed on the platinised FTO glass in a 3 electrode set up. The catalytic performance of NIR heated and conventionally heated Pt to reduce triiodide was tested using an I^-/I_3^- electrolyte solution in acetonitrile with a Ag/Ag^+ reference electrode and platinum mesh counter electrode (section 2.7) between the potentials of -0.5 and 0.8 V with a scan rate of 50 mV/s.

Dye-sensitised solar cells were constructed (section 2.2.2) with $TiCl_4$ treated oven heated TiO_2 film working electrodes and NIR heated counter electrodes (section 2.1.1) exposed for 12.5 s, see figure 4.1. Their photovoltaic properties were characterised using a solar simulator (section 2.3) and electrochemical impedance spectroscopy (EIS) (section 2.6).

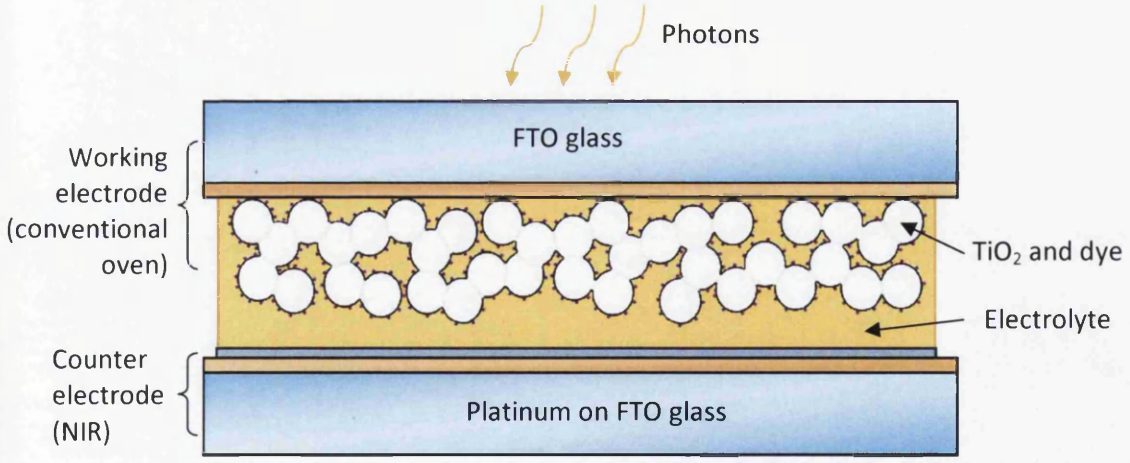

Figure 4.1: Diagram of DSCs constructed in this work with heating method shown in brackets

4.3 Results and discussion

4.3.1 Characterisation of rapidly heated chloroplatinic acid

FTO glass absorbs strongly in the NIR and IR region (as discussed in Chapter 3), due to the layer of FTO that has a high free carrier concentration. This enables it to heat significantly when subjected to the NIR heating technique; the NIR photons excite the free electrons in FTO's conduction band releasing thermal energy which is distributed extremely quickly by the free carriers. The absorbance of 5 mM chloroplatinic acid in propan-2-ol coated onto FTO glass was measured using a UV/Vis/NIR spectrophotometer (figure 4.2) to determine if the quantity used for the manufacture of a platinised DSC counter electrode would affect the temperature reached with NIR heating via any additional absorbance. Also included in the figure is NIR heated 5 mM H_2PtCl_6 on FTO glass, uncoated FTO glass and uncoated glass.

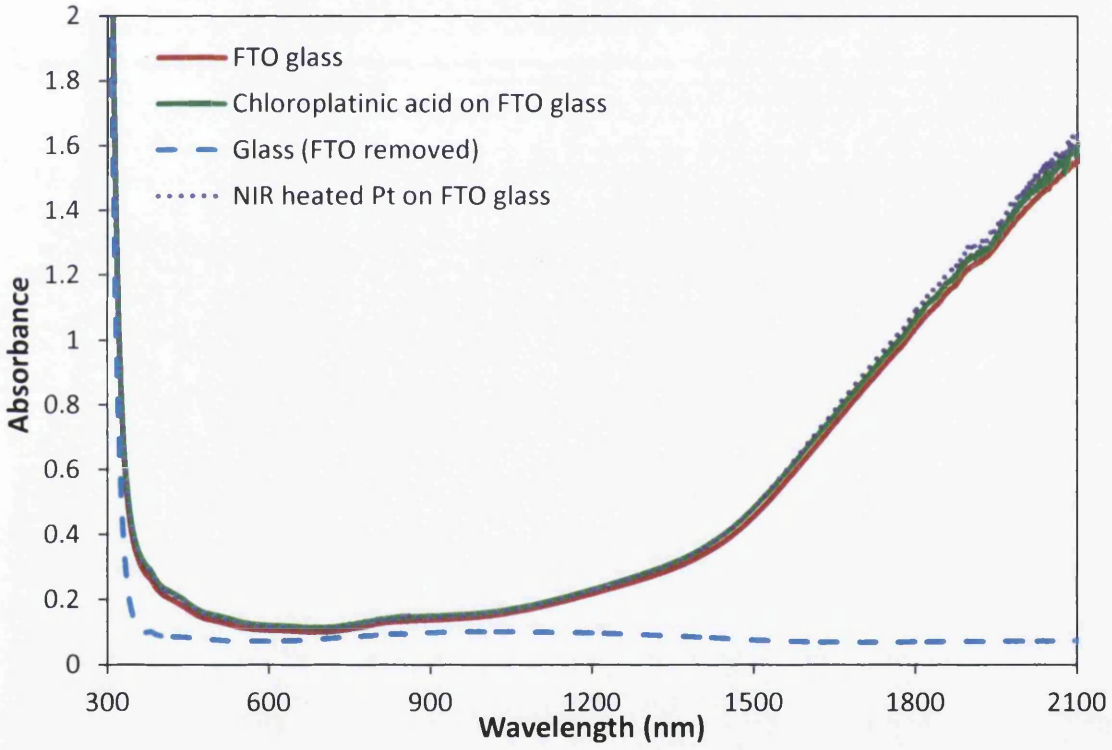

Figure 4.2: Absorbance vs. wavelength for FTO glass and FTO glass with a layer of chloroplatinic acid

There is no significant influence on the absorbance of the FTO glass with the low loading of platinum used here in the unheated 5 mM chloroplatinic acid which suggests that it would not affect the temperature reached by the FTO glass during exposure to NIR radiation. Therefore the maximum temperatures estimated for 12.5 s exposure of FTO glass in section 3.3.2, shown in Table 4.1 for reference, will be an accurate guideline for deciding which NIR

intensities may be suitable for the rapid thermal decomposition of chloroplatinic acid. The absorbance of NIR heated chloroplatinic acid (at an intensity determined to cause complete decomposition to platinum) was also measured to see if as a result of the heating to what extent the absorbance may change which may affect the absorbance in situ. There is a slight increase in the NIR region, as platinum absorbs in the IR more strongly than H_2PtCl_6 and IPA but again it would not impact the resultant temperature from NIR exposure.

Table 4.1: Temperatures estimated in Chapter 3 for 12.5 s NIR exposed FTO glass

NIR intensity (%)	Max temperature (°C)
40	270
50	389.9
60	487.7
70	564.3
80	604.7
90	647.6
100	680.9

Figure 4.3 shows scanning electron micrographs of thermally decomposed 5 mM chloroplatinic acid on FTO glass. Figure 4.3.a is conventionally thermally decomposed platinum which was heated for 30 min in an oven at 385°C. The NIR heated chloroplatinic acid (figure 4.3.b) was exposed to 12.5 s of 80% NIR lamp intensity radiation in which the FTO glass would have reached a maximum of 605°C.

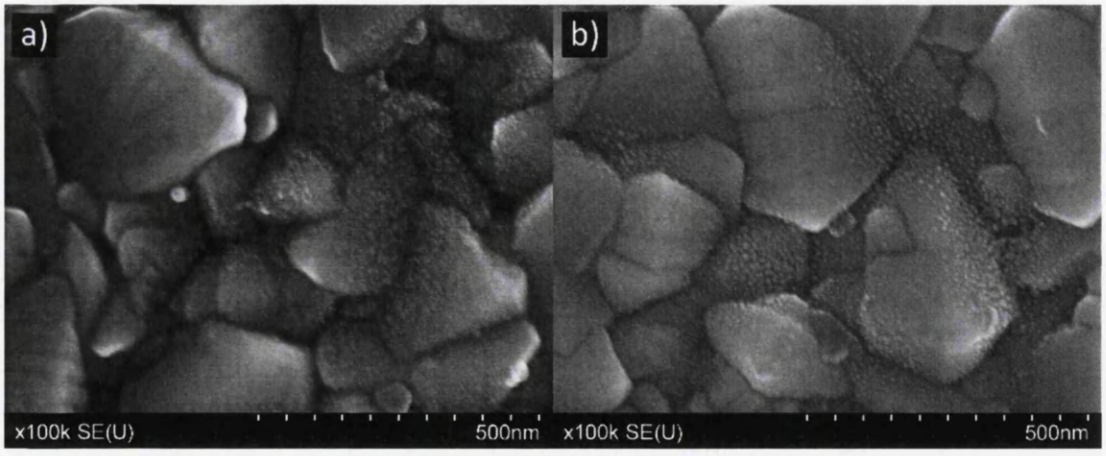

Figure 4.3: SEMs of (a) oven heated and (b) 80% NIR heated chloroplatinic acid on FTO glass at 100k magnification

Both thermal methods produced islands of nanosized platinum particles that are evenly distributed amongst the FTO grains. As is known in the literature [4] thermally decomposed

platinum does not coat in an even discernible layer but rather produces discrete clusters of platinum nanoparticles which still achieve excellent catalytic activity while only requiring small platinum loadings. The NIR heated chloroplatinic acid produced platinum particles very similar in type and size, clusters typically below 20 nm, as those produced by conventional thermal decomposition but in a timeframe 144 times quicker (12.5 s compared to 30 min). The NIR exposure of FTO glass caused it to heat significantly and this temperature was sufficient to induce the thermal degradation of the chloroplatinic acid. The NIR intensity used to expose the FTO glass in figure 4.3.b was 80% which has a predicted maximum temperature of 605°C (from section 3.3.2). This means the necessary temperature for $PtCl_2$ decomposition to Pt (375°C) was exceeded for likely the majority of the duration of the 12.5 s which enabled efficient and rapid decomposition. Figure 4.4 shows SEMs of 12.5 s NIR heated 5 mM chloroplatinic acid on FTO glass at different intensities of radiation.

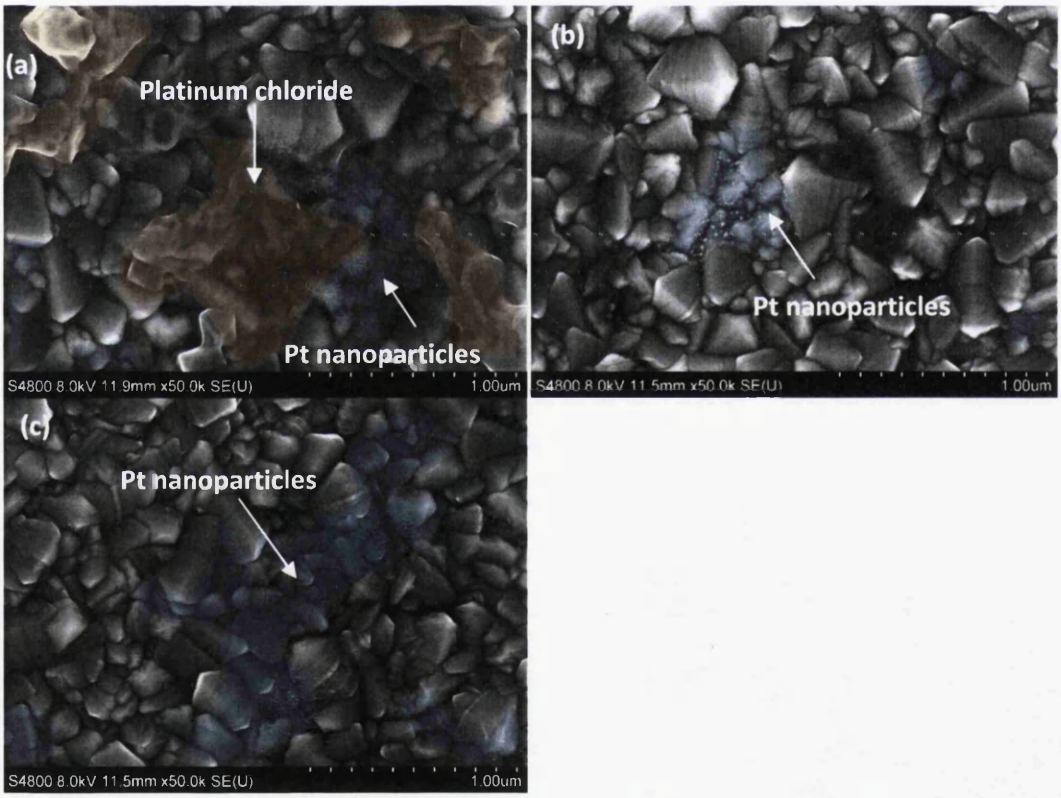

Figure 4.4: SEMs of 12.5 s exposed 5 mM chloroplatinic acid on FTO glass at lamp intensities of (a) 60%, (b) 70%, and (c) 80% with 50k magnification

Clusters of nanosized platinum particles are again present in each sample (highlighted in blue) but 80% NIR intensity (figure 4.4.c) appears more evenly distributed than 60% and 70% NIR intensity. The 60% NIR intensity sample (figure 4.4.a) has some areas of what appears to

be non-decomposed platinum chloride (highlighted in orange) and platinum nanoparticles which are quite isolated compared to 80% NIR and oven heating (figure 4.3.a). For 70% NIR intensity (figure 4.4.b) there does not appear to be any trace of residual platinum chloride and the areas of platinum nanoparticles are less isolated than in the 60% NIR sample but less numerous than the 80% NIR sample. To confirm the identity of the nanoparticles and the residual platinum chloride precursor EDX was used to obtain elemental analysis of the 60% and 80% NIR samples (figure 4.5).

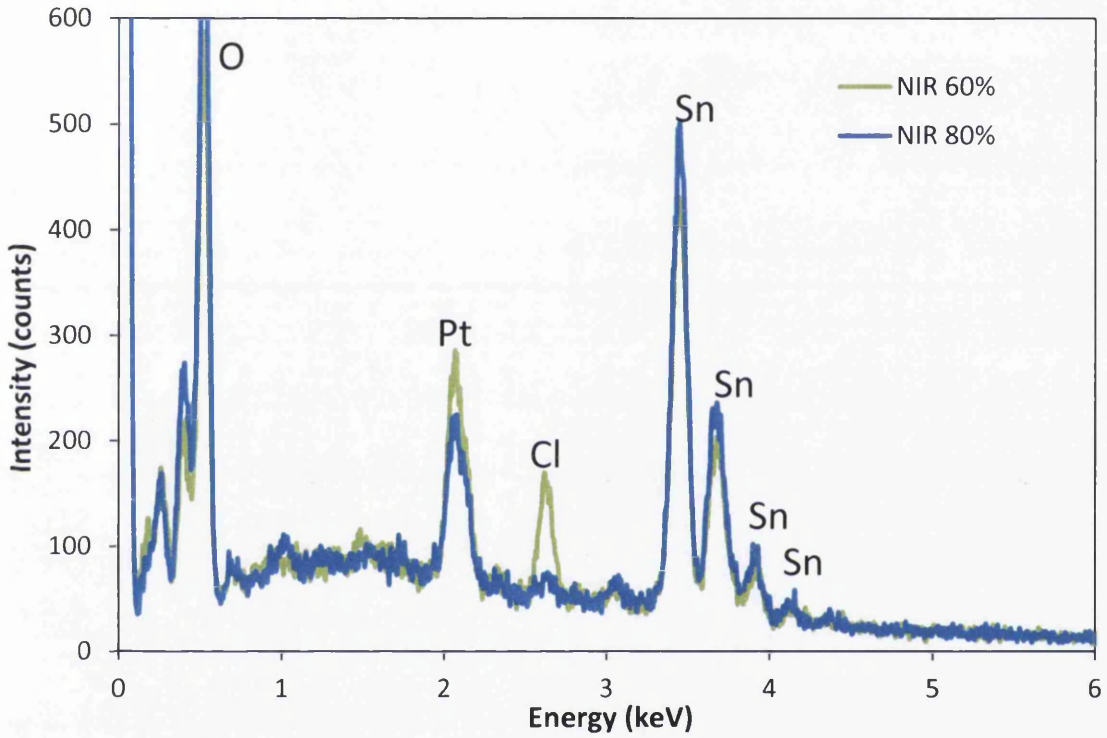

Figure 4.5: EDX analysis of 60% and 80% NIR intensity 12.5 s heated chloroplatinic acid on FTO glass

The EDX showed that the 80% NIR sample contains platinum with no chlorine present which further demonstrates that the platinum chloride was fully decomposed and suggest that because the platinum nanoparticles as seen in figure 4.3 appear similar to the conventional oven method they should behave with identical catalytic affinity in a DSC device. Some Cl^- was observed for the 60% NIR sample suggesting that the thermal energy it received was insufficient to achieve complete degradation of the Pt-Cl. From this technique it is not possible to identify which form each element is present in but it is established that the following reversible reactions involved in the conversion of chloroplatinic acid to platinum occur around these temperatures [6]:

125-220°C $(H_3O)_2PtCl_6.xH_2O \rightleftharpoons PtCl_4 + 2\,HCl + (x+2)\,H_2O$

300-375°C $PtCl_4 \rightleftharpoons PtCl_2 + Cl_2$

Above 375°C $PtCl_2 \rightleftharpoons Pt + Cl_2$

At temperatures above 300°C $PtCl_4$ converts to $PtCl_2$ and chlorine. According to the estimations in Chapter 3 the FTO glass reaches a temperature of about 488°C at 60% NIR lamp intensity upon exit from the lamp after 12.5 s exposure. Due to the warming of sample during heating and the lower temperature gradient it seems that the 60% NIR sample did not receive enough thermal energy to break all of the Pt-Cl bonds in 12.5 s of exposure. The $PtCl_2$ was most likely above the necessary temperature of 375°C for only a few seconds compared to the 80% NIR sample which is assumed to have been in excess of this for at least half the exposure duration. The incomplete conversion of platinum chloride to platinum reduces the potential amount of active platinum available on the surface of the FTO in turn limiting the counter electrode's ability to reduce triiodide in a DSC.

The electrochemical behaviour of NIR exposed chloroplatinic acid on FTO glass was investigated using cyclic voltammetry (section 2.7, theory discussed in section 1.5.4). In cyclic voltammetry the reversibility of the electrode is determined by its ability to follow the Nernstian equilibrium. The Nernst equation relates the reduction potential of a half cell at any point in time to standard conditions of the reactions and species used. For a reversible reaction the electrons transfer back and both according to the Nernst equation and diagnostic equations can be used to validate reversibility as described here [8]. To evaluate the performance of the platinum for use as a counter electrode in DSCs cyclic voltammetry was run in an I^-/I_3^- system giving an indication of its ability to facilitate the charge transfer reactions that occur between the species of:

$$2I_3^- \underset{+2e^-}{\overset{-2e^-}{\rightleftharpoons}} 3I_2$$

$$3I^- \underset{+2e^-}{\overset{-2e^-}{\rightleftharpoons}} I_3^-$$

The reaction of importance in a DSC is the cathodic reaction, $I_3^- + 2e^- \rightarrow 3I^-$ (the reduction of triiodide to iodide), which occurs at the counter electrode. It is necessary so that the electrolyte can be regenerated and continue to donate an electron to the oxidised dye ($2S^+ + 3I^- \rightarrow 2S + I_3^-$). If this reaction is sluggish, if the charge transfer reaction cannot be facilitated with sufficient speed, then the return of an electron to the sensitizer becomes a limiting step

in the device as there will be a depletion of I^- ions. A catalyst with an affinity to the I^-/I_3^- redox couple is required for this reaction as FTO alone is insufficient [9]. Because platinum is an extremely efficient catalyst for DSCs [4] it does not normally limit the DSC's performance but any suboptimal platinum here will manifest itself in the cell performance and reduce the fill factor. This will be shown in the cyclic voltammetry if the charge transfer is impaired by broader (because diffusion will be more dominant) less reversible peaks or no redox reactions will occur if there is no catalytic affinity. So the more reversible the reactions the more able the platinum is to facilitate the I^-/I_3^- redox reactions and therefore the more efficient it will be as a catalyst in a DSC. The electrolyte used for cyclic voltammetry was an I^-/I_3^- redox couple in acetonitrile, this differs to that used in subsequent DSC manufacture; it has a lower concentration to reduce the rate limiting diffusion so the redox peaks are more defined and a different solvent to be more compatible with the reference electrode which was Ag/Ag^+ in acetonitrile. In this system the reaction is quasi-reversible; it is slower in the reverse direction than the forward direction (insufficient to maintain Nernstian equilibrium) so it cannot perfectly match the reversible diagnostic criteria but it is not totally irreversible.

Figure 4.6 shows cyclic voltammograms of 12.5 s NIR exposed chloroplatinic acid on FTO glass at different lamp intensities with a conventionally heated thermally decomposed platinum on FTO glass (in an oven for 30 min at 385°C). The current has been normalised to the approximate submerged area of the working electrode and the charge transfer reactions are annotated on each peak. Table 4.2 shows the corresponding data extracted from the cyclic voltammograms to give an indication of the reversibility. These are the peak separation (ΔE_p) which is the distance between the anodic peak E^a_p ($3I^- \rightarrow I_3^- + 2e^-$) and the cathodic peak E^c_p ($I_3^- + 2e^- \rightarrow 3I^-$), and the ratio of the peak current densities ($|j^a_p/j^c_p|$) where j^a_p is the height of the anodic peak and j^c_p is the height of the cathodic peak [8]. These give an indication of the reversibility of the charge transfer reactions where a smaller ΔE_p shows a more reversible reaction and a ratio of 1 also shows reversibility. Each NIR sample is 12.5 s of exposure unless otherwise stated and the oven was 385°C.

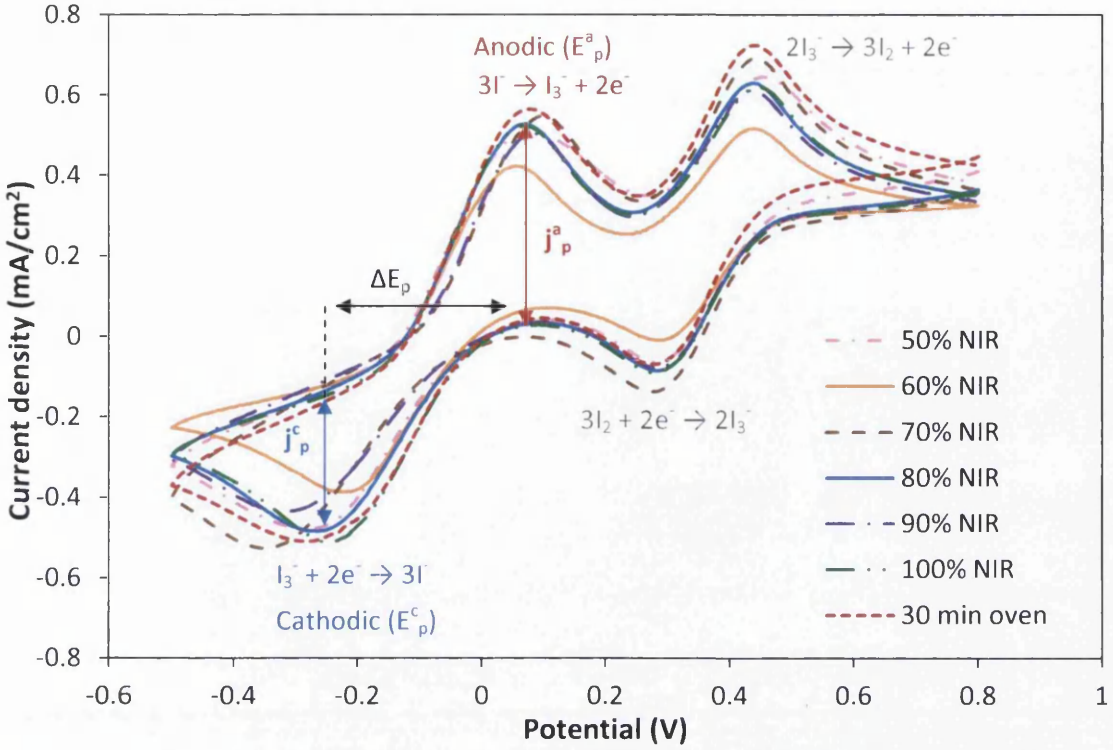

Figure 4.6: Cyclic voltammograms of 12.5 s NIR heated and oven heated (385°C, 30 min) chloroplatinic acid on FTO glass in iodide electrolyte at a scan rate of 50 mV/s

Table 4.2: Data from cyclic voltammetry for peak separation and peak current density ratio

Sample	ΔE_p (V)	j^c_p (mA/cm^2)	j^a_p (mA/cm^2)	j^a_p/j^c_p
50% NIR	0.35	-0.33	0.47	1.43
60% NIR	0.305	-0.27	0.38	1.40
70% NIR	0.445	-0.32	0.55	1.73
80% NIR	0.33	-0.34	0.50	1.46
90% NIR	0.39	-0.29	0.47	1.64
100% NIR	0.31	-0.37	0.50	1.35
50% NIR (25 s)	0.34	-0.41	0.58	1.42
30 min oven	0.35	-0.33	0.52	1.58
30 s oven	0.39	-0.22	0.35	1.58

Chloroplatinic acid exposed to 12.5 s of 50% intensity NIR shows marginally broader peaks than the other cyclic voltammograms suggesting that rate of diffusion of species towards the electrode surface was overcoming the electron transfer reactions. This is most likely indicative of less platinum nanoparticles present which would be expected as 50% NIR intensity would not receive as much thermal energy as other samples so less platinum chloride would convert to catalytic platinum. However it does have a comparable peak separation and current density ratio to the others suggesting the platinum present is still facilitating the electron transfer in both directions with sufficient quasi-reversibility. 60% NIR

intensity shows the closest peak separation, best peak current density ratio and has fairly sharp peaks with good reversibility suggesting that it would perform well to the reduction of triiodide in a DSC. This would seem to contradict figures 4.4.a and 4.5 somewhat that show the presence of chlorine as $PtCl_2$ but it may be that the platinum that is present is catalytic. It should also be noted that the peak current density is much lower for 60% NIR than the other samples perhaps suggesting there is less platinum present and supporting that some potential surface area of platinum is lost to residual platinum chloride. There is fairly similar catalytic activity for the 80% and 100% NIR and 30 min oven samples as shown by the similar peak separation and current density ratios. It was confirmed in figure 4.5 that 80% NIR exposed chloroplatinic acid had fully converted to platinum nanoparticles and in figure 4.3 that they look similar to oven heated chloroplatinic acid so the similarity of the reversibility of 30 min oven to platinum decomposed 144 times faster is extremely promising and suggests that the NIR heated platinum could perform equally well in DSC devices. Figure 4.7 shows different cycles for the same sample (10 cycles were run for each experiment), 80% NIR intensity, to show the drift in peaks.

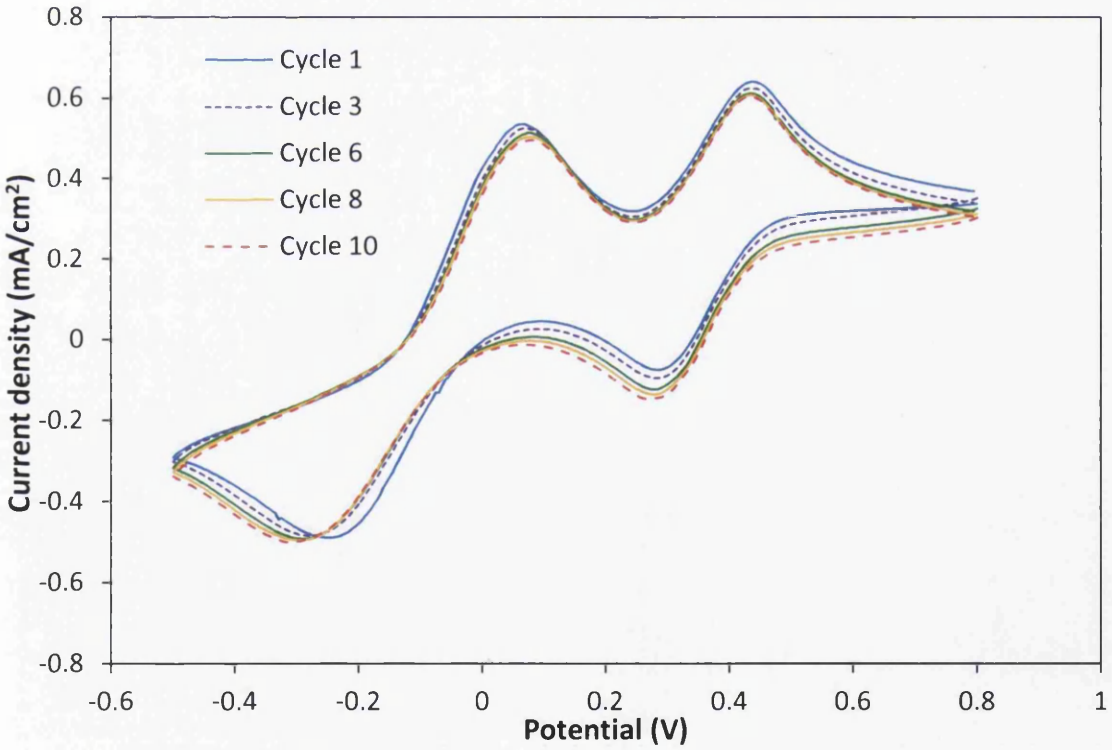

Figure 4.7: Different cycles for 80% NIR intensity heated platinum

The first cycle deviates the most from the norm as it the first time that the surface is exposed. It removes some fouling from the surface, such as oxygen that arises from heating

(both NIR and oven samples are heated in air) and has the closest peak separation [8]. There are some spikes in the first cycle around the cathodic peak which are due either to the refference electrode or fouling, the latter is more likely. It should be noted that the cyclic voltammograms plotted in figure 4.6 were derived from the second cycle. Upon cycling a diffusion layer is established and the concentration of the species at the electrode/electrolyte interface depletes, meaning kinetics can only be calculated on first cycle. So it was the lowest cycle possible to ensure what seeing is not a result of diffusion or concentration changes. As the cycling of the reactions stabilises the peaks stabilise and stop drifting. An additional test for the reversibility is to vary the scan rate which is shown in figure 4.8 for two oven heated and two NIR heated samples.

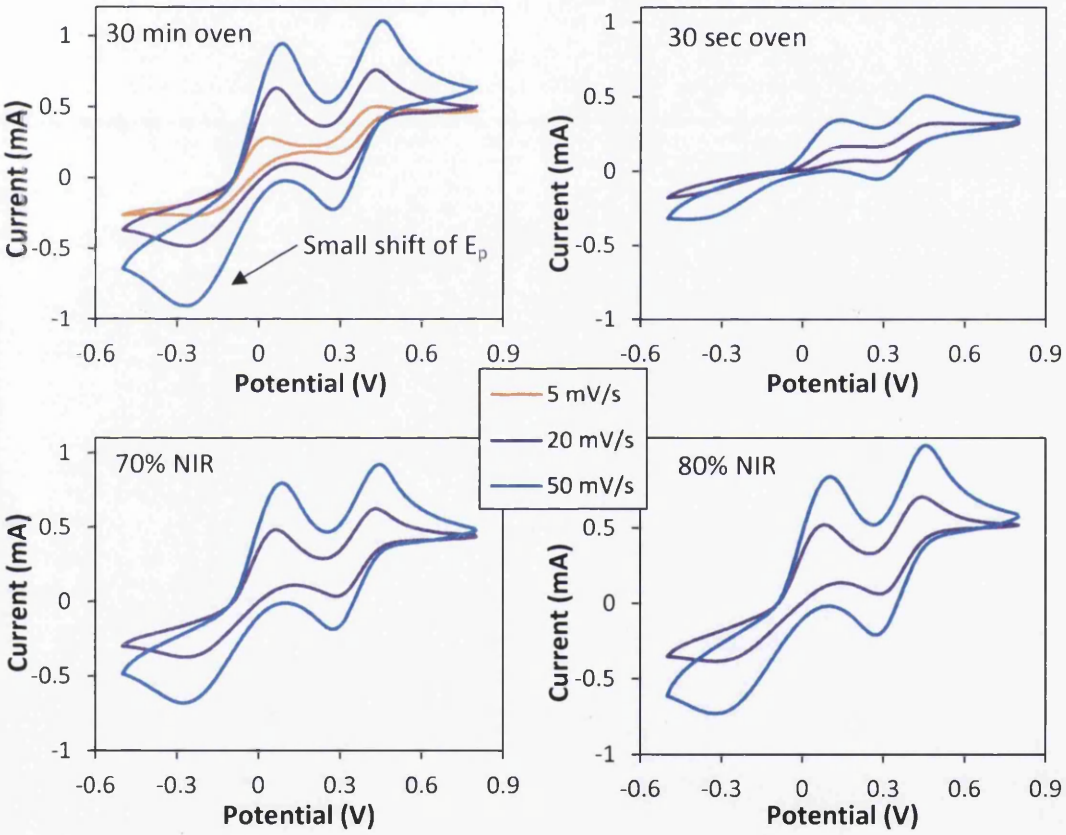

Figure 4.8: CVs of 30 min oven, 30 s oven, 70% NIR and 80% NIR measured at different scan rates

These are of different samples to the ones shown earlier and the current has not been normalised to area. There is a drift in peak cathodic and anodic potential for 30 min oven and 70% and 80% NIR which appears to be fairly consistent for each sample. If the reaction was truly reversible the peaks would stay in the same position regardless of scan rate. In this

system the peaks drift because the kinetics of the reaction can't keep up with increase in scan rate, to catch up the reactions happen across a wider potential so get a broadening of the peaks. The current and sharpness of the peaks increase at higher scan rates because there is less time for diffusion to take place. It should also be noted that 70% NIR has a very similar peak position to 80% NIR in figure 4.8 suggesting that there was some experimental inconsistency earlier. The 30 s oven sample shows an arguable cathodic peak at 50 mV/s scan rate but no peak at 20 mV/s because the electron transfer is not strong enough to fight off the diffusion that has more time to take place with a slower scan rate. Figure 4.9 shows cyclic voltammograms of oven heated chloroplatinic acid in lower timeframes as a direct comparison with bare FTO glass to illustrate that it has no catalytic affinity for the reduction of triiodide [9].

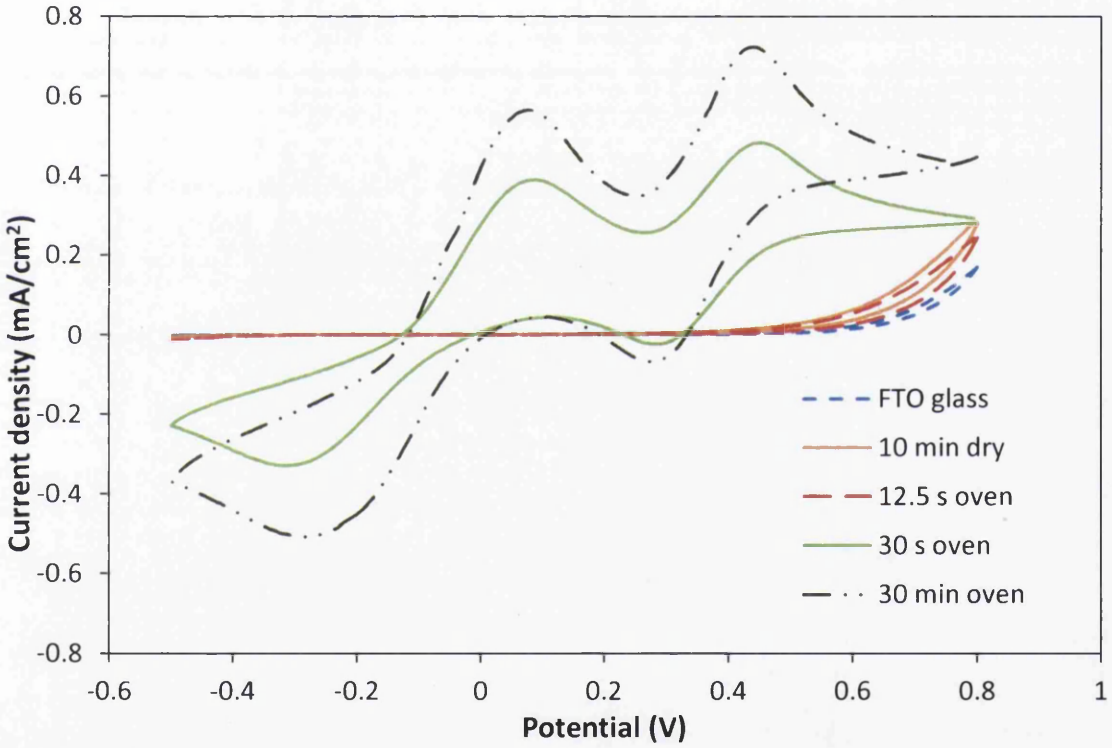

Figure 4.9: Cyclic voltammograms of oven heated chloroplatinic acid on FTO glass (at 385°C) with bare FTO glass and chloroplatinic acid that has been dried at 60°C for 10 min in iodide electrolyte at a scan rate of 50 mV/s

FTO glass shows no ability to facilitate the redox reactions in this electrolyte which is why a DSC requires a catalyst to function. 12.5 s of heating in an oven is insufficient to convert any platinum chloride to platinum because conventional heating is slow and relies on the entire substrate warming up which it would not have in this timeframe so it shows no catalytic

activity. A sample of chloroplatinic acid was dried in the oven to remove all IPA and test its catalytic activity to determine if any of the electron transfer reactions could be facilitated by platinum chloride alone and has shown that it is not catalytic in this system. 30 s of oven heating at 385°C does begin show catalytic activity, it shows both sets of redox peaks and has a fairly similar peak separation and peak current density ratio (Table 4.2) to other samples. Some platinum nanoparticles must be present to show any activity so between 12.5 and 30 s in an oven a small fraction of platinum chloride was converted to platinum. Finally figure 4.10 shows cyclic voltammograms of NIR heated chloroplatinic acid at the same intensity (50%) with different exposure times, 12.5 s and 25 s.

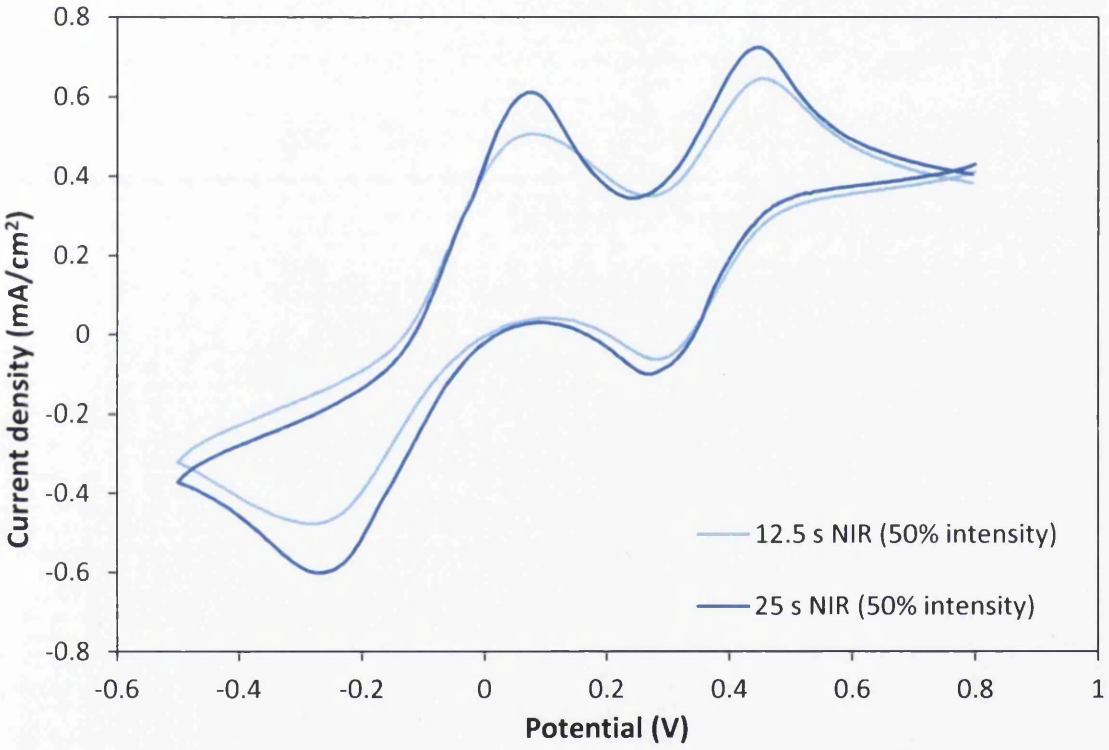

Figure 4.10: Cyclic voltammograms of 50% intensity NIR heated chloroplatinic acid on FTO glass exposed for 12.5 s and 25 s in iodide electrolyte at a scan rate of 50 mV/s

50% NIR intensity at 12.5 s exposure shows very broad peaks and small peak current values. This was attributed to an incomplete conversion of all platinum chloride to platinum nanoparticles because there was insufficient thermal energy in the 12.5 s. However with longer exposure, 25 s, at the same power the cyclic voltammograms suggests that all $PtCl_2$ has been converted to catalytic platinum and it has a smaller peak separation and better peak current density ratio. As was mentioned earlier from Table 4.2 it has the second best demonstration of reversibility for all platinum samples. If a DSC counter electrode can

achieve comparable catalytic activity to the 30 min oven conventional method in only 12.5 s this would be more desirable than 25 s timewise. However using 50% NIR intensity could save energy and it is interesting that all the platinum chloride bonds can be broken with this intensity, as was hypothesised that there was insufficient time at the given temperature to produce the thermal energy required in 12.5 s.

4.3.2 Dye-sensitised solar cells with a rapidly heated counter electrode

To test the performance of the fast processed counter electrodes, DSC devices were created and their photovoltaic characteristics compared to those made conventionally (30 minutes at 385°C). Table 4.3 shows the four key parameters related to photovoltaic performance; open circuit voltage (V_{OC}), short circuit current density (J_{SC}), fill factor (FF) and the efficiency (η).

Table 4.3: Average parameters for 3 cells with 1 standard deviation of error shown

NIR (%)	V_{OC} (V)	J_{SC} (mA/cm^2)	FF (%)	Efficiency (%)
60	0.74 ± 0.03	13.06 ± 0.24	50.05 ± 0.19	4.81 ± 0.10
70	0.75 ± 0.00	12.59 ± 0.78	54.63 ± 6.18	5.16 ± 0.27
80	0.76 ± 0.00	12.76 ± 0.51	65.17 ± 5.04	6.33 ± 0.38
90	0.75 ± 0.03	12.87 ± 0.23	63.97 ± 6.82	6.17 ± 0.80
Oven	0.77 ±0.01	13.08 ± 0.75	64.33 ± 2.03	6.48 ± 0.19

Each DSC device was constructed identically with only the heating method of the counter electrode varied and used a $TiCl_4$ treated 9 μm thick oven sintered working electrode with an active area of 1 cm^2. It is clear that the dominant factor affecting overall performance to be that of the fill factor. This is related to the catalytic performance of the counter electrode. The platinum facilitates the charge transfer reaction of the reduction of triiodide to iodide ($I_3^- + 2e^- \rightarrow 3I^-$); if there are insufficient catalytic platinum nanoparticles present then this reaction is sluggish. This would cause a depletion of iodide ions that are necessary to donate an electron to the oxidised dye sensitizer ($2S^+ + 3I^- \rightarrow 2S + I_3^-$) which consequently limits the absorption of photons by the dye. Figure 4.11 shows IV curves of the NIR and oven heated counter electrode DSCs demonstrating this rise in fill factor with higher NIR intensities through the improving shape of the IV curves (as discussed in section 1.5.1) where the I_{SC} and V_{OC} does not vary significantly.

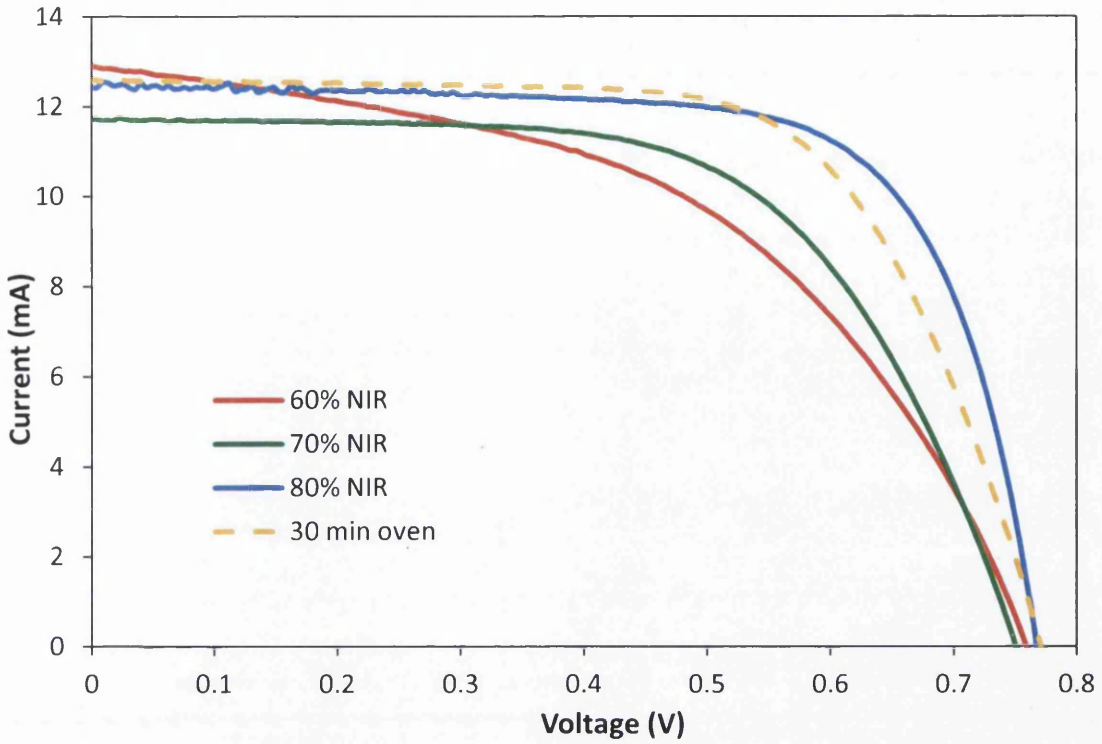

Figure 4.11: Typical IV curves of 12.5 s NIR exposed and 30 min 385°C oven heated counter electrode DSCs demonstrating the variation in fill factor but similar I_{SC} and V_{OC}

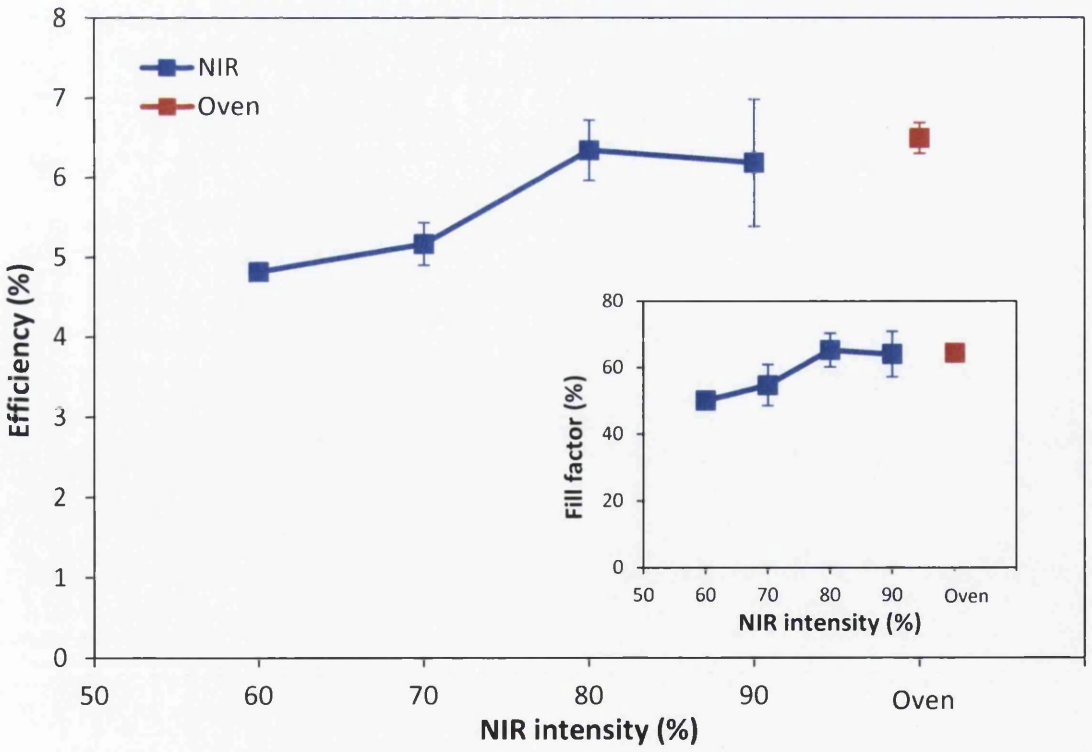

Figure 4.12: Average efficiency against NIR lamp intensity for 12.5 s heated counter electrode DSCs with an oven DSC for comparison; inset the same for average fill factor

Figure 4.12 shows the average efficiency and fill factor of the 12.5 s heated NIR counter electrode devices against NIR lamp intensity with a conventional 30 min oven heated device. The trend for average efficiency and fill factor is identical. For the 12.5 s NIR heated counter electrode devices the efficiency and fill factor increases up to 80% NIR intensity and is slightly lower for 90%. Although 60% NIR intensity showed good catalytic affinity for the reduction of triiodide as indicated by cyclic voltammetry in iodide electrolyte (showing the smallest peak separation and best peak current density ratio), it does not have a large surface area of platinum nanoparticles due to incomplete conversion of platinum chloride to platinum as shown by EDX and SEM. This limits the platinum available for triiodide reduction and thus the fill factor. As mentioned previously the incomplete conversion to platinum chloride is due to insufficient thermal energy received during the 12.5 s timeframe as the maximum temperature reached by FTO glass of 488°C would not have sustained a temperature above 375°C (the ideal temperature for $PtCl_2$ decomposition) for long enough. The average V_{OC} value for these devices increases from around 0.73 V at 60% NIR power to around 0.75 V at 70% NIR power and around 0.76 V at 80% NIR power. The lower V_{OC} values are likely due to incomplete H_2PtCl_6 decomposition so that some catalytically inactive Pt-Cl still remains on the counter electrode substrate. 80% NIR intensity shows the highest average efficiency and fill factor for the NIR heated counter electrode devices. It has a similar efficiency, fill factor and V_{OC} to the conventional oven DSC devices. This supports the cyclic voltammetry data well which showed a similar level of reversibility for both NIR and oven heated platinum, and SEM images which showed platinum nanoparticles almost identical in size and performance. The ability to produce a counter electrode in 12.5 s of equal performance to the conventional method is extremely useful as a time saving step for the manufacture of DSCs.

Figure 4.13 shows the average efficiency of 12.5 s NIR and 30 min oven heated counter electrode devices against temperature (estimated from Chapter 3 in the case of NIR). This gives an idea of the maximum temperature required to achieve sufficient thermal energy for such a rapid platinum chloride conversion to catalytic platinum. It also shows the wide processing window for the maximum temperature where, although suboptimal, similar efficiencies were obtained.

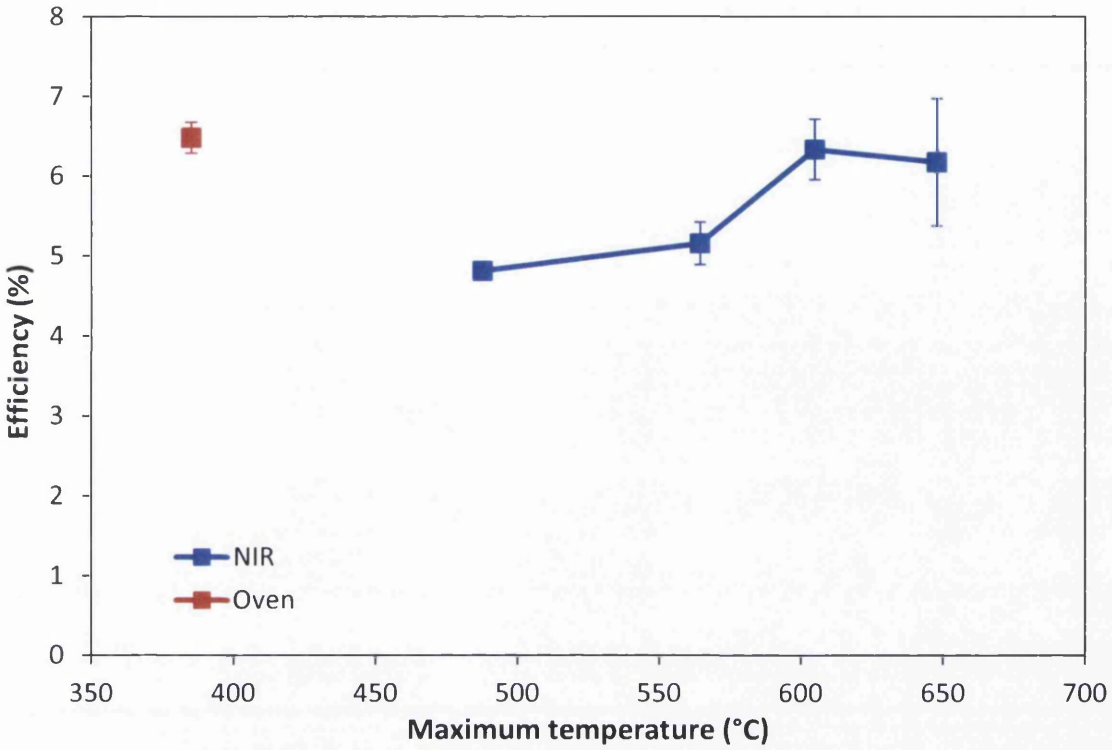

Figure 4.13: Average efficiency vs. temperature for oven and NIR heated counter electrode DSCs

12.5 seconds was chosen as an exposure time under the NIR lamp as this represents a target process line speed of 2m/min. However in addition to NIR heating counter electrodes for 12.5 s a slower line speed, 1 m/min resulting in an exposure time of 25 s, was used to construct DSC devices to investigate if a longer exposure time could utilise lower power intensities to save energy as indicated by the cyclic voltammetry of a 25 s NIR sample which showed good catalytic activitiy. Table 4.4 shows the average PV parameters for 50% and 60% NIR counter electrode devices that were exposed for 25 s rather than 12.5 s.

Table 4.4: Average parameters for 3 cells with 1 standard deviation of error shown for additional NIR settings and shorter oven heating times

Heating	Time	V_{OC} (V)	J_{SC} (mA/cm^2)	FF (%)	Efficiency (%)
NIR (50%)	25 s	0.76 ± 0.01	12.30 ± 0.37	55.39 ± 5.59	5.14 ± 0.30
NIR (60%)	25 s	0.73 ± 0.06	10.50 ± 3.62	55.46 ± 3.00	4.13 ± 0.89
Oven (385°C)	12.5 s	0.70 ± 0.09	3.73 ± 0.77	9.93 ± 4.86	0.26 ± 0.15
Oven (385°C)	25 s	0.72 ± 0.02	6.72 ± 3.32	13.18 ± 9.08	0.76 ± 0.77
Oven (385°C)	30 min	0.77 ±0.01	13.08 ± 0.75	64.33 ± 2.03	6.48 ± 0.19

50% NIR exposure (25 s) shows a similar efficiency and fill factor to 70% NIR exposure (12.5 s). Cyclic voltammetry in section 4.3.1 also showed that it had good catalytic activity with a

small peak separation and good peak current density ratio compared to the same NIR intensity exposed for only 12.5 s owing to the increased time available for the complete thermal decomposition of platinum chloride to platinum. The 60% NIR (25 s) cells had a poorer performance, it is believed this may be because they were too hot; it was observed that some of the FTO glass counter electrodes produced cracked during heating. Lower intensities at 25 s exposure could be investigated in the future to determine if less energy could be used. In terms of saving time further, shorter NIR exposure times (faster speeds), were not tried because 80% NIR intensity is close to the maximum power so a slightly faster speed and 100% NIR intensity would likely yield an equivalent result and the speed used here, 2 m/min, corresponded well to desired line speed. The speed and lamp intensity of NIR radiation used here would only be suitable for the same model and specifications of NIR radiating equipment but it shows that any NIR equipment can yield similar results with most likely a range of balancing speed and intensity settings with a wide possible temperature range suitable as shown in figure 4.13.

As a direct comparison DSC devices were also constructed for oven heated counter electrodes at 385°C for times equivalent to the two NIR heating times; 12.5 s and 25 s (see Table 4.4). As is expected 12.5 s and 25 s is not long enough to produce any platinum with conventional heating and the cell has no fill factor. The slightly longer heating for the 25 s oven produced an improvement in efficiency which is supported by the appearance of the two pairs of redox peaks from cyclic voltammetry in section 4.3.1 (figure 4.9) but the reaction is completely irreversibility as shown by the high peak current density ratio.
In DSC devices it is essential that the counter electrode must be catalytically active in order to ensure rapid reduction of the I_3^- ions. Platinum is a suitable catalyst as triiodide ions dissociate to iodine atoms upon adsorption, enabling a rapid one-electron reduction. The resistance of this charge transfer process can be analysed using impedance spectroscopy and so can serve as a measure of catalytic performance. A poor counter electrode will affect the current-voltage characteristics of the DSC by lowering the fill factor [10].

Electrochemical impedance spectroscopy (EIS) was performed on the NIR (12.5 s) and oven heated counter electrode DSC devices. Figure 4.14 shows a Nyquist plot for these cells illustrating the extraction of the charge transfer resistance (R_{CE}) and figure 4.15 shows R_{CE} vs. measuring bias for the different DSC devices.

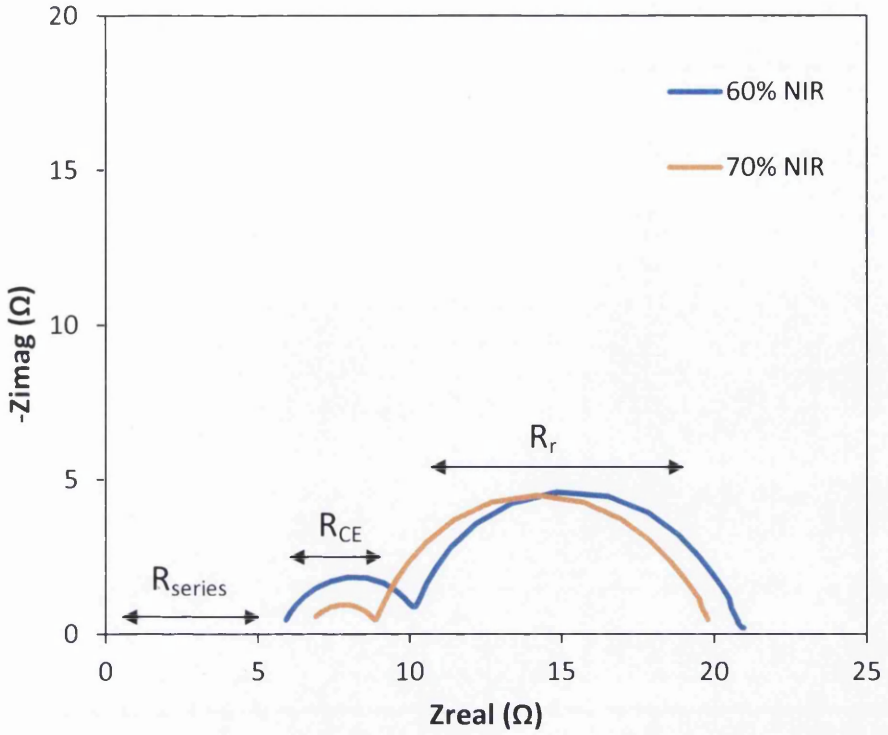

Figure 4.14: Typical Nyquist plot at -720 mV for NIR heated counter electrode DSCs showing the variation in R_{CE} with increased NIR intensity heating but the similar R_r (resistance at TiO_2/electrolyte interface) as the working electrodes were prepared identically

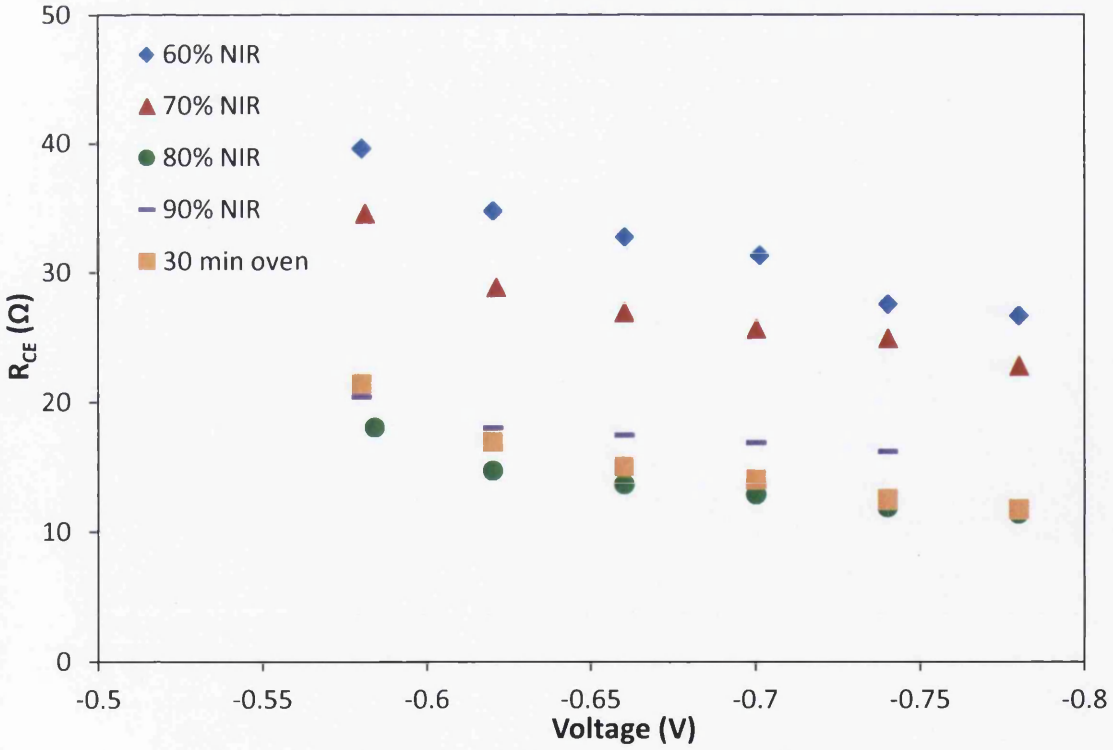

Figure 4.15: Charge transfer resistance against measuring potential obtained from impedance spectroscopy of NIR and oven heated counter electrode DSCs

The charge transfer resistance (R_{CE}) is the resistance between the catalyst and the electrolyte, the resistance to platinum reducing the triiodide. The charge transfer resistance influences the fill factor of a DSC and should ideally be ≤ 10 Ωcm^2 [11]. The general trend in figure 4.15 is that the R_{CE} increases with decreasing NIR intensity. It is similar for both 80% and 90% NIR and the conventional oven device. Between these three the 80% device marginally has the lowest R_{CE} with the 90% device slightly higher than the oven device. The trend for R_{CE} matches that for the previous trends in both current density from cyclic voltammetry measurements and the fill factor from the IV curve. Greater resistance in the exchange rate may be caused by inactive $PtCl_2$ which was shown to be present from EDX for the 60% NIR sample (section 4.3.1). In this instance, the increased charge transfer resistances of counter electrodes heated at lower power settings indicates that H_2PtCl_6 decomposition is not as effective as conventional thermal decomposition which fits with observations made during EDX analysis on samples and with the device fill factor of assembled DSCs.

4.4 Conclusions

NIR radiation was used to thermally decompose chloroplatinic acid to catalytic platinum on FTO glass for use as a counter electrode in a DSC device in only 12.5 s of heating time, 144 times faster than the conventional lab method. With 80% NIR intensity the DSC devices performed equally to conventionally platinised DSCs which normally require 30 min of heating in an oven at 385°C. This is the first example of a rapidly heated counter electrode for a DSC device and demonstrates the possibility of being able to drastically reduce the time required for one of the most limiting stages in DSC manufacture. 12.5 s of NIR exposure with adequate lamp intensity was capable of providing sufficient thermal energy to cleave all platinum chloride bonds and produce catalytically active nanoparticles of platinum of identical size and nature to conventional thermal platinisation.

Adequately performing DSCs from counter electrodes exposed to lower intensities of NIR radiation in 12.5 s were also produced. Even at 60% NIR intensity, which had $PtCl_2$ remaining, was incorporated into a working DSC device with suboptimum fill factor and slightly impaired V_{OC} but still reasonable performance. This is very promising as it demonstrates a possible wide temperature processing window with NIR to still obtain sufficient performance, reducing the risk of wastage (due to non tolerable low performance) if there were slight variations in the power output of NIR lamps on an industrial scale.

This is also the first application of using NIR radiation to heat FTO glass (which was investigated in the previous chapter) and confirms that FTO glass can indeed reach significantly high temperatures extremely rapidly as metallic substrates have previously been shown to. It suggests that similar heating stages should also be possible by exposing FTO glass to NIR radiation; this will be explored further in Chapter 5.

4.5 References

[1] B. O'Regan, M. Grätzel, A low-cost, high-efficiency solar cell based on dye-sensitized colloidal TiO_2 films, Nature. 353 (1991) 737–740.

[2] M.K. Nazeeruddin, P. Péchy, T. Renouard, S.M. Zakeeruddin, R. Humphry-Baker, P. Comte, et al., Engineering of Efficient Panchromatic Sensitizers for Nanocrystalline TiO_2-based Solar Cells, J. Am. Chem. Soc. 123 (2001) 1613–24.

[3] A. Yella, H.-W. Lee, H.N. Tsao, C. Yi, A.K. Chandiran, M.K. Nazeeruddin, et al., Porphyrin-sensitized solar cells with cobalt (II/III)-based redox electrolyte exceed 12 percent efficiency, Science (80-.). 334 (2011) 629–34.

[4] N. Papageorgiou, W. Maier, M. Grätzel, An Iodine/Triiodide Reduction Electrocatalyst for Aqueous and Organic Media, J. Electrochem. Soc. 144 (1997) 876–884.

[5] A. Hauch, A. Georg, Diffusion in the electrolyte and charge-transfer reaction at the platinum electrode in dye-sensitized solar cells, Electrochim. Acta. 46 (2001) 3457–3466.

[6] A. Schweizer, G. Kerr, Thermal Decomposition of Hexachloroplatinic Acid, Inorg. Chem. 17 (1978) 8–9.

[7] T. Watson, I. Mabbett, H. Wang, L. Peter, D. Worsley, Ultrafast near infrared sintering of TiO_2 layers on metal substrates for dye-sensitized solar cells, Prog. Photovoltaics Res. Appl. 19 (2010) 482–486.

[8] A. Bard, L. Faulkner, Electrochemical Methods: Fundamentals and Applications, 2nd ed., John Wiley & Sons, 2001.

[9] K. Suzuki, M. Yamaguchi, M. Kumagai, S. Yanagida, Application of Carbon Nanotubes to Counter Electrodes of Dye-sensitized Solar Cells, Chem. Lett. 32 (2003) 28–29.

[10] A. Hagfeldt, G. Boschloo, L. Sun, L. Kloo, H. Pettersson, Dye-sensitized Solar Cells, Chem. Rev. 110 (2010) 6595–6663.

[11] A. Haunch, R. Kern, Second World Conference and Exhibition on Photovoltaic Solar Energy Conversion, in: Vienna, Austria, 1998.

5. Rapid Sintering of TiO_2 Films on FTO glass for Dye-sensitised Solar Cells using Near Infrared Radiation

5.1 Introduction

As discussed previously (section 1.2) a DSC consists of a dyed TiO_2 working electrode, a platinised counter electrode and a liquid iodide/triiodide electrolyte to facilitate regeneration of the dye's electrons. To function as a working electrode the titanium dioxide film of a DSC needs to have a high surface area and mesoporosity; this is to attain as much dye monolayer coverage as possible and allow the electrolyte to penetrate through the TiO_2 (see section 1.2.3.1). To achieve this a colloid of nanoparticles is used as the source of TiO_2 which was major breakthrough in the development of a DSC [1]. Anatase crystals are more desirable than the rutile phase of TiO_2 due to their smaller size. Most commonly they are incorporated into a slurry or paste and deposited by doctor blading, screen printing or other coating methods. The nanoparticles require a means of separation to prevent aggregation (as this would result in effectively larger particles reducing the potential surface area); steric stabilisation and electrostatic stabilisation are two such methods. The former is a more common method, an organic binder is added to the paste such as ethyl cellulose or polyethylene glycol which both helps prevents the particles from aggregating together and binds the colloid together to enable easy deposition.

To obtain a mesoporous layer from the nanoparticle containing TiO_2 paste heating is required which performs two functions; (1) to remove the binder and (2) to sinter the TiO_2 particles together. The binder needs to be removed so that the TiO_2 particles and pores can be exposed to maximise the available surface area for dye adsorption. The TiO_2 particles also require good interconnectivity so that electrons can be transported through them to the transparent conducting oxide (TCO) layer where they are extracted. Sintering involves fusing the particles as atoms on the surface diffuse together from pressure or heat, and occurs at a higher rate with increasing temperatures. The optimum temperature for sintering of TiO_2 has been found to be 450-500°C [2]. Lower temperatures may not remove the binder and decrease the rate of diffusion but higher temperatures may drive the diffusion too strongly resulting in smaller pores and thus lower surface area. At a temperature of over 610°C the anatase phase is thermodynamically unstable so transformation to rutile may begin to occur but it is more dominant at temperatures between 700 and 1000°C [3].

Currently the laboratory method for the manufacture of a dye-sensitised solar cell (DSC) (outlined in section 2.2) involves two major heating stages; thermal decomposition of platinum for the counter electrode and sintering of titanium dioxide for the photoelectrode. The traditional method for creating the working electrode of a DSC is to heat a binder containing TiO_2 paste in a conventional oven at a temperature of 450-500°C for 30 minutes which is a long time consuming process. This not very feasible on an industrial scale, especially in a roll-to-roll process where the substrate will move at speed through the system, both in terms of time and floor space. A faster process is required such as near infrared (NIR) radiative heating (section 1.4.2). This involves high energy density NIR radiation penetrating through the coating and being absorbed by the substrate which consequently heats up and rapidly heats the coating above it. NIR heating has been previously demonstrated to sinter TiO_2 working electrodes on metallic substrates [4][5] but this work will concern fluorine-doped tin oxide (FTO) coated glass as a substrate.

In Chapter 3 of this work it was shown that FTO glass absorbs in the NIR region due to the high concentration of free carriers in FTO. The plasma frequency of FTO (the frequency at which its behaviour switches from a dielectric to a metal) is in the NIR region so it is transparent in the visible but absorbs and reflects in the NIR and IR. Consequently it heats significantly upon exposure to NIR radiation compared to uncoated glass. In Chapter 4 platinisation of an FTO glass counter electrode was addressed using NIR radiative heating to reduce the heating process dramatically from 30 minutes to 12.5 s (a time reduction of 144 times) while still fabricating a DSC device of equal performance to an oven heated one. A similar ambition is proposed here for the working electrode. The main challenge is if the FTO glass can reach a temperature high enough to both remove all the binder from the TiO_2 paste and fuse the TiO_2 particles together in such a short timeframe (12.5 s).

5.2 Experimental

Titanium dioxide films were prepared by doctor blading commercially available pastes onto 7.5 Ω/□ FTO glass (TEC 8, NSG Pilkington) and heated in a conventional oven or by NIR radiation (section 2.1.1). A UV/Vis/NIR spectrophotometer (section 2.8) was used to measure the absorbance and reflectance of the pastes. The efficacy of the binder removal was investigated by thermogravimetric analysis (TGA) (section 2.10) and Fourier Transform IR spectroscopy (FTIR-ATR) (section 2.9) to ascertain which paste would be suitable for a working electrode. X-ray diffraction (XRD) (section 2.12) and scanning electron microscopy

(SEM) (section 2.7) was used to analyse the structure and appearance of the NIR heated films to observe the crystal sizes and surface porosity.

To determine the interconnectivity of the NIR heated TiO_2 particles working electrodes were assembled into DSC devices (figure 5.1) (section 2.2.2) and their photovoltaic properties characterised using IV measurements (section 2.3) and optoelectronic transient measurements (section 2.5) to obtain data such as electron lifetime which will give information about the electron transport through the TiO_2 film to compare against conventional heating.

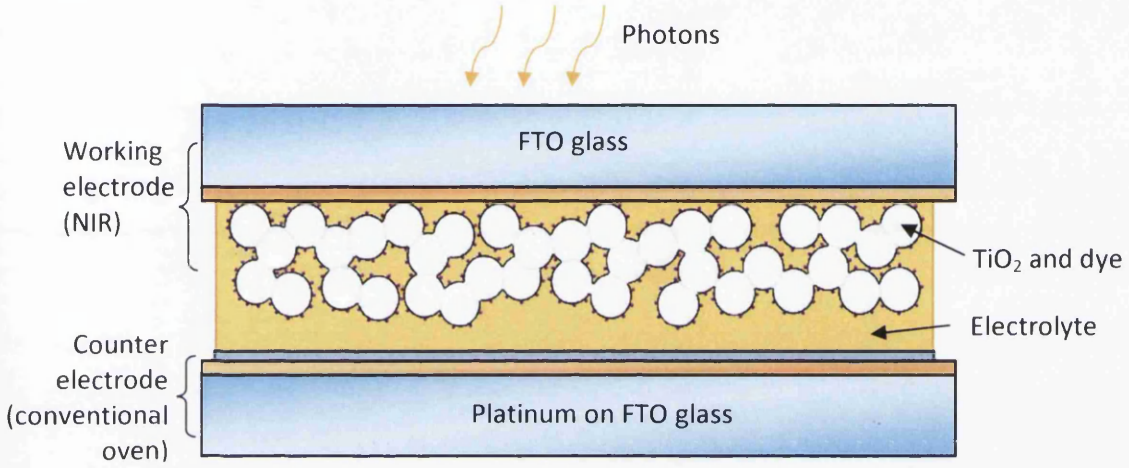

Figure 5.1: Diagram of DSCs constructed in this work with heating method shown in brackets

5.3 Results and discussion

5.3.1 Investigation of binder removal for NIR heated TiO_2 pastes on FTO glass

As established in Chapter 3 FTO glass absorbs in the NIR region; greatly enhanced by the 600 nm FTO layer compared to the glass alone. Commercial TiO_2 pastes were doctor bladed (at one tape height) onto FTO glass (figure 5.2) and their absorbance measured using a UV/Vis/NIR spectrophotometer (figure 5.3). This was to determine if the pastes had any additional absorbance in the NIR region which would affect the temperature reached upon NIR radiation exposure.

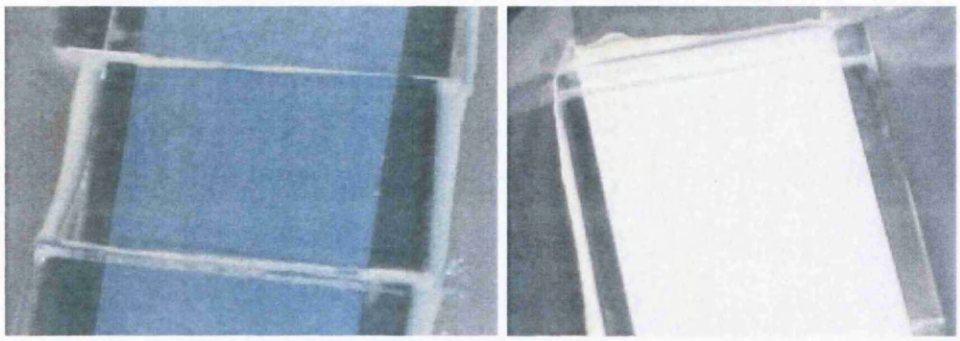

Figure 5.2: Appearance of doctor bladed wet films of DSL 18NR-T (left) and DSL 18NR-AO (right)

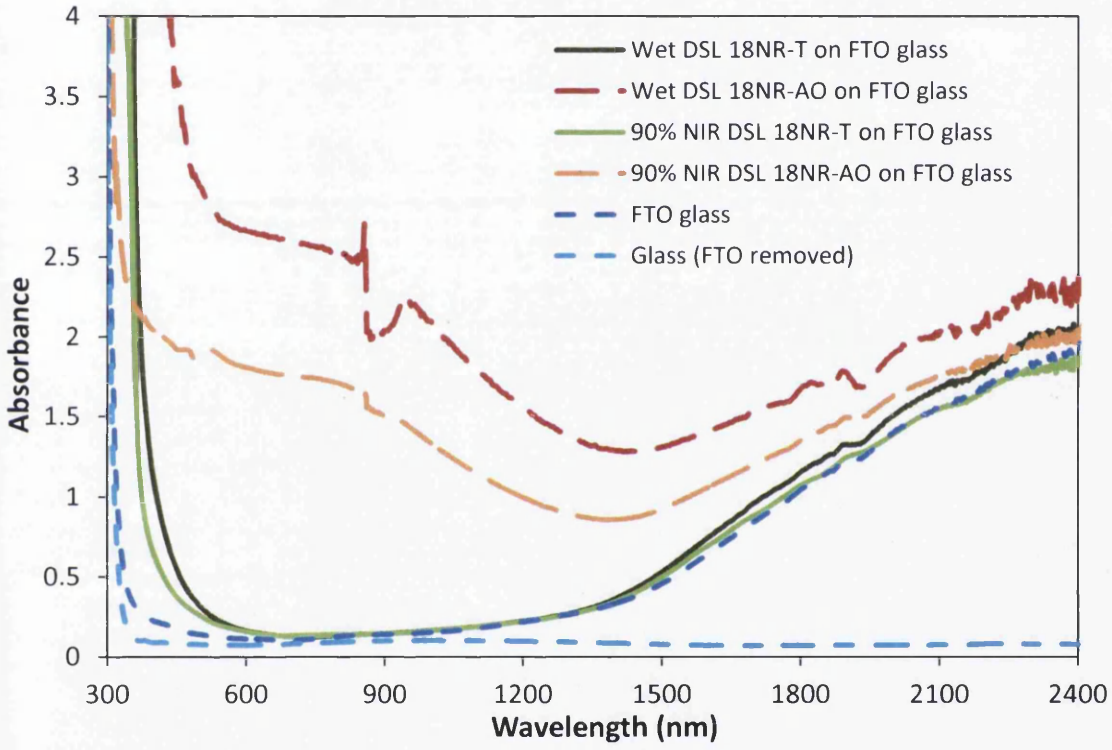

Figure 5.3: Absorbance vs. wavelength for commercial TiO_2 pastes on FTO glass alongside uncoated FTO glass and glass with FTO removed

The transparent paste (Dyesol 18NR-T) produces a dry film about 7-8 µm thick and the opaque paste (Dyesol 18NR-AO) produces a dry film about 9-10 µm thick; they contain the same solvent, binder and anatase TiO_2 particles of 20 nm in size. The opaque paste also contains larger particles of about 200 nm in size to induce scattering. As expected the pastes absorb very strongly in the UV region due to the presence of TiO_2 which in its anatase form has a band gap of 3.2 eV. They also absorb in the visible region, wet DSL 18NR-T appears clear yellow when deposited and wet DSL 18NR-AO appears white (figure 5.2). The wet DSL 18NR-T paste does not absorb much compared to FTO glass between 600 and 1400 nm so is

essentially transparent in this region. Above 1500 nm the absorption is enhanced slightly which is still within the range of IR radiation emitted by the NIR equipment but beyond the peak range. Also shown is a sintered DSL 18NR-T film (one exposed to 12.5 s of 90% NIR intensity radiation) which is more transparent owing to the absence of the binder and solvents. The wet DSL 18NR-AO paste absorbs significantly more radiation than the transparent paste as expected by its opaque appearance. This continues into the NIR and IR region, it is extremely enhanced compared to FTO glass between 600 and 1500 nm which includes the peak irradiance range of the NIR emitter. The sintered DSL 18NR-AO film (12.5 s of 90% NIR intensity radiation) still absorbs significantly across the spectrum compared to FTO glass but is again more transparent due to the removal of the solvent and binder. Figure 5.4 shows the reflectance of the same pastes doctor bladed onto FTO glass.

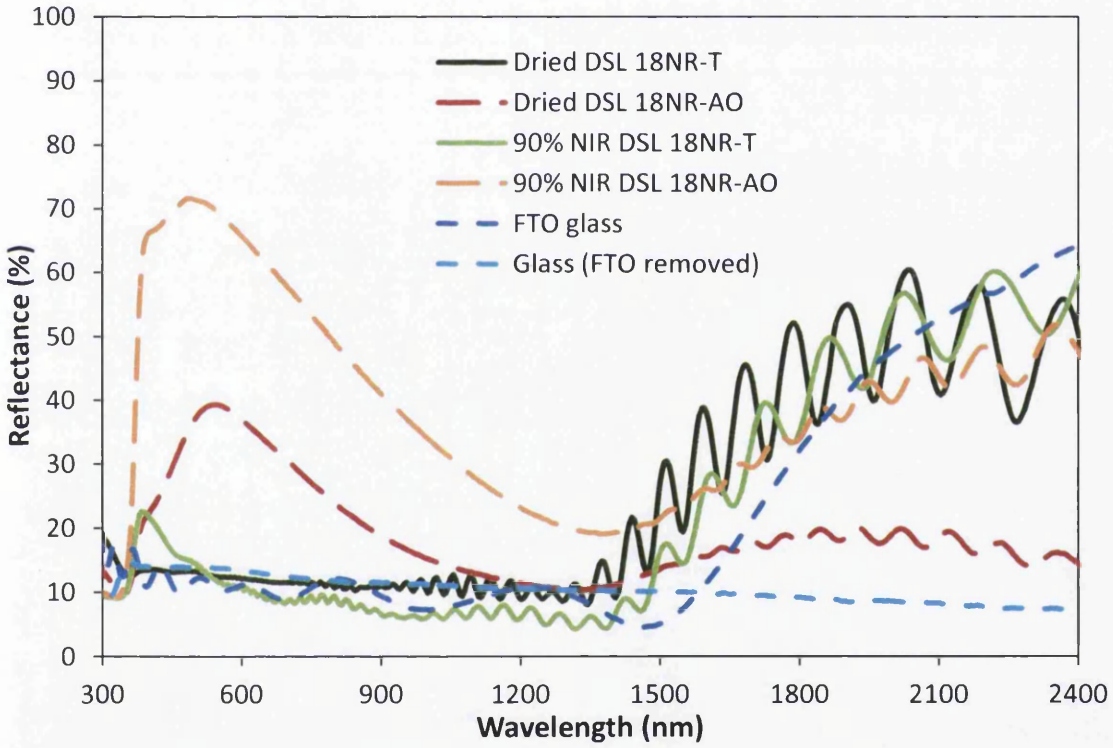

Figure 5.4: Reflectance vs. wavelength for commercial TiO_2 pastes on FTO glass alongside uncoated FTO glass and glass with FTO removed

Reflectance is shown for dried paste films (heated for 10 min at 100°C) rather than wet films because it was not possible to measure wet films in the instrument. The dried DSL 18NR-T on FTO glass has similar reflectance to FTO glass with slightly higher reflectance between 1400 and 1900 nm. This extra reflectance in a region where the NIR equipment emits (albeit not the most strongly) may reduce the temperature the FTO glass will reach upon exposure

to NIR radiation (compared to what was predicted in Chapter 3) by blocking a small proportion of it but the effect is unlikely to be significant. The sintered DSL 18NR-T on FTO glass (12.5 s of 90% NIR intensity radiation) has a lower reflectance overall than the dried paste because it no longer contains any solvent or binder and is more transparent.

Both the dried and the sintered (12.5 s of 90% NIR intensity radiation) DSL 18NR-AO on FTO glass reflect in the visible region; the sintered TiO_2 to a greater extent because it is fairly opaque and contains larger 200 nm sized TiO_2 scattering particles which are more exposed after the removal of all of the solvent and binder. After 1650 nm the dried DSL 18NR-AO reflects less than the FTO glass which should allow most radiation from this region to pass through to the FTO and reach a similar temperature to that predicted in Chapter 3. After sintering the reflectance in this region is higher and similar to FTO glass.

Three different commercial pastes were investigated as potential candidates for an NIR heated TiO_2 film on FTO glass; DSL 18NR-T, DSL 18NR-AO and Solaronix Ti-D. TGA was performed on each wet paste to show at which temperatures weight loss occurs and relate this to a component of the paste (figure 5.5). In the case of both DSL 18NR-T and DSL 18NR-AO the solvent is terpineol and the binder is ethyl cellulose [6][7]. As such the TGA profiles are fairly similar, the difference between the pastes is the TiO_2 content; the transparent paste contains only particles of 20 nm anatase whereas the opaque paste contains some larger anatase particles in addition to the nanoparticles which scatter light and are about 200 nm in size. For the Solaronix Ti-D paste [8] the solvent is water and ethanol so is removed by about 150°C. Solaronix have not disclosed what their binder is, it is assumed to be polyethylene glycol. It has a lower TiO_2 content than the other two pastes, which consists of nanoparticles (15-20 nm) and scattering particles (>100 nm). It is an opaque paste like DSL 18NR-AO so should absorb and reflect similarly but to a lesser extent because it is a thinner film when doctor bladed with the same tape height. The weight % of each component as calculated from the TGA profiles is shown in Table 5.1 along with the dry film thickness for each paste.

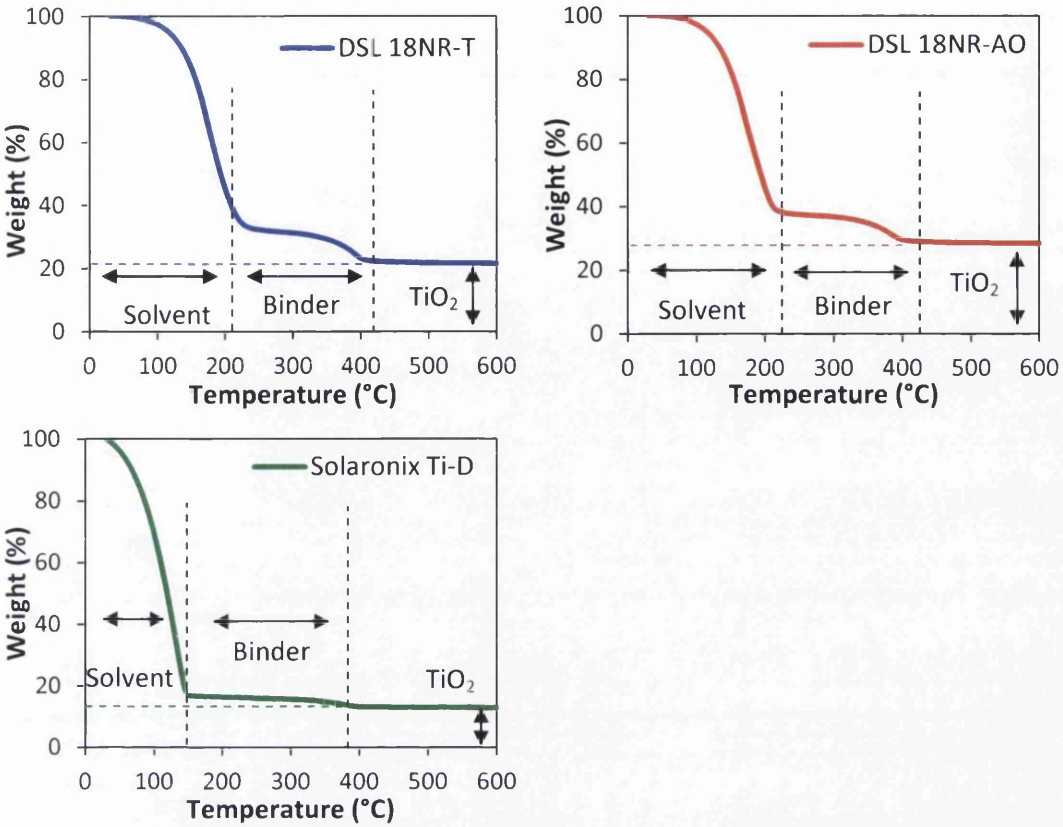

Figure 5.5: Weight % vs. temperature obtained from TGA for unheated DSL 18NR-T, DSL 18NR-AO and Solaronix Ti-D TiO_2 pastes with annotation

Table 5.1: Weight % of each component of the commercial pastes and their dry film thicknesses

Paste	Content of paste (wt%)			Dry film thickness (μm)
	Solvent	Binder	TiO_2	
DSL 18NR-AO	65	15	20	9-10
DSL 18NR-T	62	10	28	7-8
Sol Ti-D	80	7	13	3

Complete binder removal was achieved at around 420°C for the Dyesol pastes and 380°C for the Solaronix paste. Therefore temperatures exceeding this would need to be attained by the NIR method to remove all binder and solvent. As mentioned previously the purpose of heating the TiO_2 paste for a DSC working electrode is to remove binder and solvent (which are there to prevent the TiO_2 particles from aggregating together so the film can maintain mesoporosity) and to sinter the TiO_2 particles so that electrons can be transported through the film. If any binder remains in the film it will reduce the available active area of the TiO_2 for dye adsorption and so reduce the photocurrent of the DSC device. To assess the extent that the solvents and binders had been removed TGA was performed (from 30-600°C) on

films after heat treatment. If any weight loss occurs then this would be as a result of binder and solvent which was not removed after heat treatment. This would give an indication of how sufficiently and evenly heated the films were and it was believed that if full removal was achieved the remaining TiO_2 would have started to sinter together. This was first investigated for oven heated pastes; figure 5.6 shows TGA profiles of pastes after they had been heated in an oven at 450°C for varying lengths of time.

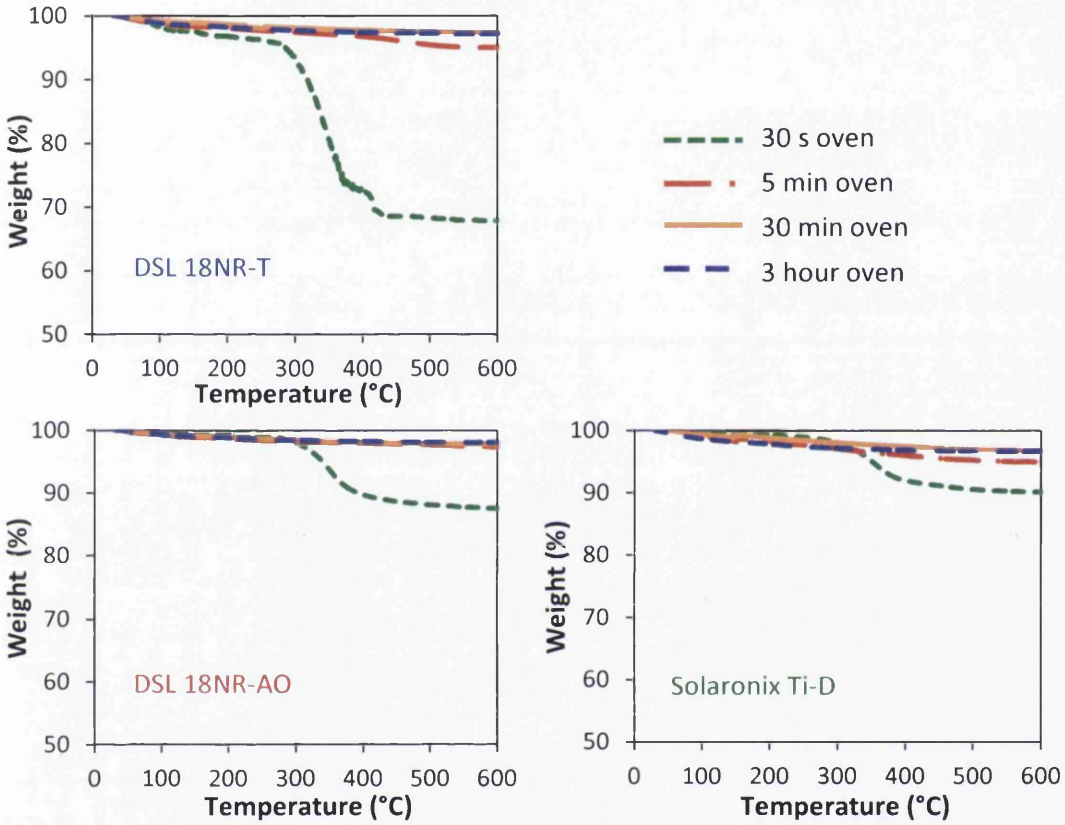

Figure 5.6: TGA profiles (original weight % vs. temperature) for TiO_2 films following oven heating at 450°C for varying oven time; weight loss is as a result of insufficient oven heating time and the profile shows at which temperature range this weight loss occurs to attribute it to solvent or binder

After 30 seconds of heating in the oven at 450°C both the Dyesol pastes experienced rapid weight loss in the TGA after 270°C due to the burning of the ethyl cellulose, the solaronix paste has rapid weight loss after about 300°C which is burning of the polyethylene glycol. This suggests that the short conventional heating was sufficient to remove most of the solvent but not the binder which would be expected as conventional heating is very low energy intensive and the sample was still heating up from the outside in via thermal conduction. The DSL 18NR-T paste loses more weight % of binder than the opaque paste and

also has sharper loss up to 180°C which may be trapped terpineol. The 5 min heated samples undergo almost no weight loss for the DSL 18NR-AO paste and relatively little for the other two pastes indicating that the binder has been almost completely removed. It is anticipated that although the binder was removed in this short timeframe of conventional heating, the TiO_2 particles would have poor interconnectivity. At this temperature the diffusion across the grain boundaries of the TiO_2 is slow hence the optimum DSC working electrode sintering time at 450°C for conventional heating is at least 30 min. The 30 min oven and 3 hour oven TGA profiles are identical for all pastes indicating that there was no further binder to be removed. The 5 min, 30 min and 3 hour oven samples experience gradual weight loss which is attributed to water adsorption by the TiO_2 because the TiO_2 is porous [9]. The gradual weight loss is relatively absent for the 30 s sample which instead experiences a sudden sharp weight loss at the onset of binder burning temperature. This is because TiO_2 is not as porous (due to binder still being present) so less water was adsorbed. Figure 5.7 shows the weight remaining after thermogravimetric analysis for oven heated TiO_2 pastes against heating time to visualise the progression of binder removal more easily.

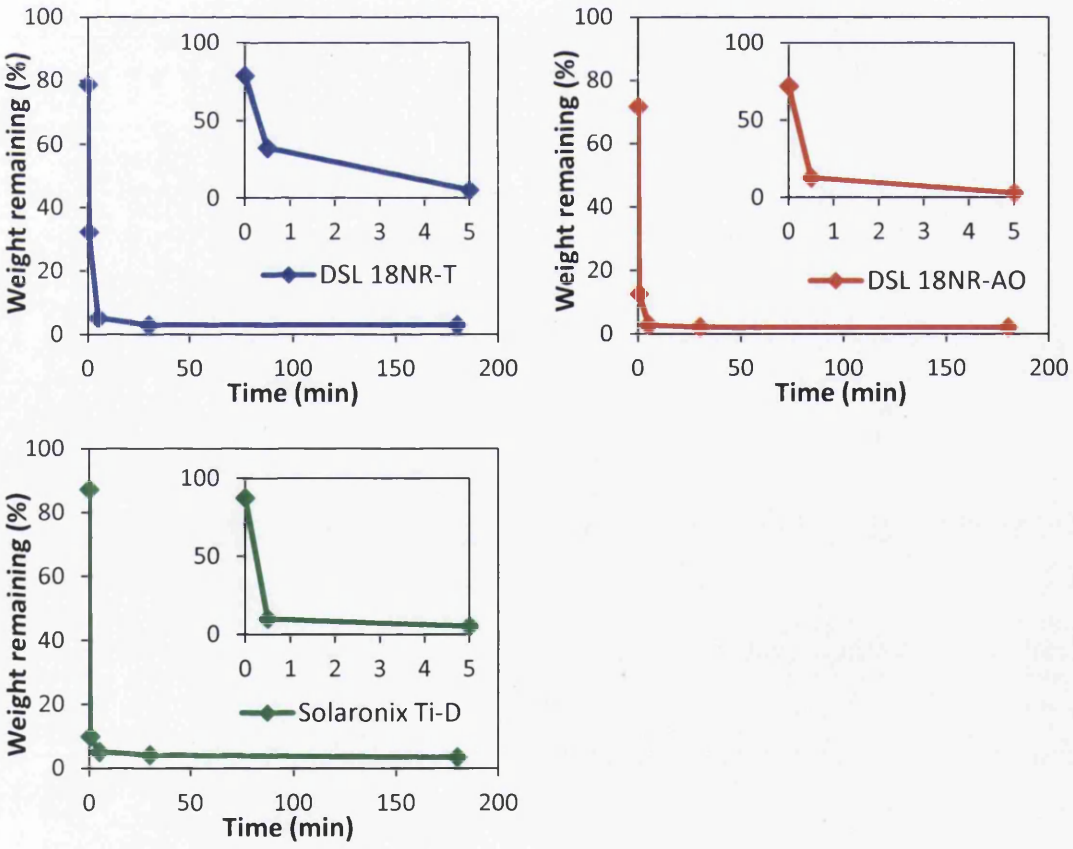

Figure 5.7: Amount of weight remaining after pastes were heated in an oven at 450°C for varying lengths of time as calculated with TGA (0-5 min shown inset for clearer detail)

For the oven heated pastes the vast majority of weight loss occurs in the first 30 second and this is attributed to the solvent evaporating which is 60-80 wt% of each paste. The weight remaining as calculated from the TGA is related to the proportion of binder each paste contains; the solaronix paste has the least binder content so had the least weight remaining and DSL 18NR-T had the highest binder content so had the most weight remaining. To perform TGA of the pastes they were heated on FTO glass slides and the paste had to be scraped off but this proved to be a problem for the 30 s oven samples which were extremely well adhered to the slides rendering removal difficult. As a consequence less material was obtained for testing and what was obtained was less representative of the overall TiO_2 film (because some of the binder remained on the slide) so the actual weight remaining may be underestimated. The majority of binder removal has been achieved after 5 min except for DSL 18NR-T which is most likely due to the higher binder starting content. TGA was performed on NIR heated pastes in an identical fashion to the oven heated pastes. Figure 5.8 shows TGA profiles for 12.5 s NIR exposed TiO_2 pastes.

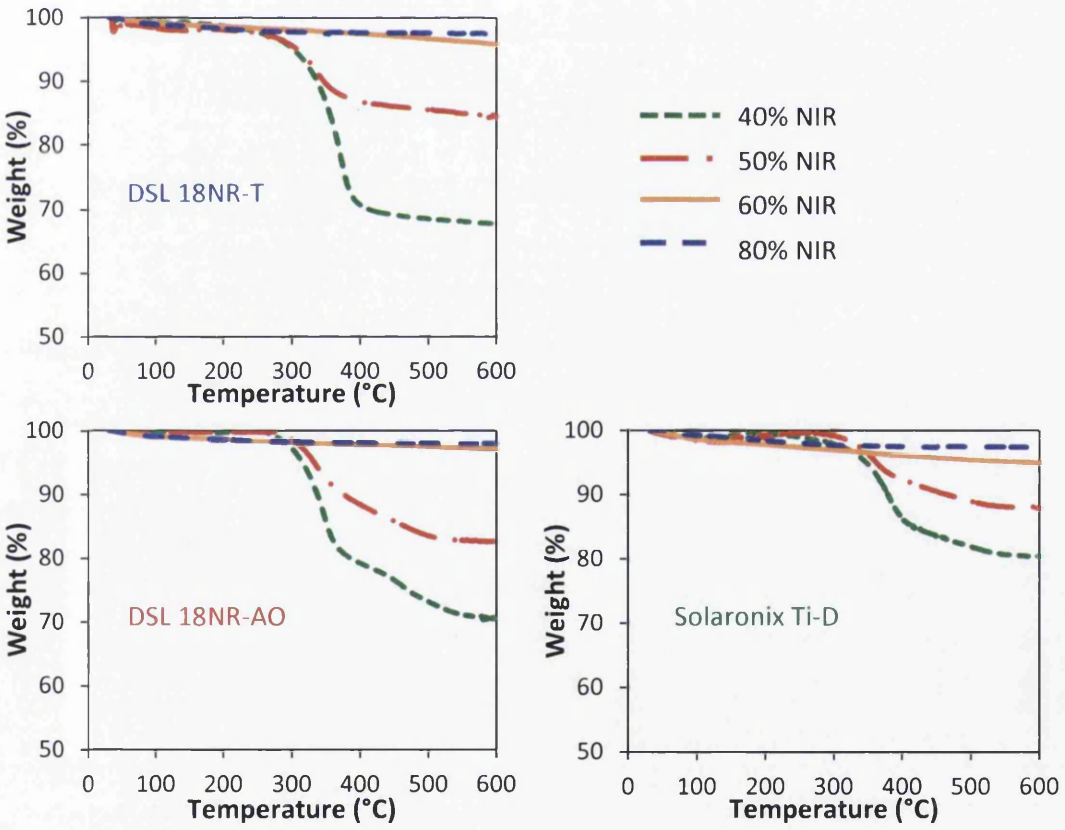

Figure 5.8: Weight % vs. temperature TGA profile for films following 12.5 s of NIR exposure at various NIR lamp intensities; weight loss is as a result of insufficient heating of the paste by the NIR intensity and the profile shows at which temperature range this weight loss occurs to attribute it to solvent or binder

All NIR samples of TiO_2 paste on FTO glass were exposed to 12.5 s of NIR radiation which should reach similar maximum temperatures as those predicted in Chapter 3 as shown in Table 5.2. As discussed previously from absorbance and reflectance of transparent and opaque pastes the transparent paste may shield some NIR radiation but not a significant amount resulting in a marginally lower temperature and the opaque paste may absorb some creating localised heating in the paste as well as the FTO layer.

Table 5.2: Temperatures estimated in Chapter 3 for 12.5 s NIR exposed FTO glass

NIR intensity (%)	Max temperature (°C)
40	270
50	389.9
60	487.7
70	564.3
80	604.7
90	647.6
100	680.9

For the 40% and 50% lamp intensity samples there is rapid weight loss after about 270°C for the Dyesol pastes and 300°C for the Solaronix paste. These are both attributed to binder burning which was not completely removed during the NIR exposure at these lower lamp intensities. The Solaronix paste contains less weight proportion of binder than the two Dyesol pastes so experiences less weight % loss. The predicted maximum temperatures for 12.5 s NIR exposure of FTO glass is 270°C for 40% NIR intensity and 390°C for 50% NIR intensity which fits in well with the higher proportion of binder removal for the latter due to the higher temperature reached by the FTO glass. After 60% NIR exposure, which was predicted to achieve a maximum temperature of 488°C, there is a dramatic decrease in weight % loss because the temperature was sufficient in 12.5 s to burn off most of the binder. At 80% NIR intensity there is no weight loss (no binder or solvent remaining) which is to be expected as a maximum temperature of 605°C during the 12.5 s greatly exceeds that required for burning off binder. The 60% and 80% NIR samples were subjected to gradual weight loss throughout heating, which again is attributed to water adsorbed by the TiO_2 [9]. The gradual weight loss is relatively absent from the 40% and 50% samples which instead experience a sudden sharp weight loss at the onset of binder burning temperature. This is because TiO_2 is not as porous (due to binder still being present) so less water was absorbed. Table 5.3 shows the percentage of binder remaining out of the binder total for each NIR intensity assuming that after NIR exposure the paste contains only binder and TiO_2, no

solvent and that all binder is removed by 80% NIR and this weight loss is water. This is safe to assume because it is also the case for conventional oven heating (450°C for 30 min) which showed weight loss which was not binder but water.

Table 5.3: Binder remaining after NIR exposure estimated from TGA profiles

Paste	Binder remaining (%)			
	NIR 40%	NIR 50%	NIR 60%	NIR 80%
DSL 18NR-T	75.3	36.4	3.5	0
DSL 18NR-AO	97.4	66.2	3.8	0
Sol Ti-D	56	34.9	7.1	0

This shows that after 40% NIR intensity there is large proportion of binder remaining for DSL 18NR-AO compared to the solaronix paste and is related to the thickness of film which is three times thicker for the Dyesol paste so there is more binder to be removed. By 60% NIR intensity there is only a small percentage of binder remaining for each paste, lowest for the two Dyesol ones. There appears to be no weight loss attributed to solvent in these samples suggesting each of them exceeded the temperature required for solvent evaporation.

Figures 5.9 shows weight remaining after thermogravimetric analysis for NIR heated TiO_2 pastes represented against NIR intensity to map the progression of binder removal with increasing lamp power. This illustrates the sharp decrease of weight remaining from 40% NIR to 60% after which the weight remaining remains fairly constant and is expected to be water loss from the porous films. Although at lower NIR intensities, 40% and 50%, the solaronix paste showed more binder removal than the two Dyesol pastes (probably due to the smaller thickness of film) by 60% NIR these were fairly even with the Dyesol pastes slightly ahead. All of the commercial pastes were suitably heated by only 12.5 s of NIR exposure so for further investigation the best paste to make a DSC working electrode could be chosen. DSL 18NR-AO was chosen because it has scattering particles to improve light harvesting and because it creates the thickest layer with doctor blading under identical conditions keeping the method simple.

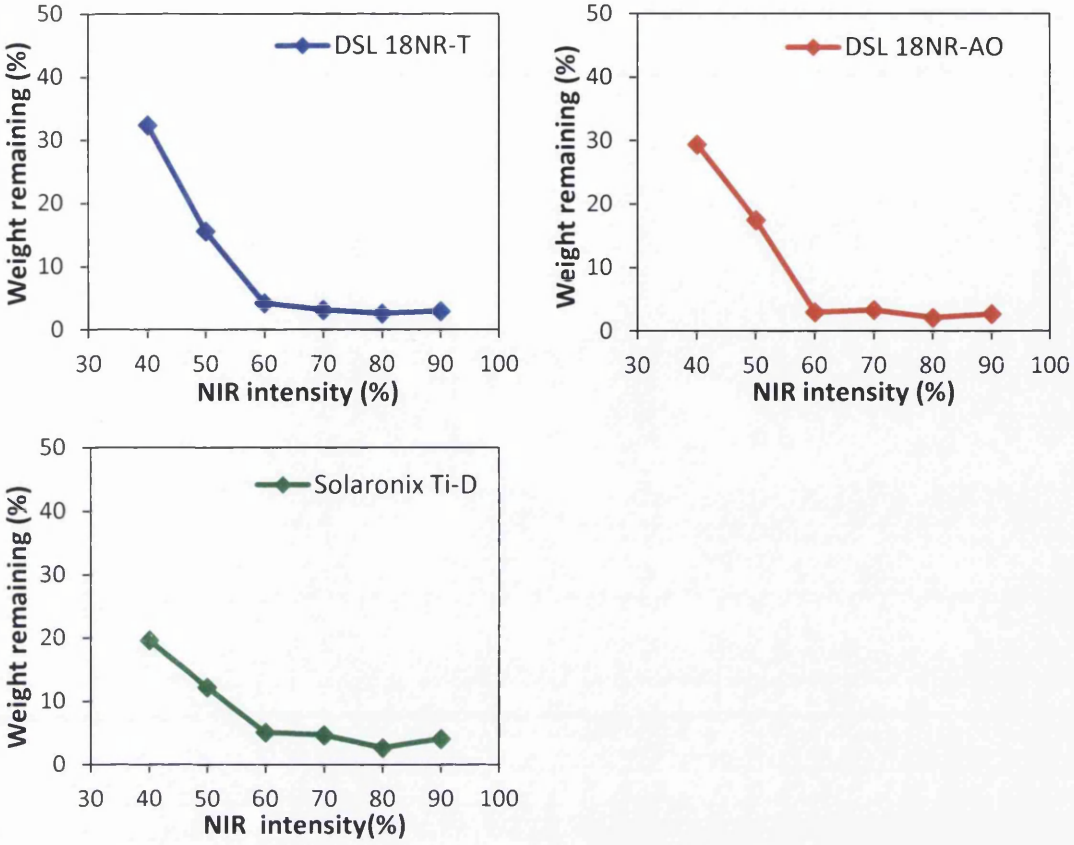

Figure 5.9: Amount of weight remaining after pastes were exposed to 12.5 s of NIR radiation at various NIR lamp intensities as calculated with TGA

FTIR-ATR was used to analyse the organic functional groups present in oven and NIR heated DSL 18NR-AO paste. This would confirm if the weight loss of samples was solvent or binder and if the weight loss in the higher intensity NIR samples was water (by the lack of binder or solvent functional groups). Figure 5.10 shows FTIR spectra overlaid for the components of the paste (anatase TiO_2 [10], terpineol [10] and ethyl cellulose) with wet DSL 18NR-AO paste. The relevant peaks for each functional group have been annotated A-J and are described in Table 5.4.

The terpineol peak A is attributed to an OH stretch as is the ethyl cellulose peak E which has a smaller range due to the fewer OH bonds. Peaks B and F correspond to stretching of CH bonds for terpineol and ethyl cellulose respectively and have different shapes. Peak C is a C=C stretch and D bending of CH bonds. The ethyl cellulose peaks G and H correspond to CH_2 and CH_3 bending, and out of plane bending of CH bonds. Peaks I, J, and K are absorption peaks for anatase phase TiO_2. The wet DSL 18NR-AO paste shows each of these peaks, some differ slightly due to the different isomers of terpineol and crystal sizes of anatase TiO_2. FTIR-

ATR was performed on oven heated samples of DSL 18NR-AO paste at 450°C to identify any organic functional groups present and is shown in figure 5.11.

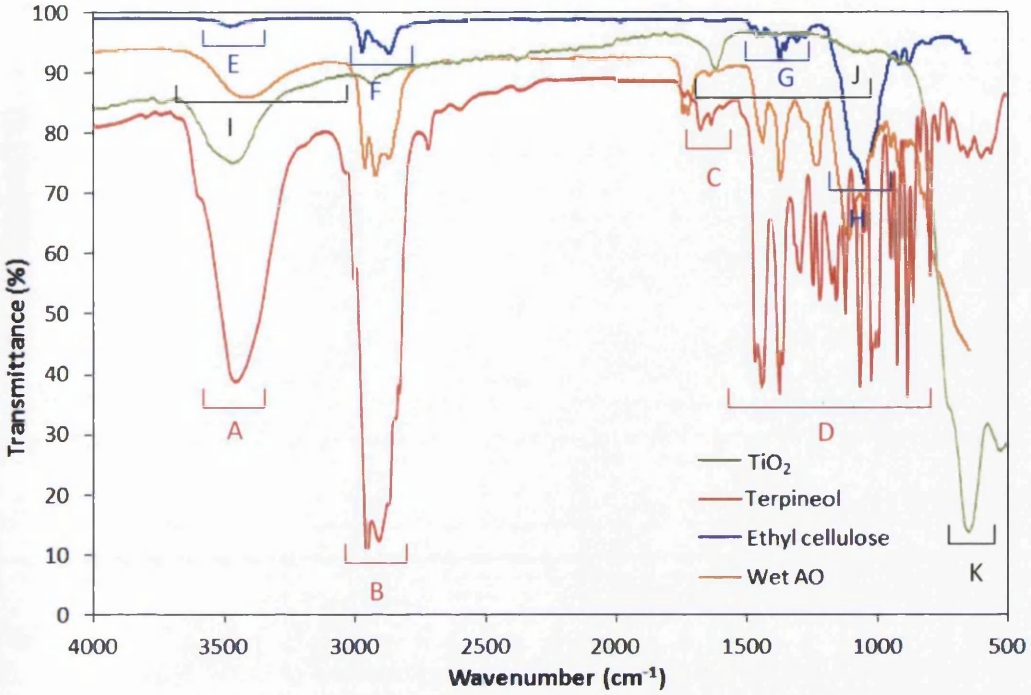

Figure 5.10: FTIR spectra of wet DSL 18NR-AO paste with TiO_2 [10], terpineol [10] and ethyl cellulose with annotation

Table 5.4: Functional group peak labels and locations as annotated in figure 5.10

Peak	Source	Range (cm^{-1})
A	Terpineol	3600-3250
B	Terpineol	3050-2750
C	Terpineol	1800-1670
D	Terpineol	1550-750
E	Ethyl cellulose	3550-3450
F	Ethyl cellulose	3050-2750
G	Ethyl cellulose	1500-1300
H	Ethyl cellulose	1300-900
I	TiO_2	3700-2700
J	TiO_2	1800-1350
K	TiO_2	800-500

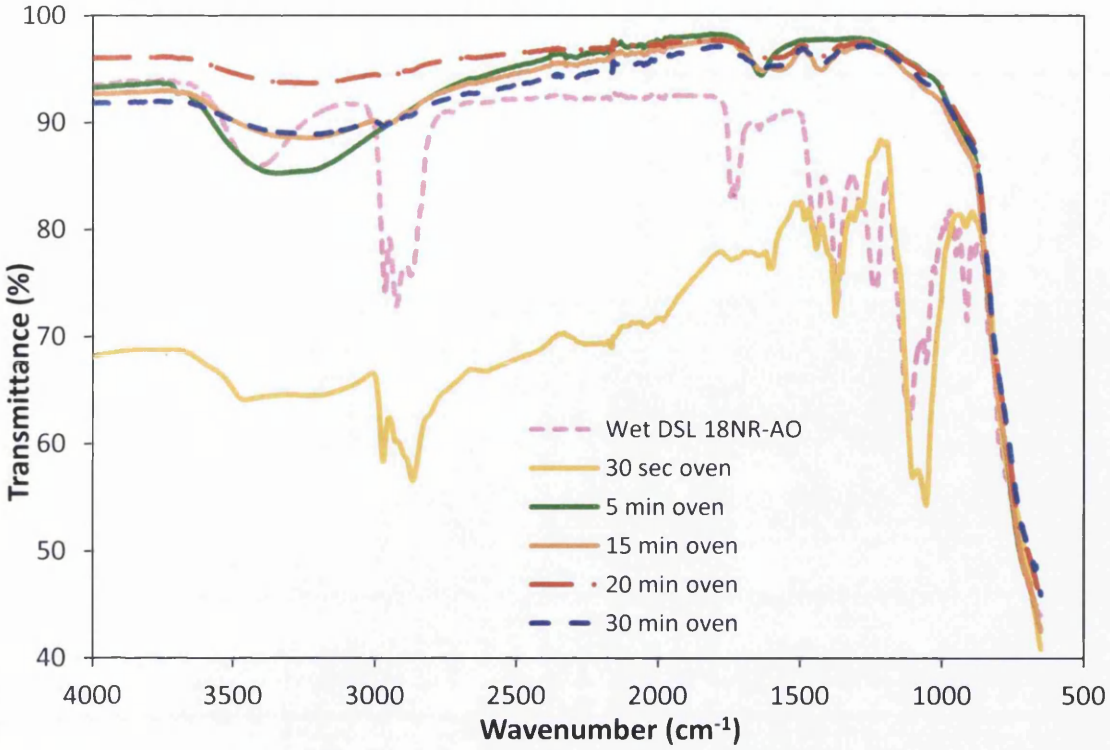

Figure 5.11: IR spectra for oven heated DSL 18NR-AO paste obtained with FTIR-ATR

For the wet paste all the peaks are present because it contains all components; TiO_2, terpineol and ethyl cellulose. After 30 s heating in an oven at 450°C the terpineol peaks A-D are absent indicating as suggested from the TGA data that all the solvent has been removed. Peaks E-H, which are attributed to ethyl cellulose, all still remain suggesting that the majority of the binder remains and it has not started to break down. After 5 min of heating all the ethyl cellulose traces seem to have disappeared although there may be a peak near G of a combustion product which is largely obstructed by the TiO_2 peak. This suggests almost all of the binder was removed as the TGA data showed. After 5 min heating each paste shows only TiO_2 peaks because all the binder has been removed. The time at which sufficient interparticle connectivity is achieved will be investigated in section 5.3.3 by constructing DSCs from oven heated working electrodes. Figure 5.12 shows transmittance vs. wavenumber for NIR exposed DSL 18NR-AO paste for 12.5 s at varying NIR lamp power obtained with FTIR-ATR.

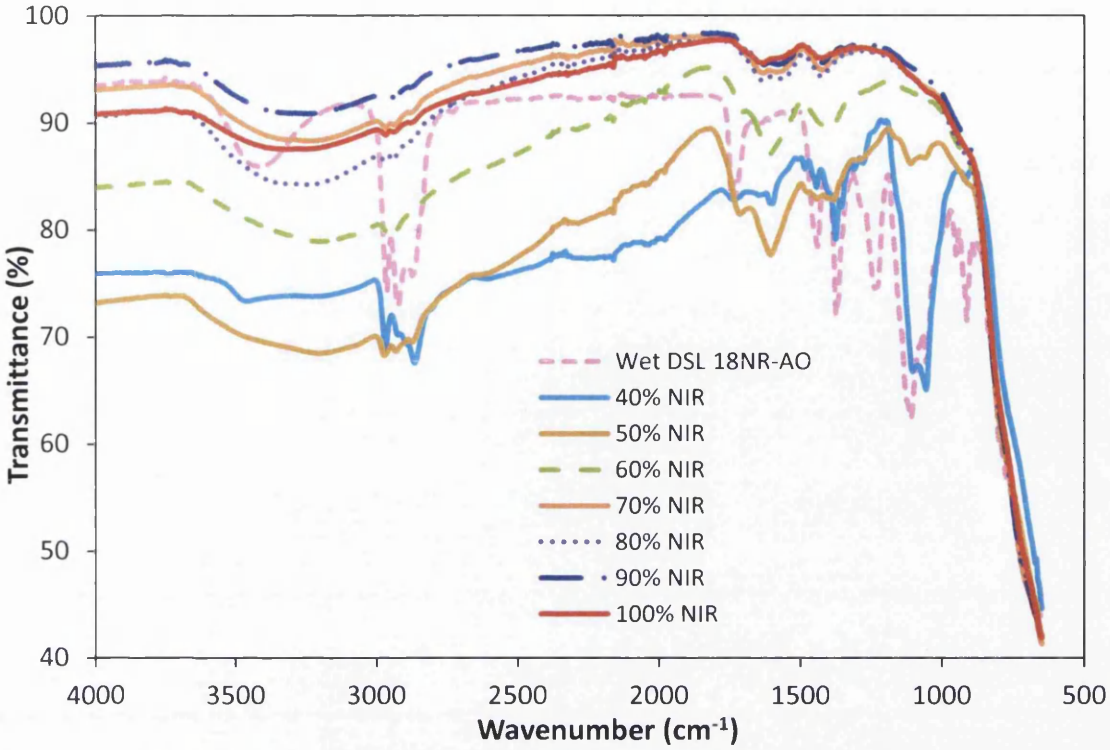

Figure 5.12: IR spectra of 12.5 s NIR heated DSL 18NR-AO paste obtained with FTIR-ATR

Similarly to the oven heated FTIR spectra the same peak labels have been used as identified in Table 5.4. After 12.5 s of 40% lamp intensity NIR exposure the peaks A-D that are attributed to terpineol are absent. This suggests that the maximum temperature reached by the FTO glass with 40% NIR exposure, 270°C, was sufficient to evaporate off all of the solvent as maintained by the TGA data in which no weight loss was believed to be from solvent. The peaks that are attributed to ethyl cellulose, E-H, are present and fairly strong, 97% of the binder content remains as estimated using the TGA data (Table 5.3). At 50% NIR intensity the ethyl cellulose peak E has disappeared, which is an OH bond so has been readily combusted, and the peak H is heavily diminished. Peaks near F and G appear to be new and as a result of combustion products from the ethyl cellulose breaking down, about 66% of the binder was estimated to remain in the 50% NIR sample. At 60% NIR intensity the ethyl cellulose peaks are mostly absent. There appears to be a trace of combustion products at around 1700 cm^{-1} but they are partly obscured by the TiO_2 peak J which is more prominent; there is estimated to be less than 4% of the binder remaining. This reinforces the conclusion from the TGA data that almost all the binder was removed with 12.5 s of 60% NIR intensity exposure. Samples 70-100% NIR intensity show no ethyl cellulose or hydrocarbon peaks and only the TiO_2 peaks, I, J, and K. As expected all of the solvent and binder has been removed for these samples which have exceeded the required maximum temperature in the 12.5 s

timeframe to achieve sufficient thermal energy for rapid combustion of the organic materials. Both the TGA data and the FTIR-ATR data suggest that the prospect of creating a 9 µm thick mesoporous layer of TiO_2 onto FTO glass in 12.5 s is extremely promising. If there was sufficient heat energy to remove the majority of the binder there may have been sufficient heat energy to also sinter the TiO_2 particles together which will be investigated in sections 5.3.2 and 5.3.3.

As discussed in Chapter 3 the FTO layer is integral to the high temperature heating of glass substrates with NIR radiation due to its higher absorption in the IR region causing over 300°C of extra heat in 12.5 s of exposure. To emphasis this point DSL 18NR-AO paste was heated on 2.2 mm thick glass (FTO glass that had had its FTO layer chemically etched away) by NIR exposure and conventional heating and analysed using TGA and FTIR-ATR to compare to the previous samples. The expected outcome for conventional heating is that the due to the paste being heated from the outside slowly inwards the substrate does not influence the temperature and therefore the lack of FTO layer will not affect the solvent and binder removal of the paste. However since the NIR heating method depends on the substrate absorbing NIR radiation causing it to release energy as heat using uncoated glass, which absorbs less radiation than FTO coated glass, should result in the films having less binder and solvent removed at identical NIR intensities. Figure 5.13 shows the weight remaining obtained from TGA profiles for uncoated glass vs. FTO glass when heated by an oven and heated by 12.5 s NIR exposure.

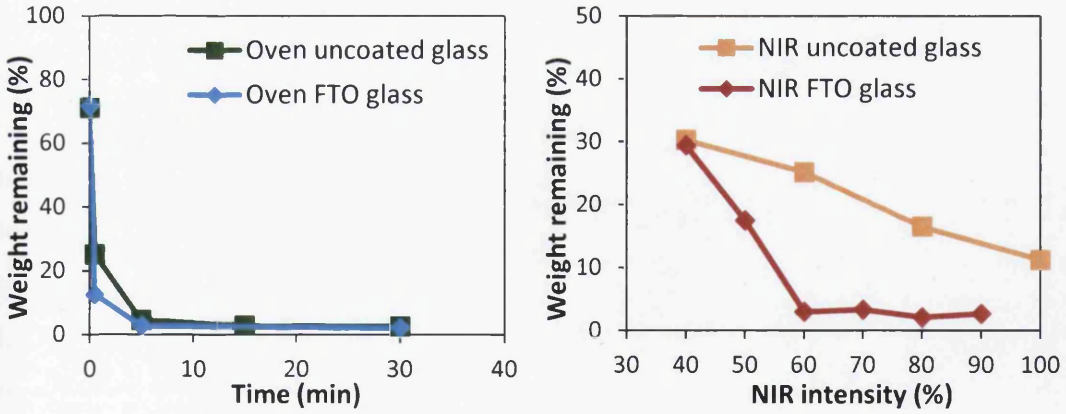

Figure 5.13: Amount of weight remaining of DSL 18NR-AO paste on FTO glass and uncoated glass as calculated from TGA after heating at 450°C in an oven (left) and via 12.5 s NIR exposure (right)

Uncoated glass seems to have very little influence on the weight remaining of oven heated DSL 18NR-AO opaque paste indicating that it did not impact the ability of the oven heating to remove the solvent and binder from the TiO_2 films. There is slight variation at 30 s of oven heating but this is understandable as the sample was still reaching temperature in this short time and even the time the oven door was left open before it was shut when placing the samples inside could have perturbed this. The 5 min samples and the 30 min samples are virtually identical so as expected the lack of FTO layer seems to have had little impact on the heating of the paste in an oven. In conventional heating the sample heats from the outside inwards with convection and conduction and the outermost exposed areas for both FTO glass and uncoated glass is the glass substrate and the top of the TiO_2 paste film where the thermal conductivity of these would be identical irrespective of the presence of an FTO layer. The FTO layer, which has a higher thermal conductivity than glass, is a relatively small surface area compared to the other exposed surfaces so has negligible influence on this method of heating.

For the NIR heated films the presence of an FTO layer on the glass substrate has a strong influence on the weight remaining after 12.5 s of NIR exposure. At 40% NIR intensity the weight remaining is fairly similar for both glasses. This may be explained by both the TGA profile for wet DSL 18NR-AO paste (figure 5.5) and the percentage of binder remaining after 40% NIR exposure of FTO glass (Table 5.3) which was estimated to be 97%. This shows that there is a large temperature window between the majority of solvent weight loss and the majority of binder weight loss and according to Chapter 3 the uncoated glass should reach a temperature of around 133°C. Although this is lower than required to remove all solvent it could be possible if the absorbance - reflectance of DSL 18NR-AO paste was enough to increase the temperature slightly and aid the solvent evaporation which should not require too much energy. This suggests that the uncoated glass sample has reached the temperature for majority of solvent removal and the FTO glass sample has not quite reached the temperature required for rapid binder removal so both result in a similar weight remaining from the TGA. For the other NIR intensities the uncoated glass samples had less weight remaining for each respective NIR intensity up to 100% lamp power where there still appears to be binder present illustrating the significance of the FTO layer in heating the TiO_2 paste where an identically thick glass substrate could not achieve this.

Figure 5.14 shows transmittance vs. wavenumber obtained from FTIR-ATR for oven heated DSL 18NR-AO on FTO glass and uncoated glass which reinforces that the binder and solvent removal was almost identical and independent of the substrate for conventional heating. The two 30 s oven samples overlap showing the ethyl cellulose peaks as discussed earlier, and the two 30 min oven samples overlap confirming that the substrate has negligible influence on the conventional heating method. Figure 5.15 shows transmittance vs. wavenumber obtained from FTIR-ATR for DSL 18NR-AO paste heated by 12.5 s NIR radiation comparing FTO glass and uncoated glass.

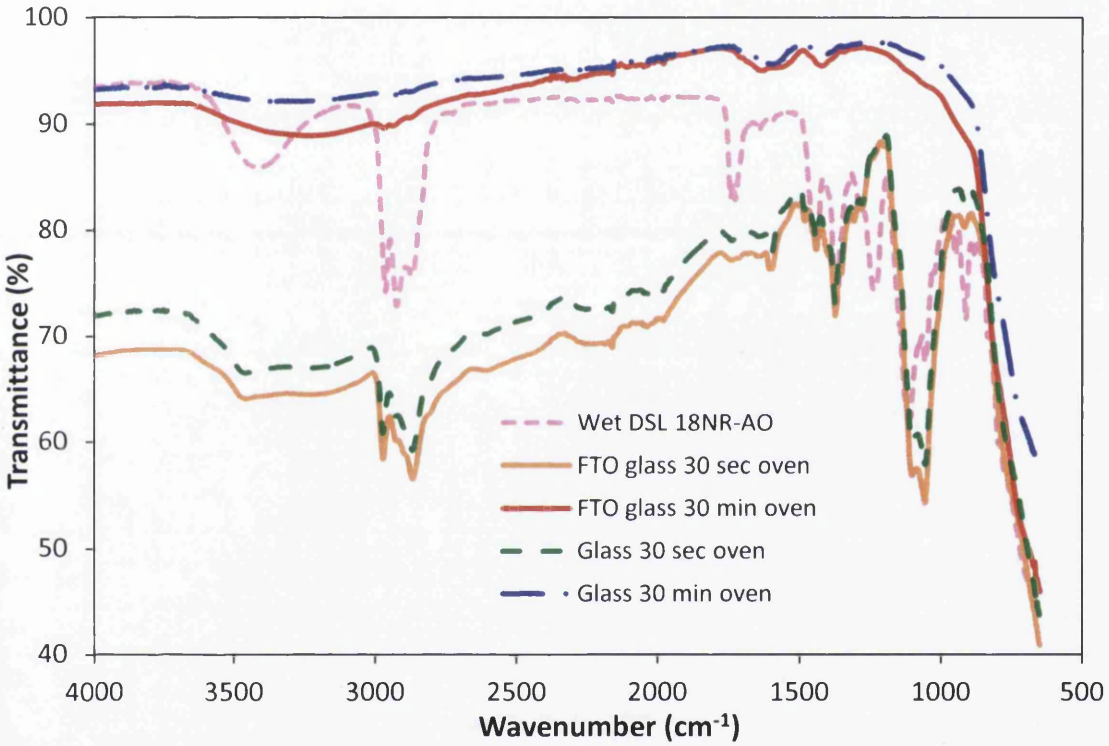

Figure 5.14: Transmittance vs. wavenumber for DSL 18NR-AO paste heated at 450°C in an oven on FTO glass and uncoated glass

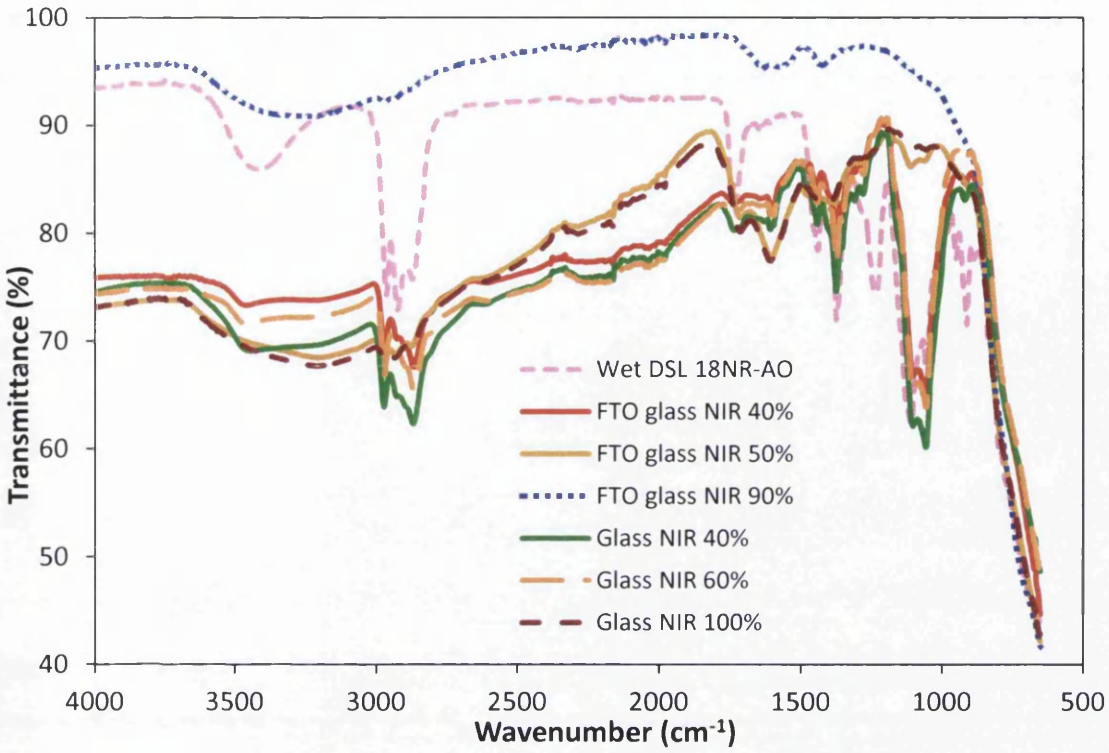

Figure 5.15: Transmittance vs. wavenumber for DSL 18NR-AO paste heated by 12.5 s NIR exposure on FTO glass and uncoated glass

For 40% NIR heated DSL 18NR-AO on uncoated glass all of the ethyl cellulose peaks (as identified in Table 5.4) are present. It is similar to the FTO glass 40% NIR sample but the peaks are slightly weaker in the latter. 60% NIR intensity on uncoated glass also shows the same ethyl cellulose peaks showing that most of the binder still remains. It overlaps with the 40% FTO glass sample with similar strength peaks suggesting the same level of binder removal; that some binder has been removed but the ethyl cellulose has not yet been broken down. The samples 50% NIR FTO glass and 100% NIR uncoated glass almost overlap each other perfectly. There is a slight signal at peak H for the 50% NIR FTO glass film corresponding to ethyl cellulose which is stronger in this sample compared to the uncoated one which may explain the slightly greater weight loss experienced from the TGA profile. Otherwise these samples are extremely similar; the FTO glass was predicted to have reached 40°C higher at 50% NIR intensity than the uncoated glass at 100% NIR intensity which suggests the temperature estimated for the uncoated glass may be underestimated but not significantly as both samples reached a similar temperature.

Finally the colour change of the pastes was recorded by photographing samples prepared for TGA or FTIR-ATR in a light box for colour analysis. Figures 5.16 and 5.17 show DSL 18NR-AO paste heated by oven and NIR on FTO glass and uncoated glass respectively.

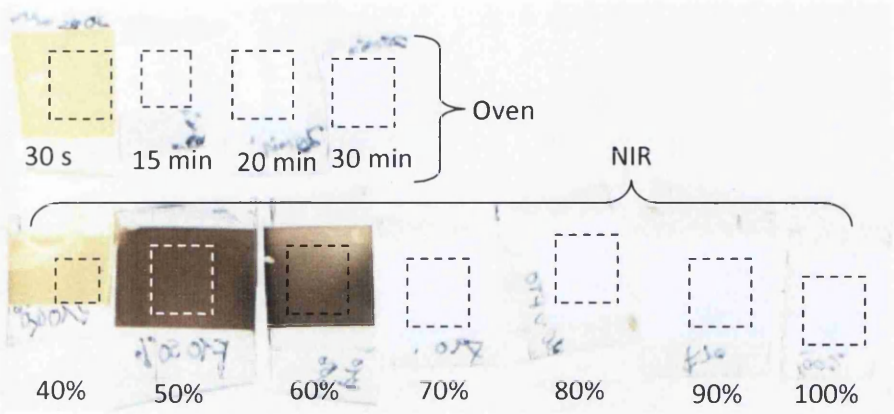

Figure 5.16: Oven heated and NIR heated DSL 18NR-AO paste on FTO glass for colour analysis

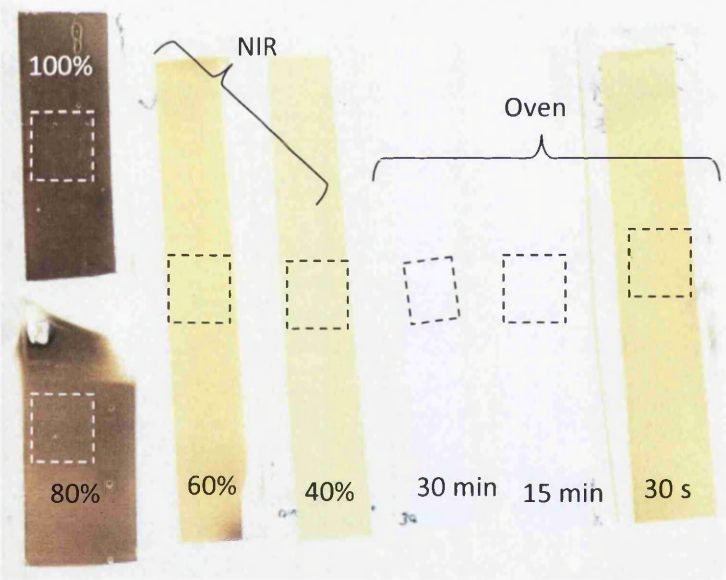

Figure 5.17: Oven heated and NIR heated DSL 18NR-AO paste on uncoated glass for colour analysis

From these photographs it is clear that once DSL 18NR-AO has had all binder removed it appears white. This colour is similar to that in figure 5.2 of a wet opaque paste. So the paste begins as white once doctor bladed then as it is heated it turns light yellow gradually becoming darker until dark brown and then finally white again. This is as a result of the ethyl cellulose burning and hydrocarbons being converted into carbon which would appear black.

The 60% NIR sample on FTO glass shows the onset of the film's final transition to white where not all of the binder combustion products have yet been removed. Although a dark brown/white film would seem unsuitable for a DSC device oddly it was observed they sometimes work, it may be that the film underneath is sintered well and the char left behind by the binder has no affect in these cases. However there is some variation between the samples and the 60% NIR films that were used for construction of a working electrode in section 5.3.3 were almost completely white with only a few areas of brown. At 40% NIR and 30 s oven on FTO glass the films appear yellow because all the solvent has been removed but the majority of the ethyl cellulose remains with the TiO_2. Samples longer than 15 min in the oven and NIR 70-100% are white because only TiO_2 remains. For the uncoated glass samples 40% NIR is very pale yellow the lightest of all of the samples suggesting that it has the most intact ethyl cellulose out of the heated samples. Again 30 s heating in an oven is yellow and the longer times are white. For the NIR heated samples 60% on uncoated glass is still yellow with a bit of brown indicating some combustion of the binder. The 80% and 100% samples are both still brown because the heating was not sufficient to burn off all of the binder. Average Red Blue Green (RBG) values were obtained from each film in the areas shown in figures 5.16 and 5.17 and plotted in figures 5.18 and 5.19.

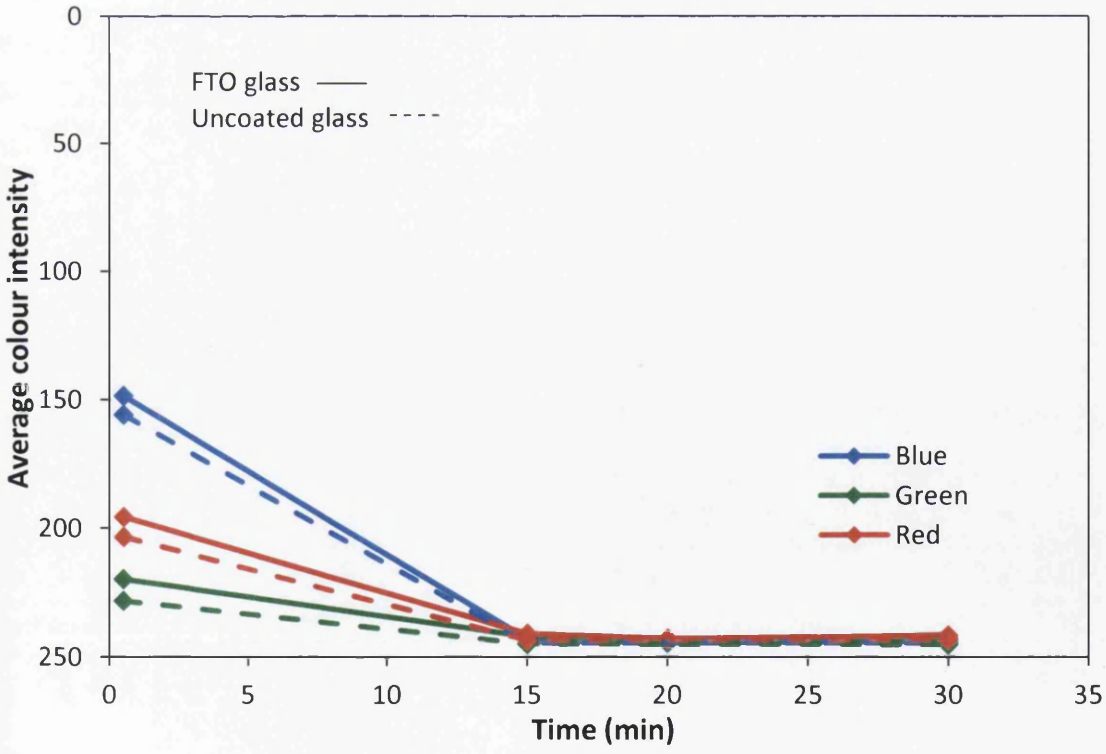

Figure 5.18: Average RBG values for photographs of TiO_2 pastes heated in an oven at 450°C for varying time on FTO glass (solid line) and uncoated glass (dashed line)

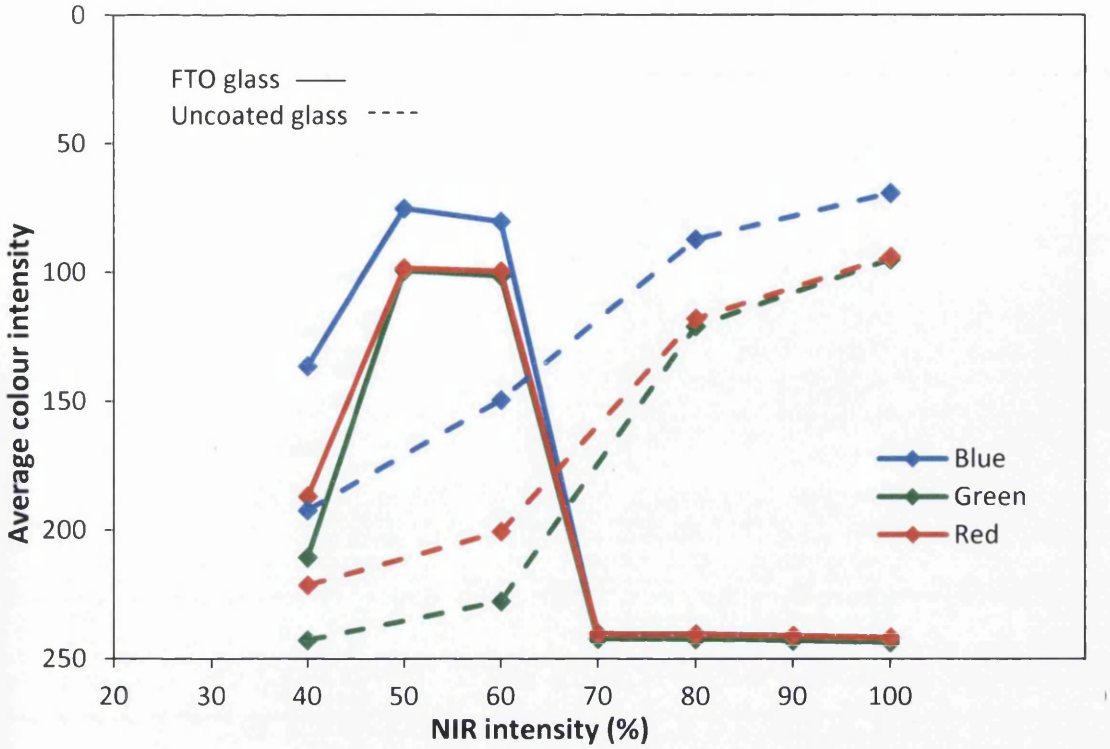

Figure 5.19: Average RBG values for photographs of TiO_2 pastes exposed to 12.5 s of NIR radiation at varying NIR intensity on FTO glass (solid line) and uncoated glass (dashed line)

Pastes that are white have high values for blue, red and green; these are pastes with full binder removal. The pastes that still contain a lot of binder, which appear quite yellow, have blue as the lowest value followed by red and then green as the highest value. Pastes that have partial binder removal and are approaching full binder removal, which are dark brown, have low blue, red and green values getting gradually and equally lower. Figure 5.18 reinforces that the heating is extremely similar in an oven regardless of the substrate. In figure 5.19 it is illustrated that the uncoated glass is continuing to get darker at a much higher NIR intensity and so binder remains, the FTO glass substrates begin to darken at 50% NIR intensity and at 70% are white. Using this technique the colours of heated TiO_2 films of the same pastes could be quantitatively compared to each other, which may be useful for in situ monitoring of paste sintering, if the differences between blue and red/green intensities are easily distinguishable at the beginning of heating when the pastes are almost white and not to be confused with after sintering where the colour levels are identical.

5.3.2 Micrographs and crystal structure of NIR heated titanium dioxide

It was shown in section 5.3.1 that 12.5 s of NIR radiation was sufficient to remove all the solvent and binder from TiO_2 paste on FTO glass which allows the creation of a mesoporous 9 µm thick TiO_2 film. However the TiO_2 particles also require enough thermal energy to sinter them together to allow for efficient charge transport. SEM images of the NIR and oven heated DSL 18NR-AO paste films on FTO glass were taken are shown in figure 5.20.

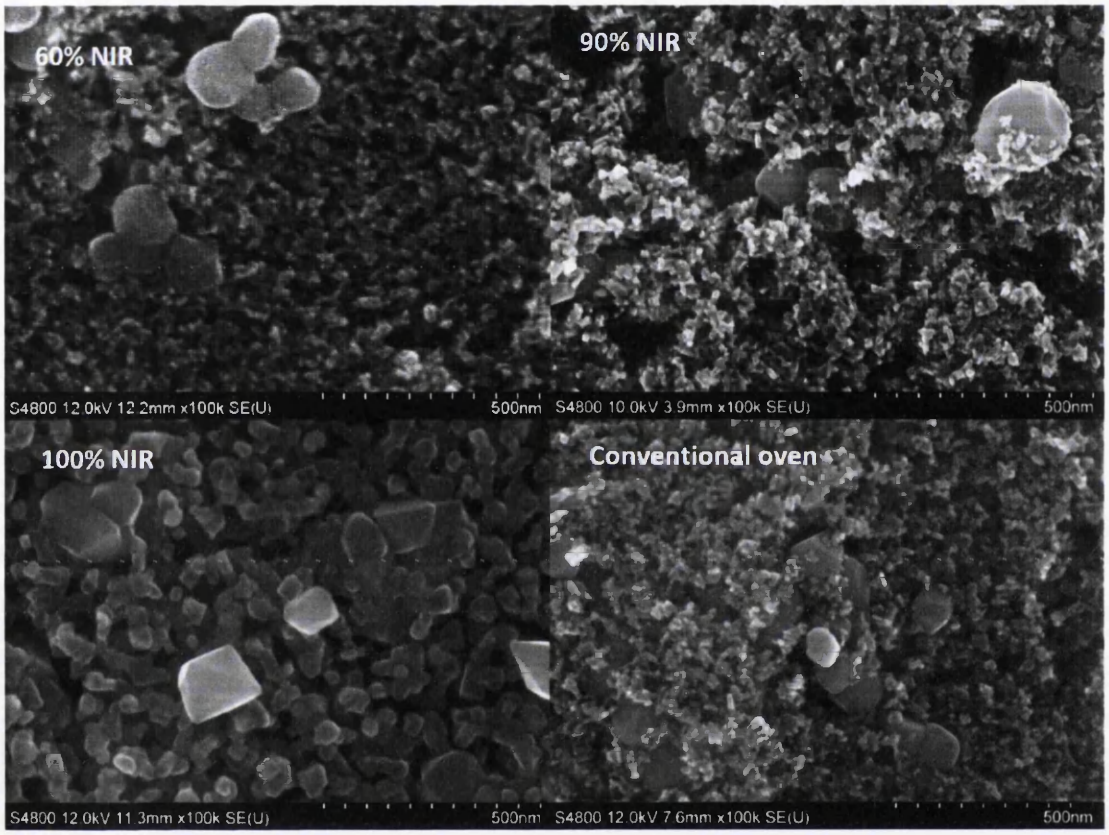

Figure 5.20: Micrographs of TiO_2 films from DSL 18NR-AO TiO_2 paste on FTO glass heated with 12.5 s of NIR radiation at 60%, 90% and 100% intensity and a conventionally sintered film, all at the 100k magnification

DSL 18NR-AO paste contains small 20 nm sized anatase particles as well as 100 nm scale scattering particles which tend to cluster together as shown in figure 5.20. At 90% NIR intensity the particles appear well sintered and comparable to the conventional oven film with good porosity. At 60% NIR intensity the film appears less porous due to some charred binder remaining which has also manifested itself in the quality of the SEM image as there is some interference from the organic residue. The similarity of the 12.5 s heated 90% NIR intensity film to the 30 min at 450°C conventionally heated film is extremely promising and it is anticipated that they may function with identical effectiveness, which will be addressed in

section 5.3.3 with their use in DSC devices. At 100% NIR intensity there appears to be some growth of the anatase crystals suggesting that the higher temperature accelerated the sintering of the particles and led to them coarsening. This was previously observed for the NIR heating of TiO_2 paste on titanium and was attributed to a high peak metal temperature of 785°C [5]. The maximum temperature for FTO glass at this intensity is predicted to be around 680°C but its lower thermal conductivity compared to titanium could mean it was subjected to a high enough temperature for grain growth for longer. It was also observed on the 100% NIR sample that the FTO glass appeared affected by the heating as shown in figure 5.21.

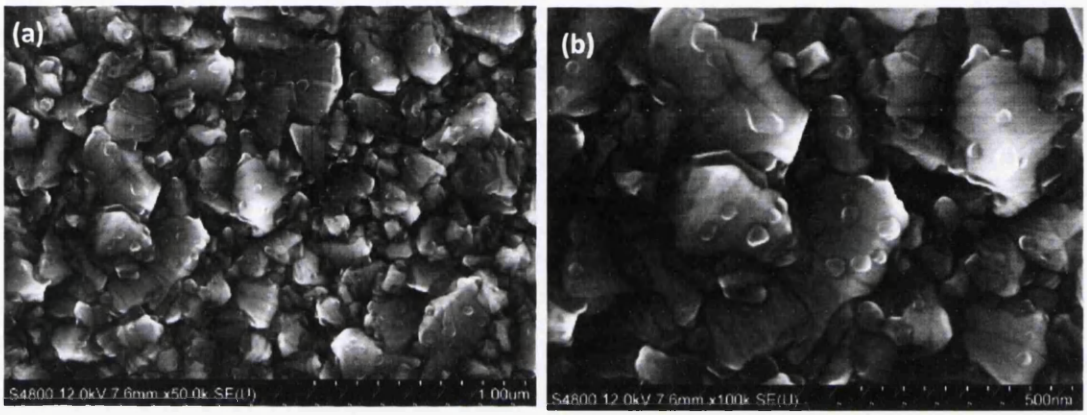

Figure 5.21: FTO glass of 100% NIR intensity heated TiO_2 at (a) 50k magnification and (b) 100k magnification

There appears to be fragments evenly distributed on the grains of FTO. Energy-dispersive X-ray spectroscopy was performed on these areas and showed peaks for titanium which means that these fragments are TiO_2. This observation was unique to the 100% NIR sample; the FTO grains of all other films were free from debris. It is unclear how the FTO grains became scattered with TiO_2. It could be that it was contaminated with speck of paste at the edges perhaps while removing the scotch tape from the sample. However due to the consistency of the coverage and its jagged appearance on the FTO grains it may be the high temperature attained by the FTO glass from 12.5 s of NIR exposure at the maximum power setting, 681°C, caused such a sudden rise in temperature driving off the binder that some TiO_2 was physically ablated away. This was not observed for other NIR heated samples of TiO_2.

It is expected that because of the grain growth observed for the 100% NIR sample it would be a substandard film for a DSC working electrode because of the reduced surface area. SEM

is limited to observing the surface of the films rather than a representing the entire film so it is not possible to conclude the properties of the bulk from this technique. X-ray diffraction was used to determine the crystal structure of NIR and oven heated TiO_2 films on FTO glass and the obtained spectra are shown in figure 5.22.

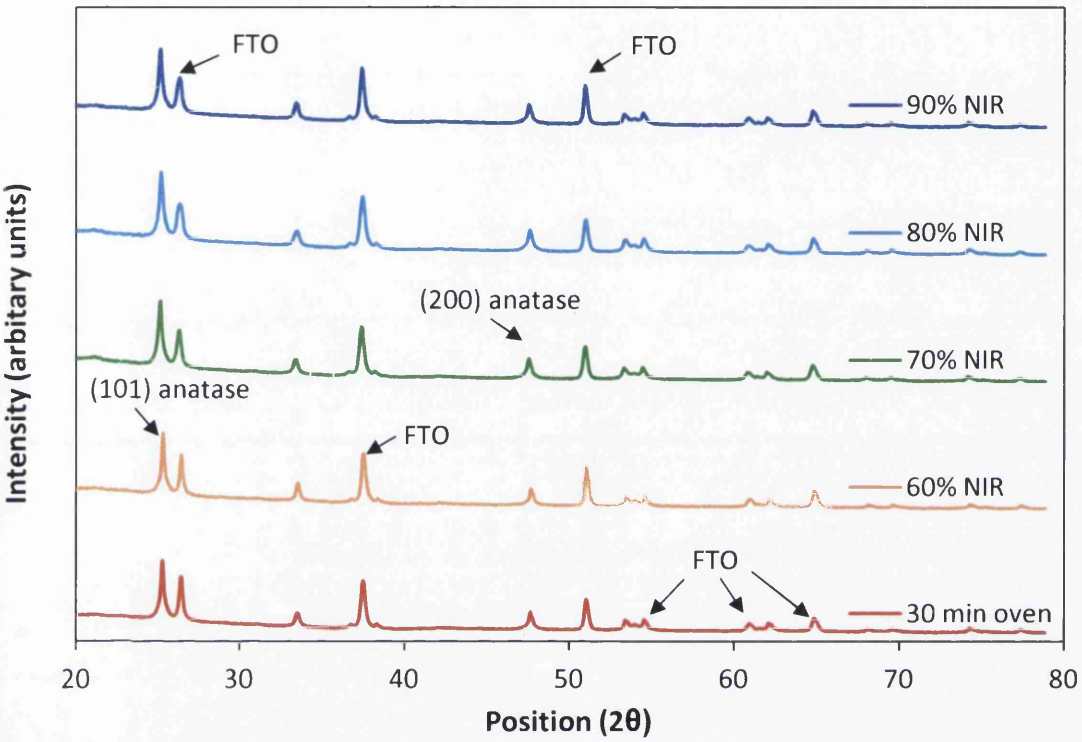

Figure 5.22: XRD spectra of NIR and oven heated TiO_2 films on FTO glass with annotated peaks

The XRD data for each film looked identical with no significant differences. All of the films show (101) and (202) anatase peaks and several peaks for the FTO grains. However no narrowing of the (101) anatase peaks was observed, which would to relate to a growth in the crystal size, and no rutile TiO_2 peaks were present. The NIR heating technique heats from the surface of the FTO upwards so the areas with the most prolonged exposure directly above this would have received the most thermal energy, more thermal energy than the surface as observed using SEM. Therefore XRD was used to determine if any grain growth beneath the surface but it has shown that there was none, and none of the NIR films reached the temperature required for rutile transformation. With an identical crystal structure to the oven heated films it is again anticipated that the NIR heated TiO_2 should perform similarly in a DSC device.

5.3.3 Using NIR heated TiO_2 to produce working electrodes on FTO glass for DSCs

Following on from the thermogravimetric analysis of the TiO_2 pastes in section 5.3.1, DSL 18NR-AO was chosen as the paste for NIR heated FTO glass working electrodes due to its complete removal of binder and solvent in 12.5 s and superior performance in DSC devices from scattering particles that increase photocurrent. 12.5 s NIR heated TiO_2 films were constructed into working electrodes for DSCs and compared to conventionally heated working electrodes that were prepared in oven at 450°C for 30 min (the average IV parameters under 1 sun illumination are shown in Table 5.5). The DSCs were assembled identically with a conventionally heated platinised counter electrode and had an active area of 1 cm^2. Figure 5.23 shows a graph of average efficiency against NIR intensity with a conventional oven comparison and current density shown inset for the same.

Table 5.5: Average parameters for NIR heated working electrode DSCs for 3 devices with 1 standard deviation of error

NIR (%)	V_{OC} (V)	J_{SC} (mA/cm^2)	FF (%)	Efficiency (%)
60	0.61	3.37	69.00	1.43
70	0.72 ± 0.01	8.44 ± 0.94	72.04 ± 0.99	4.37 ± 0.46
80	0.72 ± 0.01	8.00 ± 1.47	72.35 ± 0.11	4.16 ± 0.73
90	0.73 ± 0.00	9.57 ± 0.33	70.55 ± 1.98	4.94 ± 0.21
100	0.70 ± 0.00	8.90 ± 0.11	69.56 ± 2.10	4.32 ± 0.08
Oven	0.72 ± 0.00	9.29 ± 0.11	71.93 ± 1.93	4.83 ± 0.17

A maximum efficiency of 5.2% was obtained for 90% NIR DSC compared to 5% for a conventionally heated DSC for these simply constructed devices. The efficiency and current density show the same trend with the fill factors and open circuit voltages are fairly consistent for all cells except 60% NIR which has a poor V_{OC}. At 60% NIR intensity although the majority of the binder was removed the particles do not appear to be sufficiently sintered for charge transport as indicated by the low current density. With a maximum temperature of 487°C after 12.5 s exposure it is unlikely that the film would have been at a sufficiently high enough temperature for long enough to allow complete sintering during the time scale. At 70% NIR the maximum temperature is about 80°C higher allowing enough heat energy to transfer to particles to sinter more effectively. This continues to 648°C at 90% NIR intensity where sintering comparable to conventional sintering has occurred. At 100% NIR the efficiency is slightly lower due to a lower surface area for dye adsorption as suggested by the SEM in figure 5.20 because the high temperature has accelerated the sintering into crystal growth.

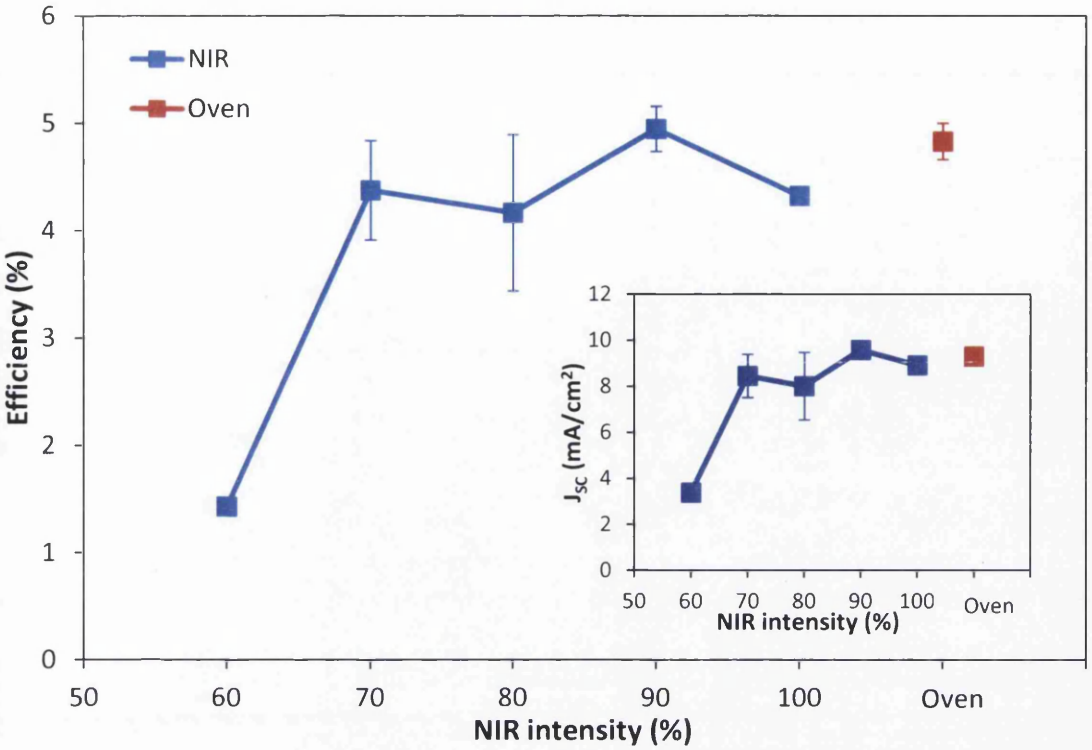

Figure 5.23: Average efficiency for 12.5 s NIR heated working electrode DSCs with 30 min oven DSCs on the left and average current density inset

As is shown the voltage is fairly constant (except 60% is rather low) and the fill factor is also fairly constant. As would be expected the main impact on efficiency in these devices is the current density which generally rises with increasing NIR lamp intensity. 60% NIR intensity has a very low current density and this was the only cell that worked. It suggests that the charge transport is extremely poor due to insufficient sintering of the TiO_2 film. So although TGA data shows at 60% NIR almost complete solvent and binder removal was achieved it appears as though adequate sintering was not. As with the current density the efficiency rises with increasing NIR intensity. 70% and 80% NIR intensity showed similar efficiencies but 80% had a larger variation. This is probably merely due to disparities in the cell building. 90% NIR was the highest performing intensity and showed equal efficiency to the oven heated identically constructed devices. This shows that a TiO_2 working electrode film produced in 12.5 s can perform as well as one produced in 30 min, 144 times faster.

DSCs were also constructed from oven heated working electrodes at 450°C with varying times to see the threshold for sufficient charge transport to create a working device. Figure 5.24 shows the average efficiency and average current density for these devices. A working electrode from 30 s heating in the oven was also attempted but due to the film still

containing binder it dissolved during the dyeing. TGA and FTIR data in section 5.3.1 showed that from 5 min oven heating all binder and solvent had been removed from the paste. The DSC devices show that a working electrode can be constructed from a 5 min heated film but with a compromise on current density. With increased time the TiO_2 particles continue to sinter together to improve charge transfer and thus increase current density as shown with 30 min as the most efficient. This reinforces the time dependent nature of the sintering of TiO_2 to achieve an equal charge transport to 30 min in a conventional oven and shows that the ability to do this in 12.5 s with the NIR absorption of FTO glass is extremely promising for achieving rapidly built DSCs with no compromise in efficiency.

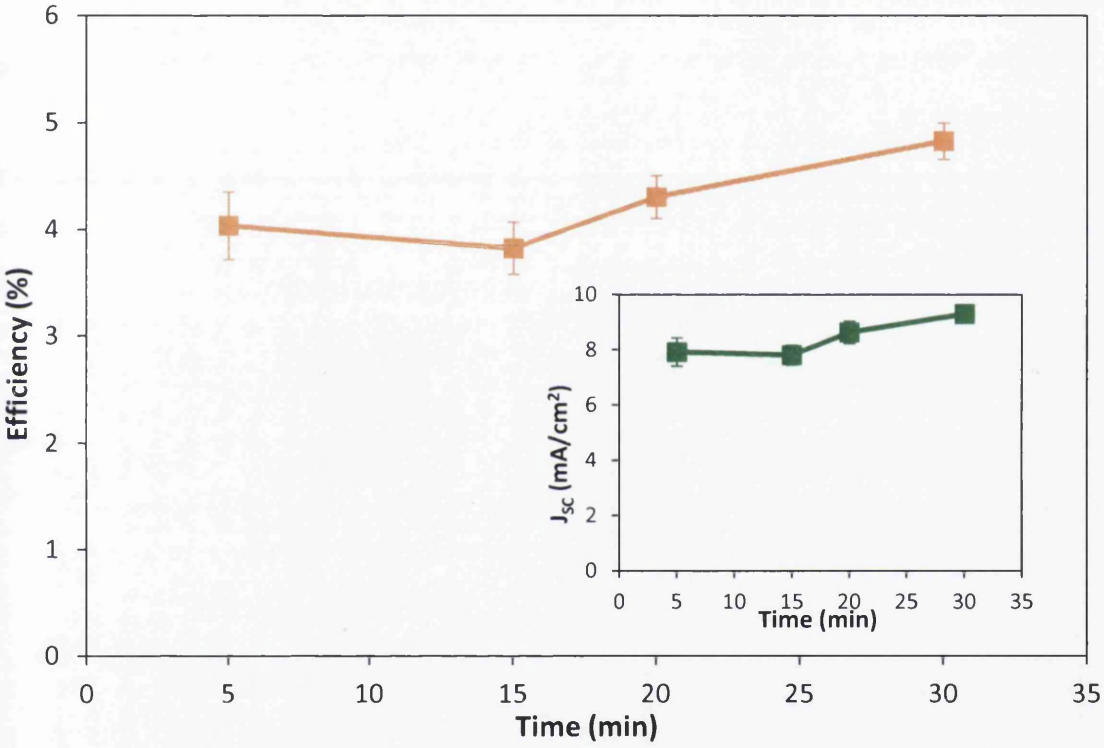

Figure 5.24: Average efficiency vs. time for oven heated working electrodes at 450°C with current density inset

Optoelectronic transient measurements as described in [11] were carried out to analyse the interconnectivity of the NIR heated TiO_2 films by determining the charge transport and recombination kinetics in DSC devices. Figure 5.25.a shows the charge density at V_{OC} measured via charge extraction. All devices except those exposed to 60% NIR lamp intensity have near identical charge densities, which could indicate a similar density of electronic trap states. The 60% NIR heated samples have received insufficient thermal energy in order to sinter effectively resulting in a decrease in trap states at the particle interface boundaries.

Figure 5.25.b shows the short circuit current transient lifetime vs. charge density at J_{SC} giving an indication of electron transport kinetics as a function of charge density. For all devices except 60% NIR the transport lifetime is similar, suggesting that the particle connectivity and trap density is comparable for conventionally sintered TiO_2 films and NIR heated films above 70% intensity; for 60% NIR the sintering the transport kinetics are faster due to fewer particle interface boundaries. Figure 5.25.c shows electron lifetime at open circuit voltage vs. V_{OC}, and figure 5.25.d shows the electron lifetime at open circuit voltage vs. the charge density at open circuit voltage, both giving an indication of recombination kinetics. This is measuring the rate at which the electrons in the TiO_2 recombine with I_3^- or I_2 to form I^- ions rather than being collected by the FTO layer. The fastest rate of recombination is observed in the 60% NIR heated devices suggesting that there are less available neighbouring TiO_2 particles to accept the electron, due to the poor sintering, increasing the chance of recombination. A broad trend is then observed whereby recombination increases with increasing NIR intensity. This supports an increasing density of trap states [11] as a consequence of improved sintering from increased thermal energy during NIR exposure. The exception to this trend is that devices sintered using the highest NIR lamp intensity at 100% show an increase in the rate of recombination. The increased crystal size shown in SEM and the slight decrease in J_{SC} seen in these devices could indicate a decrease in dye loading whilst still allowing recombination to take place so that there is more available surface area for recombination with I_3^- than in the other devices where dye loading is greater.

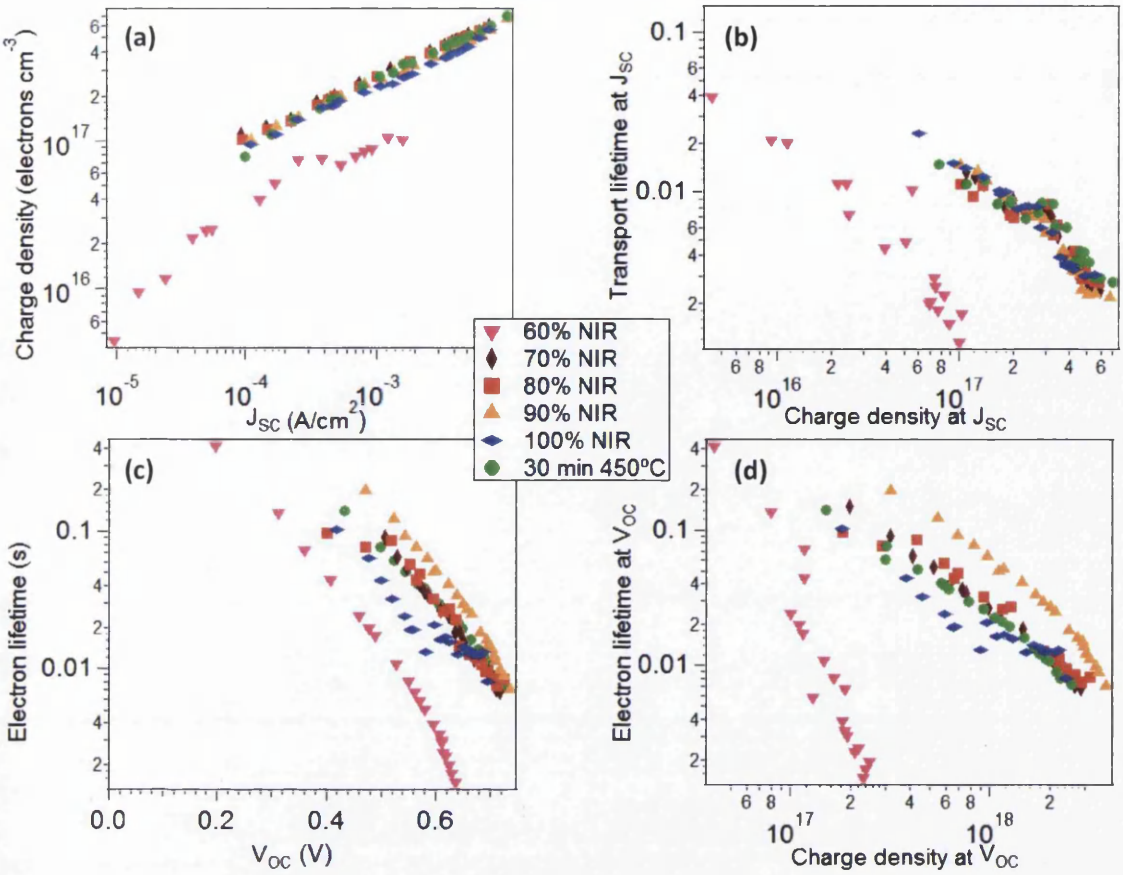

Figure 5.25: Optoelectronic transient measurements for (a) charge density vs. J_{SC}, (b) transport lifetime vs. charge density at J_{SC}, (c) electron lifetime vs. V_{OC}, and (d) electron lifetime at V_{OC} vs. charge density at V_{OC}

5.4 Conclusions

In this chapter NIR radiation was used to sinter TiO_2 onto FTO glass for the construction of a DSC working electrode with identical performance to a conventional device in only 12.5 s, a heating time reduction of 144 times. The use of NIR radiation to sinter TiO_2 films in 12.5 s has been previously demonstrated on metallic substrates but this is the first time it has been shown on glass based substrates. In the case of DSCs the ability to heat a working electrode on FTO glass eliminates the necessity of reverse illumination and any chemical incompatibilities associated with metals, allowing the potential for very high efficiency devices with fast manufacturing times.

Crucially the TiO_2 sintering stage of DSC manufacture shares many similarities to other technologies and applications, for example perovskite solar cells, solid state DSCs, and photocatalysts. So the use of NIR radiation to significantly reduce heating times on FTO glass could easily be expanded to other devices. Additionally it should be possible to achieve a

mesoporous film of any metal oxide similar, such as ZnO or Al_2O_3, that are contained in a similar paste where binder needs to be removed, with little modification to this method.

Finally this chapter again highlights FTO glass as a very compatible substrate for rapid heating to significantly high temperatures with NIR radiation. Potentially any electronic device based on FTO glass which requires a long heating step could benefit from this technique. The FTO layer was demonstratively shown to be an integral component for the NIR absorption, as discussed in Chapter 3, because TGA and FTIR data shows uncoated glass did not reach the temperatures required to remove binder from TiO_2 paste at NIR intensities where for FTO glass it did successfully remove it.

5.5 References

[1] B. O'Regan, J. Moser, M. Anderson, M. Grätzel, Vectorial electron injection into transparent semiconductor membranes and electric field effects on the dynamics of light-induced charge separation, J. Phys. Chem. 94 (1990) 8720–8726.

[2] B. O'Regan, M. Grätzel, A low-cost, high-efficiency solar cell based on dye-sensitized colloidal TiO_2 films, Nature. 353 (1991) 737–740.

[3] K. Kalyanasundaram, M. Grätzel, Applications of functionalized transition metal complexes in photonic and optoelectronic devices, Coord. Chem. Rev. 177 (1998) 347–414.

[4] T. Watson, I. Mabbett, H. Wang, L. Peter, D. Worsley, Ultrafast near infrared sintering of TiO_2 layers on metal substrates for dye-sensitized solar cells, Prog. Photovoltaics Res. Appl. 19 (2010) 482–486.

[5] M.J. Carnie, C. Charbonneau, P.R.F. Barnes, M.L. Davies, I. Mabbett, T.M. Watson, et al., Ultra-fast sintered TiO_2 films in dye-sensitized solar cells: phase variation, electron transport and recombination, J. Mater. Chem. A. 1 (2013) 2225.

[6] [Online]. Available at: http://www.dyesol.com/download/MSDS_Titania_Paste_transparent.pdf. [Accessed: 22-Jan-2013].

[7] [Online]. Available at: http://www.dyesol.com/download/MSDS_Titania_Paste_opaque.pdf. [Accessed: 24-Apr-2013].

[8] [Online]. Available at: http://www.solaronix.com/products/versatiletitania/tinanoxided/. [Accessed: 22-Jan-2013].

[9] M.K. Nazeeruddin, A. Kay, I. Rodicio, R. Humphry-Baker, E. Muller, P. Liska, et al., Conversion of Light to Electricity by cis-X_2Bis(2,2'-bipyridyl-4,4'-dicarboxylate)ruthenium(II) Charge-Transfer Sensitizers (X = Cl^-, Br^-, CN^-, and SCN^-) on Nanocrystalline TiO_2 Electrodes, J. Am. Chem. Soc. 115 (1993) 6382–6390.

[10] NIST Chemistry, [Online]. Available at: http://webbook.nist.gov/chemistry. [Accessed: 11-Sep-2013].

[11] P.R.F. Barnes, K. Miettunen, X. Li, A.Y. Anderson, T. Bessho, M. Grätzel, et al., Interpretation of optoelectronic transient and charge extraction measurements in dye-sensitized solar cells, Adv. Mater. 25 (2013) 1881–922.

Further Reading

K. Kalyanasundaram, Ed., *Dye-sensitized Solar Cells*, 1st ed. Lausanne: EPFL Press, CRC Press, 2010.

M. N. Rahanan, Ed., *Ceramic Processing and Sintering*, 2nd ed. New York: Marcel Dekker Inc., 2003.

D. Pavia, G. Lampman, and G. Kriz, *Introduction to Spectroscopy*, 2nd ed. Saunders College Publishing, 1996.

6. Tin-doped Indium Oxide Glass as a Substrate for High Temperature Processed Dye-sensitised Solar Cells

6.1 Introduction

Fluorine-doped tin oxide (FTO) remains the transparent conducting oxide (TCO) of choice in dye-sensitised solar cells (DSCs) due to its high temperature stability and relatively low cost. Tin-doped indium oxide (ITO) is a widely used TCO in the electronics industry and used in some solar cell technologies but is usually not used in DSCs since the high temperatures required to process DSCs (namely sintering of TiO_2 and thermal decomposition of platinum) would cause its resistivity to significantly rise [1][2]. There appears to be some discrepancy in the literature over the extent that this impairs the photovoltaic performance. C. Sima et. al reported an ITO glass working electrode DSC of efficiency 1.93% after sintering TiO_2 at 450°C for 2 hours in oxygen compared to an FTO glass device of 8.93% [2]. S. Lee et. al used hydrogen annealing and electrochemical treatment to produce an ITO glass work electrode. They used hydrogen to reduce the ITO film after sintering so that the oxygen vacancies were recovered, then the TiO_2 film was electrochemically oxidised because H_2 annealing generates defects in TiO_2 [3]. The ITO glass working electrode device had an efficiency of 4.4% compared to 3.3% with no hydrogen annealing (untreated ITO) and the FTO glass device was 4.3%, all were sintered in an O_2 atmosphere at 450°C for 1 hour so the untreated ITO glass device does seem strangely efficient and even had the highest current density. However without resorting to lengthy rescue processes it still remains a problem to build a DSC on ITO glass if not using low temperature techniques. Vacuum annealing is another method to recover the lost oxygen vacancies in indium oxide films and regain some conductivity [4].

The main advantage of ITO over FTO is that it has a higher carrier concentration, almost by a factor of two, because the solubility of fluorine in SnO_2 is inferior to that of Sn in In_2O_3 [5]. There have been some attempts to combine ITO and fluorine-doped tin oxide (FTO) to utilise the high conductivity of ITO with the high temperature stability of FTO. An FTO coated ITO film was deposited via spray pyrolysis by T. Kawashima et. al with a resistivity of 1.4×10^{-4} Ωcm, visible transparency of >80% and after exposure of 300-600°C for 1 hour in air there was just a 10% increase in resistivity [6]. DSC devices have been constructed from double layer TCOs with efficiencies of 3.7% (FTO/ITO) [7] and 6% (SnO_2/ITO) [8]. This is another example of the desire to use ITO as a conducting layer in DSCs.

In Chapter 3 of this work it was shown that an alternative heating technique, near infrared (NIR) radiation, can heat ITO glass without a large increase in resistivity. The ITO glass was exposed to 12.5 s of NIR radiation at various lamp intensities. It was shown that with NIR heating of ITO glass, as a consequence of the extremely rapid temperature rise, the detrimental rise in resistivity is severely reduced. The short exposure limits the time dependent oxygen diffusion up to an extent but at higher temperatures the oxygen diffusion is faster therefore there is some resistivity rise. At 90% NIR intensity and below the rise in resistivity is not significant, 90% NIR (max temperature 523°C) resulted in a sheet resistance of 18.3 Ω/□, so it is hoped that it may be possible to reach temperatures capable of creating a working DSC on ITO glass without a sharp rise in resistivity.

In Chapters 4 and 5 DSCs were constructed using an NIR heated FTO glass counter electrode and working electrode respectively with the optimal maximum temperature after 12.5 s NIR exposure of 605°C for platinisation and 648°C for sintering of TiO_2. This is higher than for the conventional methods, 385°C and 450°C, because the NIR method occurs much faster and requires an accumulation of enough thermal energy to achieve sufficient heating in such a short timeframe. This suggests that the potential thermal platinisation and TiO_2 sintering on ITO glass will be suboptimal if sheet resistance is to be maintained; because the substrate used in this work has a thin layer of ITO (150 nm of ITO compared to 600 nm of FTO for FTO glass) it does not absorb as highly in the IR region so fewer photons will interact to release thermal energy. However the NIR technique offers a range of processing temperatures for similar performance and sufficient platinisation and TiO_2 sintering on FTO glass was achieved at a minimum max temperature of 488°C and 564°C respectively. Although it is unlikely that an ITO glass DSC device will perform as well as an FTO glass one the main purpose of this work is to demonstrate that it can be done and that most importantly other TCOs are suitable for NIR treatment.

6.2 Experimental

Prior to manufacturing DSC devices the prospective NIR heated counter electrodes were characterised as follows. ITO glass (13 Ω/□, Sigma Aldrich) was coated with 3 drops of 5 mM chloroplatinic acid in propan-2-ol using a capillary tube (section 2.2.2) and heated either in a conventional oven at 385°C for 30 min or using NIR radiation at a speed of 2 m/min for 12.5 s lamp exposure (section 2.1.1). Scanning electron micrographs were taken of one of the samples (section 2.11). Cyclic voltammetry was performed on the platinised ITO glass in a 3

electrode set up. The catalytic performance of NIR heated and conventionally heated Pt to reduce triiodide was tested using an I^-/I_3^- electrolyte solution in acetonitrile with a Ag/Ag^+ reference electrode and platinum mesh counter electrode (section 2.7) between the potentials of -0.5 and 0.8 V with a scan rate of 50 mV/s.

To assess the performance of counter electrodes built on ITO glass DSCs were constructed (section 2.2.2) with $TiCl_4$ treated oven heated TiO_2 film working electrodes on FTO glass and NIR heated counter electrodes (section 2.1.1) on ITO glass exposed for 12.5 s. Their photovoltaic properties were characterised using a solar simulator (section 2.3) and electrochemical impedance spectroscopy (EIS) (section 2.6).

Titanium dioxide films were prepared by doctor blading DSL 18NR-AO paste onto ITO glass. They were heated in a conventional oven at 450°C or by 12.5 s of NIR radiation (section 2.2.2). The binder removal of the films was investigated using FTIR-ATR (section 2.9) and the appearance of the films was imaged using SEM (section 2.11).

To assess the sintering of the NIR heated TiO_2 particles DSC devices were constructed (section 2.2.2) with NIR heated ITO glass working electrodes and oven heated FTO glass counter electrodes. IV measurements (section 2.3) and optoelectronic transient measurements (section 2.5) were used to characterise them. Finally DSC devices with both ITO glass working electrode and ITO glass counter electrode (figure 6.1) were built from the optimal NIR settings found.

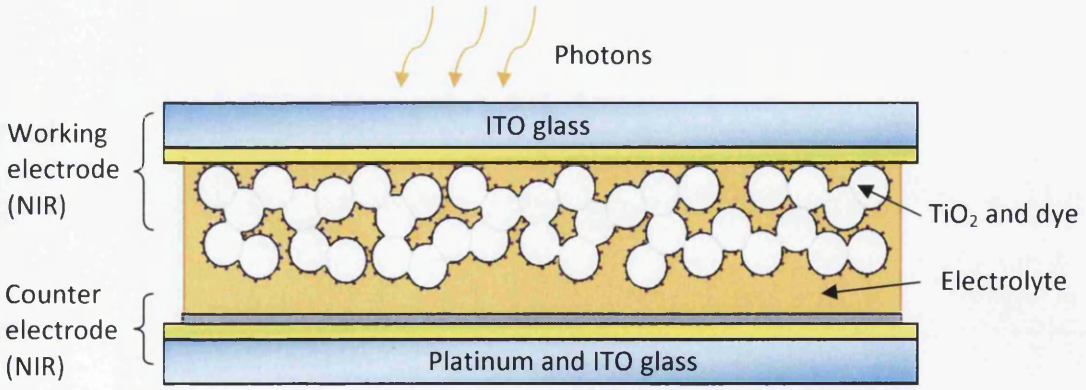

Figure 6.1: Diagram of DSCs constructed on ITO glass with heating method shown in brackets

6.3 Results and discussion

6.3.1 Thermal platinisation of ITO glass using NIR radiation

6.3.1.1 Characterisation of rapidly heated chloroplatinic acid

It was shown in Chapter 4 that 5 mM chloroplatinic acid does not absorb significantly in the NIR region at the quantities used for conventional thermal platinisation so NIR heated chloroplatinic acid coated onto ITO glass is expected to achieve but not exceed the temperatures estimated in Chapter 3 with 12.5 s exposure, shown in Table 6.1. That is, ITO coated with a layer of chloroplatinic acid will heat up in the same way as the bare ITO glass investigated previously. Figure 6.2 shows a scanning electron micrograph of chloroplatinic acid on ITO glass exposed to 70% NIR intensity radiation for 12.5 s.

Table 6.1: Temperatures estimated in Chapter 3 for 12.5 s NIR exposed FTO glass

NIR intensity (%)	Max temperature (°C)
40	200
50	300
60	382.4
70	481.1
80	504.9
90	523.3
100	552.6

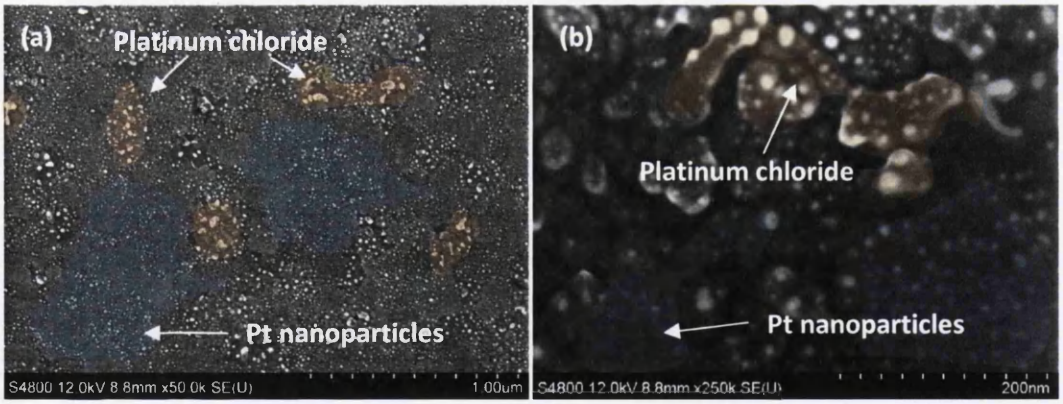

Figure 6.2: SEM image of 70% NIR intensity chloroplatinic acid on ITO glass at (a) 50k and (b) 250k magnification with some areas of Pt and $PtCl_2$ labelled

At low magnification (figure 6.2.a) there appears to be a number of particles of various sizes spread evenly over the ITO grains. Some of these resemble platinum nanoparticles and this was confirmed with EDX. They are about 20 nm, similar in size to those on NIR heated FTO glass but the coverage appears to be more substantial which may be due to the smoother ITO grains either facilitating better adhesion. Alternatively it may be that in the case of the

rough FTO grains the depth of field of the SEM does not allow all the nanoparticles to be in focus. At 70% NIR intensity the ITO glass should reach 481°C upon exit from the lamps which is similar to 60% NIR exposure for FTO glass. In some areas there are very large agglomerates; figure 6.2.b shows one of these agglomerates at higher magnification. It is approximately 100 nm in size and resembles platinum chloride (most likely as $PtCl_2$ rather than $PtCl_4$ because the high occurrence of Pt suggests most decomposition of platinum chloride would have occurred).

Cyclic voltammetry (theory in section 1.5.4) was used to assess the prospective NIR heated platinum counter electrodes on ITO glass (section 2.7). As discussed in section 4.3.1 to evaluate the performance of the platinum for use as a counter electrode in DSCs cyclic voltammetry was run in an I^-/I_3^- system giving an indication of its ability to facilitate the charge transfer reactions that occur between the species of:

$$2I_3^- \underset{+2e^-}{\overset{-2e^-}{\rightleftharpoons}} 3I_2$$

$$3I^- \underset{+2e^-}{\overset{-2e^-}{\rightleftharpoons}} I_3^-$$

The reaction of importance in a DSC is the cathodic reaction, $I_3^- + 2e^- \rightarrow 3I^-$ (the reduction of triiodide to iodide), which occurs at the counter electrode, as it keeps the supply of I- ions available to donate an electron to the oxidised dye ($2S^+ + 3I^- \rightarrow 2S + I_3^-$) so that this can then absorb another photon. If there is insufficient platinum present the charge transfer will be sluggish, this will be shown by the cyclic voltammetry as broader less reversible peaks. If there was no catalytic activity then no redox reactions will occur. The rise in sheet resistance of ITO after heating which was discussed in Chapter 3 will also affect the charge transfer increasing the difficulty for the electrons to reach the external circuit. This is a quasi-reversible system; it is slower in the reverse direction than the forward direction (insufficient to maintain Nernstian equilibrium) so it cannot perfectly match the reversible diagnostic criteria [9] but it is not totally irreversible and it is possible to compare against different platinum samples. Reversibility describes the ease of electron transfer for the reaction; if it is facilitated in both directions and sustainable then it is more efficient. If a platinum sample was more reversible in the I^-/I_3^- system this suggests it would be a better catalyst in a DSC.

Figure 6.3 shows cyclic voltammograms of 12.5 s NIR exposed and oven heated (30 min at 385°C) chloroplatinic acid on ITO glass and Table 6.2 shows the corresponding data extracted from the cyclic voltammograms to give an indication of the reversibility [9]; peak separation, ΔE_p, ratio of the peak current densities ($|j^a_p/j^c_p|$) as well as the sheet resistance, R_{sh}, after heating of ITO glass from Chapter 3.

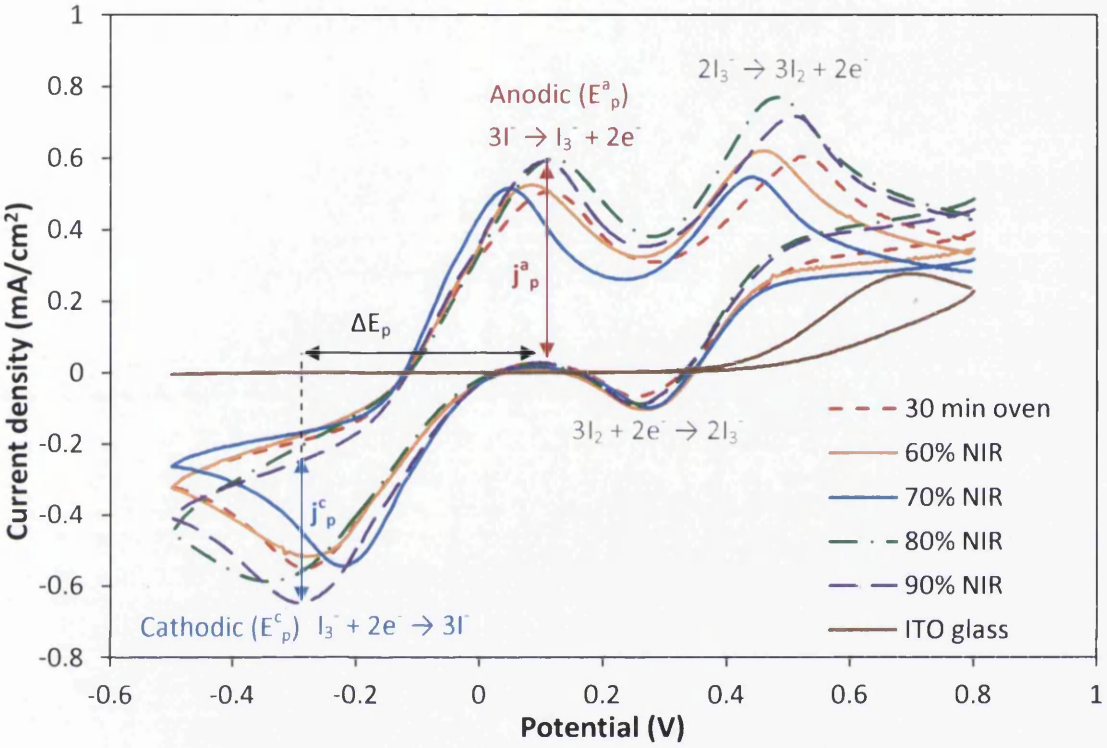

Figure 6.3: Cyclic voltammograms of NIR heated chloroplatinic acid (12.5 s exposure) and oven heated chloroplatinic acid (30 min at 385°C) on ITO glass in iodide electrolyte at a scan rate of 50 mV/s

Table 6.2: Data from cyclic voltammetry for peak separation and peak current density ratio with corresponding measured ITO glass sheet resistance from heating method

Sample	ΔE_p (V)	j^c_p (mA/cm^2)	j^a_p (mA/cm^2)	j^a_p/j^c_p	R_{sh} (Ω/□)
60% NIR	0.36	-0.35	0.51	1.48	12.91
70% NIR	0.265	-0.40	0.51	1.26	13.17
80% NIR	0.45	-0.34	0.58	1.70	15.39
90% NIR	0.395	-0.40	0.57	1.41	18.27
30 min oven	0.395	-0.36	0.48	1.34	39.5

As is expected bare ITO glass substrate has no ability to facilitate the redox reactions in this electrolyte. However all of the NIR and oven thermally platinised ITO glass samples do show affinity to this redox system albeit with massive variations in the peak separations and peak current density ratios. The 60% NIR heated chloroplatinic acid on ITO glass has a close peak separation, an adequate peak current density ratio and fairly well defined peaks which suggests that the platinum is facilitating the redox reactions well. Similarly to lower NIR intensity heated Pt on FTO glass in section 4.3.1 it has lower current values than the other samples. This may indicate that there is less platinum present because there is some unconverted platinum chloride, as would be expected from the lower temperature reached of only 382°C, but that the platinum nanoparticles present are catalytic. The 70% NIR sample has the smallest peak separation, significantly smaller than the other samples, and the best peak current density ratio, much closer to 1 than the others suggesting better reversibility of the triiodide reduction reaction. The current values are fairly similar to 60% NIR and still fairly small. SEM did suggest that there was some unconverted platinum chloride and the temperature estimated for 70% NIR heated ITO glass corresponds well to 60% NIR heated FTO glass which also showed residual $PtCl_2$ but still functioned in a DSC device with adequacy. Unlike 60% NIR heated ITO glass there is a slight increase in sheet resistance for the bare ITO glass heated in Chapter 3 (0.2 Ω/□) but this is most likely negligible.

80% NIR intensity has the further peak separation and poorest peak current density ratio which is out of the trend of 90% NIR which seems to recover some catalytic activity so may be an experimental abnormality. 80% NIR also has a very broad cathodic peak showing that the charge transfer here is sluggish and not very reversible. They both show much higher current values than the other samples which may indicate that the majority of platinum chloride has been converted to platinum so there is more platinum present to facilitate charge but it is not as reversible as others. As is reiterated in Table 6.2 there should be some resistivity rise for these samples as measured in Chapter 3, a rise of 2.4 and 5.4 Ω/□ respectively, but it does not seemed to have manifested itself here as it is still relatively low. 30 min oven shows marginally poorer peak separation and peak current density ratio but comparable to 90% NIR. It is predicted to have a sheet resistance of around 39.5 Ω/□ (extrapolated at 385°C from the sheet resistance vs. temperature plot for 30 min oven heating in section 3.3.3) which is fairly high so it may be expected to manifest itself in the performance.

Figure 6.4 shows the cyclic voltammogram of 70% NIR heated chloroplatinic acid on ITO glass with the optimal NIR heated FTO glass and conventional oven on FTO glass for comparison from Chapter 4. The peaks appear much closer in the platinised ITO glass and more defined which indicates it has higher reversibility for the iodide redox reactions than the NIR and oven platinised FTO glass samples. An important point to note is that 60% NIR intensity on FTO glass also showed the best catalytic reversibility but contained platinum chloride that reduced the potential platinum surface and thus its performance in a DSC device (but although suboptimal still very functional). 70% NIR intensity on ITO glass was shown in Chapter 3 to reach a similar temperature than 60% NIR exposed FTO glass, 481°C compared to 488°C, so it would suggest that in 12.5 s insufficient thermal energy would be received for full conversion as also indicated by the SEM images of 70% NIR heated ITO glass. However although the cyclic voltammetry may not be a direct correlation to DSC performance, as was observed in Chapter 4, it is still promising that the 70% NIR heated ITO glass sample shows great catalytic activity especially compared to the two FTO glass samples.

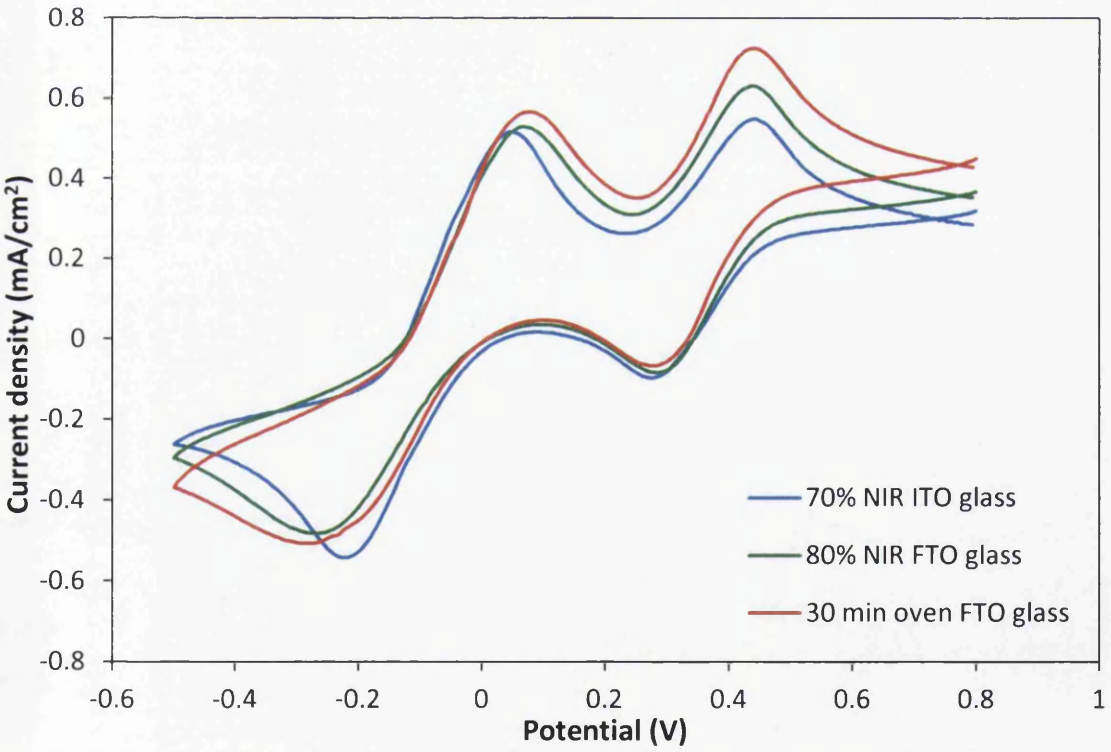

Figure 6.4: Cyclic voltammograms of NIR heated chloroplatinic acid (12.5 s exposure) on ITO glass with the DSC device optimal NIR heated FTO glass and oven heated FTO glass (from Chapter 4) in iodide electrolyte at a scan rate of 50 mV/s

6.3.1.2 Dye-sensitised solar cells with a rapidly heated ITO glass counter electrode

DSC devices were constructed incorporating an NIR heated counter electrode on an ITO glass substrate with a standard conventionally heated FTO glass working electrode. Figure 6.5 shows the average efficiency of these devices, which were all heated for 12.5 s, against NIR lamp intensity with an oven heated ITO glass counter electrode DSC included. Inset the graph is the average fill factor of these devices which is related to the ability of the catalyst to reduce triiodide. Table 6.3 shows the average PV parameters for the ITO glass counter electrode DSCs and an oven heated FTO glass counter electrode device with identical working electrode as a comparison.

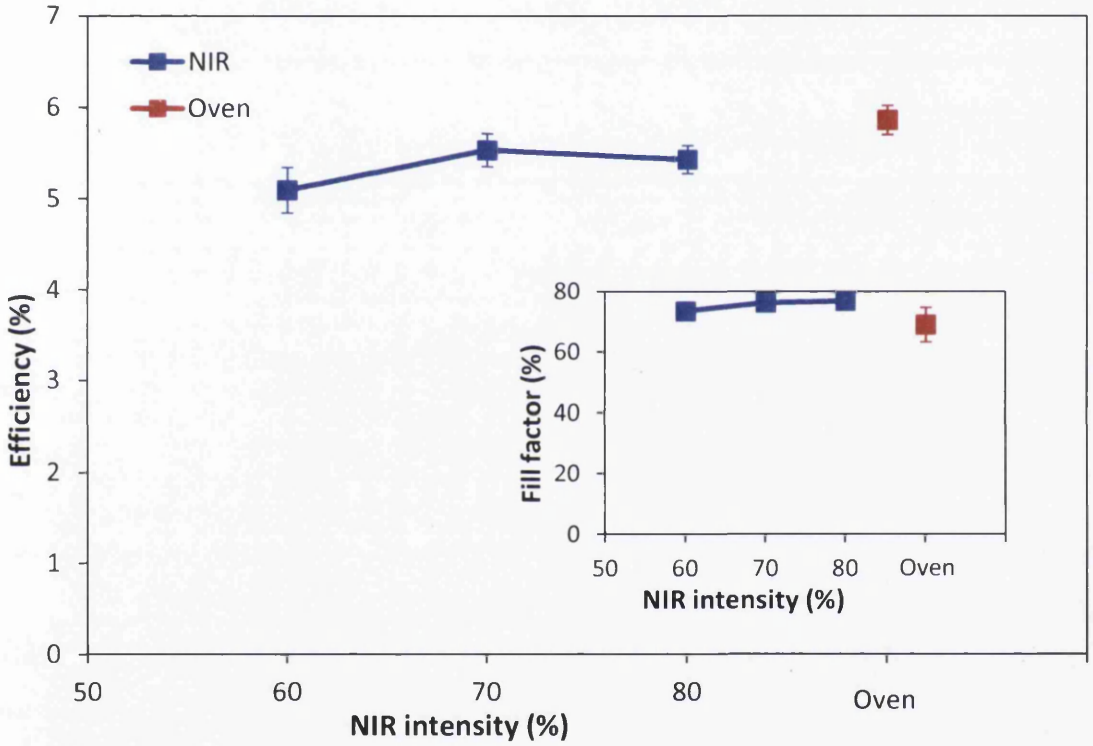

Figure 6.5: Average efficiency vs. NIR lamp intensity for 12.5 s heated ITO glass counter electrode DSC devices and oven heated ITO glass; inset the same for average fill factor

Table 6.3: Average parameters of 3 devices for ITO glass counter electrode DSCs and an equivalent FTO glass DSC, error is 1 standard deviation

NIR (%)	V_{OC} (V)	J_{SC} (mA/cm^2)	FF (%)	Efficiency (%)
60	0.73 ± 0.01	9.43 ± 0.36	73.46 ± 2.13	5.09 ± 0.25
70	0.74 ± 0.00	9.80 ± 0.34	76.32 ± 1.76	5.53 ± 0.18
80	0.74 ± 0.00	9.49 ± 0.27	76.86 ± 0.35	5.43 ± 0.15
Oven ITO glass	0.73 ± 0.03	11.73 ± 1.84	69.05 ± 5.69	5.86 ± 0.16
Oven FTO glass	0.77 ±0.01	13.08 ± 0.75	64.33 ± 2.03	6.48 ± 0.19

The efficiency of all devices is fairly consistent. For the oven devices the efficiency seems to be very high despite the significant rise anticipated in the sheet resistance (as proposed in Chapter 3) conversely the fill factor is lower than that of the others. It is predicted to have a sheet resistance, R_{sh}, of around 39.5 Ω/□ after 30 min of heating in an oven at 385°C, significantly higher than the starting R_{sh} of 13 Ω/□. This should impair the transfer of electrons at the counter electrode to the triiodide. The oven heated counter electrode does show an extremely high variation in both the current density and the fill factor, the higher J_{SC} explaining why the average FF is lower, suggesting the behaviour of the oven heated cells is not very reproducible. There was noticeable noise in the IV curves of the oven DSCs likely due to this higher resistance but was not present for the NIR heated DSCs which had smooth IV curves. For the NIR heated counter electrodes there is a slight peak at 70% NIR intensity with 60% and 80% NIR intensity showing slightly lower although similar efficiencies. This supports the cyclic voltammetry data which showed 70% NIR to be the most reversible and thus suggested it to work well as a DSC catalyst, although it contradicts the cyclic voltammetry data obtained for the 80% NIR sample which was most likely experimental error. The optimum ITO glass counter electrode device, 70% NIR, is 0.85 times the efficiency of an oven heated FTO glass device and 0.87 times that of a NIR heated FTO glass device which is fairly acceptable considering the platinum conversion was predicted to be suboptimal at the temperature it reached. The ITO glass substrate also has a higher original as purchased R_{sh} than the FTO substrate, 13 Ω/□ compared to 7.5 Ω/□, which would possibly contribute to a lower efficiency.

The resistance of the triiodide charge transfer process was analysed for the DSC devices using electrochemical impedance spectroscopy (EIS) to serve as a measure of catalytic performance. Figure 6.6 shows the charge transfer resistance at the counter electrode, R_{CE}, against V_{OC} modelled from impedance measurements of the 12.5 s NIR heated and 30 min oven heated ITO glass counter electrode DSCs. The 60% and 70% NIR heated cells show the lowest R_{CE} with 80% at higher R_{CE} (this particular cell has slightly higher R_{CE} than some of the other 80% cells which lie between this and 60% NIR but is more illustrative of the overall problem of rising R_{CE} with higher intensity NIR exposure). The oven cell has the highest R_{CE} and all cells show a sharp rise in R_{CE} at less negative measuring potential. The low R_{CE} of 60% and 70% NIR heated counter electrodes show that the charge transfer between platinum and triiodide is occurring with little resistance which suggests that the platinum is catalytically active. This is fairly well supported by the photovoltaic data and cyclic

voltammetry data. Both 80% NIR and the oven cell have higher R_{CE} because their sheet resistance has increased which impairs the TCO's ability to transfer electrons to the platinum to subsequently reduce the triiodide.

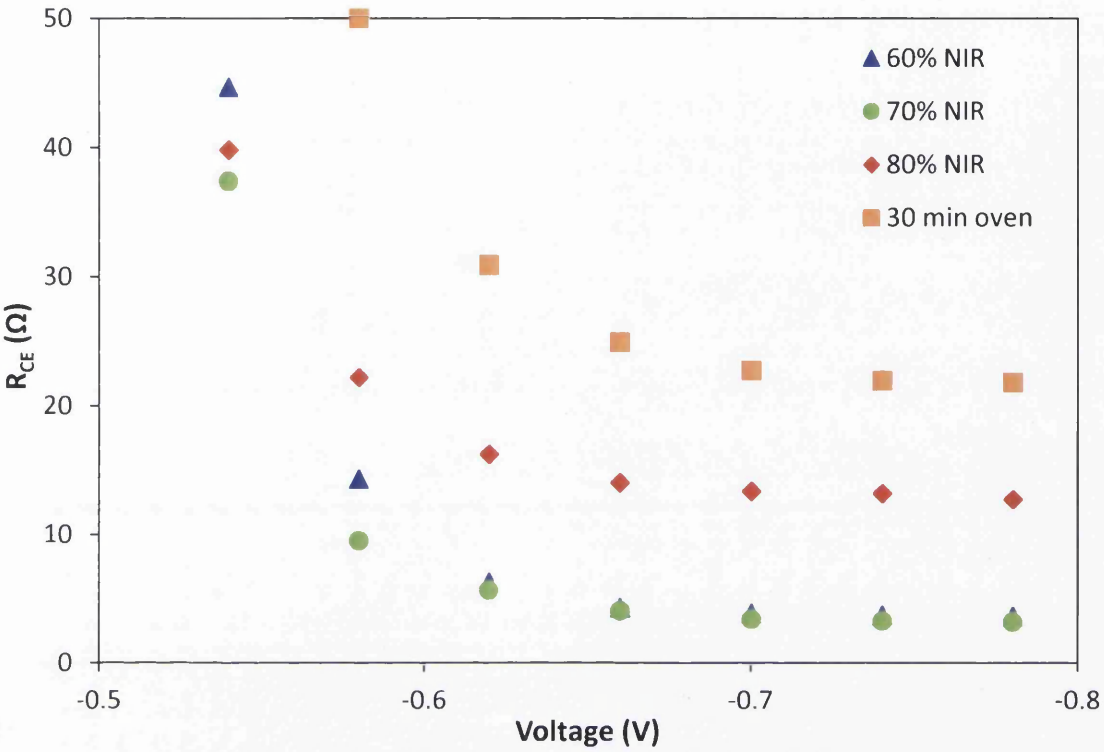

Figure 6.6: Resistance at counter electrode vs. measuring potential obtained from impedance spectroscopy for NIR and oven heated ITO glass counter electrode DSCs

Series resistance, R_s, was also obtained from the EIS data, at a bias of -0.78 V. The series resistance in this model is represented by a single resistor so the FTO R_{sh} and the ITO R_{sh} cannot be distinguished (of the working electrode and counter electrode substrates). However for an FTO glass cell the R_s is usually the same value as the sheet resistance of the substrate e.g. 7 Ω. For 60% NIR the R_s is 14 Ω which closely matches the R_{sh} of the ITO substrate used. The R_s steadily increases for the NIR heated cells and is extremely high for the oven cell. The series resistance obtained from EIS and sheet resistance measured in Chapter 3 for the bare ITO glass substrates was plotted together in figure 6.7 to compare the impact the resistivity rise is having on the cell performance compared to previous isolated substrate readings and give an indication of ITO's thermal degradation.

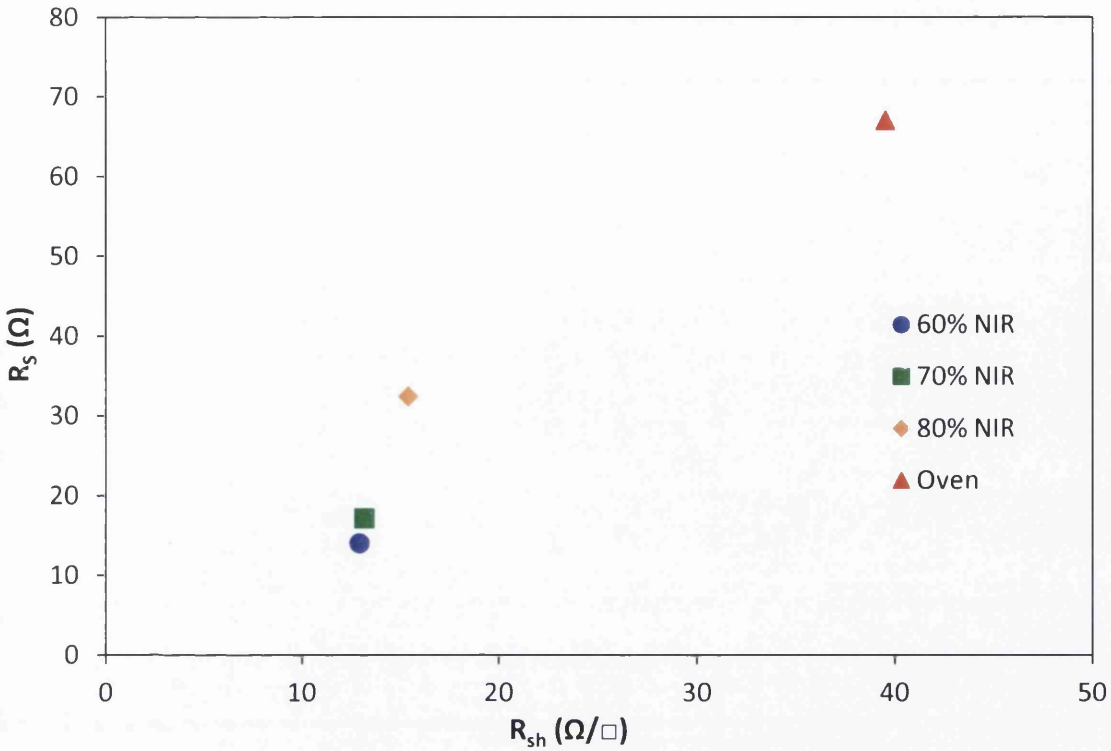

Figure 6.7: Series resistance for ITO glass counter electrode cells vs. sheet resistance for ITO glass after heating with the same technique

This illustrates the discrepancy between the R_s obtained for the DSC devices and the R_{sh} measured for heated ITO glass, although there is an additional contribution for the DSCs from the two different TCO types, since the working electrode is 7.5 Ω/□ FTO glass. For the 60% cell the values are fairly similar but the R_s becomes increasingly higher than the R_{sh} for uncoated ITO glass with higher NIR intensity. The series resistance of the oven cell is extremely high, even higher than predicted in Chapter 3, which explains the manifestation of high noise in the IV curve. Promisingly the series resistance isn't too much higher than predicted for the 70% NIR DSC. Together with its good performance as a catalyst shown by cyclic voltammetry and in DSC devices it appears to be a viable alternatively to sputtered platinum on ITO glass and entirely possible to thermally decompose platinum on ITO glass without severely increasing the sheet resistance while still achieving 0.85 times the efficiency of an equivalent FTO glass device.

6.3.2 Sintering of TiO_2 on ITO glass using NIR radiation

6.3.2.1 Characterisation of rapidly heated TiO_2 paste

In Chapter 5 the binder removal of three different commercial pastes was investigated on FTO glass and it was discovered that NIR radiation was able to remove all binder for NIR heated DSL 18NR-AO paste (9 µm dry film) on FTO glass. Therefore this paste was chosen for the NIR heating of ITO glass working electrodes as it produces DSCs with higher photocurrent than the other two pastes. It should also be recalled that DSL 18NR-AO absorbs some NIR radiation which may enhance its heating locally within the film which should also hopefully enable the TiO_2 to sinter with less damage to the ITO layer. To analyse the binder removal of the DSL 18NR-AO TiO_2 paste for each heating technique on ITO glass FTIR-ATR was used. Figure 6.8 shows FTIR spectra overlaid for the components of the paste (anatase TiO_2 [10], terpineol [10] and ethyl cellulose) with wet DSL 18NR-AO paste. The relevant peaks for each functional group have been annotated A-J and are described in Table 6.4.

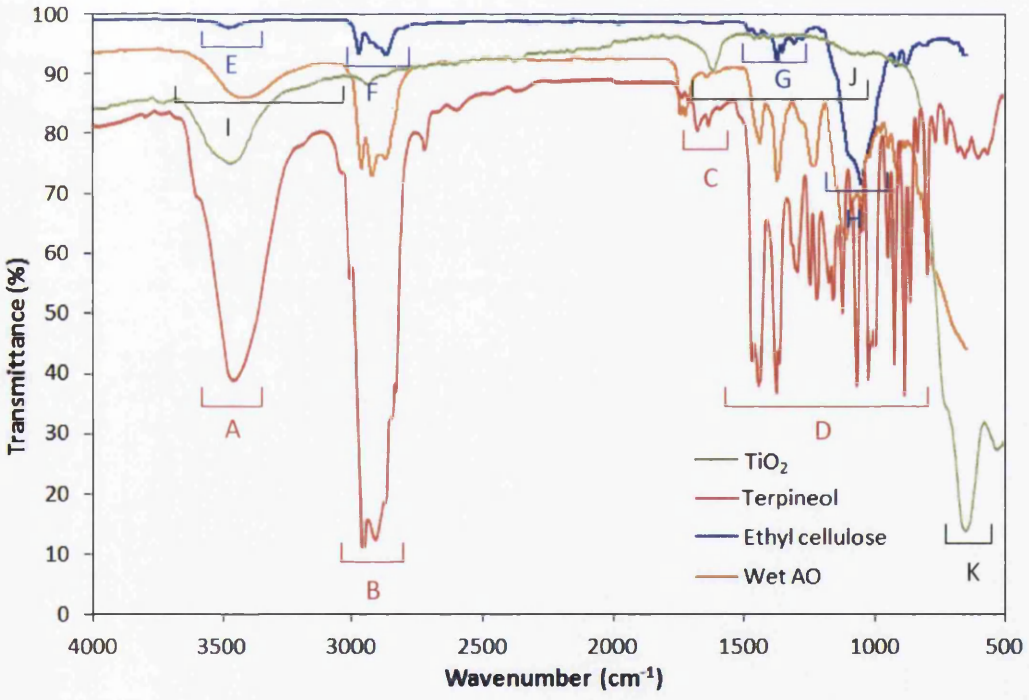

Figure 6.8: FTIR spectra of wet DSL 18NR-AO paste with TiO_2 [10], terpineol [10] and ethyl cellulose

Table 6.4: Functional group peak labels and locations as annotated in figure 6.8

Peak	Source	Range (cm^{-1})
A	Terpineol	3600-3250
B	Terpineol	3050-2750
C	Terpineol	1800-1670
D	Terpineol	1550-750
E	Ethyl cellulose	3550-3450
F	Ethyl cellulose	3050-2750
G	Ethyl cellulose	1500-1300
H	Ethyl cellulose	1300-900
I	TiO_2	3700-2700
J	TiO_2	1800-1350
K	TiO_2	800-500

As discussed in Chapter 5 the terpineol peak A is attributed to an OH stretch as is the ethyl cellulose peak E which has a smaller range due to the fewer OH bonds. Peaks B and F correspond to stretching of CH bonds for terpineol and ethyl cellulose respectively and have different shapes. Peak C is a C=C stretch and D bending of CH bonds. The ethyl cellulose peaks G and H correspond to CH_2 and CH_3 bending, and out of plane bending of CH bonds. Peaks I, J, and K are absorption peaks for anatase phase TiO_2. The wet DSL 18NR-AO paste shows each of these peaks, some differ slightly due to the different isomers of terpineol and crystal sizes of anatase TiO_2. Figure 6.9 shows transmittance vs. wavenumber for NIR exposed DSL 18NR-AO paste for 12.5 s on ITO glass at varying NIR lamp power obtained with FTIR-ATR. 30 min oven heated TiO_2 paste on ITO glass was not measured because its spectra would be identical to that of other substrates as seen in Chapter 5 and it is established that 450°C in a conventional oven is sufficient to remove all binder and sinter the TiO_2 film regardless of the substrate used so this can be safely assumed.

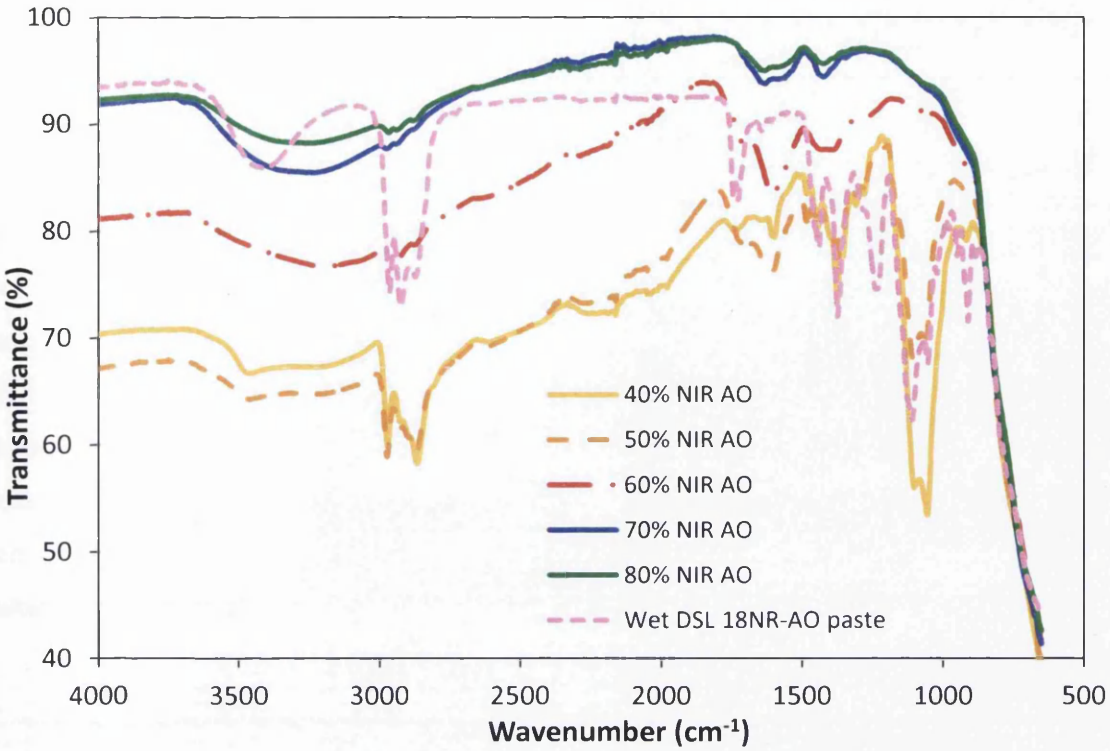

Figure 6.9: Transmittance vs. wavenumber for DSL 18NR-AO paste heated with NIR for 12.5 s at various lamp intensities

The wet paste sample (unheated) shows all peaks as it contains each component of the paste. Some peaks such as the two TiO_2 peaks are hard to distinguish and are masked by the other peaks present in the same range. As the ITO glass is heated by NIR radiation the terpineol associated peaks begin to diminish. 40% NIR heated ITO glass shows a very weak peak at C which corresponds to terpineol suggesting a low quantity of solvent may still be trapped in the film. It shows all the peaks associated with ethyl cellulose because all the binder remains. The trend is similar for 50% NIR heated ITO glass but the terpineol peaks seem to have disappeared, the TiO_2 peaks are becoming slightly more prominent and the peak at H for ethyl cellulose is reducing. The difference between 50% and 60% NIR is extremely pronounced. All ethyl cellulose and terpineol peaks have disappeared and there is a very strong TiO_2 peak at J. 70% and 80% NIR are the same as 60% but their transmittance is higher and the peak at J smaller and also appears to be a slightly different shape. This may be simply due to the loading of TiO_2 particles on the ATR crystal.

The FTIR-ATR spectra of TiO_2 on ITO glass are similar to those on FTO glass for equivalent NIR intensities as shown in figure 6.10. This is slightly contradictory to the different temperatures obtained for each substrate The 60% NIR FTO glass sample is similar to the

60% NIR ITO glass sample with the same shape and strength at peak J. They also both have less transmittance than the higher NIR intensity samples, the FTO sample slightly above the ITO sample. The two 70% and 80% NIR samples vary slightly around peak C but overlap elsewhere; these samples all have complete binder removal. This reinforces the remarkable lack of difference between the ITO glass and FTO glass samples suggesting that they reached a similar temperature to each other, both from underneath by the TCO and glass heating and from within from the TiO_2 paste absorbing radiation and heating to aid with the binder removal. It may be that each substrate is within a similar stage of the binder removal temperature window for each intensity. It could also be that because the ITO layer is much thinner than the FTO layer, 150 nm compared to 600 nm, that it heats up faster and so is at an elevated temperature for longer despite not reaching the same temperature. Therefore it would receive a similar amount of thermal energy overall.

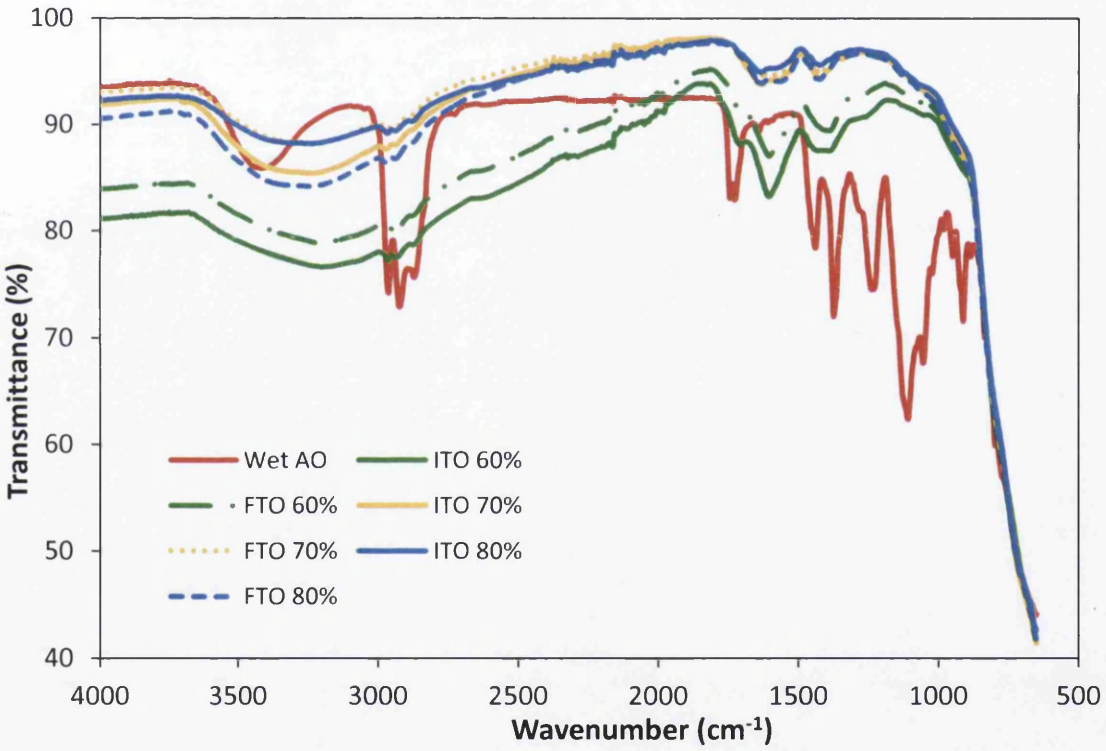

Figure 6.10: Transmittance vs. wavenumber for selected NIR heated ITO glass and FTO glass TiO_2 samples

Figure 6.11 shows scanning electron micrographs of 70% NIR heated TiO_2 on ITO glass compared to 90% NIR heated FTO glass from Chapter 5. The TiO_2 film on ITO glass shown in figure 6.11.a appears fairly similar to the TiO_2 on FTO glass shown in figure 6.11.b. Both films appear porous with agglomerates of the large scattering particles. The TiO_2 film on FTO glass

appears to have more cracks and gaps than the ITO glass film. This is likely due to better sintering and a stronger temperature gradient between the FTO glass and the paste as a result of the much higher temperature reached by the FTO (648°C) driving the sintering with more thermal stress. The ITO glass is predicted to have reached 481°C which is similar to that reached for 60% NIR FTO glass that proved to be inferior as a working electrode in Chapter 5. However the film here appears better sintered and has good porosity. There was also no charging of the sample during SEM imaging (unlike the case for 60% NIR FTO glass), which would have indicated an insulator present and increased the difficulty of obtaining an image, which suggests that the organic binder was removed during NIR heating further signifying that the paste approached sufficient temperature for sintering. This supports the theory that the ITO glass remained at a higher temperature for longer both due to its thinner film and higher free carrier concentration which would have facilitated the transfer of heat extremely efficiently, thus enabling it to achieve sufficient sintering whilst obtaining a lower maximum temperature. The high magnification images, figure 6.11.c for ITO glass and figure 6.11.d for FTO glass again reinforce that the FTO glass sample may have better porosity but they both appear well sintered.

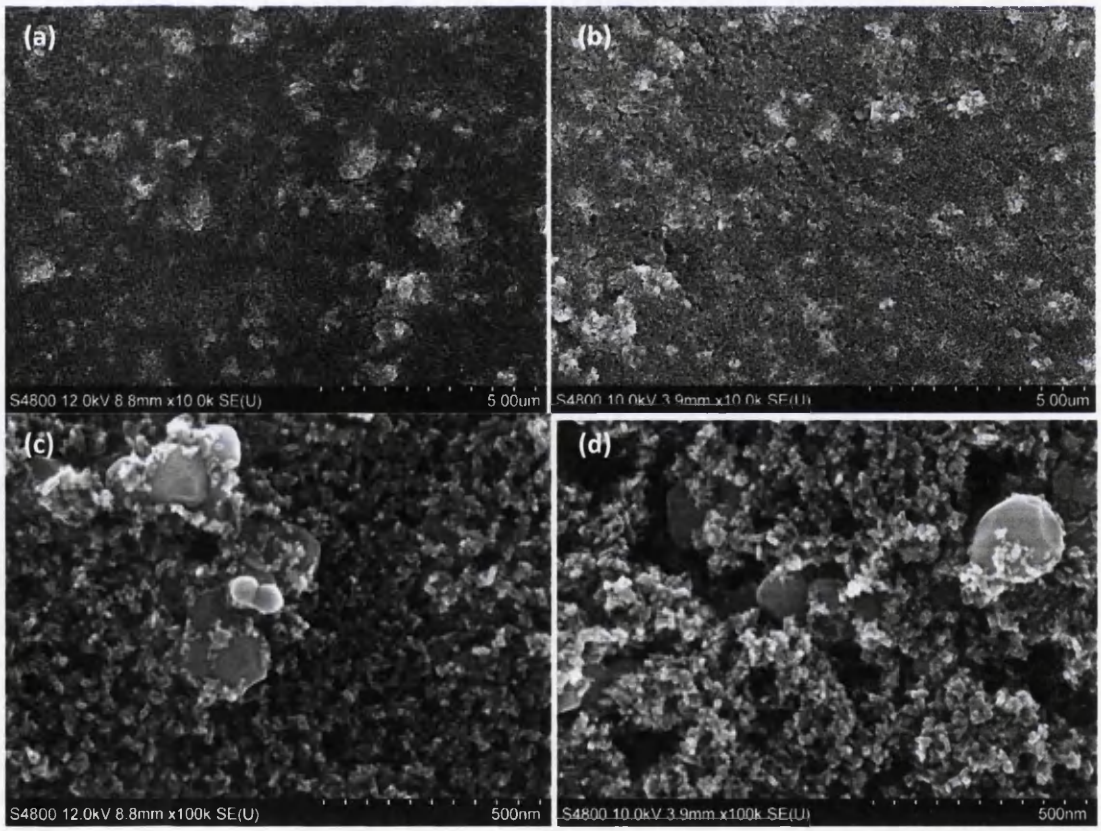

Figure 6.11: SEM of 12.5 s NIR heated DSL 18NR-AO TiO_2 paste at 70% intensity on ITO glass (a) low magnification, (c) high, and 90% intensity on FTO glass (b) low magnification, (d) high

6.3.2.2 Dye-sensitised solar cells with a rapidly heated ITO glass working electrode

DSCs were constructed from 12.5 s NIR heated TiO_2 coated ITO glass working electrodes and conventional oven heated FTO glass counter electrodes. Figure 6.12 shows the average efficiency for these devices, along with their current density shown inset, against NIR lamp intensity. Also shown is an oven heated ITO glass working electrode (30 min at 450°C). The average IV parameters are shown in Table 6.5.

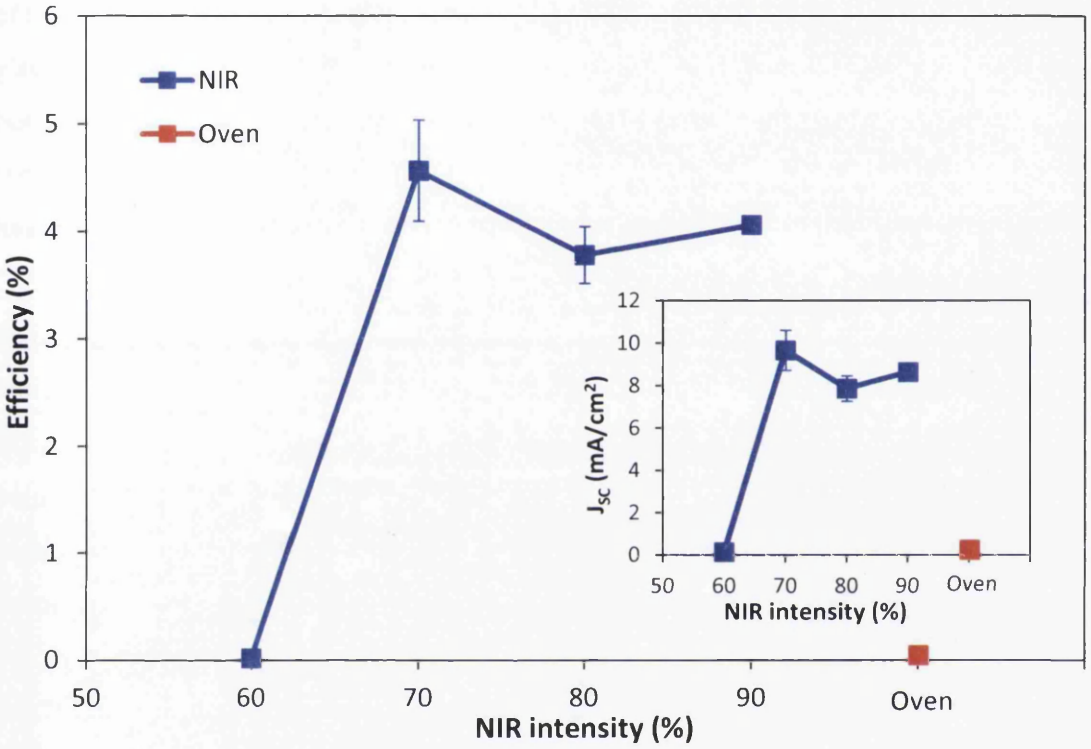

Figure 6.12: Average efficiency vs. NIR intensity for 12.5 s NIR heated ITO glass working electrode DSCs with an oven heated ITO glass DSC; inset the same for current density

Table 6.5: Average of 3 devices for ITO glass working electrode DSCs and an equivalent FTO glass working electrode DSC, with 1 standard deviation of error

Heating	Time	V_{OC} (V)	J_{SC} (mA/cm^2)	FF (%)	Efficiency (%)
NIR (60%)	12.5 s	0.29 ± 0.13	0.13 ± 0.09	38.71 ± 3.67	0.02 ± 0.02
NIR (70%)	12.5 s	0.69 ± 0.00	9.66 ± 0.95	68.17 ± 0.27	4.56 ± 0.47
NIR (80%)	12.5 s	0.70 ± 0.00	7.86 ± 0.60	68.36 ± 0.01	3.78 ± 0.26
NIR (90%)	12.5 s	0.69 ± 0.01	8.64 ± 0.05	68.22 ± 0.20	4.06 ± 0.01
Oven (450°C)	30 min	0.38 ± 0.08	0.24 ± 0.18	42.41 ± 1.38	0.04 ± 0.04
FTO glass	30 min	0.72 ± 0.00	9.29 ± 0.11	71.93 ± 1.93	4.83 ± 0.17

The 60% NIR heated devices did not function well despite FTIR-ATR spectra showing no terpineol or ethyl cellulose peaks suggesting that all solvent and binder was burnt off. This

was similar for the 60% NIR heated working electrodes on FTO glass. It is expected that there is insufficient charge transport for these cells due to the temperature being too low for diffusion of the TiO_2 particles to occur during the short 12.5 s exposure time and subsequent cooling of the film. At 70% NIR exposure the efficiency and charge density have risen significantly and it is almost comparable to an equivalent standard non-$TiCl_4$ treated FTO glass working electrode DSC. The high efficiency and J_{SC} seem to suggest that despite the predicted temperature being lower for ITO glass it may indeed be receiving a similar amount of thermal energy, a sufficient amount for sintering, as the more optimal NIR exposed FTO glass samples. This is believed to be because the ITO may be heating faster than the FTO, both due to its thinner layer and higher free carrier concentration, enabling it to sustain a temperature high enough for sintering for longer than the FTO glass such as 60% FTO which has the same maximum temperature but does not function well.

As the NIR intensity increases beyond 70% there is a slight dip in efficiency and current density. The 90% NIR cells performed well and extremely reproducibly compared to the 70% NIR cells which had some variation. However it was decided that 70% NIR exposure should be used for future devices rather than 90% to err on the side of caution with respect to resistivity. Finally the 30 min oven cells also have almost nonexistent photovoltaic properties. This is unsurprising because the long exposure to 450°C would have increased the sheet resistance to at least 53.6 Ω/□ severely impairing any flow of electrons through the TCO. There would have been no problem with binder removal or sintering of the TiO_2 film because heating at 450°C for 30 min is well known to be sufficient as supported by the equivalent FTO glass cell shown in Table 6.5.

Optoelectronic transient measurements were taken for the ITO glass working electrode DSC devices to study the TiO_2 particle interconnectivity. Figure 6.13 shows a measurement taken at short circuit, charge density vs. current density. The charge density is fairly similar for 70%, 80% and 90% NIR showing no significant different between the charges collected in each of the TiO_2 films. The charge density is also sufficient indicating a well sintered film for 12.5 s NIR exposed ITO glass at these intensities. The 60% NIR and oven heated films show lower charge density and are quite irregular. 60% NIR doesn't collect as much charge because TiO_2 film has more trapped states from particles not connected. For the oven heated film it may be that once the dye has injected an electron into the TiO_2 and this has been transferred to the TCO because it has more difficulty travelling through due to the

large sheet resistance it is not being returned to the counter electrode as efficiently so that the electrolyte can subsequently replenish the dye and more charge be collected.

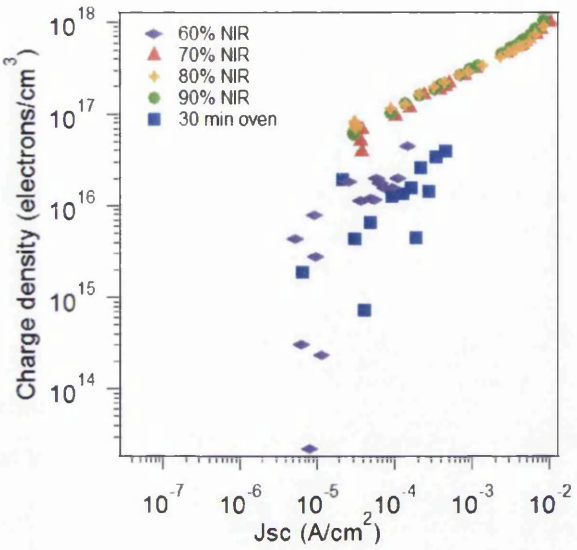

Figure 6.13: Charge density vs. current density for NIR heated ITO glass working electrode DSCs

Figure 6.14.a shows recombination lifetime vs. open circuit voltage taken from optoelectronic transient measurements at open circuit. There is a trend with NIR intensity whereby 70% NIR has the best recombination lifetime, 90% and 80% NIR are slightly behind although again they are fairly similar to each other, and 60% NIR has an extremely poor recombination lifetime. This is that the rate at which TiO_2 electrons recombine with I_3^- or I_2 to form I^- ions, rather than get collected by the TCO. As in the case of 60% NIR it is fast relative to charge transport the photocurrent is reduced which suggests there are less available neighbouring TiO_2 particles to accept the electron. The oven heated cell also has a poor recombination lifetime which may be due to electrons finding it harder to be transported from the ITO layer because of the high sheet resistance causing them to be exposed to the electrolyte longer giving them more opportunity to recombine. Figure 6.14.b shows transient tau at V_{OC} vs. charge density at V_{OC}. The trend for recombination lifetime vs. charge density is similar to figure 6.14.a and also but it also shows the lack of charge density in the 60% NIR and oven heated TiO_2 films as previously seen in figure 6.12. The other NIR heated cells have a good correlation between charge density and recombination lifetime measured at V_{OC} further suggesting the TiO_2 is well sintered.

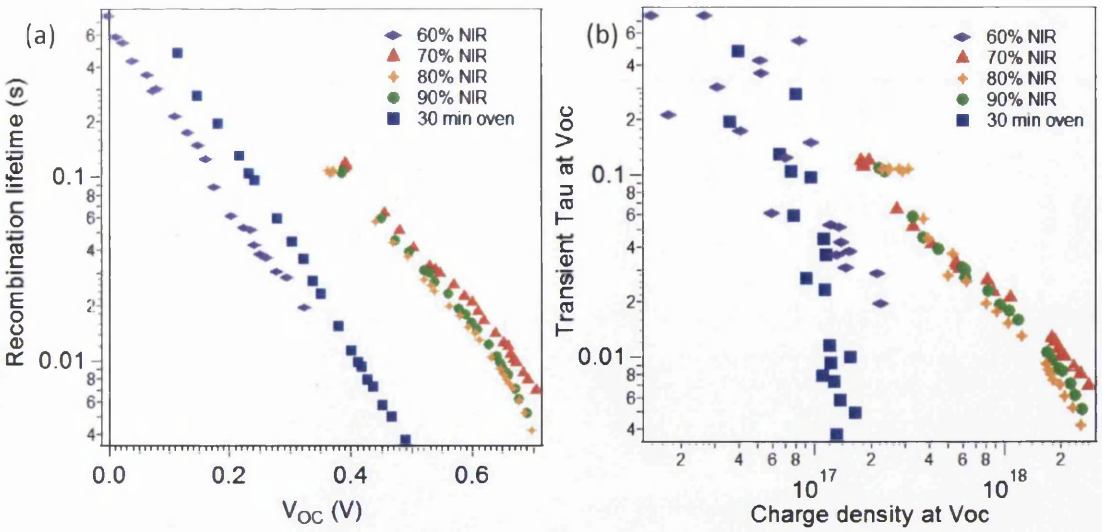

Figure 6.14: (a) recombination lifetime vs. V_{OC} and (b) Transient tau at V_{OC} vs. charge density at V_{OC} for NIR heated ITO glass working electrode DSCs

Using NIR radiative heating TiO_2 working electrodes for DSCs were built on ITO glass at an efficiency 0.95 times that of an equivalent simple oven heated FTO glass DSC device with a heating time of 12.5 s. This was achieved by balancing the temperature required for sufficient TiO_2 sintering (controlled by the NIR lamp intensity) with that which would cause a rapid rise in resistivity by introducing oxygen into the oxygen vacancies of the ITO. The heating is believed to be not only due to the ITO glass substrate absorbing NIR radiation but also locally within the TiO_2 paste due to additional absorption which may be a factor in the ability to achieve higher temperatures without damaging the ITO. The FTO glass devices are built on a lower sheet resistance TCO and are also textured which assists with light harvesting for the dye through light scattering so if the substrate were equal in quality it may be possible to build a device on ITO glass of equal efficiency to FTO glass without requiring a low temperature method for the TiO_2 film.

6.3.3 All ITO glass and rapidly heated dye-sensitised solar cells

Using the optimum 12.5 s NIR exposure lamp intensity for an ITO glass counter electrode and an ITO glass working electrode, both found to be 70%, high temperature DSC devices were built entirely on ITO glass. As well as combining the ITO counter electrode and working electrode together different NIR heating methods were varied for the working electrode as described in section 2.2.2.1. These are shown in Table 6.6 and figure 6.15.

Table 6.6: Description of different NIR $TiCl_4$ variations and their relation to figure 6.15

Schematic	Method name	No. of NIR runs	$TiCl_4$ treatment
a	Single run	1	None
b	Double run	2	None
c	Fast $TiCl_4$	2	Dab with solution
d	Slow $TiCl_4$	2	Soak in solution (80°C, 30 min)

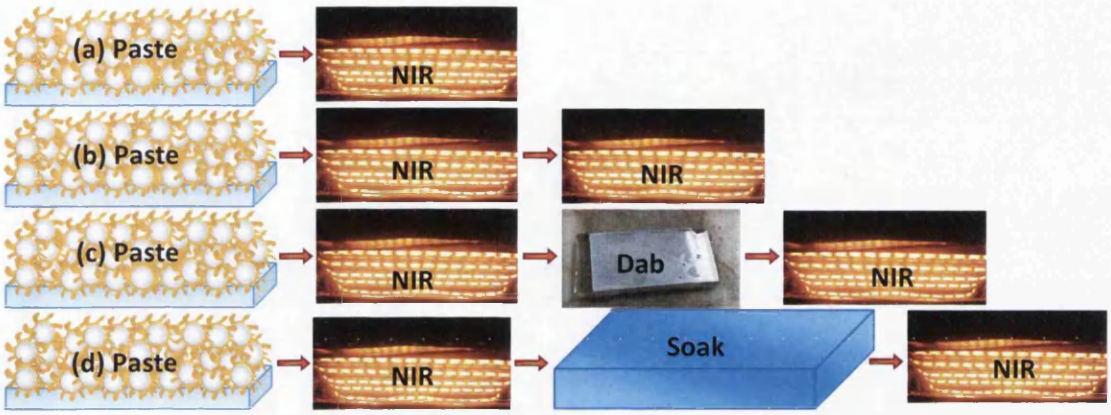

Figure 6.15: Schematic of different NIR $TiCl_4$ treatments; (a) Single, (b) Double, (c) Fast, (d) Slow

The control of one single run of NIR for 12.5 s at 70% NIR intensity (as the optimum of section 6.3.2) was called single run "S". For the fast $TiCl_4$ method "F" the 1 wt% $TiCl_4$ solution was dabbed onto the sintered TiO_2 with a cotton bud to cover the entire film and then exposed to NIR as soon as it had dried (at room temperature). For the slow $TiCl_4$ "T" method the sintered films were submerged in $TiCl_4$ solution at 80°C for 30 min in an oven as normal, washed off, dried and then subjected to a second run of NIR. To compare the effect of a second NIR run films without $TiCl_4$ treatment were subjected to two non-continuous runs known as double run "D". Figure 6.16 shows the average efficiency of these devices and Table 6.6 their average PV parameters.

The single run ITO glass WE/CE DSC performs fairly well, although it has a lower J_{SC} than the NIR heated ITO glass WE with an FTO glass oven CE its performance is respectable as it undergoes a total heating time of just 25 s and is constructed entirely on ITO glass heated in air. The "fast" $TiCl_4$ treated cells (2 runs of 70% NIR on the working electrode, the second run after being coated with $TiCl_4$ solution) are very interesting; it seems that the brief application of TiO_2 precursor solution may have resulted in some small nanoparticle synthesis and adhesion to the existing mesoporous film during the second run of 12.5 s NIR exposure. The V_{OC} and current density have returned to a similar level that it was for the NIR heated ITO

glass working electrodes with FTO counter electrode, with the high fill factor also of the ITO glass counter electrode cells. The average efficiency is higher than the best ITO glass working electrode/FTO counter electrode device and almost on par with the standard oven heated FTO glass device. This is an extremely promising demonstration of NIR radiation as a high temperature heating technique compatible with ITO for electronic devices.

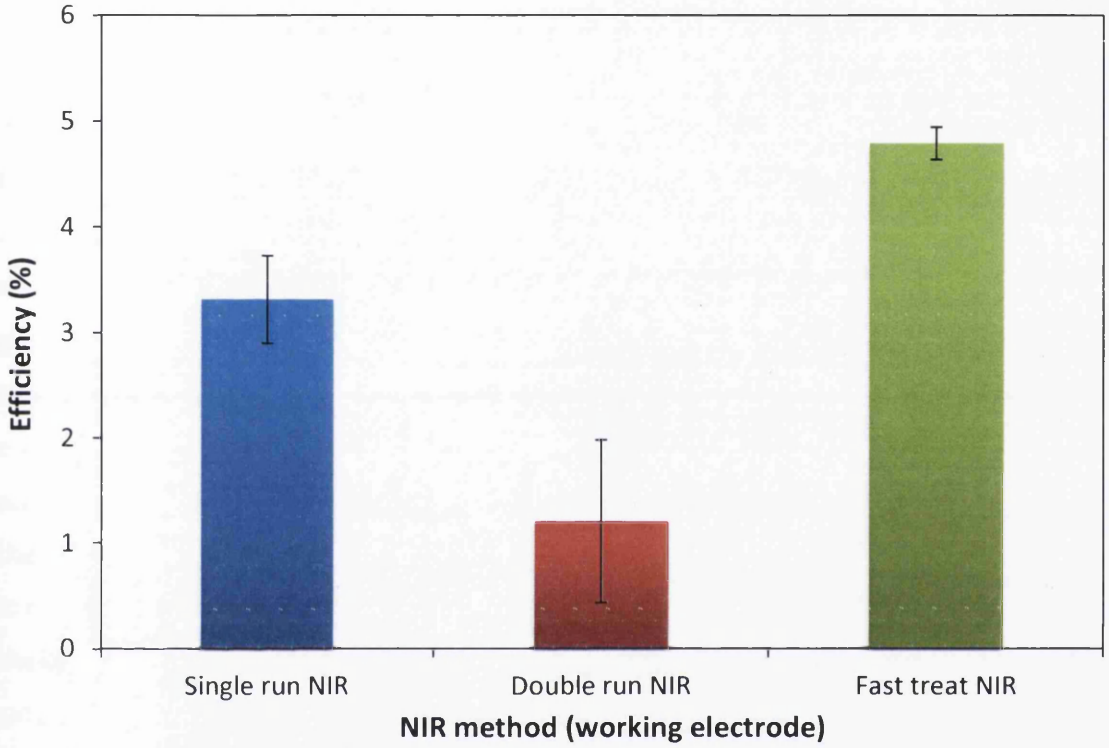

Figure 6.16: Average efficiency of fast heated NIR ITO glass DSC devices against working electrode variation

Table 6.6: Average of 4 devices for all ITO glass DSC devices with time and method shown for working electrode heating, 1 standard deviation of error

Method	Time	V_{OC} (V)	J_{SC} (mA/cm^2)	FF (%)	Efficiency (%)
Single NIR	12.5 s	0.66 ± 0.02	7.17 ± 0.54	68.87 ± 3.73	3.32 ± 0.41
Double NIR	25 s	0.61 ± 0.04	3.21 ± 1.65	58.62 ± 5.19	1.21 ± 0.78
$TiCl_4$ NIR	25 s	0.69 ± 0.02	9.32 ± 0.28	74.72 ± 4.34	4.79 ± 0.15

The ITO glass working electrodes prepared via the slow $TiCl_4$ method "T" could not be used because the $TiCl_4$ solution reacted with the ITO and stripped away the sintered TiO_2 layers as has been reported here [11]. This further reinforces how remarkable it was that such a brief application $TiCl_4$ solution managed to enhance the TiO_2 film of an ITO glass working electrode where it would not have otherwise been able to be used. Further work will be

required to assess whether the fast $TiCl_4$ treatment has had an impact on the surface area or interconnectivity. It is also remarkable considering the stark difference in efficiency of the double run NIR devices which were built identically save for the application a few drops of 1% $TiCl_4$ solution in water. The second run of NIR may have lead to severe cracking, grain growth or other film defects which were either absent or offset by the addition of small nanoparticles increasing the photocurrent in the case of the fast $TiCl_4$ DSCs.

6.4 Conclusions

In Chapter 3 it was shown that 12.5 s of NIR exposure on ITO glass would allow it to reach high temperatures without a significant rise in sheet resistance. In this Chapter chloroplatinic acid on ITO glass exposed to 12.5 s of NIR radiation was used as a counter electrode in a DSC device and it was 0.85 times as efficient as an equivalent oven heated FTO glass device and 0.87 times as efficient as a NIR heated counter electrode FTO glass device. This is extremely significant both in terms of the drastic time reduction attractiveness and producing an electrode for on ITO glass for a DSC without requiring a cumbersome post annealing step to regain the oxygen vacancies in the ITO. The optimal NIR setting for the thermal decomposition of chloroplatinic acid on ITO glass, 12.5 s of 70% NIR exposure, had a low charge transfer resistance and series resistance (obtained from EIS) suggesting that its sheet resistance did not rise significantly upon NIR exposure. It also showed extremely good catalytic affinity for the reduction of triiodide as observed from cyclic voltammetry, comparable to that of Pt on FTO glass, coupled with its good efficiency and fill factor in a DSC device suggests that an optimal balance of sufficient catalytic platinum thermally reduced and not overheating the ITO which would drastically speed oxygen diffusion into the vacancies even in a 12.5 s timeframe. The other NIR settings showed similar performance enabling a large processing window for the manufacture. The 30 min oven heated DSCs had catalytic platinum but also extremely high charge transfer resistance, series resistance and a low fill factor suggesting that the high sheet resistance was having an impact on the cell's performance.

Using NIR radiative heating at 70% lamp intensity TiO_2 working electrodes for DSCs were built on ITO glass at an efficiency 0.95 times that of an equivalent simple oven heated FTO glass DSC device with a heating time of only 12.5 s. This is extremely promising for the use of NIR radiation to heat ITO glass because an efficiency so close to that of the equivalent FTO

glass DSC without necessary post sintering treatments to reintroduce the ITO vacancies has not been published before in the literature.

High temperature DSCs were also built entirely on ITO glass with only 25 s or 37.5 s total heating time. The optimum device utilised $TiCl_4$ solution with a few drops before a second run of NIR exposure increasing the efficiency dramatically to just above that of a simple standard FTO glass device. The average efficiency is higher than the best ITO glass working electrode/FTO counter electrode device and almost on par with the standard oven heated FTO glass device. This is an extremely promising demonstration of NIR radiation as a high temperature heating technique compatible with ITO for electronic devices. Although ITO glass is an unlikely candidate for the commercialisation of DSCs it is used for many other devices, such as OLEDs, especially where smoothness is required and NIR radiation could be used to reduce heating times and extend the temperature processing window for any application where ITO is desirable.

6.5 References

[1] K. Goto, T. Kawashima, N. Tanabe, Heat-resisting TCO films for PV cells, Sol. Energy Mater. Sol. Cells. 90 (2006) 3251–3260.

[2] C. Sima, C. Grigoriu, S. Antohe, Comparison of the dye-sensitized solar cells performances based on transparent conductive ITO and FTO, Thin Solid Films. 519 (2010) 595–597.

[3] S. Lee, J. Noh, S. Bae, I. Cho, Indium-Tin-Oxide-Based Transparent Conducting Layers for Highly Efficient Photovoltaic Devices, J. Phys. Chem. C. 113 (2009) 7443–7447.

[4] J.W. Bowers, H.M. Upadhyaya, T. Nakada, A.N. Tiwari, Effects of surface treatments on high mobility ITiO coated glass substrates for dye sensitized solar cells and their tandem solar cell applications, Sol. Energy Mater. Sol. Cells. 94 (2010) 691–696.

[5] H. Kostlin, Application of thin semiconductor metal films in energy technology, in: Aachen P.G. (Ed.), Festkorperprobleme 22, Springer Berlin Heidelberg, 1982: pp. 229–254.

[6] T. Kawashima, H. Matsui, N. Tanabe, New transparent conductive films: FTO coated ITO, Thin Solid Films. 445 (2003) 241–244.

[7] T. Kawashima, T. Ezure, K. Okada, H. Matsui, K. Goto, N. Tanabe, FTO/ITO double-layered transparent conductive oxide for dye-sensitized solar cells, J. Photochem. Photobiol. A Chem. 164 (2004) 199–202.

[8] S. Ngamsinlapasathian, T. Sreethawong, Y. Suzuki, S. Yoshikawa, Doubled layered ITO/SnO_2 conducting glass for substrate of dye-sensitized solar cells, Sol. Energy Mater. Sol. Cells. 90 (2006) 2129–2140.

[9] A. Bard, L. Faulkner, Electrochemical Methods: Fundamentals and Applications, 2nd ed., John Wiley & Sons, 2001.

[10] NIST Chemistry, [Online]. Available at: http://webbook.nist.gov/chemistry. [Accessed: 11-Sep-2013].

[11] S. Fan, C. Li, G. Yang, L. Zhang, Influence of $TiCl_4$ treatment on performance of dye-sensitized solar cell assembled with nano-TiO_2 coating deposited by vacuum cold spraying, Rare Met. 25 (2006) 163–168.

Further Reading

A. Delahoy and S. Guo, "Transparent Conducting Oxides for Photovoltaics," in *Handbook of Photovoltaic Science and Engineering*, 2nd ed., A. Luque and S. Hegedus, Eds. Wiley, 2011, pp. 716–796.

D. Pavia, G. Lampman, and G. Kriz, *Introduction to Spectroscopy*, 2nd ed. Saunders College Publishing, 1996.

7. Near Infrared Heating of Flexible Substrates

7.1 Introduction

One of the greatest advantages of dye-sensitised solar cells (DSCs) is that their thin layers allow them to be flexible. This is extremely desirable for building integrated photovoltaics where the solar cell could be incorporated within the building material as a coating, and also lightweight portable applications such as remote power in poorer countries and personal electronics (which also tailors to DSC's good low light performance and tuneable dyes for high absorption of visible indoor lighting). Flexibility also enables greater compatibility for roll-to-roll production, thinner substrates saving material, weight and cost, as well as robustness for the finished device where a glass one would be brittle and fragile.

In this chapter metal and plastic, discussed in detail in sections 1.2.2.2 and 1.2.2.3 respectively, will be subjected to near infrared (NIR) radiation in an attempt to drastically reduce heating stages associated with the fabrication of DSCs on substrates capable of being manufactured into flexible DSCs to combine both of these desirable criteria towards commercialisation.

Metal substrates are generally flexible with high conductivity, which is extremely important for reducing resistive losses over large areas. The efficiencies for DSCs with a metal working electrode [1][2] are lower than those for an FTO glass device predominantly because the former requires reverse illumination through the counter electrode which results in reduced photocurrent [3] from increased recombination [4]. A metallic counter electrode would allow for forward illumination of the cell and so avoid this efficiency loss. The thermal decomposition of chloroplatinic acid on metal substrates is usually performed in a conventional oven at 385°C but for 15 min or less rather than 30 min to limit oxide growth [5]. There lies a compromise in platinised metal counter electrodes between attaining a high surface area of catalytically active platinum nanoparticles (derived from cleaving as many platinum chloride bonds as possible) and not overexposing the metal to heat which forms an insulating or semiconducting oxide layer. Similarly to Chapter 6 where the time dependent diffusion of oxygen into ITO's oxygen vacancies was limited by using rapid NIR radiation it is hoped that the oxide formation of titanium can also be reduced through rapid processing to achieve efficient titanium counter electrode DSCs.

Plastic is transparent so is not restricted to reverse illumination. However its major drawback is thermal stability; the two most common plastic substrates for DSCs are ITO PET and ITO PEN and the maximum temperature these plastics can withstand is approximately 150°C. NIR radiation is proposed here for both plastic working electrodes and counter electrodes in an attempt to find a fast and vacuum free process. NIR radiation has been used for the curing of PEDOT:PSS onto PET substrates, where PEDOT:PSS is the main absorber of the radiation, which although a low temperature process required tight control to avoid degradation of the substrate [6]. In the case of ITO PET the ITO layer will be the main absorber of radiation and is expected to heat significantly compared to the PET as was the case for TCOs and glass. It is hoped that short repetitive exposures of NIR radiation can achieve some level of platinisation or functional TiO_2 film such as by gradually cleaving platinum chloride bonds at a lower temperature than the melting point of the plastic without overexposing the ITO and causing it to melt the PET.

7.2 Experimental

7.2.1 Metallic substrates

NIR heated titanium working electrodes DSCs were constructed to discuss the NIR heating of metallic substrates (established here [7]) compared the NIR heating of FTO glass substrates from Chapter 5. DSCs were fabricated (section 2.2.3) with an NIR heated titanium working electrode and oven heated FTO glass counter electrode (figure 7.1) and characterised using IV measurements (section 2.3) and optoelectronic transient measurements (section 2.5).

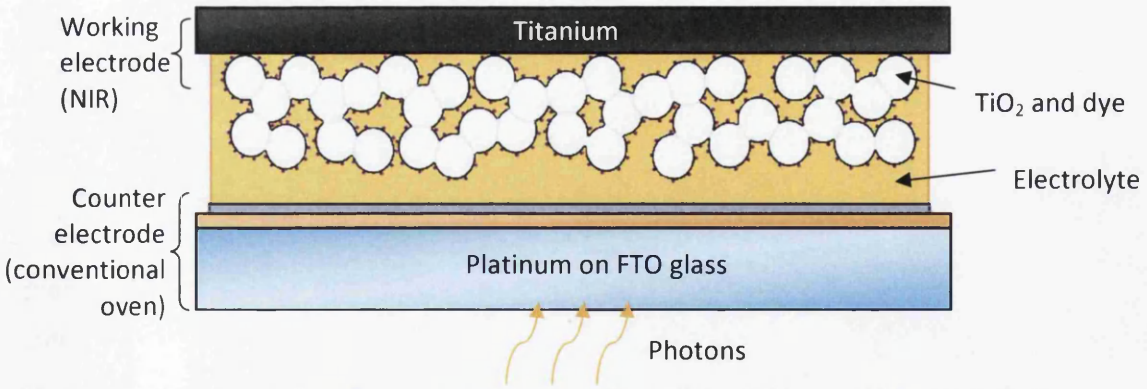

Figure 7.1: Schematic of a DSC incorporating an NIR heated titanium working electrode illuminated from the counter electrode

NIR heated titanium counter electrodes were investigated by firstly performing cyclic voltammetry on chloroplatinic acid coated titanium substrates (Goodfellows 99.6% 1.1 mm thick). The catalytic performance of NIR heated and conventionally heated Pt to reduce triiodide was tested (section 2.7) between the potentials of -0.5 and 0.8 V with a scan rate of 50 mV/s. DSC devices (figure 7.2) were constructed from NIR heated titanium counter electrodes and conventional oven heated FTO glass $TiCl_4$ treated working electrodes (section 2.2.3) and characterised using IV measurements (section 2.3).

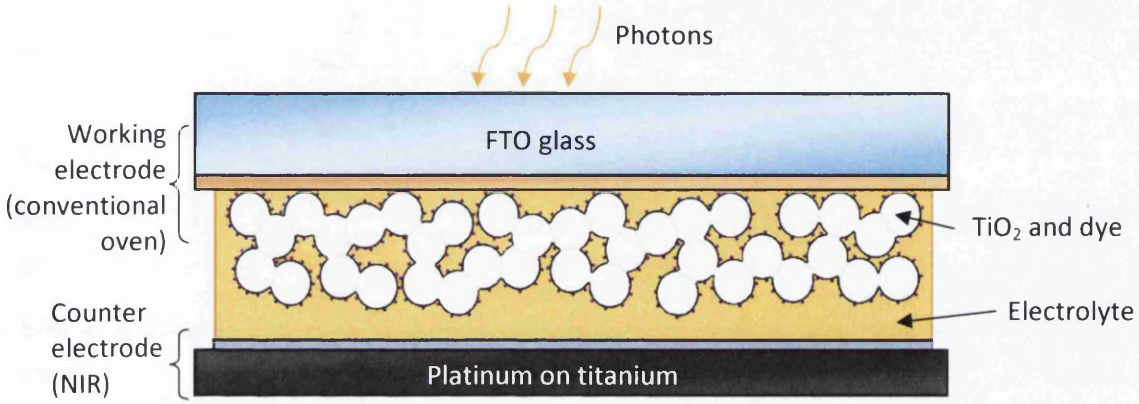

Figure 7.2: Schematic of a DSC incorporating an NIR heated titanium counter electrode

7.2.2 Plastic substrates

Two plastic substrates were studied; ITO coated PET and an ITO free conducting plastic substrate consisting of a nickel grid embedded in PET called Epimesh (Epigem). The absorbance and reflectance of ITO PET (EMI-ito15, Optical Filters) and uncoated PET (ITO PET with the ITO chemically removed) was measured using a Perkin Elmer Lambda 750S spectrophotometer (section 2.8). Prior to NIR exposure of chloroplatinic acid or TiO_2 paste, the optimal NIR settings were investigated for each plastic substrate to find the limit of thermal degradation and any possible increase in resistivity. NIR settings were also tested for ITO PET that had been doctor bladed with different varieties of TiO_2 pastes to observe if there was any difference to the heating behaviour. Their thicknesses were measured using a profilometer (section 2.14) and they were immersed in dye to determine if there was sufficient porosity for dye adsorption resulting in significant colour change. Scanning electron microscopy was also used to image the TiO_2 coated substrates (section 2.12). DSCs were constructed using NIR heated ITO PET working electrodes following the method in section 2.2.4 (figure 7.3) and characterised using a solar simulator (section 2.3).

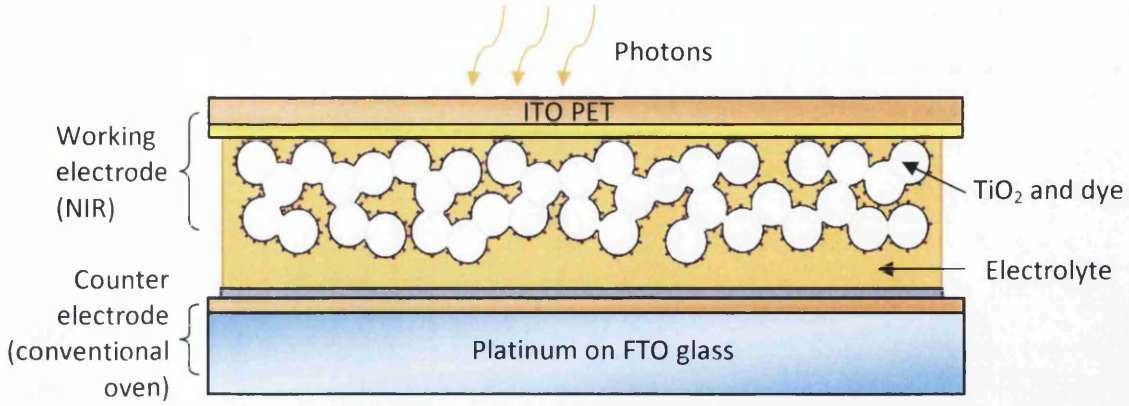

Figure 7.3: Schematic of a DSC incorporating an NIR heated ITO PET working electrode

Counter electrodes on plastic substrates were also created using the optimal NIR settings and three drops of 5 mM hexachloroplatinic acid in 2-propanol was applied to ITO PET and Epimesh. As a conventional comparison platinum was also sputtered onto ITO PET using a Quorum Q150 ES desktop sputterer/evaporator. The plastic counter electrodes were constructed into dye-sensitised solar cells (section 2.2.4) with $TiCl_4$ treated oven heated TiO_2 film working electrodes on FTO glass (figures 7.4 and 7.5). Their photovoltaic properties were characterised using a solar simulator (section 2.3).

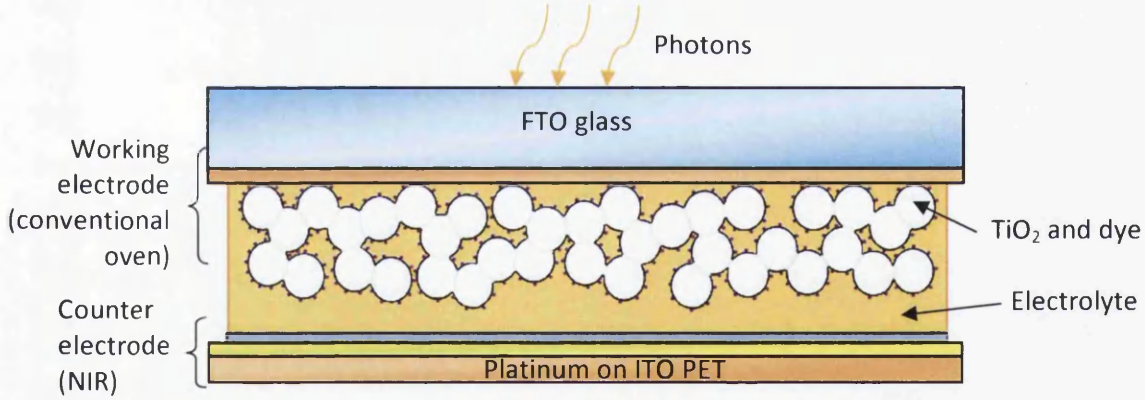

Figure 7.4: Schematic of a DSC incorporating an NIR heated ITO PET counter electrode

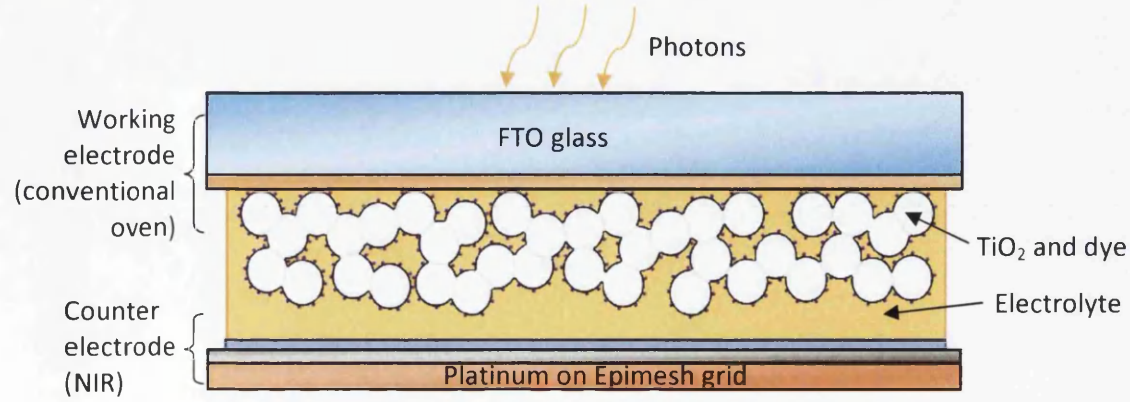

Figure 7.5: Schematic of a DSC incorporating an NIR heated Epimesh counter electrode

7.3 Results and discussion

7.3.1 Titanium

7.3.1.1 NIR sintered titanium working electrodes for DSCs

The ability of metal to heat when exposed to NIR radiation has been previously been demonstrated for use in DSC working electrodes [7][8] and will be briefly discussed here as an introduction to the NIR heating of titanium, which will also be explored in section 7.3.1.2, and in comparison to the NIR heating of TiO_2 on other substrates. Metals are conductors and absorb highly in the infrared region. Titanium is opaque and fairly dull and absorbs what it does not reflect resulting in high temperatures when exposed to 12.5 s of NIR radiation [8]. It has been shown that NIR radiation can sinter TiO_2 on titanium in 12.5 s with equal performance to oven heated titanium working electrodes that require 30 min [7]. In Chapter 5 it was shown that 12.5 s NIR exposed TiO_2 working electrodes on FTO glass also perform equally in DSC devices to oven heated working electrodes. Both substrates induce the binder removal of TiO_2 paste and sintering of the TiO_2 particles by creating a large thermal gradient between the surface of the substrate and the paste that transfers the heat by conduction extremely rapidly. In the case of the NIR heating of FTO glass the main absorbing layer is the FTO which only 600 nm thick. Although some heat does originate from the NIR exposure of uncoated glass (Chapter 3) when there is a coating of FTO the NIR photons will be absorbed by this layer first and only any transmitted photons will reach the glass. Therefore the thermal energy that is transferred to the TiO_2 paste will almost exclusively be from the FTO layer. The titanium used here is 1.1 mm thick and as a metal has many free carriers in its bulk available for absorption of the radiation to release phonons and transfer of the heat. Consequently it is capable of attaining higher temperatures than the FTO glass upon the same level of NIR exposure. However it is likely that the majority of the absorption of NIR occurs on the surface of the titanium as the photons interact with the nearest electrons and that less reach the bulk of the material so heating in a similar fashion to the FTO glass.

DSCs were constructed from 12.5 s (2 m/min line speed) NIR heated DSL 18NR-AO TiO_2 paste on titanium with conventionally heated FTO glass counter electrodes with the average IV parameters shown in Table 7.1 and a graph of average efficiency and current density shown in figure 7.6. Additionally a longer exposed NIR heated working electrode DSC (1.5 m/min corresponding to 19 s exposure) and a conventionally heated working electrode on titanium (30 min at 450°C in a conventional oven) are shown. The TiO_2 film thickness is the same as

used in previous chapters, 9 µm, but due to the necessary reverse illumination when measuring the cells the current density is lower.

Table 7.1: Average IV parameters for NIR heated titanium metal working electrode DSCs (12.5 s of NIR exposure unless otherwise stated) and oven heated DSCs for 3 devices with 1 standard deviation of error

NIR (%)	V_{OC} (V)	J_{SC} (mA/cm^2)	FF (%)	Efficiency (%)
60	0.69 ± 0.06	3.77 ± 1.42	76.03 ± 2.35	1.99 ± 0.86
70	0.71 ± 0.00	5.61 ± 0.30	75.50 ± 0.45	3.01 ± 0.14
80	0.73 ± 0.00	5.30 ± 0.86	70.94 ± 4.27	2.77 ± 0.60
80 (19 s)	0.77 ± 0.01	3.40 ± 1.37	69.65 ± 0.75	1.81 ± 0.72
30 min oven	0.72 ± 0.02	5.02 ± 0.63	76.16 ± 2.05	2.75 ± 0.22

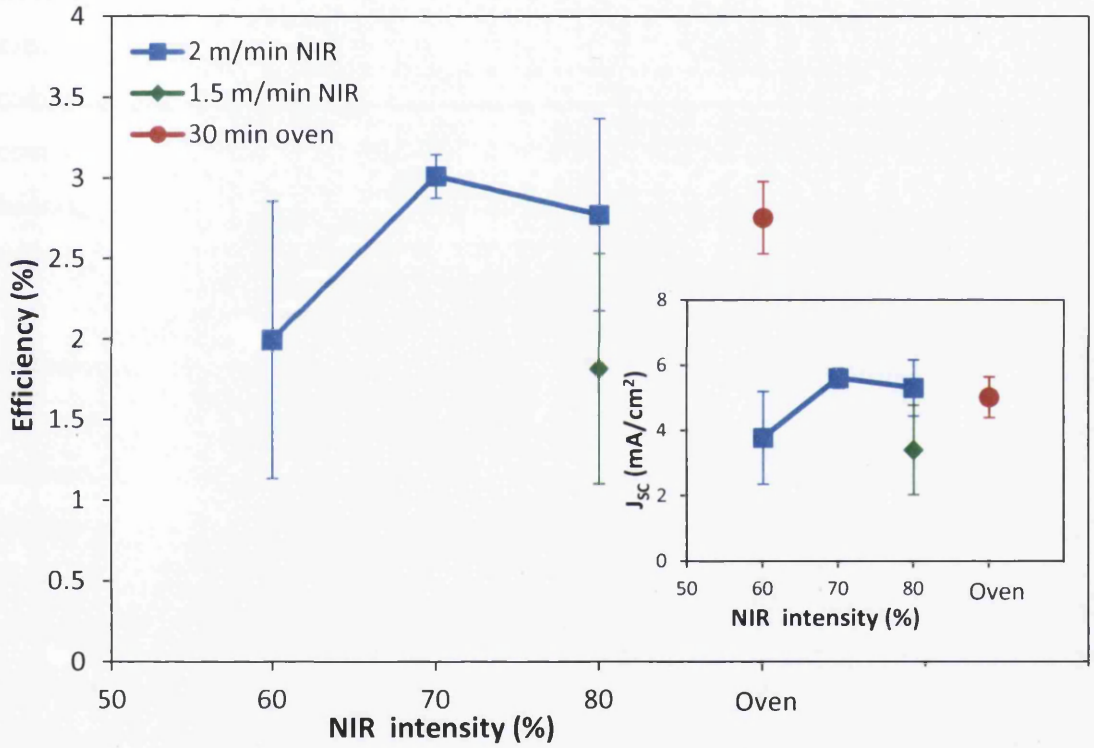

Figure 7.6: Average efficiency of NIR heated titanium metal working electrode DSCs (2 m/min or 1.5 m/min) and average current density (inset)

As is shown in figure 7.6 NIR radiation can sinter TiO_2 on titanium in 12.5 s with equal performance to oven heated titanium working electrodes that require 30 min. For 12.5 s NIR exposure as the NIR intensity increases the current density increases which is due to better sintering of the TiO_2 particles improving the transport of the electrons through the TiO_2. 70% NIR intensity has the best current density and thus efficiency. It also has the least variation between devices indicating very reproducible results. For 80% NIR intensity there is a larger

variation which may mean that it is slightly above the optimum temperature window for sintering TiO_2 where there may be a chance some grain growth in TiO_2 films. Any grain growth would result in a lower surface area for dye adsorption therefore less photons absorbed and a reduced photocurrent density as shown by the lower average J_{SC} for 80% NIR but the large error suggests this may not have occurred in every working electrode. The phase transformation of anatase to rutile TiO_2 occurs at temperatures above 610°C [9] which would have occurred at 80% for the slower speed of 1.5 m/min (19 s) as the longer exposure time at elevated temperatures would have allowed more time for the kinetic diffusion of TiO_2 and phase transformation. The average J_{SC} is significantly lower for the 19 s 80% NIR DSC devices so it suggests that this was the case and the grain growth and rutile TiO_2 presents a smaller surface area for dye adsorption. The 30 min oven heated titanium working electrode DSC has comparable efficiency and current density to the optimum NIR exposed working electrode but with a slightly higher variation. There appears to be no compromise with the faster thermal processing of the TiO_2 on titanium substrate, 12.5 s compared to 30 min, which corresponds to what was previously found [7][8] that NIR heating of TiO_2 films can be achieve equal or greater performance than the conventional heating.

Optoelectronic transient measurements as described in [10] were carried out in order to determine the charge transport and recombination kinetics in fast sintered devices, the data obtained is summarised in figure 7.7. Figure 7.7.a shows the charge density at V_{OC} measured via charge extraction. The charge density is extremely similar for each TiO_2 film. Figure 7.7.b shows the short circuit current transient lifetime vs. charge density at J_{SC} giving an indication of electron transport kinetics as a function of charge density. 60% NIR has slightly faster transport lifetime which could be attributed to fewer trap states indicating lower particle connectivity than the others. 70% and 80% NIR and conventional oven all have fairly similar transport lifetime suggesting similar particle connectivity and trap density. Figure 7.7.c shows electron lifetime at open circuit voltage vs. V_{OC}. All samples have fairly similar electron lifetime but strangely the oven sintered films seem to have the fastest rate of recombination and 60% NIR appears to have the slowest. It may be that each film has a similar level of dye loading from similar surface areas and that just the degree of sintering is stronger for above 60% NIR which is affecting the charge transport rather than the recombination. Figure 7.7.d shows the electron lifetime at open circuit voltage vs. the charge density at open circuit voltage also giving an indication of the recombination kinetics but against the charge

density. This presents a similar trend as figure 7.7.c but 80% NIR intensity showing an improved electron lifetime.

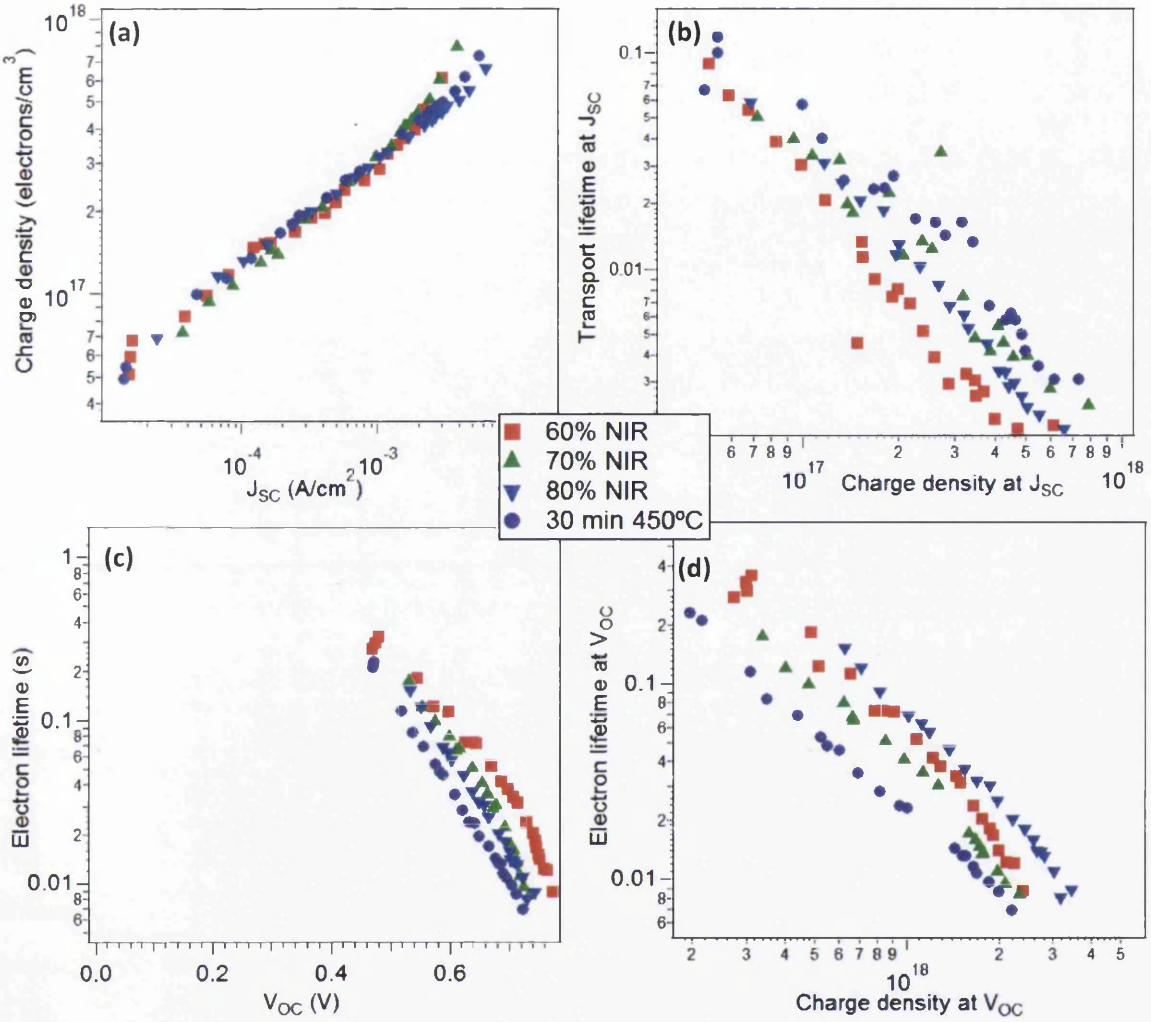

Figure 7.7: Optoelectronic transient measurements for (a) charge density vs. J_{SC}, (b) transport lifetime vs. charge density at J_{SC}, (c) electron lifetime vs. V_{OC}, and (d) electron lifetime at V_{OC} vs. charge density at V_{OC}

7.3.1.2 NIR heated titanium counter electrodes

Bare titanium substrates were heated with NIR exposure and conventional oven heating to observe any oxide formation. The titanium oxide formed when heating although not detrimental when the substrate is used as a working electrode such as in section 7.3.1.1, is an issue when titanium is used as a counter electrode because it is semiconducting so reducing the electrical contact between platinum and the metallic titanium. In addition, a titanium oxide interlayer reduces the adhesion of the platinum to the titanium thus resulting in less platinum catalytic sites for the reduction of triiodide in the electrolyte. A photograph

of the titanium substrates heated by various heating conditions is shown in figure 7.8 under controlled lighting conditions (described in section 2.16) to give a comparative indication of the oxide formation. It is proposed that the NIR exposure of the titanium may heat the substrate fast enough to avoid the kinetic oxygen diffusion into titanium; akin to the NIR heating of ITO glass in Chapter 3 where higher temperatures were obtained without resistivity increase as a result of oxygen diffusion into ITO's vacancies.

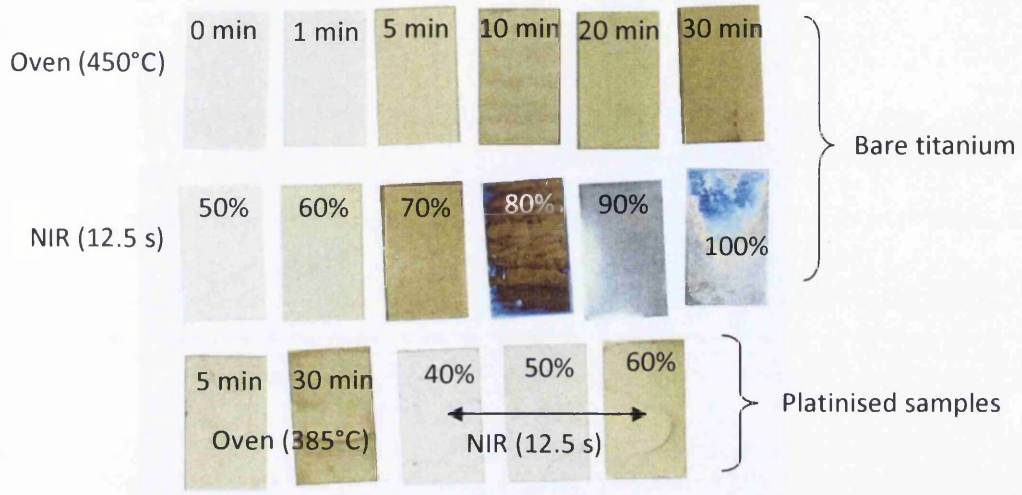

Figure 7.8: Light box photos of the titanium substrates heated

The conventional oven heating of bare titanium substrates was performed at 450°C and is shown on the top row of figure 7.8. After 1 min of heating (where the sample may still be heating to 450°C) the titanium is still similar in colour to the unheated substrate (0 min) with a shiny grey appearance as it is has not had time form a noticeable oxide layer. After about 5 min oven heating the substrate appears pale gold coloured which signals that an oxide layer is forming. At longer heating times this titanium oxide layer is thicker as shown by the darkening of the gold colour. For the 12.5 s of NIR exposure (middle row) 50% NIR intensity does not appear to have formed a noticeable oxide layer and looks similar in appearance to 1 min of oven heating. At 60% NIR intensity there does appear to be oxide formation although less so than 5 min of oven heating as indicated by the lighter colour. At higher intensities of NIR radiation the oxygen diffusion is accelerated by the higher temperatures attained by the titanium substrate. 70% NIR appears to have a similar oxide layer to 30 min oven heating but the 80-100% NIR may have even thicker oxide layers as they have changed colour which is related to the thickness of the titanium oxide [11]. Therefore at these intensities platinisation is unlikely to be suitable as the thick oxide layer would impede adhesion.

Cyclic voltammetry (theory in section 1.5.4) was used to assess the prospective NIR heated platinum counter electrodes on titanium (section 2.7) in an identical fashion to Chapter 4 (section 4.3.1). As mentioned previously any oxide formation on the titanium may impede the adhesion of platinum to the titanium [5] and create a semiconducting barrier which will cause an increased resistance for the transfer of electrons. Both will result in poorer charge transfer between the iodide and triiodide which will manifest itself in the cyclic voltammograms as less reversible peaks. Figure 7.9 shows cyclic voltammograms (second cycle shown) of 12.5 s NIR exposed chloroplatinic acid on titanium at different lamp intensities with two oven heated platinised titanium samples (5 min and 30 min at 385°C) and the unheated bare titanium substrate. Table 7.2 shows the corresponding data extracted from the cyclic voltammograms to give an indication of the reversibility [12]; peak separation, ΔE_p, and the ratio of the peak current densities ($|j^a_p/j^c_p|$).

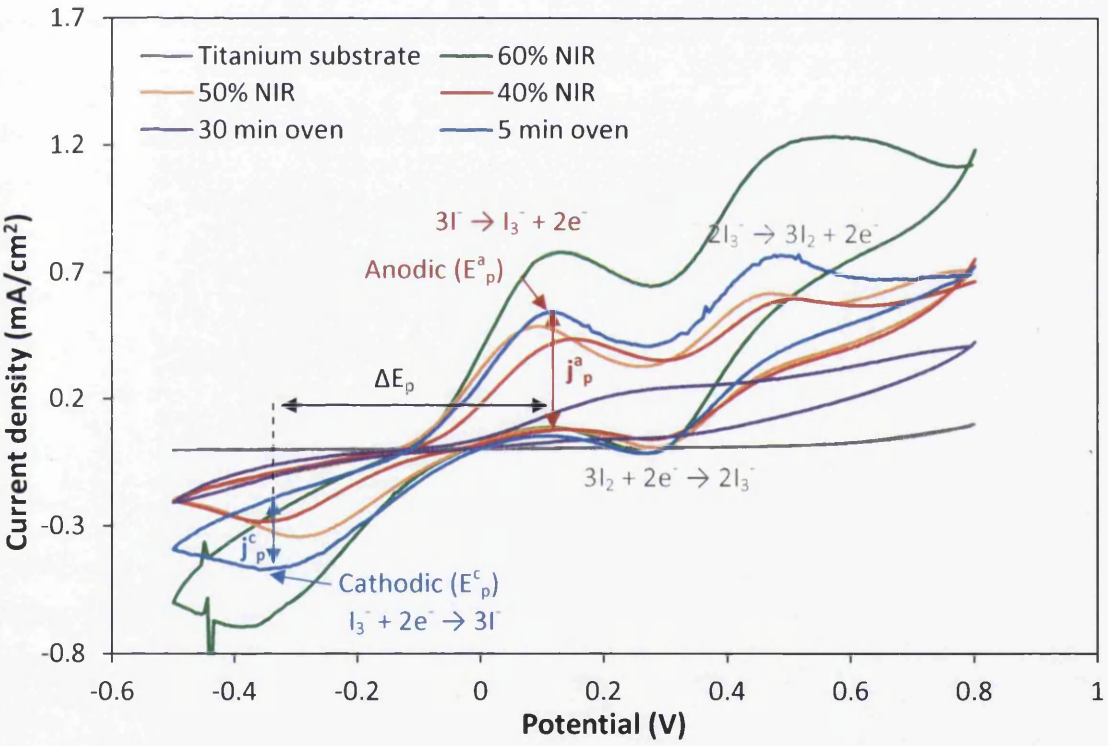

Figure 7.9: Cyclic voltammograms of NIR and oven heated chloroplatinic acid on titanium metal and bare unheated titanium in iodide electrolyte at a scan rate of 50 mV/s

Table 7.2: Data from cyclic voltammetry for peak separation and peak current density ratio to test for reversibility

Sample	ΔE_p	j^c_p	j^a_p	j^a_p/j^c_p
40% NIR	0.495	-0.19	0.36	1.91
50% NIR	0.385	-0.26	0.41	1.57
60% NIR	0.515	-0.37	0.69	1.87
5 min	0.47	-0.26	0.49	1.87
30 min	n/a	n/a	n/a	n/a
Titanium	n/a	n/a	n/a	n/a

As is expected bare titanium substrate has no affinity for the charge transfer of these reactions in this iodide electrolyte. 30 min of conventionally heating does not show any reversibility for the reduction of triiodide, there are no discernible peaks, which suggests that any platinum nanoparticles present are heavily impaired by a thick oxide layer which would have grown during the slow heating. 40% NIR also shows poor catalytic affinity for the iodine system although the two reduction and oxidation peaks are more obvious than for the 30 min oven sample, it has a large peak separation and a peak current ratio much higher than 1. For this sample it is likely that the titanium did not reach a high enough temperature to fully decompose the platinum chloride to platinum so there are not many platinum nanoparticles present to facilitate the charge transfer reactions. 50% NIR intensity has the smallest peak separation and the lowest current density ratio, although it is still higher than 1 because this reaction is quasi-reversible. This means that it has the best reversibility out of the platinised titanium samples and should function well in a DSC device as a counter electrode. It is likely that there is not a thick oxide layer impairing the platinum nanoparticles as there is for the 30 min oven sample due to the fast heating of the NIR radiation whilst still attaining catalytically active platinum nanoparticles in 12.5 s. The 60% NIR sample has a higher peak current ratio and larger peak separation suggesting it would not perform as well in a DSC device and this is likely due to the higher temperature reached during the NIR exposure accelerating the growth of the oxide layer in 12.5 s (as also shown from the photograph in figure 7.8) which may have prevented as much platinum adhering to the surface as the 50% NIR sample had. The 5 min oven sample has a similar ratio to 60% NIR but a closer peak separation suggesting it may perform slightly better in a DSC device with this electrolyte. The colours of the substrates look fairly similar so there may be a similar thickness of oxide. The shorter oven time has allowed platinum nanoparticles to adhere to the titanium surface without the relatively thin oxide layer interfering to the extent that 30 min heating does. However conventional heating is slow (as the thermal energy is delivered

by convection and conduction) so it is likely there is an incomplete conversion of platinum chloride to platinum in 5 min. This suggests there is a trade off between breaking all of the platinum chloride bonds and not producing a thick titanium oxide layer, which may not be an issue with NIR heating at the optimal intensity.

DSCs were constructed with conventional $TiCl_4$ treated TiO_2 FTO glass working electrodes and titanium counter electrode and measured through forward illumination. Table 7.3 shows the average IV parameters for these DSCs and figure 7.10 shows the average efficiency and fill factor. Figure 7.11 shows an IV curve for each heating variation of the platinised titanium counter electrode DSCs.

Table 7.3: Average IV parameters for NIR heated and oven heated titanium metal counter electrode DSCs for 3 devices with 1 standard deviation of error

Heating	V_{OC} (V)	J_{SC} (mA/cm^2)	FF (%)	Efficiency (%)
5 min oven	0.72 ± 0.00	9.39 ± 0.23	64.37 ± 3.42	4.38 ± 0.36
30 min oven	0.73 ± 0.01	9.07 ± 0.21	42.66 ± 4.90	2.84 ± 0.39
40% NIR	0.69 ± 0.00	9.32 ± 0.52	65.87 ± 4.70	4.24 ± 0.07
50% NIR	0.73 ± 0.00	9.18 ± 0.22	66.08 ± 0.31	4.44 ± 0.12
60% NIR	0.72 ± 0.01	9.15 ± 0.14	62.17 ± 3.37	4.09 ± 0.13

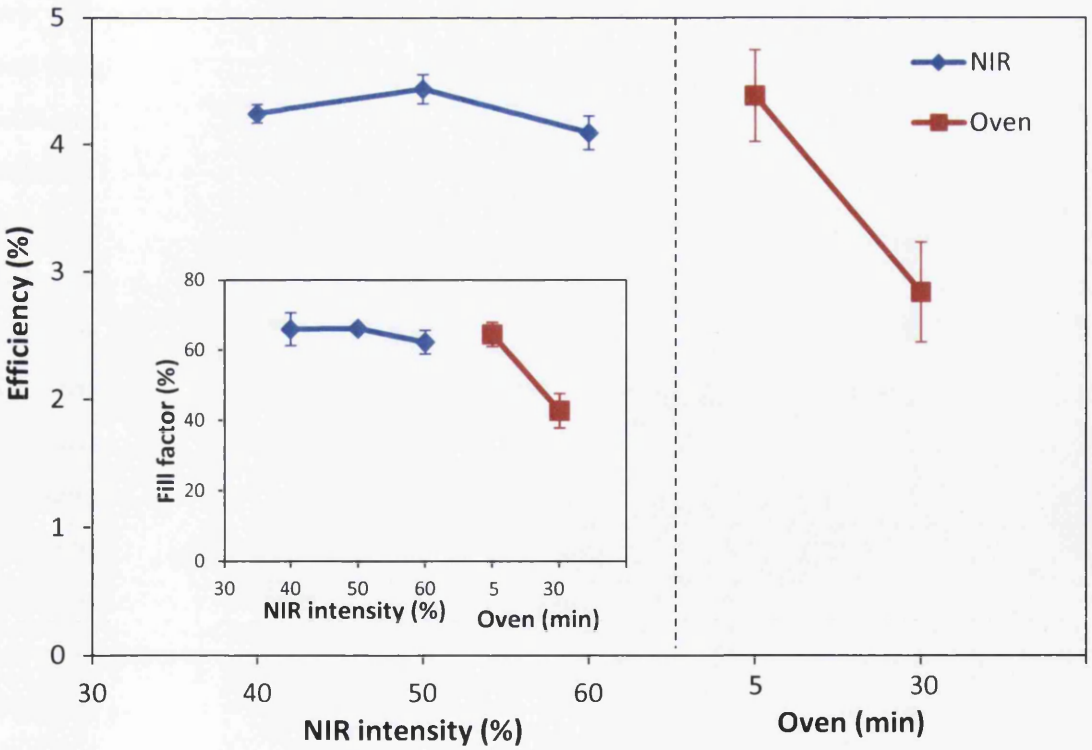

Figure 7.10: Average efficiency of NIR and oven heated titanium counter electrode DSCs and fill factor (inset) for 3 devices with 1 standard deviation of error

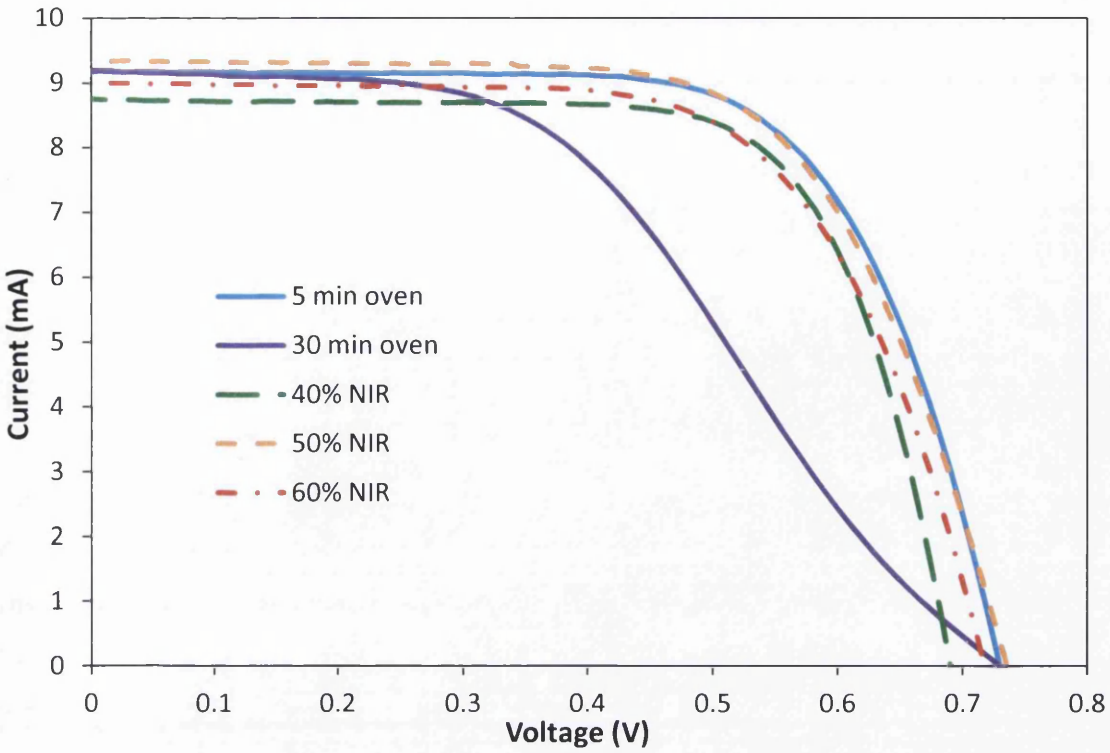

Figure 7.11: IV curves of NIR and oven heated titanium counter electrode DSCs

Each NIR heated titanium counter electrode DSC performs fairly similarly with 50% NIR radiation achieving the highest average efficiency and fill factor. This suggests there is a large processing window for platinisation which was also observed both for FTO glass (Chapter 4) and ITO glass (Chapter 6). The NIR heated counter electrodes also have good reproducibility with small error compared to the oven heated ones. The slightly lower performance for the 40% NIR heated counter electrode is likely due to a lower temperature attained during heating because there was lower intensity of radiation to absorb so less thermal energy delivered in 12.5 s for platinum chloride to platinum conversion. So there may be less platinum nanoparticles present as supported by the less reversible cyclic voltammetry data. The 50% NIR counter electrodes showed good reversibility in the cyclic voltammetry data and have the highest performance and reproducibility of the DSC devices. Unlike the 40% NIR sample there did appear to be some oxide growth for 50% NIR but less significantly than for 5 min oven. The 60% NIR counter electrodes would have reached a higher temperature than 50% and 40%, in the same timeframe of 12.5 s, and this has accelerated the growth of the oxide layer. The thicker oxide layer for 60% NIR intensity is shown by the lower average fill factor due to fewer catalytically active platinum sites to facilitate the triiodide reduction, the poorer reversibility compared to 50% NIR intensity as shown by the cyclic voltammetry, and the colour of the substrate (figure 7.8). The 30 min oven sample had an extremely poor

performance which was entirely limited by the counter electrode as shown from the poor fill factor and IV curve. This is likely due to poor adhesion of the platinum to the titanium as a result of a thick oxide layer. However the 5 min oven sample performed well and comparably to the best NIR exposed titanium counter electrode DSC although with larger variation which may be due to a thicker oxide layer manifesting in some cells more than others or just cell building. Although 5 min of oven heating at 385°C did achieve a good titanium counter electrode, 12.5 s of NIR exposure faster and may be more reproducible in DSC devices.

7.3.2 ITO PET

7.3.2.1 NIR exposure of ITO PET substrate

The absorbance and reflectance of ITO coated PET and uncoated PET is shown in figure 7.12. As discussed in Chapter 3 the ITO absorbs in the infrared region due to its high free carrier concentration which also reduces the reflectivity. This will cause the ITO PET to heat significantly higher than uncoated PET.

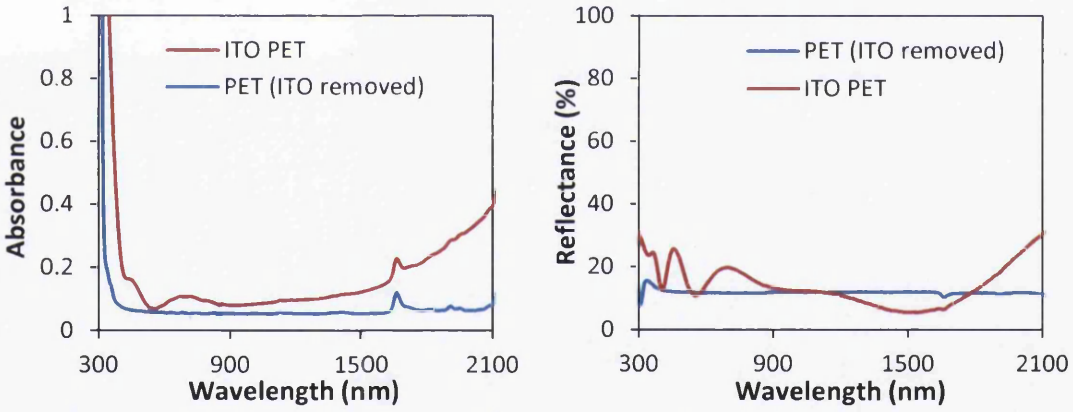

Figure 7.12: Absorbance (left) and reflectance (right) of ITO PET and identical PET with the ITO removed

Prior to NIR exposure of chloroplatinic acid or TiO_2 paste on ITO PET, the optimal NIR settings were investigated to find the limit of thermal degradation which would be suitable for multiple exposure runs without damaging the substrate. The NIR equipment (described in section 2.1) can be varied by both the intensity of the emitters and the speed of the conveyor belt which determines the exposure time for the substrate. For glass and metal substrates there was a higher processing window available for heating the substrates such that a specific line speed could be chosen and the intensity varied. However for the plastic

substrates the temperature operation window was extremely small, as experienced here for the NIR heating of PET [6], so subtle variations in the speed and intensity were necessary to find the optimum. Samples of ITO PET of roughly 2 x 2 cm were subjected to various speeds and intensities of NIR to observe their physical degradation as described in Table 7.4 and shown in figure 7.13.

Table 7.4: NIR settings used on ITO PET samples and their sheet resistance

Sample	Speed (m/min)	Intensity (%)	No. of runs	Sheet resistance (Ω/□)		
				Before	After	Change
1	25	50	1	15.45	15.15	-0.3
2	25	50	2	15.68	14.82	-0.86
3	25	50	3	15.78	15.85	0.07
4	25	50	4	15.51	15.86	0.35
5	25	50	5	15.84	15.42	-0.42
6	12	50	1	16.31	n/a	n/a
7	20	50	1	15.45	15.77	0.32
8	23	50	1	15.97	15.78	-0.19
9	25	60	1	15.2	n/a	n/a
10	25	55	1	15.55	15.45	-0.1

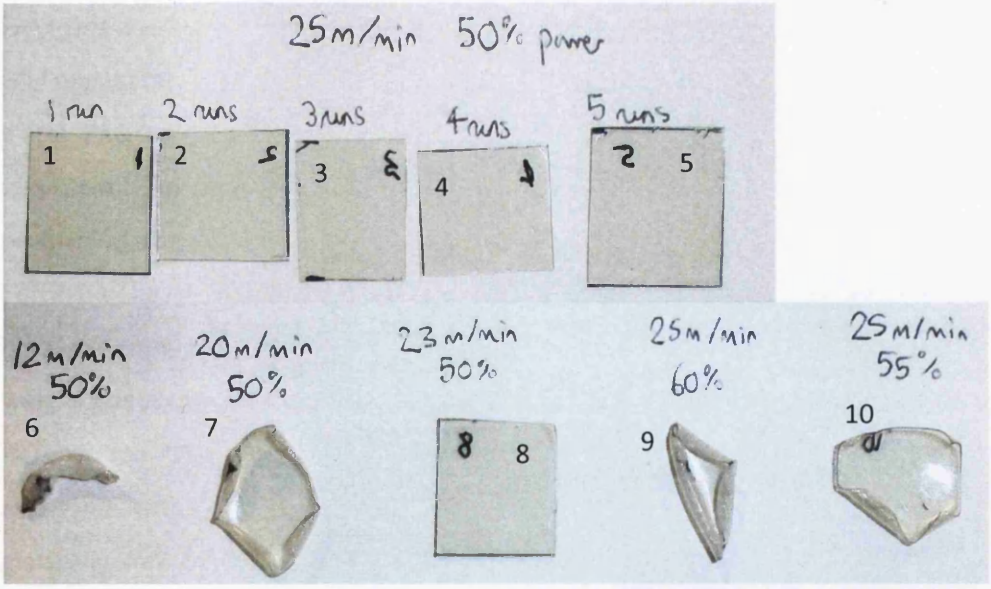

Figure 7.13: Samples 1-10 of ITO PET after NIR exposure corresponding to Table 7.4

Samples 6 and 9 did not have their resistivity measured afterwards due to their state of degradation. Table 7.4 shows that the resistivity of ITO was not affected by the small amounts of NIR radiation subjected to the ITO PET samples. This would be expected as PET would melt at temperatures exceeding 250°C, temperatures before which ITO is expected to

increase in resistivity (section 3.3.3). The changes in resistivity before and after heating was assumed to be negligible and solely due to variations of resistivity within the ITO film. The integrity of the ITO PET was not affected after 5 runs of the speed 25 m/min with an intensity of 50% NIR power. Keeping the intensity constant at 50% NIR power and slower speed melts the ITO PET although 23 m/min is slow enough to not warp it. Using a higher intensity of 60% and 55% was also too high for the ITO PET. Therefore 25 m/min and 50% power was chosen as the optimum NIR setting for ITO PET which results in an exposure time of 1 second.

7.3.2.2 Rapidly heated TiO_2 paste on ITO PET for DSC working electrodes

In addition to calibrating the maximum exposure of NIR radiation that bare ITO PET could withstand the substrate was also subjected to NIR radiation with a film of doctor bladed TiO_2 paste coated as it would be for a DSC working electrode (section 2.2). It would be the case that if the TiO_2 paste did contribute to any NIR absorption it would heat more than the bare ITO PET and either assist with the heating of the paste or contribute to the temperature of the ITO PET and cause it to melt with less NIR radiation (because more radiation would be absorbed overall). The pastes used were DSL 18NR-AO and DSL 18NR-T (Dyesol) and two P25 TiO_2 (Degussa) based pastes named "PEG 0" and "PEG 30". PEG 0 contains P25 TiO_2, nitric acid and water, no binder. PEG 30 contains P25 TiO_2, 30 wt% polyethylene glycol (PEG) and water. PEG 0, PEG 30 and DSL 18NR-T had dry film thicknesses of 9.3 μm, 11 μm, and 8.3 μm respectively as measured from samples on ITO PET. Thermogravimetric analysis was performed on each paste to show weight loss over temperature (figure 7.14), only DSL 18NR-T is shown for the Dyesol pastes because they both contain the same solvent and binder so experience weight loss at the same temperatures. For PEG 0 the vast majority of weight loss occurs before 250°C with all remaining weight assumed to be P25 particles of TiO_2. For the PEG 30 paste the majority of weight loss occurred before 250°C but there was also some further weight loss after 300°C which is attributed to the PEG binder and occurs gradually until 440°C. DSL 18NR-T has two distinct regions of weight loss, the terpineol solvent up until about 220°C and then the ethyl cellulose binder up until 420°C.

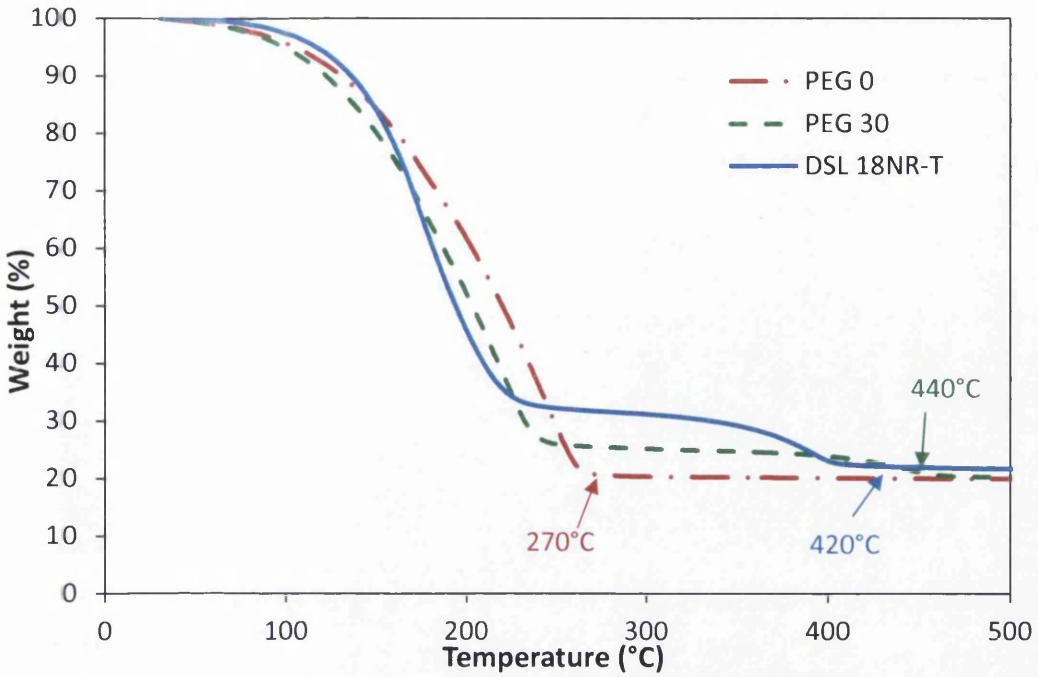

Figure 7.14: Thermogravimetric analysis profiles for PEG 0, PEG 30 and DSL 18NR-T TiO_2 pastes

Using the optimised heating regime for bare ITO PET (section 7.3.2.1), 25 m/min and 50% NIR intensity, doctor bladed TiO_2 pastes coated onto samples of ITO PET about 2 x 2 cm in size were subjected to NIR radiation as described in Table 7.5 and shown in figure 7.15.

Table 7.5: List of the paste and no. of NIR runs subjected to each sample (25 m/min, 50% power)

Sample	Paste	No. of runs
11	PEG 0	2
12	PEG 0	4
13	PEG 0	6
14	PEG 0	8
15	PEG 0	10
16	DSL 18NR-AO	4
17	DSL 18NR-AO	2
18	PEG 30	2
19	DSL 18NR-T	4
20	PEG 30	4
21	PEG 30	8
22	PEG 30	11
23	DSL 18NR-T	8
24	DSL 18NR-T	13

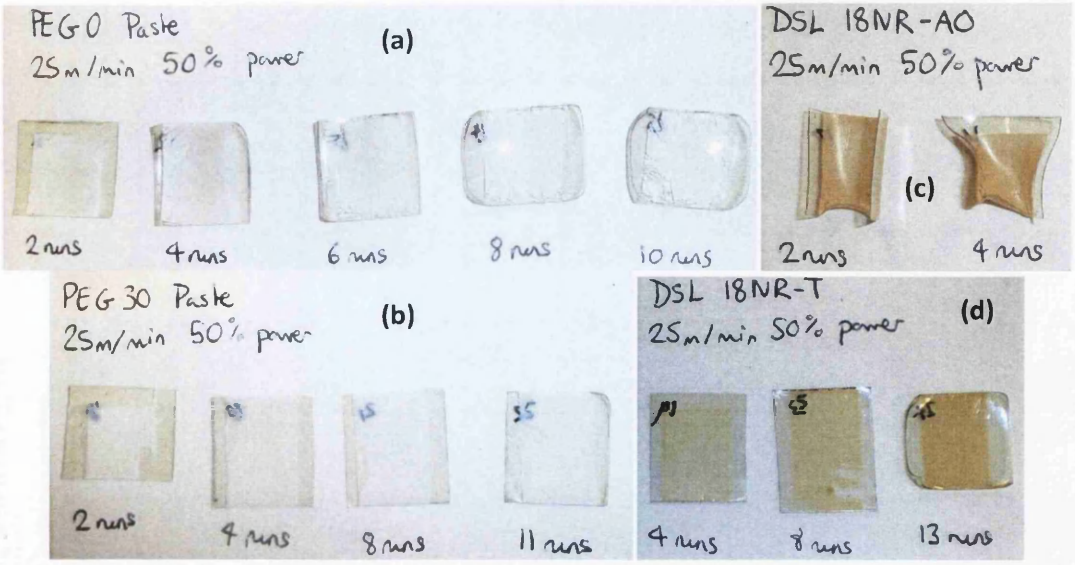

Figure 7.15: TiO_2 pastes on ITO PET subjected to various runs of 25 m/min, 50% power NIR for (a) PEG 0 paste, (b) PEG 30 paste, (c) DSL 18NR-AO, and (d) DSL 18NR-T

The PEG 0 paste experienced poor coating of the substrate during doctor blading so required multiple applications. As shown in figure 7.15.a with increasing runs of NIR radiation the paste started to crack and flake off easily and the ITO PET began to warp after 4 runs. Therefore 2 runs was considered to be the most exposure PEG 0 paste could withstand while maintaining an consistent film and was chosen for subsequent experiments. The addition of binder in the PEG 30 paste made it easier to deposit than the PEG 0 paste. As shown in figure 7.15.b the paste seemed to withstand many runs of NIR, up to 11 runs. 8 runs was chosen for subsequent experiments. DSL 18NR-AO paste warped badly even after only one run (figure 7.15.c) but was left for 2 and 4 runs. The greater extent of heating for DSL 18NR-AO supports what was proposed in Chapter 5 that this paste is absorbing NIR radiation and generating additional heat. Therefore DSL 18NR-AO was disregarded as a paste choice for ITO PET working electrodes. Figure 7.15.d shows that the DSL 18NR-T paste withstood the NIR runs quite well, up to 13 runs after which it warped. 8 runs was chosen for subsequent experiments. Using the optimised heating regime above, doctor bladed TiO_2 pastes coated onto samples of ITO PET were subjected to NIR radiation and observed using SEM (figure 7.16).

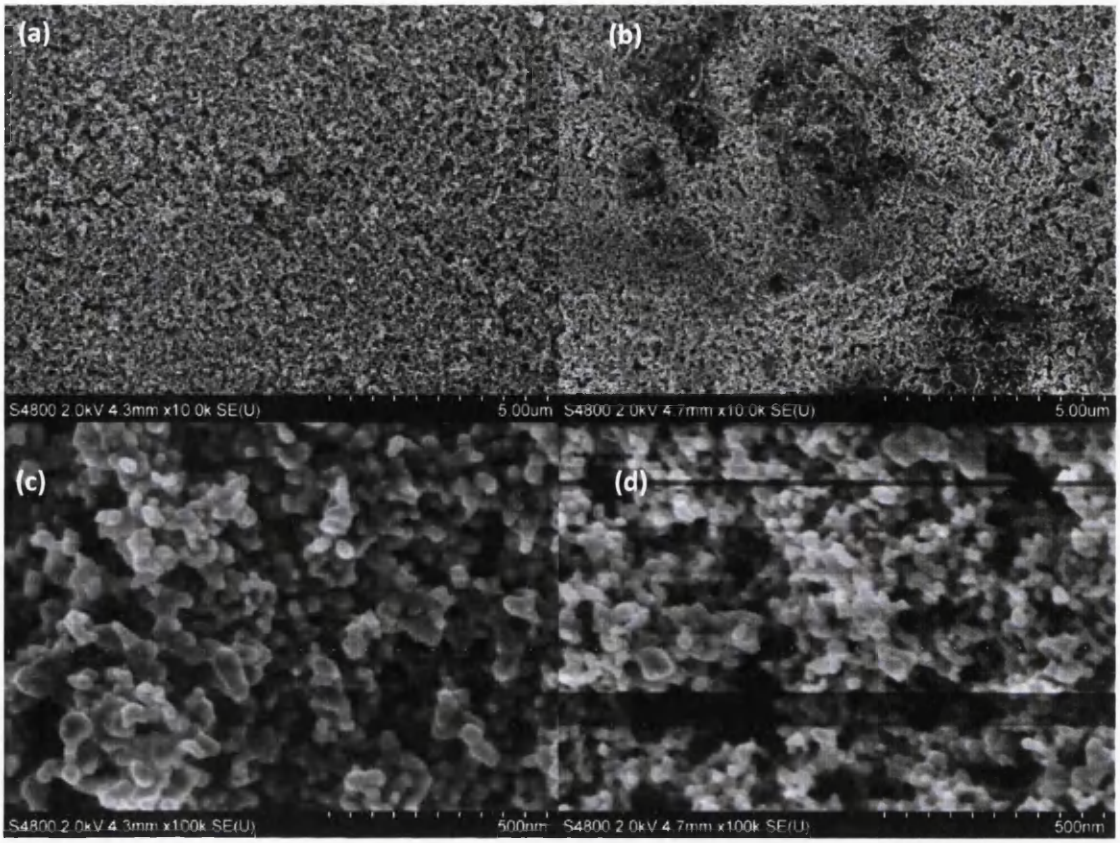

Figure 7.16: Scanning electron micrographs of TiO_2 paste on ITO PET heated with NIR radiation at low magnification (a) PEG 0 and (b) PEG 30, and high magnification (c) PEG 0 and (d) PEG 30

The NIR exposure was 50% intensity at 25 m/min, the PEG 0 paste was subjected to 2 runs (2 s total exposure) and the PEG 30 paste was subjected to 8 runs (8 s total) as was determined above to be the maximum number of runs each could withstand without degradation to the substrate. The TiO_2 film appears to have some level of porosity for both samples but it is unclear the extent of this and it is unlikely to be sintered. Figures 7.13.b and 7.13.d show that the PEG 30 paste still has binder present as would be expected from the TGA that shows weight loss attributed to binder until 440°C. It is unclear to what extent any remaining binder would impair the active surface area of the TiO_2 film and this will be observed in DSC devices.

Some of the NIR heated TiO_2 paste on ITO PET samples were immersed in dye to obtain a crude indication of how much dye they would adsorb from the colour change which would indicate any porosity. They were firstly immersed in a dye solution of 0.3 M N719 (Solaronix) in acetonitrile/tert-butanol (1:1) for 24 hr. Figure 7.17 shows a photograph of the samples after dyeing.

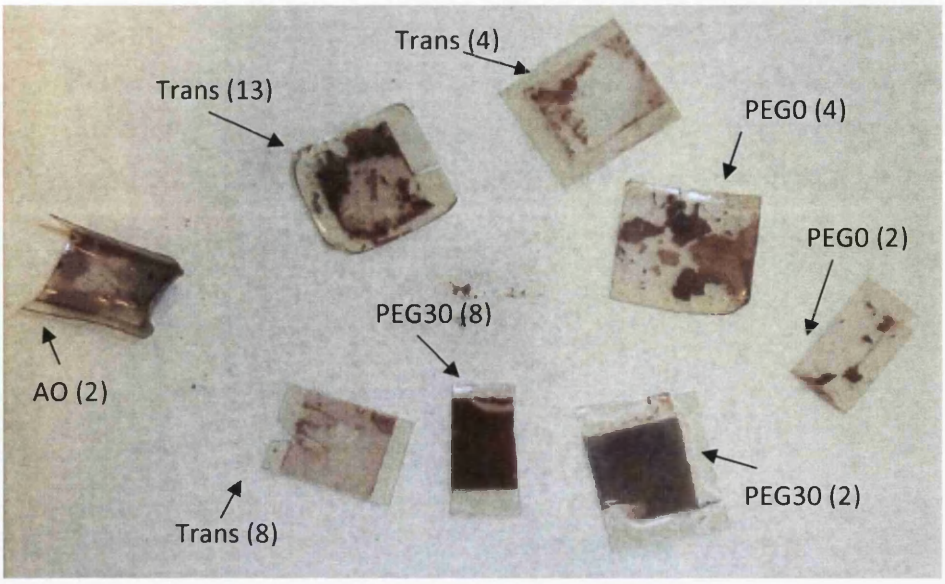

Figure 7.17: Samples of paste on ITO PET after 24 hr dye immersion in ACN/T-But solution

As is clear from figure 7.17 most of the TiO_2 film remained in the dye. ITO is extremely smooth so this will reduce the adhesion of TiO_2 to the electrode. This is not usually an issue for FTO because FTO is quite rough and facilitates the adhesion of TiO_2 extremely well. The stripping of the ITO PET does vary by paste and no. of NIR runs. PEG 0 and DSL 18NR-T paste seem to fare the worst whereas PEG 30 seems quite resilient and was not stripped. The adhesion was also increased with no. of runs of NIR radiation. DSL 18NR-AO was immersed in the dye anyway despite not being a candidate for further work and seemed to be less stripped than the all the pastes except PEG 30. The paste being removed by the dye was of course a drawback and it was unclear whether this was due to the films being too poorly adhered to the ITO PET or if the solvent was affecting it. Just in case it was the latter other samples of paste on ITO PET were immersed in an identical dye solution this time in ethanol (shown in figure 7.18).

The ethanol based dye yielded less aggressive results. Although stripping was present on some of the flakier TiO_2 films it is nowhere near to the same extent of the ACN/T-But based dye and the previous stripping can perhaps be attributed to the bulkier solvent. As a direct comparison the PEG 0 (2 runs) sample is used in both (it was cut in half) and was almost completely removed in the ACN/T-But based dye but the film remains intact in the ethanol based dye. Therefore ethanol based dye was used in the fabrication of ITO PET working electrodes for DSC devices.

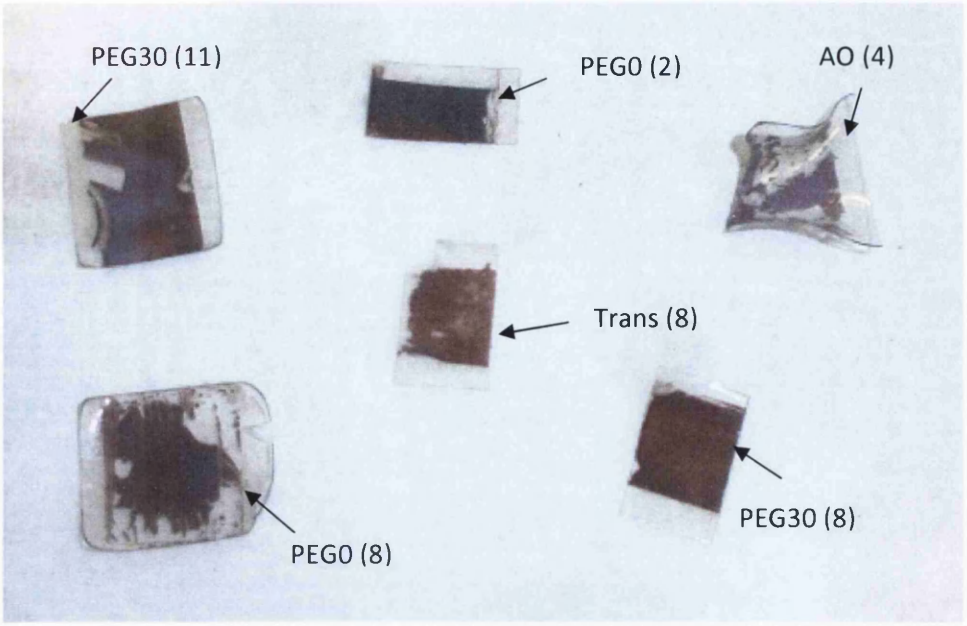

Figure 7.18: Samples of paste on ITO PET after 24 hr dye immersion in ethanol solution

Using DSL 18NR-T, PEG 0 and PEG 30 pastes, TiO_2 films were doctor bladed onto ITO PET exposed to non-consecutive runs of 1 sec each at 50% NIR intensity and dyed with N719 for use as DSC working electrode. As discussed in the appendix the use of acetonitrile/tert-butanol solvent for the 0.3 mM N719 dye resulted in the TiO_2 films being stripped away. This was found to not be case when tested using ethanol solvent but as shown in figure 7.19 when this was repeated for the manufacture of working electrodes it did strip away the DSL 18NR-T paste.

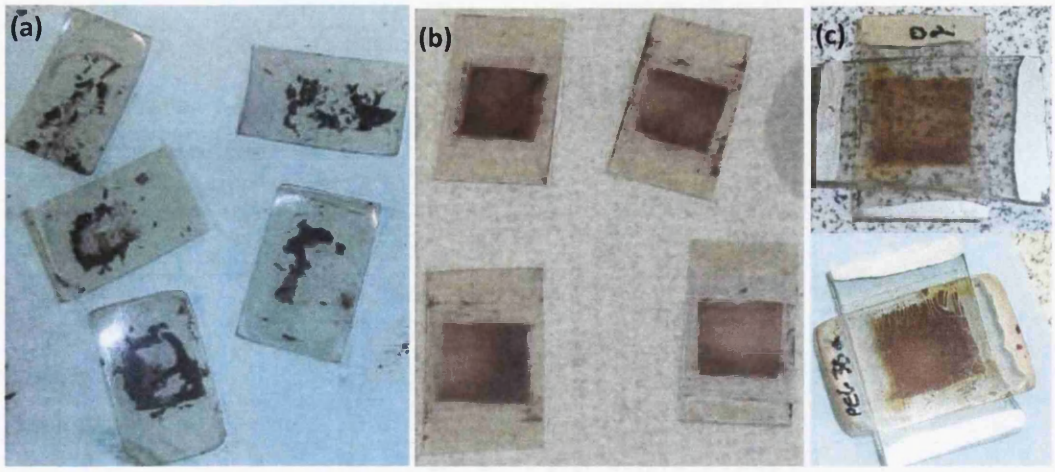

Figure 7.19: (a) Attempt at DSL 18NR-T working electrodes on ITO PET showing that the dye had stripped away the TiO_2 film, (b) PEG 0 working electrode on ITO PET after dye immersion, and (c) ITO PET working electrode/FTO glass counter electrode DSC devices

DSC devices (figure 7.19.c) were constructed with the PEG 0 and PEG 30 ITO PET working electrodes (figure 7.19.b) and conventional oven heated counter electrodes. Table 7.6 shows the IV parameters and figure 7.20 shows JV curves. PEG refers to the PEG 30 paste (only one PEG 30 DSC worked) and binder free refers to the PEG 0 paste (only two devices worked labelled as a and b).

Table 7.6: IV parameters

Paste	V_{OC} (V)	J_{SC} (mA/cm^2)	FF (%)	Efficiency (%)
PEG	0.69	0.37	63.91	0.16
Binder free a	0.80	1.54	60.76	0.75
Binder free b	0.79	0.73	72.19	0.42

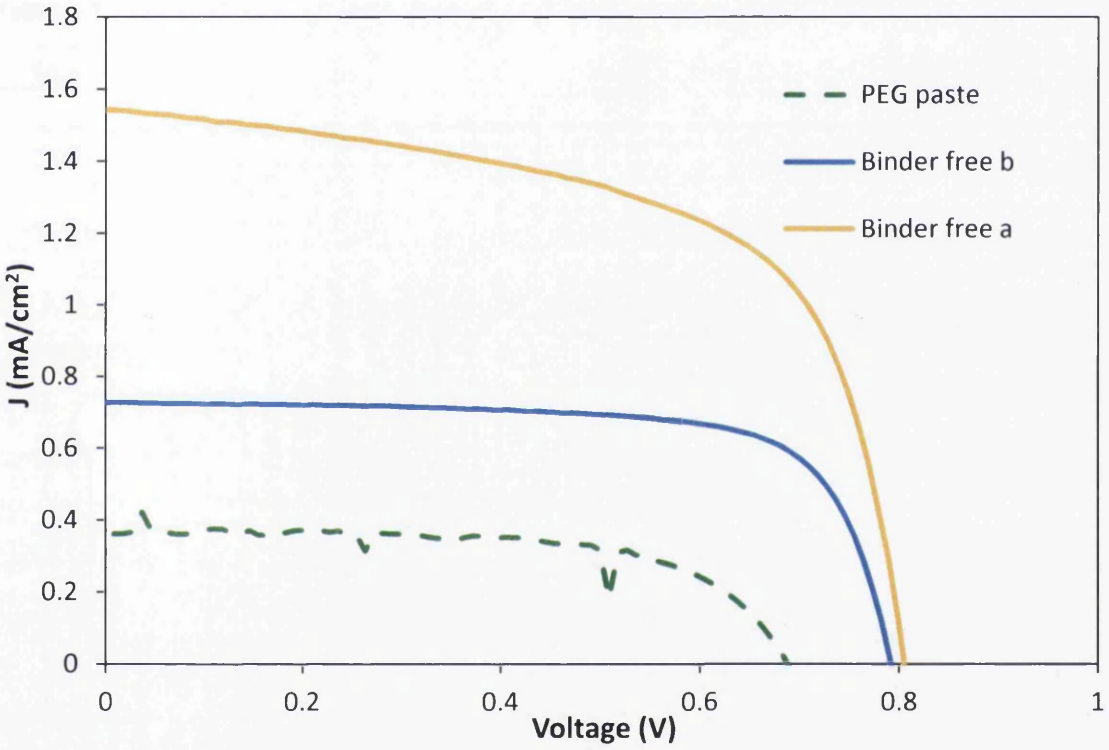

Figure 7.20: JV curve of plastic working electrode DSCs

There was much difficulty in sealing the cells together due to constructing a device of a flexible and rigid substrate and the slight curviness of the ITO PET working electrodes as a result of too much NIR exposure. As a result only a few cells were constructed successfully and these had sub 1cm^2 area because the electrolyte had not fully infiltrated the cell. As expected the cells were severely limited by the current density suggesting that the TiO_2 film has poor charge transport due to no sintering. The PEG containing paste has a noisy IV curve but the other two curves are smooth.

7.3.2.3 Platinisation of ITO PET for DSC counter electrodes

DSCs were constructed using NIR heated chloroplatinic acid on ITO PET at a speed of 25 m/min and intensity of 50% power with a conventionally heated $TiCl_4$ treated TiO_2 working electrode on FTO glass. There was again difficulty in the cell building of FTO glass/ITO PET DSCs so on average only one of counter electrode type DSC worked. This was due to short circuiting problems and the difficulty of assembly. The best cell from each is shown in Table 7.7 and as a control platinum was sputtered onto ITO PET to represent the usual method of obtaining a platinum ITO PET counter electrode DSC device and reinforce that the limitation is of the method of platinisation rather than the substrate. Figure 7.21 shows IV curves for each cell and figure 7.22 shows a graph of the efficiency vs. no. of runs.

Table 7.7: The best cells for each no. of runs, sputter Pt on ITO PET is an average of 2 devices

No. of runs	V_{OC} (V)	J_{SC} (mA/cm^2)	FF (%)	Efficiency (%)
0	0.74	0.90	13.96	0.09
2	0.70	5.21	19.13	0.70
4	0.74	5.45	31.93	1.28
8	0.73	9.29	40.50	2.75
10	0.72	10.72	41.93	3.24
12	0.73	10.32	31.92	2.40
Sputtered Pt	0.77 ± 0.00	11.72 ± 0.14	62.84 ± 0.80	5.67 ± 0.01

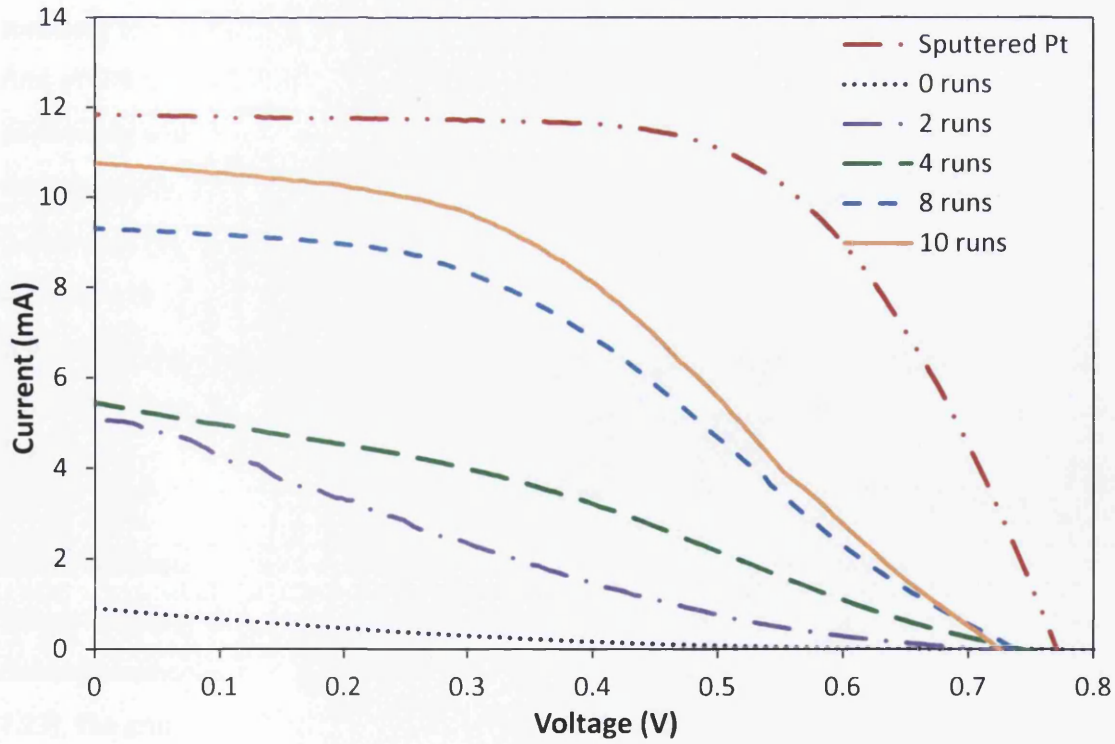

Figure 7.21: IV curves for ITO PET counter electrode DSCs

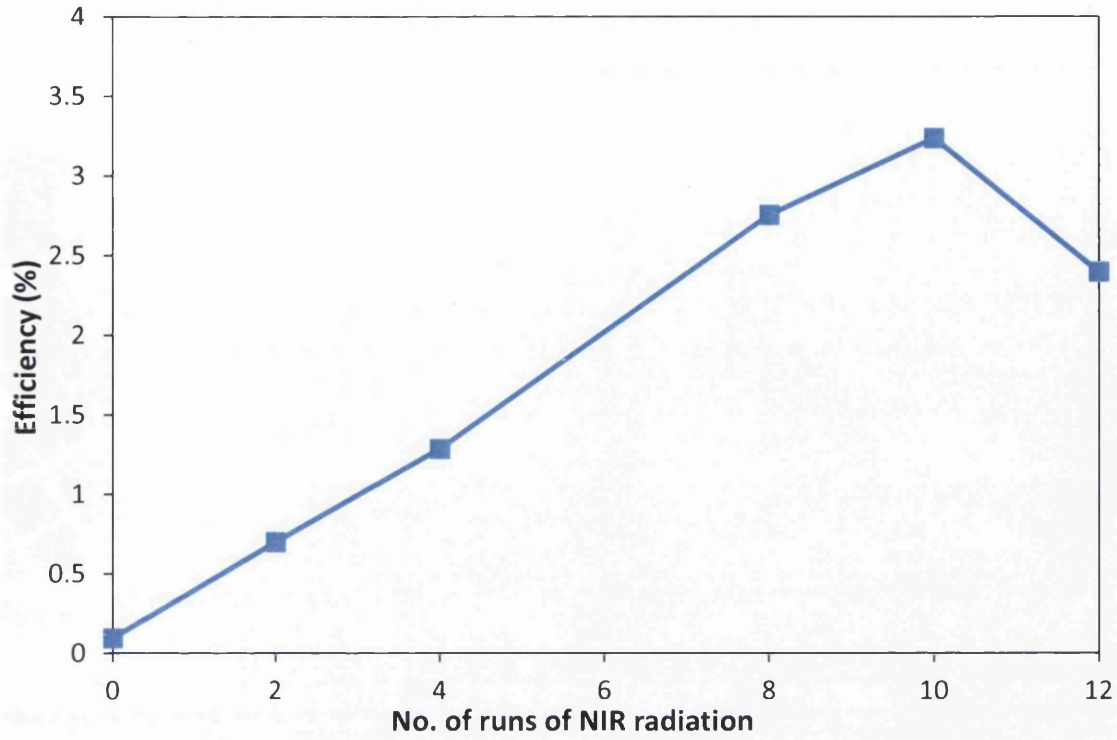

Figure 7.22: Efficiency for various runs of NIR radiation at 25 m/min speed and 50% intensity

For the NIR heated chloroplatinic acid on ITO PET counter electrodes the fill factors are quite low which is to be expected as a low conversion rate of platinum chloride to catalytic platinum would be experienced at such low temperatures. However the NIR radiation was sufficient to create a working thermally produced counter electrode on ITO PET, with 10 runs of NIR radiation (10 s of non-consecutive exposure at 50% NIR intensity) being the best performing with an efficiency of 3.2%. It is certainly not optimised in terms of reproducibility, since only one of each type worked the results cannot conclude that 10 runs is definitely the optimum and further work would need to be done, but demonstrates that it is possible to use an NIR heated ITO PET counter electrode to create a working DSC device. With a FF of only 42% the counter electrode is very much the limiting factor in the DSC's performance as would be expected. The sputtered Pt counter electrode works well as expected.

7.3.3 Platinisation of ITO free flexible polymeric substrate for DSC counter electrodes

Epimesh (Epigem) is an ITO alternative to a flexible polymeric substrate and consists of a nickel-phosphorus alloy microgrid embed into a polymer coated onto a PET film (figure 7.23). The grid pitch is 40 µm with the lines 6 µm wide and 4 µm thick, protruding 100 nm

above the polymer. This substrate was investigated for use as a plastic counter electrode for DSCs.

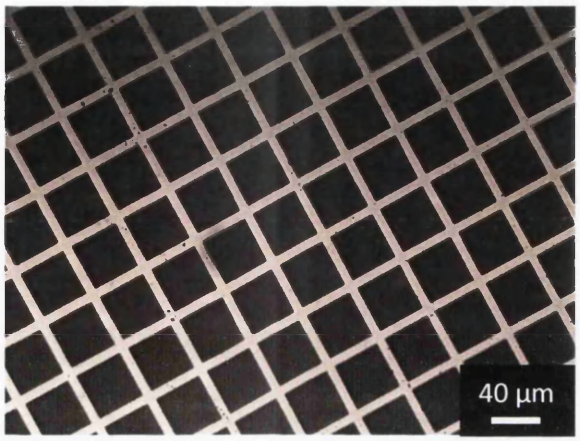

Figure 7.23: Optical micrograph of the Epimesh substrate

The Epimesh substrate was subjected to 50% NIR intensity radiation but at a speed of 50 m/min (0.5 s exposure) due to its melting at 25 m/min. DSCs were constructed with NIR exposed chloroplatinic acid on Epimesh and conventionally heated $TiCl_4$ treated TiO_2 working electrode on FTO glass. Table 7.8 shows the IV parameters and figure 7.24 shows the efficiency and fill factor vs. number of NIR runs.

Table 7.8: No. of runs of NIR exposure (0.5 s per run at 50% intensity) for Epimesh grid counter electrode DSCs, average of 3 devices where error is shown, bare grid for the Epimesh substrate unheated with no chloroplatinic acid

No. of runs	V_{OC} (V)	J_{SC} (mA/cm^2)	FF (%)	Efficiency (%)
Bare grid	0.62	1.32	21.65	0.18
0	0.74 ± 0.02	6.80 ± 0.40	27.50 ± 4.16	1.38 ± 0.28
4	0.69 ± 0.06	7.30 ± 0.31	34.55 ± 0.47	1.74 ± 0.20
8	0.73 ± 0.00	6.99 ± 0.13	39.10 ± 1.08	2.00 ± 0.02
12	0.78	4.15	40.39	1.31
16	0.55	6.74	32.14	1.19
20	0.75	6.75	24.36	1.23

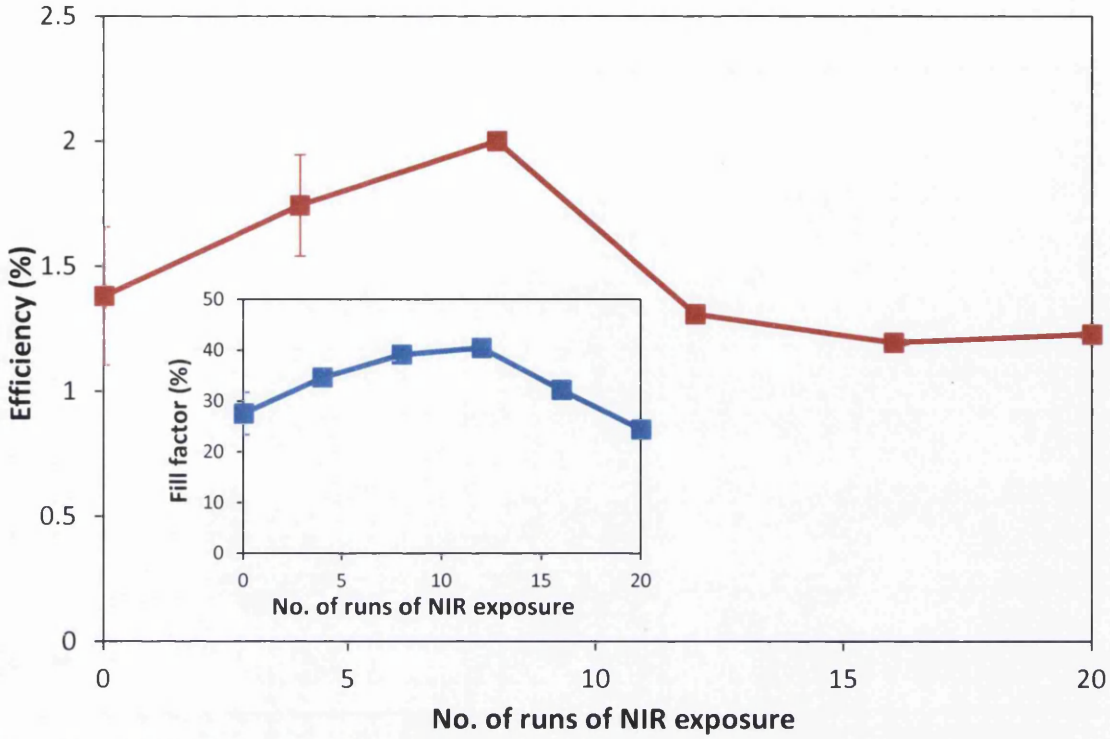

Figure 7.24: Efficiency for Epimesh grid counter electrode DSCs (average of 3 devices for 0-8 runs) with fill factor inset

The optimum exposure of runs seems to be 8 where an efficiency of 2% was achieved but a fill factor of only 39%. A major drawback with the conductive grid is that only Pt in contact with the grid (where electrons are present) will be catalytic active and able to contribute to the reduction of triiodide manifesting itself as a severely limited fill factor. The NIR radiation would be primarily absorbed by the metallic grid rather than the areas of bare polymer so only the platinum chloride in these areas would have had some conversion to platinum.

7.4 Conclusions

NIR heated titanium counter electrodes DSCs achieved equal performance to oven heated counter electrode on titanium but with higher reproducibility. This gives the potential for rapidly producing a flexible DSC which is highly desirable for commercialisation due to savings of cost, time, and the ability to incorporate into a building material. There is a compromise between the thermal energy delivered in 12.5 s to convert platinum chloride to platinum nanoparticles and the thermal energy to grow an oxide layer which would grow faster with a higher a temperature. The optimal setting for this is 12.5 s of 50% NIR intensity.

NIR radiation was used to heat ITO PET substrates but extremely tight processing conditions were necessary to avoid melting the substrate. It did show to be very suitable for high temperature applications but may be useful for lower temperature applications sub 150°C where NIR can still be used to reduce any heating time.

7.5 References

[1] S. Ito, N.-L.C. Ha, G. Rothenberger, P. Liska, P. Comte, S.M. Zakeeruddin, et al., High-efficiency (7.2%) flexible dye-sensitized solar cells with Ti-metal substrate for nanocrystalline-TiO_2 photoanode., Chem. Commun. (2006) 4004–6.

[2] J. Park, Y. Jun, H. Yun, S.-Y. Lee, M. Kang, Fabrication of an Efficient Dye-Sensitized Solar Cell with Stainless Steel Substrate, J. Electrochem. Soc. 155 (2008) 145–149.

[3] M. Kang, N. Park, K. Ryu, S. Chang, K. Kim, A 4.2% efficient flexible dye-sensitized TiO_2 solar cells using stainless steel substrate, Sol. Energy Mater. Sol. Cells. 90 (2006) 574–581.

[4] H. Lindström, H. Rensmo, S. Södergren, A. Solbrand, S.-E. Lindquist, Electron Transport Properties in Dye-Sensitized Nanoporous - Nanocrystalline TiO_2 Films, J. Phys. Chem. 100 (1996) 3084–3088.

[5] T. Ma, X. Fang, M. Akiyama, K. Inoue, H. Noma, E. Abe, Properties of several types of novel counter electrodes for dye-sensitized solar cells, J. Electroanal. Chem. 574 (2004) 77–83.

[6] D. Bryant, I. Mabbett, P. Greenwood, T. Watson, M. Wijdekop, D. Worsley, Ultrafast near-infrared curing of PEDOT:PSS, Org. Electron. 15 (2014) 1126–1130.

[7] T. Watson, I. Mabbett, H. Wang, L. Peter, D. Worsley, Ultrafast near infrared sintering of TiO_2 layers on metal substrates for dye-sensitized solar cells, Prog. Photovoltaics Res. Appl. 19 (2010) 482–486.

[8] M.J. Carnie, C. Charbonneau, P.R.F. Barnes, M.L. Davies, I. Mabbett, T.M. Watson, et al., Ultra-fast sintered TiO_2 films in dye-sensitized solar cells: phase variation, electron transport and recombination, J. Mater. Chem. A. 1 (2013) 2225.

[9] J. Banfield, B. Bischoff, M. Anderson, TiO_2 accessory minerals: coarsening, and transformation kinetics in pure and doped synthetic nanocrystalline materials, Chem. Geol. 110 (1993) 211–231.

[10] P.R.F. Barnes, K. Miettunen, X. Li, A.Y. Anderson, T. Bessho, M. Grätzel, et al., Interpretation of optoelectronic transient and charge extraction measurements in dye-sensitized solar cells, Adv. Mater. 25 (2013) 1881–922.

[11] M. V Diamanti, B. Del Curto, M. Pedeferri, Interference Colors of Thin Oxide Layers on Titanium, Color Res. Appl. 33 (2008) 221–228.

[12] A. Bard, L. Faulkner, Electrochemical Methods: Fundamentals and Applications, 2nd ed., John Wiley & Sons, 2001.

8. Optimising a Highly Efficient Rapidly Processed Dye-sensitised Solar Cell

8.1 Evaluating the current system

Currently the laboratory method for the manufacture of a dye-sensitised solar cell (DSC), outlined in section 2.2 (figure 8.1), involves three lengthy processes; the two major heating stages (thermal decomposition of platinum for the counter electrode and sintering of titanium dioxide for the photoelectrode) and dye uptake of the TiO_2. These stages are unfeasible for the commercialisation of DSCs because they are extremely time consuming, batch processes, and restrict roll-to-roll production output. The traditional method for creating the working electrode of a DSC is to heat a binder containing TiO_2 paste in a conventional oven at a temperature of 450-500°C for 30 minutes [1] (see discussion of the TiO_2 layer in section 1.2.3.1). For thermal platinisation the most effective method is heating H_2PtCl_6 in a conventional oven for 30 min at 385°C [2] (see discussion of the platinum catalyst in section 1.2.6.1).

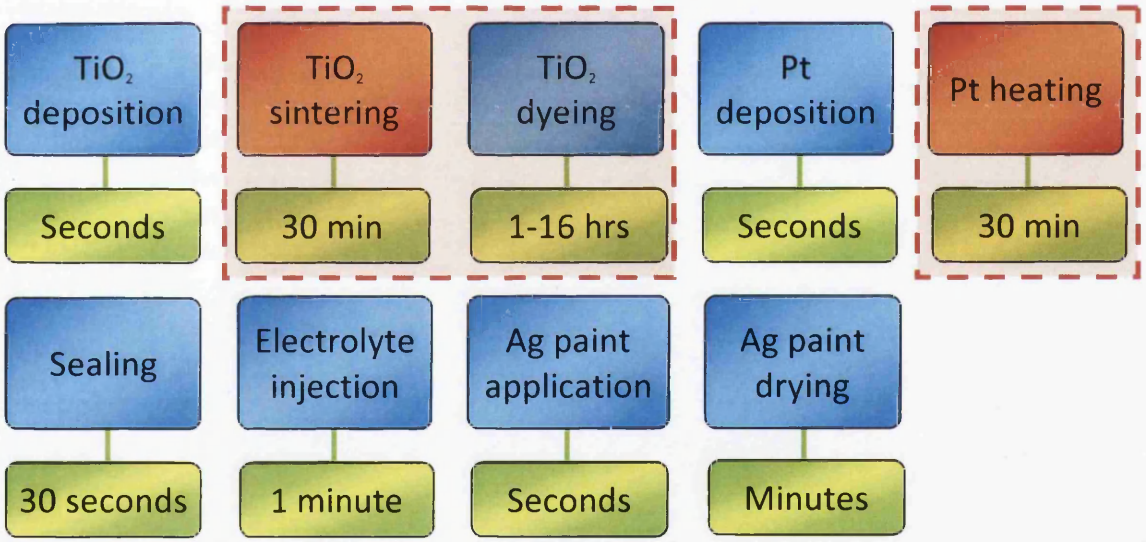

Figure 8.1: Diagram of the assembly process and associated times for laboratory built dye-sensitised solar cells consistent with the method in section 2.2

Generally dyeing the TiO_2 film (see section 1.2.4) can take up to 24 hours particularly for N719 and related ruthenium based dyes which take longer than organic dyes due to their larger molecules. The dyeing method used thus far was passive dyeing (immersing the working electrode in a 0.3 mM N719 solution either in ethanol or 1:1 acetonitrile/tert-butanol in the dark at room temperature) which becomes saturated (uptake >99.5%) after around 16 hours [3]. Dyeing time can be reduced by an increase in temperature [4], pressure

[5][6], and concentration [3][4]. Faster N719 dyeing can be achieved by immersing the working electrodes in solution at a temperature of 80°C for 1 hour as the temperature aids the diffusion of dye molecules. To achieve extremely fast dyeing times a pump dyeing technique was developed by Holliman and co-workers [7] to enable dyeing in under 5 min as well as easy co-sensitisation [8] (figure 8.2).

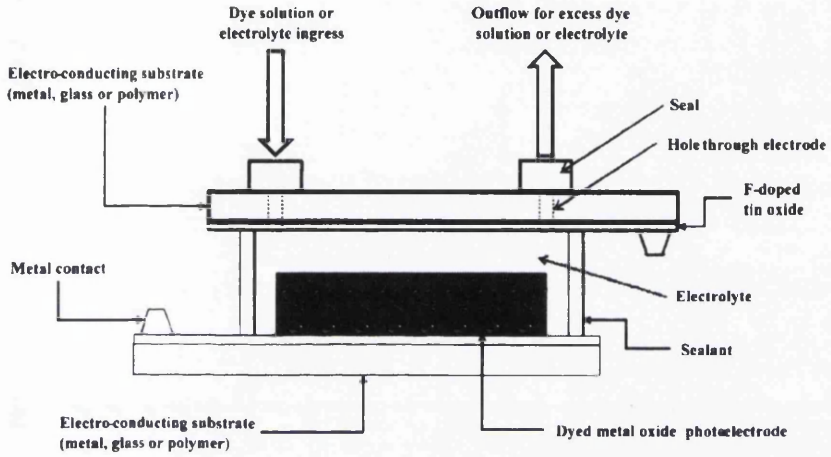

Figure 8.2: Diagram of the pump dyeing technique cell, the dye is pumped through one of the holes as shown using a pump or syringe [7]

In Chapter 3 FTO glass was shown to heat significantly upon exposure to 12.5 s of NIR radiation. In Chapter 4 this was applied to the thermal decomposition of chloroplatinic acid on FTO glass which enabled DSCs to be built with platinum obtained 144 times faster than the conventional 30 min heating method with identical catalytic performance. In Chapter 5 NIR radiation was used to sinter TiO_2 onto FTO glass in 12.5 s which achieved the same electron transport and efficiency when assembled into DSC devices as conventionally heated working electrodes but 144 times faster. In this chapter the lab making DSC method will be evaluated and time saving steps compiled together to build an efficient device as quickly as possible. Scale up processes will also be discussed. As mentioned previously the traditional DSC fabrication method is found in section 2.2 and the fast dyeing variation (using the pump dyeing technique [7]) is found in section 2.2.5. Table 8.1 shows a detailed analysis of the laboratory manufacturing method for a liquid electrolyte DSC (a 1 cm^2 device as used in this thesis) in chronological order with a time allocated for each task, whether each task can be applied to more than one cell at once, if the task can be prepared in advance and what the scaling up method could be (in terms of size and commercialisation).

Task	Time	Step type	Prepare in advance?	Scale up method
Cut FTO glass into pieces (from a 10 x 10 cm sheet)	5 min	Group	Yes	Buy to size
Clean glass	2-3 min	Group/individual	Yes	Automate process
Doctor blade paste (1 strip of cells)	20 s	Group	No	Screen printing
Heating TiO_2 (in an oven)	30 min	Group	No	Long industrial sized oven
Heating TiO_2 (with NIR)	25 s	Group	No	Industrial sized NIR
Glass cooling	1-5 min	Group	No	Speed up/use warm
Shaping TiO_2	10 s	Individual	No	Print to size
Dyeing (conventional)	16 hr	Group	No	Long dye bath
Dyeing (heat assisted)	1 hr	Group	No	Long dye bath
Dyeing (pump technique)	2 min	Individual	No	In development (Bangor University)
Drill glass for counter electrode	10 s	Individual	Yes	Automate process
Apply chloroplatinic acid	5 s	Individual	No	Spray coat
Heating chloroplatinic acid (in an oven)	30 min	Group	No	Long industrial sized oven
Heating chloroplatinic acid (with NIR)	25 s	Group	No	Industrial sized NIR
Glass cooling	1-5 min	Group	No	Forced cooling
Laser cut surlyn (A4 size sheet)	1 min	Group	Yes	Laser cutting
Assemble cell	10 s	Individual	No	Automate process
Heat seal with hot press	30 s	Group	No	Automate process
Inject electrolyte (vacuum)	1 min	Group	No	More sophisticated injection
Inject electrolyte (pump dye)	5 s	Individual	No	More sophisticated injection
Clean cell	2 s	Individual	No	More sophisticated sealing
Seal hole	10 s	Individual	No	Automate process
Apply contact (silver paint)	10 s	Individual	No	Screen printing
Silver paint drying	3 min	Group	No	NIR dry

Table 8.1: Laboratory process for a DSC evaluated by time, type, ability to prepare in advance and scale up method

The TiO_2 paste, chloroplatinic acid, dye, and electrolyte was assumed to have been made/available in advance (which is generally the case). TiO_2 could be sintered in advance and then reheated but this wouldn't be done for upscale so is not considered as a step in advance. The NIR times are taken from the lab scale NIR (section 2.1) which although the heating time is 12.5 s for 2 m/min lamp exposure the conveyor belt is longer and it takes 25 s from start to finish. This would be different for an industrial sized NIR unit and could potentially be reduced because faster speeds could be used if the unit was more powerful (assuming faster heating and cooling is not a problem for the FTO glass). Three different dyeing processes (passive, heat assisted and pump dyeing) and two different heating processes (NIR and oven) are shown as well two different electrolyte injection processes. The traditional lab method uses a vacuum to inject the electrolyte whereas the pump dyeing technique does not require a vacuum as there are two holes in the counter electrode so the electrolyte is injected in seconds. $TiCl_4$ treatment (see section 2.2.2.1) is not included in the lists of tasks for standard manufacture but it would add 30 min for soaking, an extra working electrode heating step (25 s or 30 min) and 10 s per cell to wash off and dry. Using the times from Table 8.1 with different heating and dye methods the total processing time was estimated for 1 cell and for a batch of 15 (as a common batch size). Each group step was taken to be an entire batch of cells except for doctor blading where it would be limited to 5 cells because doctor blading too many working electrodes at once decreases the uniformity of the hand drawn film. This would not be an issue for scale up where screen printing or an automated bar casting technique would be used. Each step that could be prepared in advance was disregarded for the purpose of calculating the lab processing times. Table 8.2 shows the processing times for one DSC device with each heating and dyeing method and Table 8.3 shows the same for a batch of 15 devices (taken to be a typical lab batch size).

Table 8.2: Processing times for 1 DSC device with different heating and dyeing methods

Heating method	**Dyeing method**		
	Passive dye	Heat dye	Pump dye
All Oven	17:07:37	02:07:37	01:08:47
Mixed heating	16:38:02	01:38:02	00:38:47
All NIR	16:08:27	01:08:27	00:09:12

Table 8.3: Processing times for a batch of 15 DSCs with different heating and dyeing methods

Heating method	Dyeing method		
	Passive dye	Heat dye	Pump dye
All Oven	17:21:30	02:21:30	01:50:30
Mixed heating	16:51:55	01:51:55	01:20:55
All NIR	16:22:20	01:22:20	00:51:20

The times shown are in hours:minutes:seconds. It would be unrealistic to make only 1 device with the slower dyeing methods but the times are shown for completeness. Mixed heating refers to one of the electrodes being heated in an oven and one with NIR such as the cells made in Chapters 4 and 5. Although the technique itself is fast, pump dyeing doesn't translate well to a batch of cells; it would take 30 min to dye 15 cells whereas passive heat assisted dyeing would take 1 hour and not be dependent upon the number of working electrodes, it is only limited by the size of the dye bath and oven. However the pump dyeing technique is being developed elsewhere for upscaling. Additionally it could be automated so more than one shell could be dyed at once; these times assume one pair of hands. Both NIR heating processes are assumed to be capable of heating the entire batch of 15 cells, which is possible but not done in practice due to the variation of the module for this particular unit (see section 3.3.2) which meant every sample was kept in the centre line of the platform limiting it to about 8 pieces of glass at a time. The estimations here assume that the glass takes a total of 2 min to cool and that silver paint takes 3 min to dry (at room temperature) because this is not an issue when building cells in the lab to wait a few minutes for the glass to cool and the paint to dry before measuring cells; with fast cooling and drying they were estimated to be around 30 s which will be used for the summary best case scenarios. Passive dyeing unassisted will not be considered (16 hours) instead heat assisted dyeing (1 hour at 80°C) will be used for the slow process estimation. This results in the following conclusions for 1 device manufacturing times:

A) Best case scenario oven - *2:03:07* **(123 min)**

B) Best case scenario one electrode oven, one NIR (Chapter 5) - *1:33:32* **(93.5 min)**

C) Best case scenario fast heating and passive dyeing - *1:03:57* **(64 min)**

D) Best case scenario all fast processing - *00:04:42* **(<5 min)**

E) Best case scenario all fast with fast $TiCl_4$ - *00:05:07* **(5 min)**

8.2 All NIR heated FTO glass DSCs

Following the work from Chapter 4 on NIR heated counter electrodes and the work from Chapter 5 on NIR heated working electrodes the next logical step was to construct FTO glass DSCs comprising entirely of NIR heated components. The optimal NIR intensity for the working electrode was found to be 90% and the optimal intensity for the counter electrode found to be 80%, both with a line speed of 2 m/min resulting in 12.5 s NIR exposure. Additionally to exposing the working electrode to one run of NIR, as it is in Chapter 5, TiO_2 films produced with different $TiCl_4$ treatments were investigated as discussed in section 2.2.2.1. The conventional $TiCl_4$ treatment method achieves a higher photocurrent and thus higher efficiency than a single layer of paste. However it does add a processing step which trebles the time it takes to prepare the working electrode. Therefore alternative methods were investigated to accomplish some degree of improvement by introducing smaller TiO_2 nanoparticles into the mesoporous TiO_2 film without drastically increasing the processing time. DSCs were constructed with NIR heated counter electrodes and NIR heated working electrodes with variations of $TiCl_4$ treatment as described in Table 8.4 and figure 8.3.

Table 8.4: Description of different NIR $TiCl_4$ variations and their relation to figure 8.3

Schematic	Method name	No. of NIR runs	$TiCl_4$ treatment
a	Single run "S"	1	None
b	Double run "D"	2	None
c	Fast $TiCl_4$ "F"	2	Dab with solution
d	Slow $TiCl_4$ "T"	2	Soak in solution (80°C, 30 min)

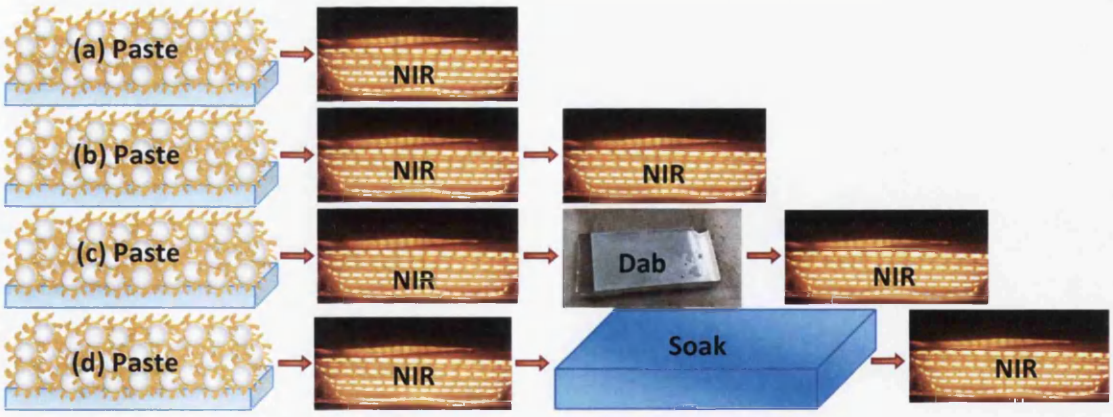

Figure 8.3: Schematic of different NIR $TiCl_4$ treatments; (a) Single, (b) Double, (c) Fast, (d) Slow

The control of one single run of NIR for 12.5 s at 90% NIR intensity (identical to that of Chapter 5) was called single run "S". For the fast $TiCl_4$ method "F", the 1 wt% $TiCl_4$ solution was dabbed onto the sintered TiO_2 with a cotton bud to cover the entire film and then exposed to NIR as soon as it had dried. For the slow $TiCl_4$ method "T", the sintered films were submerged in $TiCl_4$ solution at 80°C for 30 min in an oven as normal, washed off, dried and then subjected to a second run of NIR. To compare the effect of a second NIR run films without $TiCl_4$ treatment were subjected to two non-continuous runs known as double run "D". These devices were all passively dyed and constructed as per the standard method in section 2.2.2, the average IV parameters of 4 devices are shown in figure 8.4 and the highest performing of each cell is shown in Table 8.5.

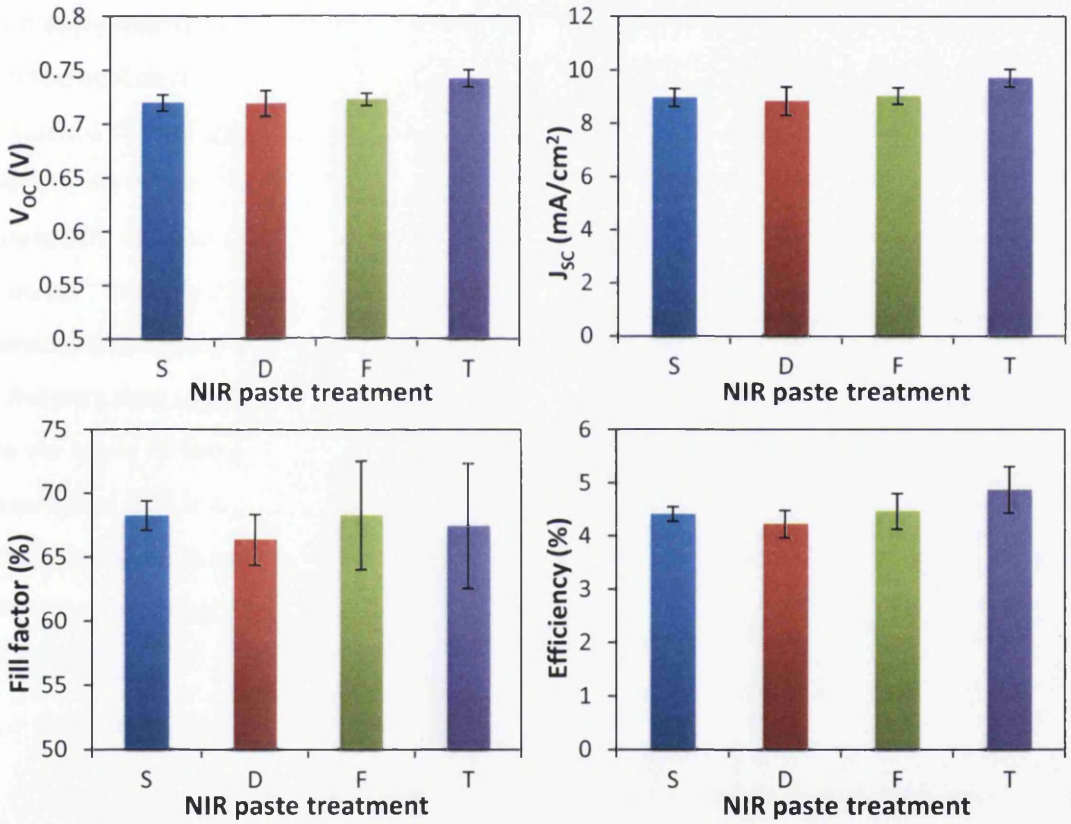

Figure 8.4: Average parameters (4 devices, 1 standard deviation error) of all NIR heated DSCs

Table 8.5: Highest performing cells of varying NIR regime for working electrode and NIR heated counter electrode

Cell	V_{OC} (V)	J_{SC} (mA/cm^2)	FF (%)	Efficiency (%)
Single run "S"	0.71	9.28	68.63	4.53
Double run "D"	0.71	9.42	65.26	4.36
Fast $TiCl_4$ "F"	0.73	9.39	71.93	4.92
Slow $TiCl_4$ "T"	0.75	9.84	72.76	5.37

The slow $TiCl_4$ treated NIR film performs the best and has a higher current density and voltage than the other films. Surprisingly the single run of NIR performs better than the double run of NIR which were the worst DSC devices with the lowest average current density and fill factor. The second run of NIR may have lead to severe cracking, grain growth or other film defects. Interestingly the fast $TiCl_4$ films performed similarly to the single NIR films. Dabbing the surface with $TiCl_4$ then applying a second run of NIR seems to have little impact but it did not cause the decrease in efficiency associated with the double run DSCs. There was strong variation in the fast $TiCl_4$ treated cells possibly due to the method of dabbing $TiCl_4$ solution, it was to get an even spread on the surface but most likely the loading varies between working electrodes. A more effective method may be a short soak; after the initial NIR run the samples could be quenched in $TiCl_4$ solution water to both cool and apply this treatment although would need to wash off the bottom and sides. However for the best devices there is an increase in V_{OC} for the fast $TiCl_4$ treated cell indicating some influence of the flash exposure of TiO_2 precursor to create a scattering layer and increase surface area. The single run NIR DSCs suffer a drop in the current density which is lower for these 90% NIR working electrodes than the cells produced in section 5.3.2, which were 9.6 mA/cm^2, the only difference between them being the counter electrode. The $TiCl_4$ treated devices had the highest average current density of 9.7 mA/cm^2, but still a slightly lower efficiency than the 90% NIR working electrode/oven counter electrode device, probably due to the lower fill factor. The open circuit voltage of these devices is also the highest at an average of 0.74 V and 0.75 V for the best device which could be due to better infiltration of the electrolyte as a result of the increased interconnectivity and surface area from the extra TiO_2 nanoparticles. SEM images were taken of NIR sintered TiO_2 films and are shown in figure 8.5.

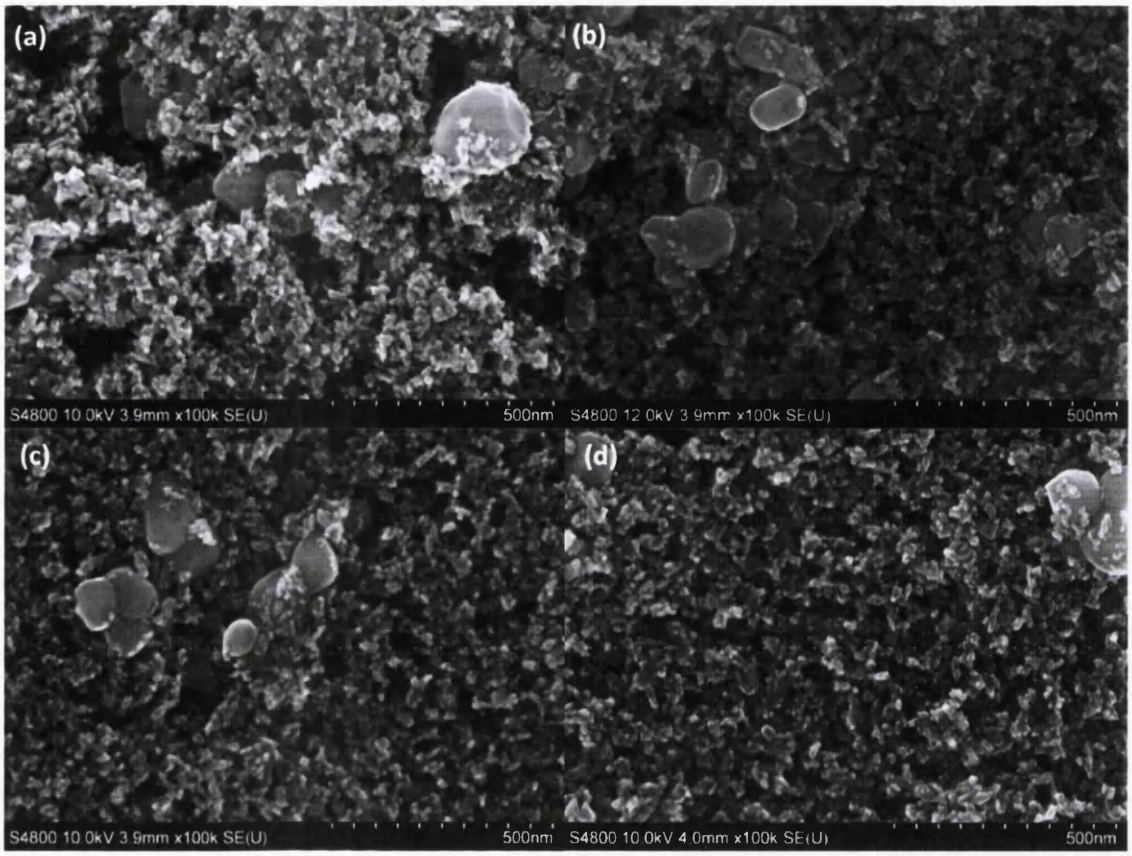

Figure 8.5: SEM images of (a) non $TiCl_4$ treated, (b) double run, (c) fast $TiCl_4$ and (d) normal $TiCl_4$ treated 90% NIR radiation sintered DSL 18NR-AO TiO_2 films at 100k x magnification

There does not appear to be a significant difference between any of the NIR exposed films. Each film was exposed at 90% NIR intensity, figure 8.5.a was for 12.5 s and figures 8.5.b-d were for 25 s total. There does not appear to be any grain growth on the surface that would reduce active area but it may be possible that beneath the surface and in closer proximity to the FTO where the heat is arising from there is some grain growth for the films exposed to two NIR runs, also the effect of the $TiCl_4$ treatment is hard to detect with the FEG-SEM because the $TiCl_4$ precursor TiO_2 nanoparticles are below 5 nm. The thermal energy derived from the second NIR exposure for figures 8.5.b-d may have been used for the forming and sintering smaller TiO_2 nanoparticles from the $TiCl_4$ for figures 8.5.c and 8.5.d, much more significantly in the latter as indicated by the much increased photocurrent and V_{OC} because there was a saturation of TiO_2 precursor as a result of the 30 min $TiCl_4$ soak. Although it may still be that there was some negative impact of the extra NIR causing cracking to the TiO_2 film. In figure 8.5.b rather than the thermal energy causing grain growth as this would have also occurred for the other double exposed films, the TiO_2 film may have cracked due to the brittle nature of porous TiO_2 and there was no increase in interconnectivity and surface area

from extra TiO_2 nanoparticles to offset this loss resulting in no voltage increase. Optoelectronic transient data was obtained for these all NIR heated cells and is discussed in section 8.3.

DSC devices comprising of both a NIR heated working and counter electrode performed slightly poorer than the equivalent oven built device with the current density lower than the identical 90% NIR working electrodes used previously. Still with a total combined heating time of only 25-37.5 s compared to 1 hour this is a step in the right direction and further work will be done to optimise the device.

8.3 Fast dyed 5 min DSC devices

In section 8.2 it was demonstrated that both the TiO_2 and the platinum oven heating steps can be replaced with NIR and obtain a similar efficiency to a conventional oven heated device. This is extremely promising as it reduces the heating time from 1 hour to 25 s or 37.5 s total meaning that the bottleneck now lies with the dyeing of the TiO_2. As was discussed in section 8.1 techniques such as pump dyeing have enabled dyeing time to be reduced to 2 min rather than a minimum of 1 hour for N719 [7]. Therefore the NIR exposure of FTO glass substrates to create working and counter electrodes of no compromise to oven heated ones in only 12.5 s each and the ultrafast dyeing of a TiO_2 film were combined as proposed in section 8.1 to manufacture a working DSC device as quickly as possible. DSCs were constructed following the method in section 2.2.5. The method was almost identical to the rest of the DSCs manufactured in previous chapters but the architecture of the cell was different. Rather than the film being a 1 x 1 cm^2 square, a 2 x 0.5 cm^2 film of TiO_2 was used with two holes drilled at either diagonal corner on the corresponding counter electrode which facilitates the pump dyeing technique better so that the dye can flow between two points with a shorter width allowing for better coverage and faster dyeing. Figure 8.6 shows the architecture of the cell and the pump dyeing in progress. The dyeing is done on a hot plate at 50°C which further aids the diffusion of the dye molecules.

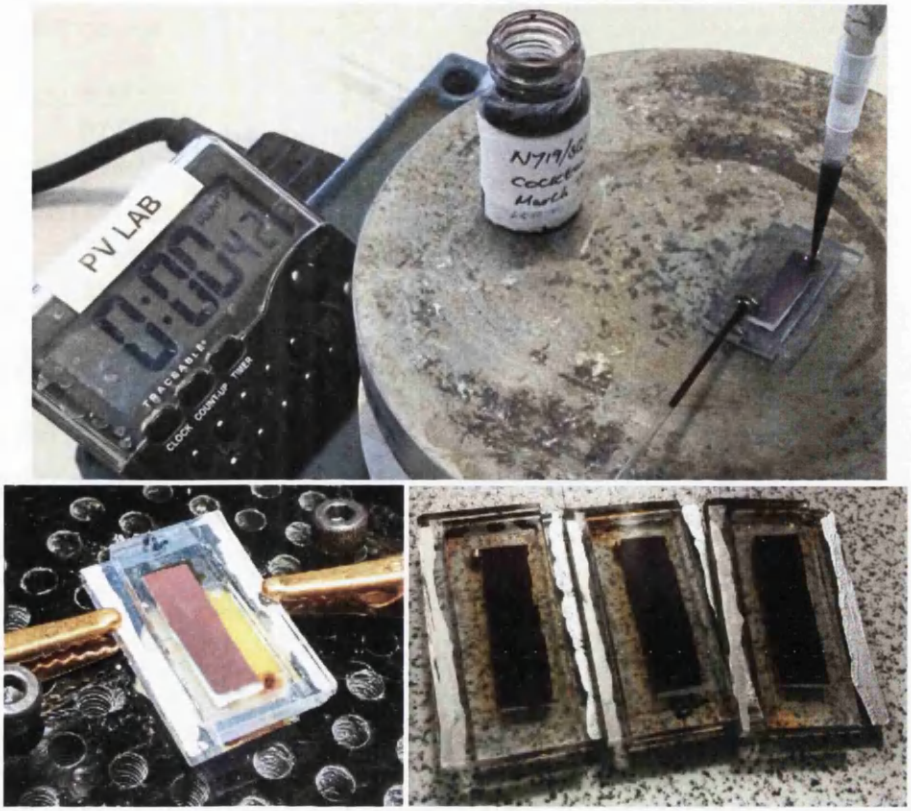

Figure 8.6: Dyeing of a shell in progress (above) and finished devices (below)

DSC "shells", which consisted of an undyed NIR heated working electrode (90% NIR intensity for 12.5 s or 25 s with the fast $TiCl_4$ method) and an NIR heated counter electrode (80% NIR intensity for 12.5 s) sealed together with 25 μm thick Surlyn and two holes in the counter electrode, were made corresponding to a manufacture time of around under 3 min. They were pump dyed using 0.5 mM N719 in 2 min and then electrolyte injected and the holes sealed. These were single sensitised 5 min DSC devices. However an advantage of the pump dyeing technique is the ease at which co-sensitisation can be achieved. It is possible to mix two or more different dyes together in solution and pump these through the DSC shells at the same time to achieve a broader absorption spectrum which would overlap between both dyes. So co-sensitised 5 min DSC devices were also manufactured. The dye used was a 1:1 ratio of 0.25 mM SQ1 with 0.5 mM chenodeoxycholic acid (CDCA) to N719 at half its saturation point. The results of these devices are shown in Table 8.6.

Table 8.6: NIR heated and fast dyed "5 min" DSC devices with different sensitisation

Cell	Dye	Fast $TiCl_4$?	V_{OC} (V)	J_{SC} (mA/cm^2)	FF (%)	Efficiency (%)
1	N719	Yes	0.76	11.22	50.61	4.31
2	N719	Yes	0.77	9.68	57.34	4.26
3	N719/SQ1	No	0.71	11.35	62.05	4.98
4	N719/SQ1	Yes	0.77	10.38	63.62	5.10
5	N719/SQ1	Yes	0.77	10.90	61.28	5.11

For all of these devices the fill factor is slightly lower and current slightly higher than the previous NIR cells because of the different architecture allowing for better current collection across the FTO with the thinner strip of TiO_2. The best single sensitisation efficiency achieved was 4.3% with a low fill factor of 50.6% which is most likely due to insufficient dyeing as the pump dyeing technique relies on skill and practice to perfect complete dye coverage. It would be expected that a higher efficiency can be obtained from N719 only but not as high as a co-sensitised device. Devices no. 3-5 were co-sensitised with the N719 and SQ1 mix described above. One of these devices used a single exposed TiO_2 working electrode rather than the fast $TiCl_4$ treated one which again showed a lower V_{OC} compared to the fast $TiCl_4$ ones. The co-sensitised solar cells all showed efficiencies above 5% which is directly comparable to a single paste layer conventional oven cell enabling the manufacture time to be reduced from 123 min to 5 min (24 times faster) with no compromise in efficiency which is an important demonstration for the translation of laboratory manufacture to scale up where time is a major issue.

Figure 8.7 shows the external quantum efficiency measured using IPCE (section 2.4) of a slow dyed and fast dyed all NIR heated N719 sensitised DSC. The fast dyed cell is of a sub-optimal dyed device so the quantum efficiency is slightly lower but it demonstrates the ease at which dyeing can be achieved in less than 2 min.

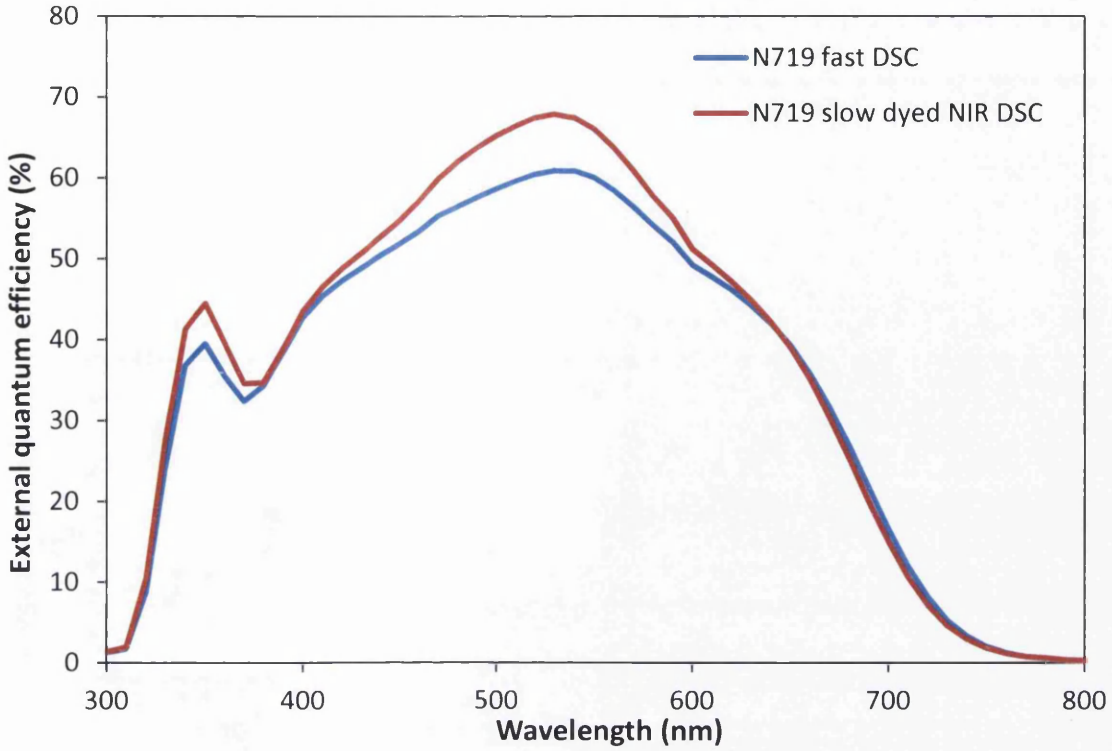

Figure 8.7: External quantum efficiency for a slow and fast dyed all NIR heated DSC

Figure 8.8 shows optoelectronic transient measurements [9] of two of the co-sensitised 5 min DSC devices with all NIR heated slow dyed devices from section 8.2. Figure 8.8.a is the charge density measured via charge extraction. The single, fast $TiCl_4$ and slow $TiCl_4$ slow dyed DSCs all show a similar charge density suggesting they have a similar level of trapped states. The double NIR exposed DSC has a slightly lower charge density and the two fast dyed 5 min cells have a lower charge density still. Figure 8.8.b shows the short circuit current transient lifetime vs. charge density at J_{SC} giving an indication of electron transport kinetics as a function of charge density. The slow $TiCl_4$ treated device has the fastest transport kinetics possibly due to the scattering layer creating greater TiO_2 connectivity with a larger surface area. The double NIR exposed and fast $TiCl_4$ treated device show fairly similar transport with the single NIR exposed layer slightly lower. The two fast dyed devices have slower transport. Figure 8.8.c shows the electron lifetime vs. V_{OC} which is the recombination lifetime. Dye is adsorbed onto most of the porous TiO_2 surface but recombination can occur at any uncoated sites. The recombination lifetime is highest in the two co-sensitised DSCs because there is more dye coverage from both SQ1 and N719 molecules so less TiO_2 exposed for recombination to occur with the electrons travelling through the TiO_2 ($2e^- + I_3^- \rightarrow 3I^-$). The SQ1 can reach sites that the N719 cannot thus achieving a higher dye coverage. For the other cells the slow $TiCl_4$ treated cell shows better recombination lifetime than the other

three which may be due to the higher surface area from the $TiCl_4$ treatment enabling better dye coverage. The others extremely are similar. Figure 8.8.d shows the electron lifetime at open circuit voltage vs. the charge density at open circuit voltage. This reinforces the higher charge density for the slow $TiCl_4$ treated DSC showing a similar trend to figure 8.8.a with an increased density of trapped states.

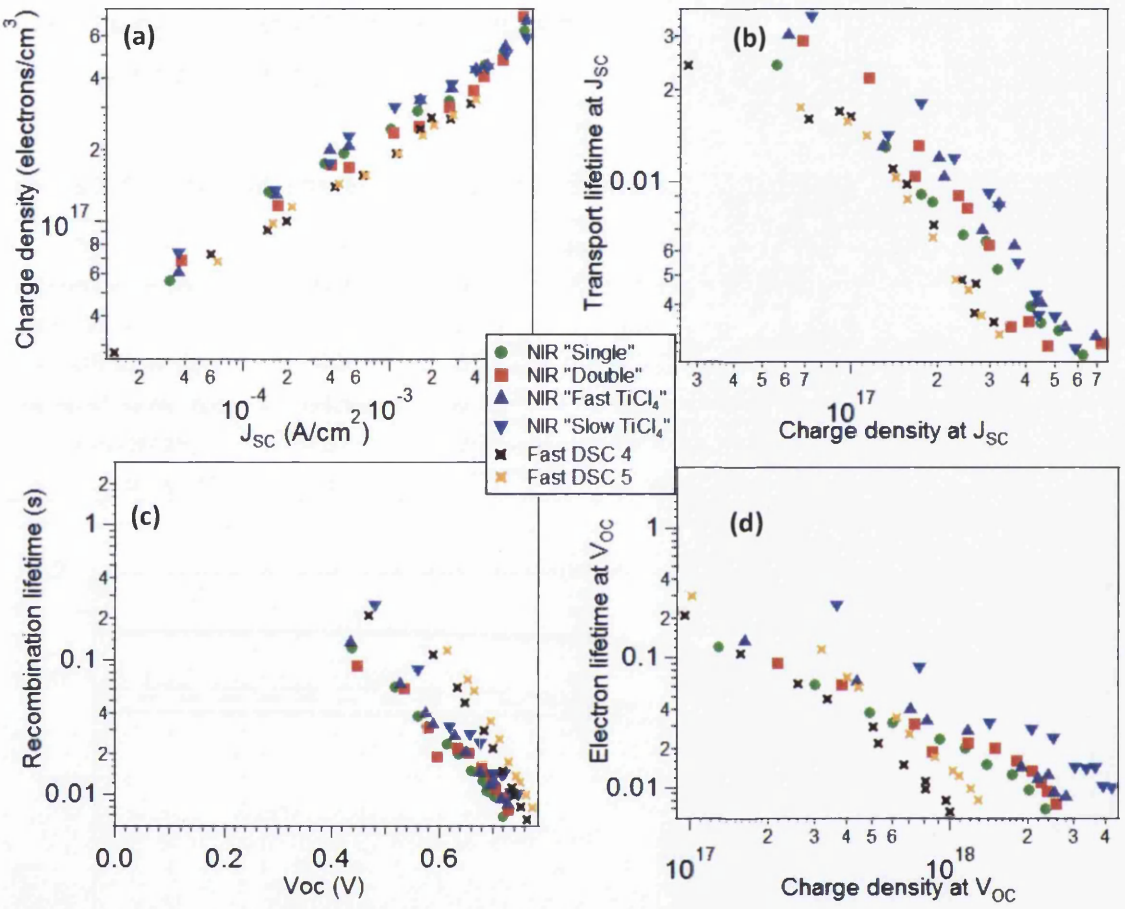

Figure 8.8: Optoelectronic transient measurements for (a) charge density vs. J_{SC}, (b) transport lifetime vs. charge density at J_{SC}, (c) electron lifetime vs. V_{OC}, and (d) electron lifetime at V_{OC} vs. charge density at V_{OC}

To summarise, figure 8.9 shows JV curves for typical NIR heated DSCs with a conventionally heated and dyed DSC with Table 8.7 showing the IV characteristics and time for each of the best cells. These correspond to the method outlined in section 8.1 as follows:

- Oven = method A, single layer of DSL 18NR-AO, working and counter electrode heated in an oven for 30 min each, sensitised with N719 for 1 hour at elevated temperature

- NIR WE = method B, single layer of DSL 18NR-AO, working electrode heated with NIR for 12.5 s, counter electrode heated in oven for 30 min, sensitised with N719 for 1 hour at elevated temperature (Chapter 5)
- All NIR = method C, both working and counter electrode NIR exposed for 12.5 s each, "single" run NIR cells shown in section 8.2
- All NIR* = method C but the "fast $TiCl_4$" NIR cells from section 8.2
- Co-dyed = method E, all NIR heating with fast $TiCl_4$ and pump dyeing, co-sensitised with N719 and SQ1

Table 8.7: DSC method, time taken and IV characteristics for each of the best cells

Method	Time (min)	V_{OC} (V)	J_{SC} (mA/cm^2)	FF (%)	Efficiency (%)
Oven slow dye	123	0.72	9.64	71.55	4.99
NIR WE/oven CE	93.5	0.74	9.67	72.39	5.17
All NIR slow dye	64	0.71	9.28	68.63	4.53
All NIR* slow dye	64.5	0.73	9.39	71.93	4.92
5 min (N719)	5	0.77	9.81	56.39	4.27
5 min (co-dyed)	5	0.77	10.90	61.28	5.11

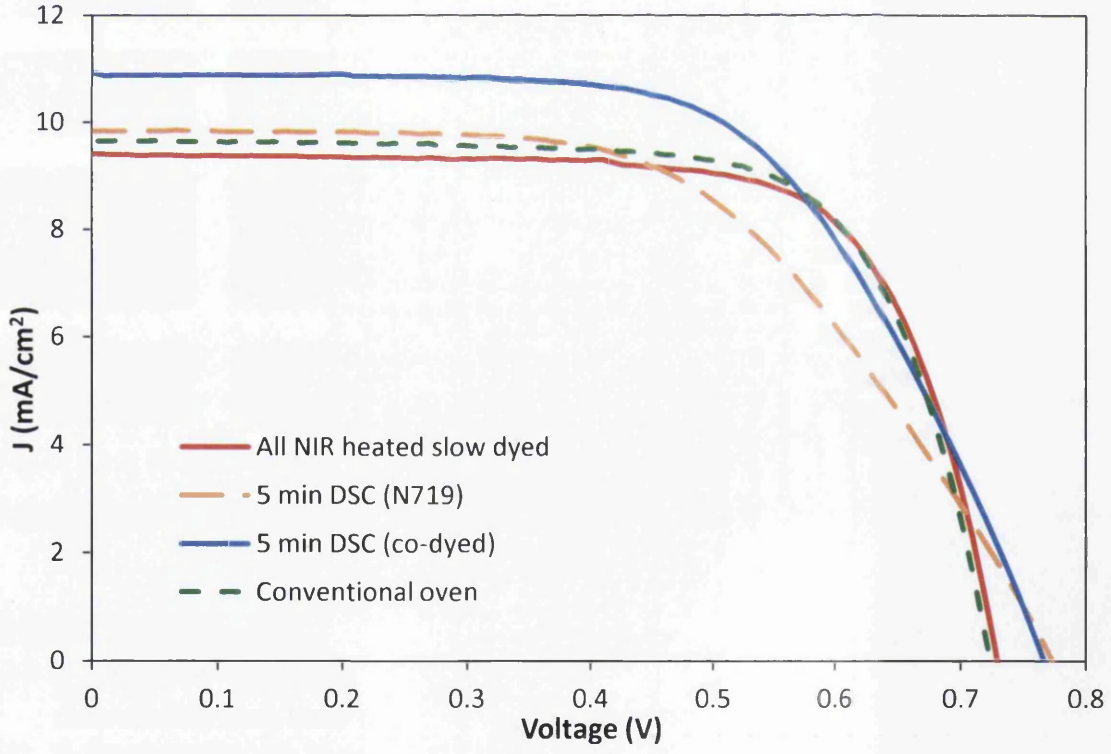

Figure 8.9: JV curves for all NIR heated slow dyed and fast dyed DSCs and a conventional oven heated and dyed DSC

Passive 16 hr dyeing was used for each slow dye rather than 1 hour elevated temperature dyeing but they are assumed to perform identically both reaching full dye loading.

8.4 Conclusions

Co-sensitised DSCs built in 5 min showed efficiencies above 5% which is directly comparable to a single paste layer conventional oven cell enabling the manufacture time to be reduced from 123 min to 5 min (24 times faster) with no compromise in efficiency. This is an important demonstration for the translation of laboratory manufacture to scale up where time is a major issue. This was achievable with NIR radiative heating for the FTO glass working and counter electrodes and high pressure pump dyeing. With optimised materials this efficiency could be improved further. The final DSC assembly laboratory method with all time saving steps is shown in figure 8.10. The NIR heating step is very suitable for upscailing to industry although for the dyeing it will be more difficult.

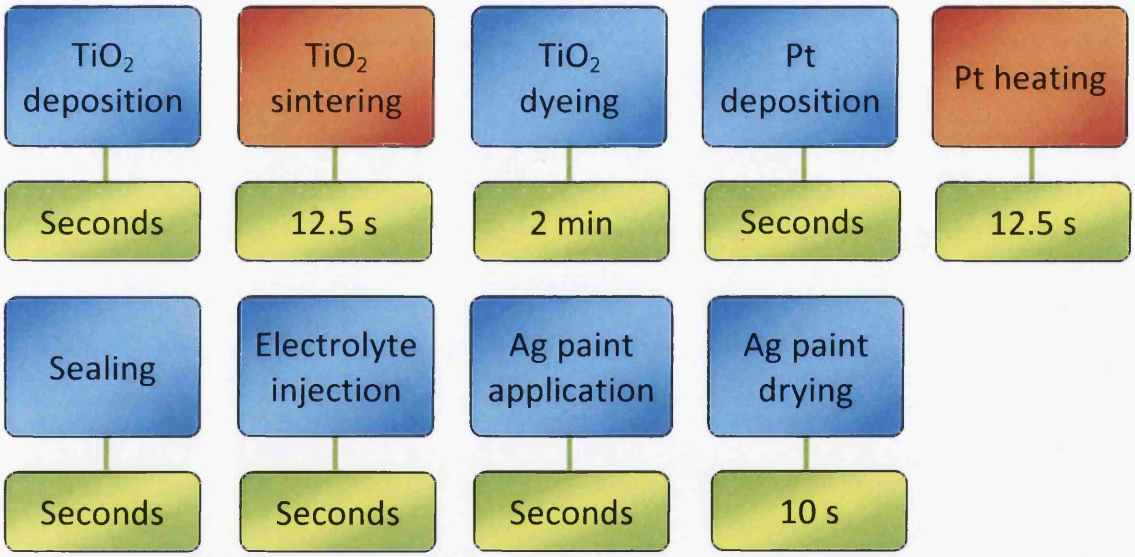

Figure 8.10: Diagram of laboratory method DSC assembly steps with associated times from fast processes

8.5 References

[1] B. O'Regan, M. Grätzel, A low-cost, high-efficiency solar cell based on dye-sensitized colloidal TiO_2 films, Nature. 353 (1991) 737–740.

[2] N. Papageorgiou, W. Maier, M. Grätzel, An Iodine/Triiodide Reduction Electrocatalyst for Aqueous and Organic Media, J. Electrochem. Soc. 144 (1997) 876–884.

[3] T. Watson, P. Holliman, D. Worsley, Rapid, continuous in situ monitoring of dye sensitisation in dye-sensitized solar cells, J. Mater. Chem. 21 (2011) 4321–4325.

[4] M.K. Nazeeruddin, R. Splivallo, P. Liska, P. Comte, M. Grätzel, A swift dye uptake procedure for dye sensitized solar cells., Chem. Commun. (2003) 1456–7.

[5] Y. Ogomi, S. Sakaguchi, T. Kado, M. Kono, Y. Yamaguchi, S. Hayase, Ru Dye Uptake under Pressurized CO_2 Improvement of Photovoltaic Performances for Dye-sensitized Solar Cells, J. Electrochem. Soc. 153 (2006) A2294–A2297.
[6] Y. Ogomi, Y. Kashiwa, Y. Noma, Y. Fujita, S. Kojima, M. Kono, et al., Photovoltaic performance of dye-sensitized solar cells stained with black dye under pressurized condition and mechanism for high efficiency, Sol. Energy Mater. Sol. Cells. 93 (2009) 1009–1012.
[7] P. Holliman, M. Davies, A. Connell, Solar cells with multiple dyes, US 2013/0167900 A1, 2013.
[8] P.J. Holliman, M.L. Davies, A. Connell, B. Vaca Velasco, T.M. Watson, Ultra-fast dye sensitisation and co-sensitisation for dye sensitized solar cells., Chem. Commun. 46 (2010) 7256–8.
[9] P.R.F. Barnes, K. Miettunen, X. Li, A.Y. Anderson, T. Bessho, M. Grätzel, et al., Interpretation of optoelectronic transient and charge extraction measurements in dye-sensitized solar cells, Adv. Mater. 25 (2013) 1881–922.

9. Conclusions and Further Work

9.1 Conclusions

For the first time NIR radiation was shown to heat FTO and ITO coated glass to significantly high temperatures, high enough to be compatible with the fabrication processes associated with dye-sensitised solar cells (DSCs), in only 12.5 s of exposure. This dramatic time reduction is very attractive for industrial manufacture, especially if traditional heating steps can be replicated to the same efficacy with the NIR heating technique. Of additional significance is the compatibility of this technique for the heating of glass based substrates which will also enable a wider range of applications, especially where transparency is desired, because previously NIR radiation had only been demonstrated for reducing heating times on metallic substrates.

NIR radiation was used to thermally decompose chloroplatinic acid to catalytic platinum on FTO glass for use as a counter electrode in a DSC device in only 12.5 s of heating time, 144 times faster than the conventional lab method. This is the first example of a rapidly heated counter electrode for a DSC device and demonstrates the possibility of being able to drastically reduce the time required for one of the most limiting stages in DSC manufacture. In addition there appeared to be a wide temperature processing window either side of the optimal NIR intensity that achieves sufficiently catalytic platinum for a well performing DSC device. This is very desirable for industrial applications where a slight variation in the power output of the NIR lamps would not risk large scale wastage of the substrate.

NIR radiation was used to sinter TiO_2 onto FTO glass for the construction of a DSC working electrode with identical performance to a conventional device in only 12.5 s, a heating time reduction of 144 times. The use of NIR radiation to sinter TiO_2 films in 12.5 s has been previously demonstrated on metallic substrates but this is the first time it has been shown on glass based substrates. In the case of DSCs the ability to heat a working electrode on FTO glass eliminates the necessity of reverse illumination and any chemical incompatibilities associated with metals, allowing the potential for very high efficiency devices with fast manufacturing times.

A further benefit revealed when using NIR radiation to heat ITO glass to significantly high temperatures in 12.5 s was the ability to reach a higher temperature than conventional

heating with no resistivity rise. A maximum predicted temperature of 505°C was obtained using 12.5 s of NIR heating with no significant rise in sheet resistance (the same rise experienced for 30 min oven exposure at 300°C) which presents a further 200°C higher temperature range for processing on ITO substrates while preserving the conductivity, broadening the possible applications. It is believed that the short exposure of NIR limits the oxygen diffusion into ITO's vacancies, which are responsible for its reduction in carrier concentration and mobility, thereby reducing the severity of a high temperature.

To explore the possibility of using ITO glass substrates outside their normal temperature processing range NIR radiation was used to heat electrodes on ITO glass for DSC devices. Although ITO glass would not replace FTO glass as the substrate of choice it would demonstrate that other higher temperature applications on ITO glass could be possible. In addition it directly compares against other methods of making DSCs on ITO glass usually involving a cumbersome post annealing step to recover the oxygen vacancies. Chloroplatinic acid on ITO glass exposed to 12.5 s of NIR radiation was used as a counter electrode in a DSC device and it was 0.85 times as efficient as an equivalent oven heated FTO glass device and 0.87 times as efficient as a NIR heated counter electrode FTO glass device. NIR exposed TiO_2 working electrodes for DSCs were built on ITO glass at an efficiency 0.95 times that of an equivalent simple oven heated FTO glass DSC device with a heating time of only 12.5 s. This is extremely promising for the use of NIR radiation to heat ITO glass because an efficiency so close to that of the equivalent FTO glass DSC without necessary post sintering treatments to reintroduce the ITO vacancies has not been published before in the literature.

High temperature DSCs were also built entirely on ITO glass with only 25 s or 37.5 s total heating time. The optimum device utilised $TiCl_4$ solution with a few drops before a second run of NIR exposure increasing the efficiency dramatically to just above that of a simple standard FTO glass device. The average efficiency is higher than the best ITO glass working electrode/FTO counter electrode device and almost on par with the standard oven heated FTO glass device. This is an extremely promising demonstration of NIR radiation as a high temperature heating technique compatible with ITO for electronic devices.

NIR heated titanium counter electrodes DSCs achieved equal performance to oven heated counter electrode on titanium but with higher reproducibility and in only 12.5 s. This gives the potential for rapidly producing a flexible DSC which is highly desirable for

commercialisation due to savings of cost, time, and the ability to incorporate into a building material.

Co-sensitised DSCs built in 5 min showed efficiencies above 5% which is directly comparable to a single paste layer conventional oven cell enabling the manufacture time to be reduced from 123 min to 5 min (24 times faster) with no compromise in efficiency. NIR radiation was used to heat both FTO glass TiO_2 working electrodes and FTO glass platinum counter electrodes in just 12.5 s, 144 times faster than conventional heating and was combined with a fast pump dyeing technique developed elsewhere to further reduce the fabrication time. This is an extremely promising demonstration for the translation of laboratory manufacture to techniques compatible on an industrial scale and could benefit the commercialisation of dye-sensitised solar cells.

9.2 Further work

The NIR heating of TCO coated glass could be very useful for a range of electronic devices. Crucially the TiO_2 sintering stage of DSC manufacture shares many similarities to other technologies and applications. This proven ability to heat TiO_2 films rapidly on FTO glass could easily be expanded to other devices, for example other solar cells such as perovskites and solid state DSCs, and photocatalysts for water purification and solar fuel cells, with little modification and should be investigated. Additionally it should be possible to achieve a mesoporous film of any metal oxide similar, such as ZnO or Al_2O_3, that are contained in a similar paste where binder needs to be removed. Further investigation is needed to explore other options for the NIR heating of glass substrates; potentially any electronic device based on TCO coated glass which requires a long heating step could benefit from this technique.

A module sized device DSC was not demonstrated here but should be investigated to compare against conventionally heated large devices. The commercialisation of DSCs may not be viable for building integrated photovoltaics that need at least 25 years lifetime due to problems with sealing of the electrolyte and stability. However a very viable use for DSCs is in portable applications such as personal electronics and cheap remote power in isolated areas where this shorter lifetime would not be an issue and the lightweight and low light and strong absorption in the visible range (for indoor lighting) becomes a huge benefit. Although sealing will always be an issue for liquid DSCs and a limiting factor in their lifetime they do not have the drawbacks that solid state perovskite solar cells have, the presence of lead

possibly restricting the market and their poor stability to moisture, so the commercialisation of DSCs is still possible and could benefit greatly from rapid NIR heating.

Although ITO glass is an unlikely candidate for the commercialisation of DSCs it is used for many other devices, such as OLEDs, especially where smoothness is required and NIR radiation could be used to reduce heating times and extend the temperature processing window for any application where ITO is desirable. The rapid high temperature heating of ITO glass should be explored further and could potentially benefit a wider range of technologies.

In addition other TCOs that exhibit resistivity problems with high temperature heating, such as aluminium doped zinc oxide (AZO), could also be investigated with NIR heating to see if higher temperatures can be attained compared to conventional heating with no increase in sheet resistance.